Biomechanical Responses of Human Surrogates under Various Frontal Loading Conditions with an Emphasis on Thoracic Response and Injury Tolerance

Devon Lee Albert

Dissertation submitted to the faculty of the Virginia Polytechnic Institute and State University in partial fulfillment of the requirements for the degree of

Doctor of Philosophy
In
Biomedical Engineering

Andrew R. Kemper, Chair
Amanda M. Agnew
H. Clay Gabler
Warren N. Hardy
Joel D. Stitzel

4/19/2018
Blacksburg, VA

Keywords: Hybrid III, THOR, PMHS, knee bolster, knee bolster airbag, frontal motor vehicle collision, thoracic injury criterion, rib, material properties

Biomechanical Responses of Human Surrogates under Various Frontal Loading Conditions with an Emphasis on Thoracic Response and Injury Tolerance

Devon Lee Albert

ABSTRACT

Frontal motor vehicle collisions (MVCs) resulted in 10,813 fatalities and 937,000 injuries in 2014, which is more than any other type of MVC. In order to mitigate the injuries and fatalities resulting from MVCs, new safety restraint technologies and more biofidelic anthropomorphic test devices (ATDs) have been developed. However, the biofidelity of these new ATDs must be evaluated, and the mechanisms of injury must be understood in order to accurately predict injury. Evaluating the biomechanical response, injury mechanisms, and injury threshold of the thorax are particularly important because the thorax is one of the most frequently injured body regions in MVCs. Furthermore, sustaining a severe thoracic injury in an MVC significantly increases mortality risk.

The overall objective of this dissertation was to evaluate the biomechanical responses of human surrogates under various frontal loading conditions. This objective was divided into three sub-objectives: 1) to evaluate the biofidelity of the current frontal impact ATDs, 2) to evaluate the effect of different safety restraints on occupant responses, and 3) to evaluate rib material properties with respect to sex, age, structural response, and loading history.

In order to meet sub-objectives 1 and 2, full-scale frontal sled tests were performed on three different human surrogates: the 50th percentile male Hybrid III (HIII) ATD, the 50th percentile male Test Device for Human Occupant Restraint (THOR-M) ATD, and approximately 50^{th} percentile male post-mortem human surrogates (PMHS). All surrogates were tested under three safety restraint conditions: knee bolster (KB), KB and steering wheel airbag (KB/SWAB), and knee bolster airbag and SWAB (KBAB/SWAB). The kinematic, lower extremity, abdominal, thoracic, and neck responses were then compared between surrogates and restraint conditions. In order to assess biofidelity, the ATD responses were compared to the PMHS responses. For both the kinematic and thoracic responses, the HIII and THOR-M had comparable biofideltiy. However, the HIII responses

were slightly more biofidelic. The ATDs experienced similar lower extremity kinetics, but very different kinetics at the upper and lower neck due to differences in design. Evaluation of the different restraint conditions showed that the SWAB and KBAB both affected injury risk. The SWAB decreased head injury risk for all surrogates, and increased or decreased thoracic injury risk, depending on the surrogate. The KBAB decreased the risk of femur injury, but increased or decreased tibia injury risk depending on the surrogate and injury metric used to predict risk.

In order to meet sub-objective 3, the tensile material properties of human rib cortical bone and the structural properties of whole ribs were quantified at strain rates similar to those observed in frontal impacts. The rib cortical bone underwent coupon tension testing, while the whole ribs underwent bending tests intended to simulate loading from a frontal impact. The rib material properties accounted for less than 50% of the variation observed in the whole rib structural properties, indicating that other factors, such as rib geometry, were also influencing the structural response of whole ribs. Age was significantly negatively correlated with the modulus, yield stress, failure strain, failure stress, plastic strain energy density, and total strain energy density. However, sex did not significantly influence any of the material properties. Cortical bone material properties were quantified from the ribs that underwent the whole rib bending tests and subject-matched, untested (control) ribs in order to evaluate the effect of loading history on material properties. Yield stress and yield strain were the only material properties that were significantly different between the previously tested and control ribs.

The results of this dissertation can guide ATD and safety restrain design. Additionally, this dissertation provides human surrogate response data and rib material property data for the validation of finite element models, which can then be used to evaluate injury mitigation strategies for MVCs.

Biomechanical Responses of Human Surrogates under Various Frontal Loading Conditions with an Emphasis on Thoracic Response and Injury Tolerance

Devon Lee Albert

GENERAL AUDIENCE ABSTRACT

Frontal motor vehicle collisions (MVCs) resulted in 10,813 fatalities and 937,000 injuries in 2014, which is more than any other type of MVC. In order to mitigate the injuries and fatalities resulting from MVCs, new safety restraint technologies, e.g., seat belts, and more biofidelic (human-like) anthropomorphic test devices (ATDs), i.e., crash test dummies, have been developed. However, the biofidelity of these new ATDs must be evaluated, and the mechanisms of injury must be understood in order to accurately predict injury. Evaluating the biomechanical response, injury mechanisms, and injury threshold of the thorax (chest) are particularly important because the thorax is one of the most frequently injured body regions in MVCs. Furthermore, sustaining a severe thoracic injury in an MVC significantly increases the risk of death.

The overall objective of this dissertation was to evaluate the biomechanical responses of human surrogates under various frontal loading conditions. This objective was divided into three sub-objectives: 1) to evaluate the biofidelity of the current frontal impact ATDs, 2) to evaluate the effect of different safety restraints on occupant responses, and 3) to evaluate rib material properties with respect to sex, age, structural response, and loading history.

In order to meet sub-objectives 1 and 2, frontal crash tests were simulated in the laboratory using a crash sled. These sled tests were performed on three different human surrogates: the Hybrid III (HIII) ATD, the Test Device for Human Occupant Restraint (THOR-M) ATD, and post-mortem human surrogates (PMHS), i.e., cadavers. All surrogates were tested under three safety restraint conditions: knee bolster (KB), KB and steering wheel airbag (KB/SWAB), and knee bolster airbag and SWAB (KBAB/SWAB). The kinematic (body movements), lower extremity, abdominal, thoracic, and neck responses were then compared between surrogates and restraint conditions. In order to assess biofidelity, the

ATD responses were compared to the PMHS responses. For both the kinematic and thoracic responses, the HIII and THOR-M had comparable biofideltiy. However, the HIII responses were slightly more biofidelic. The ATDs experienced similar lower extremity kinetics (forces and moments), but very different kinetics at the upper and lower neck due to differences in design. Evaluation of the different restraint conditions showed that the SWAB and KBAB both affected injury risk. The SWAB decreased head injury risk for all surrogates, and increased or decreased thoracic injury risk, depending on the surrogate. The KBAB decreased the risk of femur injury, but increased or decreased tibia injury risk depending on the surrogate and how injury risk was predicted.

In order to meet sub-objective 3, the material properties of human rib cortical bone and the structural response of whole ribs were quantified under experimental conditions reminiscent of what the bone would experience during a frontal impact. The rib cortical bone underwent material testing, while the whole ribs underwent bending tests intended to simulate a frontal impact. The rib material properties only partially influenced the structural response of the whole rib. This indicated that other factors, such as rib shape and thickness, were also influencing the structural response. Age was correlated to a decrease in several material properties. However, there was no significant difference between male and female material properties. Some differences in material properties were observed in cortical bone from fractured and intact ribs, indicating that the fracture influenced the rib material properties.

The results of this dissertation can guide ATD and safety restrain design. Additionally, this dissertation provides human surrogate response data and rib material property data for finite element (computer) models, which can then be used to evaluate injury prevention strategies for MVCs.

ACKNOWLEDGEMENTS

First, I would like to thank my advisor, i.e., Dr. Andrew Kemper, for teaching me about injury biomechanics, proving many opportunities I would not have had otherwise, and putting up with my stubbornness for the last four years.

I would also like to thank my committee members for their time and thoughtful input.

The members of the Injury Biomechanics Research Center at The Ohio State University were awesome collaborators. In particular, Dr. Amanda Agnew and Dr. Yun-Seok Kang provided enthusiastic support and encouragement that is much appreciated.

I would like to acknowledge my former co-workers at the University of Pittsburgh Human Movement and Balance Lab, particularly Dr. Kurt Beschorner, Jenna Trout, and Aaron Ledgerwood. They taught me how to perform academic research and were instrumental in preparing me for graduate school.

I am grateful for the support of my family and friends. In particular, Stephanie Beeman was a model grad student who taught me many things, including attention to detail. Also, Danielle Cristino was a constant source of support in both grad school and life.

Several sources of funding supported the work in this dissertation, including Toyota Motor Corporation, Autoliv, and the ICTAS Doctoral Scholars Program.

Finally, this work would not be possible without the contribution of the anatomical donors.

ATTRIBUTION

Several people contributed to the work in this dissertation. Their names are listed below for each chapter along with a description of each person's contribution.

Chapter 2:

- Stephanie M. Beeman (Virginia Tech) contributed to experimental testing and provided input during the writing process.
- Craig McNally (Virginia Tech) contributed to experimental testing.
- Andrew R. Kemper (Virginia Tech) contributed to experimental testing and provided input during the writing process.

Chapter 3:

- Stephanie M. Beeman contributed to experimental testing, contributed to the Introduction section, and provided input regarding the other sections during the writing process.
- Andrew R. Kemper contributed to experimental testing and provided input during the writing process.

Chapter 4:

- Stephanie M. Beeman contributed to experimental testing.
- Warren N. Hardy (Virginia Tech) developed the method for instrumenting the post-mortem human surrogate lower extremity.
- Andrew R. Kemper contributed to experimental testing and provided input during the writing process.

Chapters 5 - 7:

- Stephanie M. Beeman contributed to experimental testing and provided input during the writing process.
- Andrew R. Kemper contributed to experimental testing and provided input during the writing process.

Chapters 8 & 9:

- Yun-Seok Kang (The Ohio State University) contributed to the whole rib bending tests and provided input during the writing process.
- Amanda M. Agnew (The Ohio State University) contributed to the whole rib bending tests and provided input during the writing process.
- Andrew R. Kemper contributed to the coupon tension tests and provided input during the writing process.

TABLE OF CONTENTS

LIST OF FIGURES

LIST OF TABLES

CHAPTER 1: INTRODUCTION

Despite advances in vehicle safety, 10,813 fatalities and 937,000 injuries resulted from frontal motor vehicle collisions (MVCs) in 2014 alone [1]. An evaluation of AIS3+ injuries in frontal MVCs involving vehicles that scored well on the Insurance Institute for Highway Safety (IIHS) frontal offset and the National Highway and Traffic Safety Administration's (NHTSA's) New Car Assessment Program (NCAP) frontal crash tests showed that one third of severe injuries were the result of interaction with the safety restraint systems [2]. More specifically, these injuries were the result of either direct loading from the safety restraint systems or failure of the systems to properly restrain the occupant and prevent loading from other features of the occupant compartment. The occurrence of these injuries in highly rated vehicles may be a result of deficits in ATD biofidelity, ATD instrumentation, injury risk criteria, or the ability of the safety rating crash tests to represent real-world crash conditions.

In order to improve the efficacy of NHTSA's NCAP frontal crash tests at predicting occupant injuries, NHTSA plans to replace the current standard frontal anthropomorphic test device (ATD), the Hybrid III (HIII), with the Test device for Human Occupant Restraint (THOR) [3]. The THOR was designed to be more anatomically biofidelic and to produce more biofidelic kinematics and loading responses than the HIII [3]. The THOR neck was designed to be less stiff than the HIII neck [4,5]. The THOR shoulder was designed to be more anatomically correct by introducing a clavicle and the ability to displace forward and upward [6,7]. The thorax design was improved by increasing the number of ribs and incorporating a downward rib slant, which was more representative of human anatomy [8,9]. Finally, both the pelvis and abdomen were redesigned to be more anatomically-correct and produce more biofidelic interactions with restraint systems [6]. Despite all of these improvements, the current version of the THOR, the THOR-M, has yet to be evaluated under a variety of safety restraint conditions in full-scale frontal sled tests. Since the biofidelity of an ATD may vary when the ATD is exposed to different restraint conditions, It is imperative to assess the comparative biofidelities of the THOR-M and HIII under a variety of test conditions before the THOR-M is implemented as the new standard frontal ATD.

In recent years, knee bolster airbags (KBABs) have been introduced into the vehicle fleet as an added safety restraint to mitigate lower extremity injuries. KBABs are also hypothesized to mitigate thoracic injuries by limiting the forward excursion of the pelvis and thorax, thereby decreasing thoracic loading from other potentially injurious safety restraints, such as the shoulder belt and airbag [10]. However, the efficacy of KBABs as compared to the standard knee bolster (KB) has yet to be evaluated in the laboratory due to the difficulties associated with implementing these restraints in full-scale sled tests. Therefore, appropriate surrogate KBs and KBABs must be proposed and validated before the efficacy of KBABs at mitigating lower extremity and thoracic injuries can be evaluated using different human surrogates.

Evaluating the thoracic responses and injury risks of human surrogates to various safety restraint conditions is particularly important because the chest is the second most injured body region in MVCs [11]. Rib fractures are a commonly observed chest injury for post-mortem human surrogates (PMHSs) as a result of frontal thoracic loading [12-17]. Furthermore, sustaining severe (AIS3+) rib fractures in an MVC increases mortality risk, especially for older occupants [18]. Previous work using uncensored rib fracture data (i.e. data where the exact time of AIS3+ injury was known) has demonstrated that current thoracic injury risk curves over-predict the amount of chest deflection corresponding to a 50% risk of sustaining an AIS3+ injury [15]. However, the previous study used simplified experimental setups with only seat belt loading to evaluate the performance of thoracic injury criteria. It is currently unknown whether the same results would be observed for full-scale sled tests, where experimental conditions would be more similar to real-world crashes and a variety of restraint conditions can be used. Therefore, it is necessary to evaluate thoracic injury risk criteria using censored data from full-scale sled tests with multiple restraint conditions.

Older occupants are more likely to sustain and succumb to severe thoracic injuries than younger occupants [18-20]. Older females, in particular are more likely to sustain severe thoracic injuries [8,21]. In support of these epidemiological findings, experimental testing has shown that thoracic injury tolerance decreases with age [22-25]. This decrease has been attributed to several factors including changes in bone quality, material properties, and rib geometry, all of which could influence rib structural properties. Previous studies conducted whole rib bending tests on a large

number of subjects in order to quantify rib structural properties in a frontal impact scenario and investigate the effect of age, sex, and geometry on rib structural properties [26-28]. However, the contribution of material properties on the resulting structural properties has yet to be quantified. Linking cortical bone tensile material properties to whole rib structural properties would give insight into the relative contributions of material properties and rib geometry on the structural response of whole ribs. Furthermore, comparing the material properties between ribs that did and did not undergo structural bending tests would provide an opportunity to investigate rib material property changes as a result of injurious loading. This knowledge could be applied to future studies in order to generate matched datasets of structural and material properties for modeling applications. Where previous studies on rib material properties have been limited by small sample sizes [29-31], the quantification of rib material properties for a large and diverse sample would facilitate assessments on the effects of age and sex on material properties.

Research Objectives

Based on the current needs in the fields of automotive safety and injury biomechanics, several biomechanical research studies were undertaken in this dissertation to quantify the biomechanical responses of human surrogates, including the HIII and THOR-M ATDs and post-mortem human surrogates (PMHSs), to various frontal loading conditions. Particular emphasis was placed on thoracic response due to the prevalence and mortality risk of thoracic injuries in MVCs. The specific objectives of this dissertation are as follows:

1) Assess the efficacy of rigid polyurethane foams as knee bolster and knee bolster airbag surrogates in full-scale frontal sled tests
2) Evaluate the occupant kinematics of the HIII, THOR-M, and PMHSs during full-scale frontal sled tests under three safety restraint conditions: knee bolster, knee bolster and steering wheel airbag, and knee bolster airbag and steering wheel airbag
3) Evaluate the lower extremity responses of the HIII, THOR-M, and PMHSs during full-scale frontal sled tests under three safety restraint conditions: knee bolster, knee bolster and steering wheel airbag, and knee bolster airbag and steering wheel airbag

4) Evaluate the abdominal organ responses of the THOR-M and PMHSs during full-scale frontal sled tests under three safety restraint conditions: knee bolster, knee bolster and steering wheel airbag, and knee bolster airbag and steering wheel airbag
5) Evaluate the neck responses of the HIII, THOR-M, and PMHSs during full-scale frontal sled tests under three safety restraint conditions: knee bolster, knee bolster and steering wheel airbag, and knee bolster airbag and steering wheel airbag
6) Evaluate the thoracic responses of the HIII, THOR-M, and PMHSs during full-scale frontal sled tests under three safety restraint conditions: knee bolster, knee bolster and steering wheel airbag, and knee bolster airbag and steering wheel airbag
7) Investigate changes in rib cortical bone material properties with respect to age, structural properties, and injurious loading

References

1. NHTSA. *Traffic Safety Facts 2014: A Compilation of Motor Vehicle Crash Data Form the Fatality Analysis Reporting System and the General Estimates System*. Washington, DC: Transportation USDo; 2014.
2. Brumbelow ML, Zuby DS. Impact and Injury Patterns in Frontal Crashes of Vehicles with Good Ratings for Frontal Crash Protection. Paper presented at: Arlington, VA: Insurance Institute for Highway Safety. To be presented at the 21st International Technical Conference on the Enhanced Safety of Vehicles, Stuttgart, Germany2009.
3. Federal Register. *Part V. National Highway Traffic Safety Administration Consumer Information: New Car Assessment Program*. U.S. Department of Transportation; 2015.
4. Hoofman M, van Ratingen MR, Wismans J. Evaluation of the Dynamic and Kinematic Performance of the Thor Dummy: Neck Performance. Proceedings of the International Research Council on the Biomechanics of Injury conference (IRCOBI); September 16-18, 1998.
5. White RP, Zhoa Y, Rangarajan N, Haffner M. Development of an Instrumented Biofidelic Neck for the Nhtsa Advanced Frontal Test Dummy. Paper presented at: The 15th International Technical Conference on the Enhanced Safety of Vehicles; May, 1996; Melbourne, Australia.
6. Haffner M, Eppinger R, Rangarajan N, Shams T, Artis M, Beach D. Foundations and Elements of the Nhtsa Thor Alpha Atd Design. Paper presented at: 17th ESV Conference, Paper2001.
7. Törnvall FV, Holmqvist K, Davidsson J, Svensson MY, Håland Y, Öhrn H. A New Thor Shoulder Design: A Comparison with Volunteers, the Hybrid Iii, and Thor Nt. *Traffic injury prevention.* 2007;8(2):205-215.
8. Ridella SA, Rupp JD, Poland K. Age-Related Differences in Ais 3+ Crash Injury Risk, Types, Causation and Mechanisms. Paper presented at: Ircobi Conference2012.
9. Schneider LW, Haffner MP, Eppinger RH, Salloum MJ, Beebe MS, Rouhana SW, King AI, Hardy WN, Neathery RF. *Development of an Advanced Atd Thorax System for Improved Injury Assessment in Frontal Crash Environments.* SAE Technical Paper;1992. 0148-7191.

10. Roychoudhury RS, Conlee JK, Best M, Schenck D. Blow-Molded Plastic Active Knee Bolsters. Paper presented at: SAE World Congress 2004; March 8-11, 2004; Detroit, Michigan.
11. Cavanaugh JM, Yoganandan N. Thorax Injury Biomechanics. In: Yoganandan N, Nahum AM, Melvin JW, eds. *Accidental Injury Biomechanics and Prevention*. 3 ed. New York: Springer; 2015:331-372.
12. Crandall JR, Bass CR, Pikey W, Miller H, Sikorski J, Wilkins M. Thoracic Response and Injury with Belt, Driver Side Airbag, and Force Limited Belt Restraint Systems. *International Journal of Crashworthiness.* 1996;2(1):119-132.
13. Cromack JR, Ziperman HH. *Three-Point Belt Induced Injuries: A Comparison between Laboratory Surrogates and Real World Accident Victims.* SAE Technical Paper;1975. 0148-7191.
14. Kallieris D, Zerial P, Rizzetti A, Mattern R. Prediction of Thoracic Injuries in Frontal Collisions. Paper presented at: Proc. 18th International Technical Conference on the Enhanced Safety of Vehicles1998.
15. Kemper AR, Beeman SM, Porta DJ, Duma SM. Non-Censored Rib Fracture Data During Frontal Pmhs Sled Tests. *Traffic injury prevention.* 2016;17(sup1):131-140.
16. Patrick L. Frontal Force Impact Tolerance of the Human Thorax. *The Human Thorax-Anatomoy, Injury, and Biomechanics, SAE P-67, Dearborn, MI.* 1976:37-48.
17. Ramet M, Cesari D. Behavior of Restrained Dummies and Cadavers in Frontal Impacts. *Proc. 7th International Research Council on the Biomechanics of Impact.* 1979:210-219.
18. Kent R, Woods W, Bostrom O. Fatality Risk and the Presence of Rib Fractures. Paper presented at: Annals of Advances in Automotive Medicine/Annual Scientific Conference2008.
19. Bulger EM, Arneson MA, Mock CN, Jurkovich GJ. Rib Fractures in the Elderly. *Journal of Trauma and Acute Care Surgery.* 2000;48(6):1040-1047.
20. Kent R, Henary B, Matsuoka F. On the Fatal Crash Experience of Older Drivers. Paper presented at: Annu Proc Assoc Adv Automot Med2005.
21. Rhule H, Mallory A, Hagedorn A. Real World Older Occupant Crash Data and Sensitivity of Thor-Nt and Worldsid Dummy Thoraces. Paper presented at: Proceedings of the 22nd Conference on the Enhanced Safety of Vehicles, Paper2011.

22. Foret-Bruno J-Y, Hartemann F, Thomas C, Fayon A, Terrière C, Got C, Patel A. *Correlation between Thoracic Lesions and Force Values Measured at the Shoulder of 92 Belted Occupants Involved in Real Accidents.* SAE Technical Paper;1978. 0148-7191.
23. Kent R, Patrie J. Chest Deflection Tolerance to Blunt Anterior Loading Is Sensitive to Age but Not Load Distribution. *Forensic science international.* 2005;149(2):121-128.
24. Marcus JH, Morgan RM, Eppinger RH, Kallieris D, Mattern R, Schmidt G. *Human Response to and Injury from Lateral Impact.* SAE Technical Paper;1983. 0148-7191.
25. Neathery RF, Kroell CK, Mertz HJ. *Prediction of Thoracic Injury from Dummy Responses.* SAE Technical Paper;1975. 0148-7191.
26. Agnew AM, Schafman M, Moorhouse K, White SE, Kang Y-S. The Effect of Age on the Structural Properties of Human Ribs. *Journal of the mechanical behavior of biomedical materials.* 2015;41:302-314.
27. Murach MM, Kang Y-S, Goldman SD, Schafman MA, Schlecht SH, Moorhouse K, Bolte JH, Agnew AM. Rib Geometry Explains Variation in Dynamic Structural Response: Potential Implications for Frontal Impact Fracture Risk. *Annals of Biomedical Engineering.* 2017:1-15.
28. Schafman MA, Kang Y-S, Moorhouse K, White SE, Bolte JH, Agnew AM. Age and Sex Alone Are Insufficient to Predict Human Rib Structural Response to Dynamic Ap Loading. *Journal of Biomechanics.* 2016;49(14):3516-3522.
29. Kemper AR, McNally C, Kennedy EA, Manoogian SJ, Rath AL, Ng TP, Stitzel JD, Smith EP, Duma SM, Matsuoka F. Material Properties of Human Rib Cortical Bone from Dynamic Tension Coupon Testing. *Stapp Car Crash J.* 2005;49(11):199-230.
30. Kemper AR, McNally C, Pullins CA, Freeman LJ, Duma SM, Rouhana SM. The Biomechanics of Human Ribs: Material and Structural Properties from Dynamic Tension and Bending Tests. *Stapp Car Crash Journal.* 2007;51:235-273.
31. Stitzel JD, Cormier JM, Barretta JT, Kennedy EA. Defining Regional Variation in the Material Properties of Human Rib Cortical Bone and Its Effect on Fracture Prediction. *Stapp car crash journal.* 2003;47:243-265.

Biomechanical Responses of Human Surrogates under Various Frontal Loading Conditions with an Emphasis on Thoracic Response and Injury Tolerance

Devon Albert

Preliminary Examination submitted to the faculty of the Virginia Polytechnic Institute and State University in partial fulfillment of the requirements for the degree of

Doctor of Philosophy
In
Biomedical Engineering

Andrew R. Kemper
Amanda M. Agnew
H. Clay Gabler
Warren N. Hardy
Joel D. Stitzel

4/19/2018
Blacksburg, VA

Keywords: Hybrid III, THOR, PMHS, knee bolster, knee bolster airbag, frontal motor vehicle collision, thoracic injury criterion, rib

TABLE OF CONTENTS

LIST OF FIGURES

LIST OF TABLES

CHAPTER 2: EVALUATION OF RIGID POLYURETHANE FOAM AS A SURROGATE MATERIAL FOR KNEE BOLSTERS AND KNEE BOLSTER AIRBAGS IN FULL-SCALE FRONTAL SLED TESTS

Select contents published in:

Albert DL, Beeman SM, McNally C, Kemper AR, "Evaluation of Rigid Polyurethane Foam as Surrogate Material for Knee Bolsters and Knee Bolster Airbags in Full-Scale Frontal Sled Tests." Short Communications from AAAM's 60th Annual Scientific Conference," *Traffic Injury Prevention,* 17(sup1), pp205-208, 2016.

Albert DL, Beeman SM, McNally C, Kemper AR, "Foam Surrogates for Use as Knee Bolsters and Knee Bolster Airbags in Frontal Sled Tests: Evaluation of Compressive Properties and Responses Due to Occupant Loading," *Biomedical Sciences Instrumentation,* 53, 2017.

Introduction

The lower extremity and chest are two of the most frequently injured body regions in frontal crashes [1]. In recent years, knee bolster airbags (KBABs) have been introduced as an added restraint on the knees to stop forward motion of the occupant during motor vehicle collisions (MVCs) and mitigate injuries to the lower extremity and chest [2]. Previous studies assessing the efficacy of KBABs have been limited to finite element analyses [3-5] and real-world crash comparisons [6,7]. However, both types of analyses are associated with limitations. The finite element analyses lack validation data from laboratory studies, while the real-world crash comparisons are limited by small sample sizes and indirect comparisons between collisions, vehicles, and occupants. Therefore, there is a need for a controlled laboratory study to determine whether KBABs reduce injuries compared to the standard knee bolster (KB).

Previous studies have used different approaches to simulating a KB restraint in full-scale laboratory sled tests. Several studies focused on simulating a specific crush strength using aluminum [8-11] or paper [12,13] honeycomb. Viano and Culver (1979) utilized a combination of aluminum honeycomb and foam [14], while Daniel and Yost (1988) used corrugated paper to simulate a KB [15]. While the previous studies maintained specific offsets between the lower extremity and KB, Shaw *et al.* applied a stiff aluminum bolster in direct contact with the lower extremity to prevent forward motion of the lower extremities and pelvis for the duration of their sled tests [16-18]. Several studies have also integrated production bolsters into laboratory full-scale sled tests. Cheng *et al.* (1984) used a small section of a production VW Rabbit bolster, which had a different stiffness from the full bolster, to investigate femur loading [19]. Crandall *et al.* (1995) used a production bolster, as part of the occupant compartment from a production vehicle, to evaluate the unbelted occupant response to KB and steering wheel airbag loading during sled tests [20]. Subsequently, several more studies were performed using sections of production occupant compartments that incorporated KBs [21-24].

The methodologies of previous studies have demonstrated a tendency to implement surrogate KBs instead of production bolsters when the KB is not already integrated into the sled buck as part of a production occupant compartment. This limited use of production KBs and the lack of attempts to implement KBABs in full-scale laboratory sled tests are the result of several challenges. First,

the use of new vehicle parts for each test can be prohibitively expensive. Secondly, KBABs may not deploy in a repeatable manner. Finally, it can be difficult to incorporate KBs and KBABs into a sled buck due to the size and complex geometry of KBs.

The number of studies that have already employed surrogate KBs in laboratory sled tests indicates there is a known need for a KB surrogate that produces occupant responses comparable to those observed in real-world MVCs. However, none of the previous laboratory studies that used surrogate materials to simulate KBs validated their occupant responses against full-scale vehicle tests or sled tests that implemented production bolsters. The lack of validated surrogates and the challenges associated with implementing production KBs and KBABs demonstrate a clear need for a repeatable, validated surrogate for KBs and KBABs to facilitate laboratory testing.

Rigid foams show promise as KB and KBAB surrogates because they are available in a range of stiffnesses, are relatively inexpensive, and are easy to shape into complex geometries. Furthermore, previous studies have quantified the stiffnesses of several production bolsters [3,4], facilitating the selection of appropriate foam surrogates based on this property. Therefore, the purpose of this research was to assess the efficacy of rigid polyurethane foams as KB and KBAB surrogates by first characterizing the compressive properties of several rigid polyurethane foams, comparing the compressive properties to that of production KBs, and then validating the occupant response to the selected foam surrogates in full-scale frontal sled tests.

Methods

Indentation Tests

Indentation tests were performed to quantify the compressive responses of seven rigid polyurethane foams, distinguished by their compressive strength ratings (CSRs) of 19, 24, 27, 65 90, 142, and 237 psi. The tests were performed on a material testing system (MTS Systems Corporation, Eden Prairie, MN) equipped with a load cell, accelerometer, and custom indenter at loading rates of 1, 100, and 1000 mm/s (Figure 2.1).

The indenter was designed to approximate knee geometry during an impact with a KB. Rupp *et al.* (2007) impacted cadaver knees with production KBs in an effort to characterize knee impacts in

frontal crashes [25]. Fuji Film was used to record the contact between the knees and bolster. Knee contact area was then estimated from the Fuji Film results, producing an average maximum contact area of 24.5 cm^2 (3.8 in^2). Therefore, the 5.72 cm (2.25 in) diameter of the indenter was chosen to approximate this contact area. The 3.8 cm (1.5 in) radius of the impacting face was chosen to simulate the curvature of the knee and the increase in contact area between the knee and the KB with increasing knee intrusion.

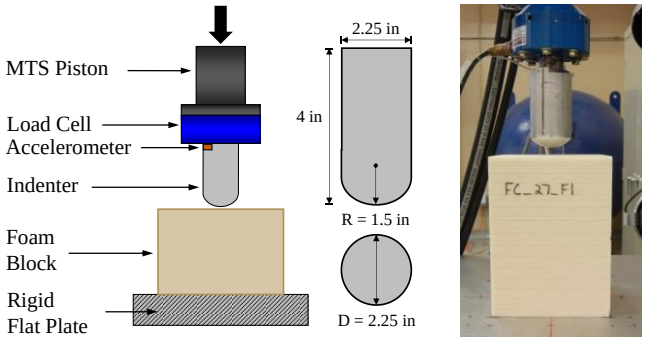

Figure 2.1: Schematics for the foam indentation test setup and indenter (left) and test setup picture for the 27 psi foam (right).

Two indentation tests per loading rate were completed for each foam type except for the 19, 24, and 27 psi foams, which underwent one test each at 1 and 100 mm/s and two tests at 1000 mm/s. The displacement and force data were collected at 0.25 kHz, 20 kHz, and 50 kHz for the 1, 100, and 1000 mm/s loading rates, respectively. The compressive properties, including the stiffness and yield point, were determined for each foam at each loading rate (Figure A2.1). The initial stiffness was quantified as the slope of the force-displacement curve between 3 and 9 mm of displacement. The yield point was defined as the intersection of an offset line with the force-displacement curve. The offset line was parallel to the initial stiffness, but was offset 0.2 mm of displacement from the origin. The secondary stiffness was quantified as the slope of the force-displacement curve between 20 and 40 mm of displacement. The initial stiffness of each foam was compared to literature values of production KB stiffness to determine which foams were the most appropriate KB surrogates.

A two-way ANOVA was performed for each compressive property to determine whether it was significantly influenced by CSR or loading rate. A linear regression was performed for

compressive properties with significant effects. The fit line, Pearson Correlation Coefficient (r), and coefficient of determination (r^2) were calculated for each regression.

Sled Tests

Full-scale frontal sled tests were performed to evaluate the dynamic responses of the foams during occupant loading in a motor vehicle collision. In order to validate the efficacies of the KB and KBAB foams as surrogates, the occupant response during the sled tests needed to be comparable to that of analogous whole vehicle frontal crash tests. Therefore, the sled tests were designed to replicate the 2012 Toyota Camry New Car Assessment Program (NCAP) frontal crash test, which involved a knee bolster airbag deployment [26]. All tests were performed on a 1.4 MN ServoSled^{TM} system (Seattle Safety LLC, Kent, WA) with a custom designed sled buck (Figure 2.2). The sled buck was designed to match the interior of a 2013 Toyota Camry SE. Specifically, the locations and geometries of the B-pillar, D-ring, retractor, knee bolster, steering column and wheel, and seat on the sled buck were in accordance with measurements taken within the interior of the aforementioned vehicle. New 2013 Toyota Camry vehicle components, including a three-point, U.S. driver side seatbelt (with a pretensioner, 4kN load limiter, retractor, and buckle), seat, steering wheel, steering column, and steering wheel airbag were employed for each test. The sled system was tuned to replicate the vehicle acceleration pulse of the 2012 Toyota Camry NCAP test (ΔV = 56 kph, peak acceleration = 470 m/s^2). The initiation of the pretensioner and deployment of the dual-stage airbag were synchronous, with both events occurring 10 ms after the initiation of sled acceleration. The timing of these events were compared to the 2012 Toyota Camry NCAP test onboard Event Data Recorder (EDR) to ensure approximate alignment with the NCAP test. An instrumented Hybrid III (HIII) 50th percentile male anthropomorphic test device (ATD) was used to represent the occupant in each test. Positioning of the HIII and vehicle components (i.e. seat track, seat back, steering column, seat belt, and knee bolster) were guided by the NCAP Test Procedure Document [27] and the NCAP Report for the 2012 Toyota Camry [26].

Based on the results of the indentation testing, select foams were chosen to simulate KBs and KBABs in the sled tests. The right and left KBs and KBABs were independent foam blocks, located on either side of the steering column, and were replaced for each test. The KB foam was 160 mm deep and 254 mm high with an average offset of 178 mm from the center of the HIII knee.

The KBAB foam had a diagonal impact surface and was 250 mm and 202 mm deep at the top and bottom of the foam, respectively, and 302 mm high. The diagonal surface was parallel to the shank with a constant offset of approximately 10 mm. The offset between the surface of the KBAB foam and the center of the HIII knee was 100 mm.

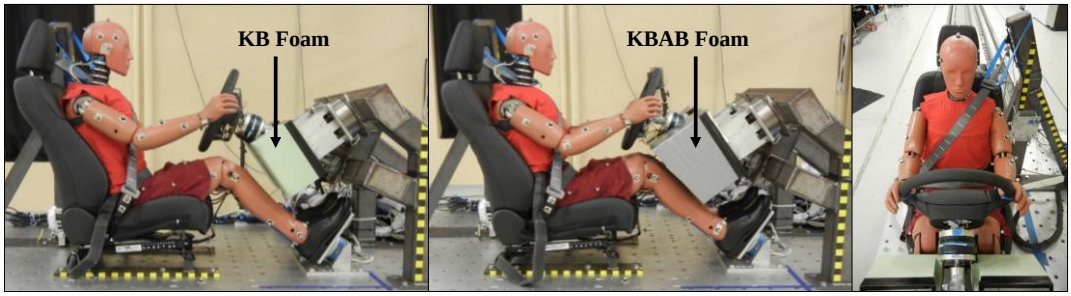

Figure 2.2: Sled test setup side view for KB condition (left), side view for KBAB condition (middle), and front view (right).

Two tests were performed for each of two conditions, KB foam and KBAB foam, for a total of four tests. The axial femur forces, axial tibia forces, anterior/posterior (A/P) chest accelerations, and A/P pelvis accelerations of the Hybrid III were collected at 20 kHz. The forces and accelerations were filtered at SAE channel frequency classes (CFCs) 600 and 180, respectively [28]. To assess the performance of each foam, the results of the KBAB and KB conditions were compared to the 2012 and 2005 Camry NCAP tests, respectively. The 2005 NCAP did not involve a knee bolster airbag deployment, making it a suitable comparison for the KB condition [29]. However, design differences between the vehicles used in the 2005 and 2012 NCAPs, the latter of which the sled tests were designed to match, limited direct comparisons between the 2005 NCAP and the KB condition.

Results

Indentation Tests

Each foam exhibited a two phase response at each loading rate consisting of initial and secondary stiffnesses separated by a yield point (Figure 2.3, Figures A2.2-A2.8, Table A2.1). The ANOVA revealed no significance ($p > 0.05$) for loading rate or the interaction between loading rate and CSR for all of the compressive properties. The CSR was found to significantly affect the initial stiffness ($p < 0.0001$), secondary stiffness ($p < 0.0001$), and yield force ($p < 0.0001$), but not the

yield deflection (p = 0.108). Therefore, linear regressions were performed for the initial stiffness and yield force with regard to CSR (Figure 2.4). A regression was not performed for the secondary stiffness because the foam's post-yield behavior was not expected to substantially influence the occupant response. The equations in Figure 2.4 are the regression lines relating CSR with initial stiffness (r = 0.976, r^2 = 0.952) and yield force (r = 0.974, r^2 = 0.949).

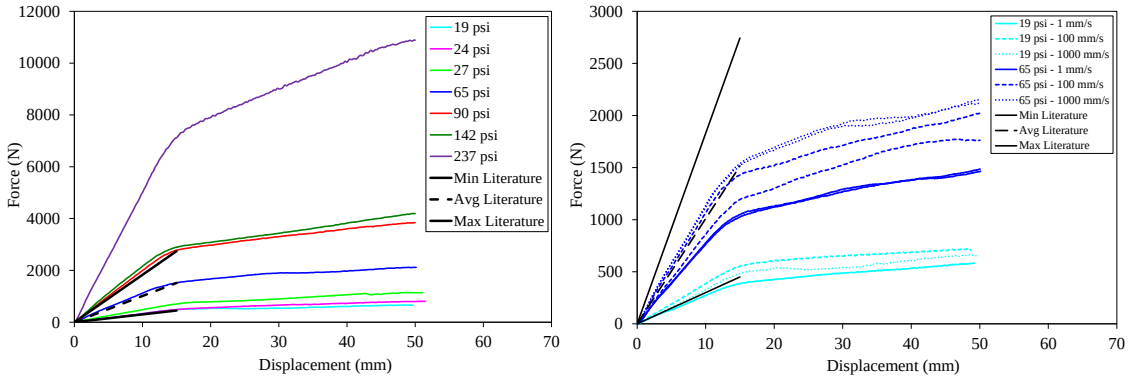

Figure 2.3: Representative force-displacement curves for all foams at a loading rate of 1000 mm/s compared to literature values (left) and force-displacement curves for the 65 and 19 psi foams at all loading rates compared to literature values (right).

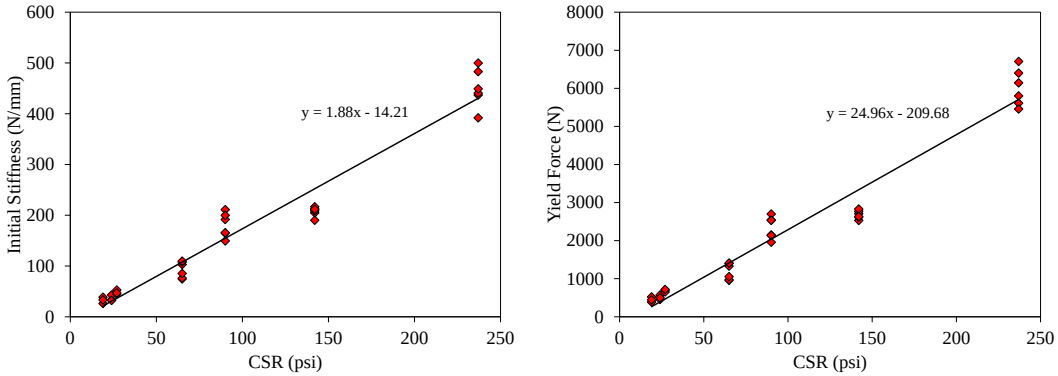

Figure 2.4: The linear fits for initial stiffness (left) and yield force (right) with respect to CSR.

As observed from Figure 2.4, the initial stiffness increased with increasing CSR. Therefore, the 19 psi foam had the lowest average initial stiffness of 33 N/mm, and the 237 psi foam had the highest average initial stiffness of 450 N/mm. The 65 psi foam had an average initial stiffness of 93 N/mm, which was closest to the average stiffness of production bolsters reported in the literature (101 N/mm) [25,30]. Consequently, the 65 psi foam was chosen to simulate the KB during the sled tests. The 19 psi foam was chosen to simulate the KBAB foam because it had the lowest stiffness.

Sled Tests

The A/P chest and pelvis accelerations showed good agreement between the sled tests and NCAP tests, but some small differences were observed (Figure 2.5). The time of onset and duration of chest accelerations were very similar between each condition and its respective analog, but both sled test conditions resulted in slightly lower magnitudes than their NCAP analogs. The pelvis accelerations from the sled tests also had similar onset timing when compared to the NCAP tests. The peak pelvis accelerations occurred at the same time for the KB condition and the 2005 NCAP. However, the peak pelvis acceleration for the KBAB condition was earlier than the 2012 NCAP test's peak.

The axial femur and tibia forces from the NCAP tests were substantially different between the right and left sides and were compared separately to the forces from the sled tests (Figure 2.5). The left femur forces were very similar between the sled tests and their NCAP analogs until the peak force. This trend was not observed for the right femur. In terms of magnitude, the sled tests had consistent peak femur forces between the right and left side, but the NCAP tests resulted in lower left femur forces and higher right femur forces. Thus, the peak magnitudes from the sled tests fell within the corridor created by the right and left sides. The duration of femur loading was longer for the 2012 NCAP tests than the KBAB condition. Similar to the femur forces, the tibia forces on the left side were most comparable between the sled tests and NCAP tests, especially for the KB condition. The peak for the 2012 NCAP test was earlier than the KBAB condition on the left side, but the peaks occurred at similar times on the right side. The peak left tibia forces were close for both conditions compared to their NCAP analogs.

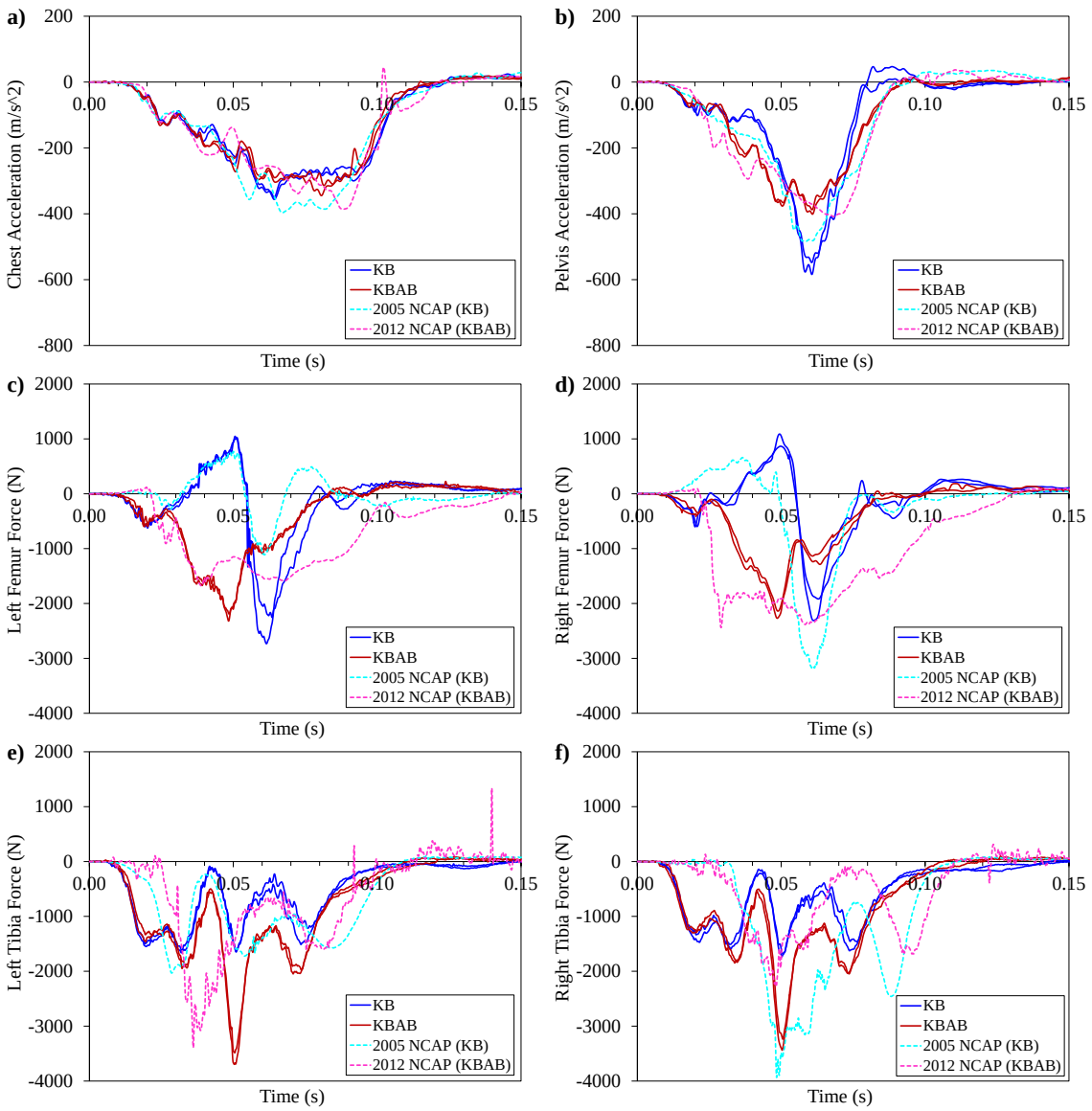

Figure 2.5: a) A/P chest accelerations (+ anterior), b) A/P pelvis accelerations, c) left axial femur forces (+ tension), d) right axial femur forces, e) left axial tibia forces, and f) right axial tibia forces.

Discussion

When comparing the sled tests conducted with foam surrogates to the NCAP tests, the axial tibia forces showed the most differences. This is likely the result of differences in pedal position and stiffness between the sled tests and the NCAP tests. The left and right rigid foot pedals in the sled tests were designed to be the same distance from the seat. However, in the NCAP tests, the right foot was positioned on the more compliant gas pedal while the left foot was placed on the footrest

[26,29], which were at different depths and angles in the foot well. Despite these differences, the peak left axial tibia forces were similar between the sled tests and the NCAP tests.

Differences were also observed between the femur forces in the sled tests and NCAP tests. The discrepancy in magnitude between the KB condition and 2005 NCAP test can be explained by structural differences between the right and left knee bolster in the NCAP tests, which produced a range of magnitudes that encompassed the results from the sled tests. For the KBAB condition, the difference in loading duration between the sled tests and the NCAP test was the result of an inherent limitation of the foam. As the ATD's knees intruded into the foam, the foam yielded and the force exerted on the knees decreased sharply after peak forward excursion was reached. However, an airbag will continue to exert a force on the knees after peak forward excursion if the air has not been released from the airbag. Even though this is a clear difference in loading, it occurred after peak forward excursion and should have a limited effect on the ATD kinematics, as was observed with the pelvic and chest accelerations.

The main limitation of the sled tests was a small sample size which precluded a meaningful statistical comparison between the sled conditions and NCAP tests. However, high consistency was observed between sled tests, allowing some conclusions to be drawn from the analysis. Another limitation was that a direct comparison could not be made between the KB condition and the 2005 NCAP test since the sled buck and acceleration pulse were designed to match the 2012 NCAP test. Therefore, some of the discrepancies between these tests could be attributed to this design difference. Future work will evaluate the injury risks associated with different safety restraint combinations involving the KBs and KBABs for the Hybrid III and other human surrogates.

Conclusions

The current study characterized the compressive properties of seven rigid polyurethane foams through indentation tests and evaluated the responses of select foams to occupant loading in full-scale frontal sled tests. Based on the indentation tests, a function relating initial stiffness and CSR was developed. This function will facilitate future testing by providing a method for determining stiffness from CSR without performing indentation testing. The results of the sled tests showed

reasonable agreement between the KB and KBAB conditions and their NCAP analogs. Therefore, the 65 psi and 19 psi foams are acceptable surrogates for KBs and KBABs, respectively. Overall, this finding provides a method for accurately simulating frontal motor vehicle collision lower extremity loading in the laboratory and assessing injury risk due to different restraint conditions.

References

1. Kuppa S, Wang J, Haffner M, Eppinger R. Lower Extremity Injuries and Associated Injury Criteria. Paper presented at: 17th International Technical Conference on the Enhanced Safety of Vehicles2001.
2. Roychoudhury RS, Conlee JK, Best M, Schenck D. *Blow-Molded Plastic Active Knee Bolsters.* SAE Technical Paper;2004. 0148-7191.
3. Danelson KA, Golman AJ, Kemper AR, Gayzik FS, Gabler HC, Duma SM, Stitzel JD. Finite Element Comparison of Human and Hybrid Iii Responses in a Frontal Impact. *Accident Analysis & Prevention.* 2015;85:125-156.
4. Nie B, Crandall JR, Panzer MB. Computational Investigation of the Effects of Knee Airbag Design on the Interaction with Occupant Lower Extremity in Frontal and Oblique Impacts. *Traffic injury prevention.* 2016;18(2):207-215.
5. Ye X, Panzer MB, Shaw G, Crandall JR. Driver Lower Extremity Response to out of Position Knee Airbag Deployment. Proceedings of the International Research Council on the Biomechanics of Injury (IRCOBI) conference; September 10-12, 2014; Berlin, Germany.
6. Patel V, Griffin R, Eberhardt AW, McGwin G. The Association between Knee Airbag Deployment and Knee–Thigh–Hip Fracture Injury Risk in Motor Vehicle Collisions: A Matched Cohort Study. *Accident Analysis & Prevention.* 2013;50:964-967.
7. Weaver AA, Loftis KL, Stitzel JD. Investigation of the Safety Effects of Knee Bolster Air Bag Deployment in Similar Real-World Crash Comparisons. *Traffic injury prevention.* 2013;14(2):168-180.
8. Atkinson P, Benny J, Sambatur K, Gudipaty K, Maripudi V, Hill T. *A Parametric Study of Vehicle Interior Geometry, Delta-V, and Instrument Panel Stiffness on Knee Injury and Upper Body Kinetic Energy.* SAE Technical Paper;1999.
9. Atkinson P, Haut R, Eusebi C, Hill T. *Application of a Knee Injury Criteria for the Hybrid Iii Dummy to Address a Variety of Car Crash and Restraint Scenarios.* SAE Technical Paper;1999. 0148-7191.
10. Rudd R, Shaw G, Crandall J. Fifth Percentile Female Hybrid Iii and Thor-Flx Performance in Sled Tests with Toepan Intrusion. Paper presented at: Proceedings of 18th International Technical Conference on the Enhanced Safety of Vehicles2003.

11. Rudd RW, Crandall JR, Shaw G. *Response of the Thor-Lx and Hybrid Iii Lower Extremities in Frontal Sled Tests.* SAE Technical Paper;2003. 0148-7191.
12. Yoganandan N, Pintar F, Moore J, Schlick M, Humm J, Rinaldi J, Maiman DJ. Sled Tests Using the Thor-Nt Device and Post Mortem Human Surrogates in Frontal Impacts. Paper presented at: Proceedings of the International Research Council on the Biomechanics of Injury conference2012.
13. Yoganandan N, Pintar FA, Schlick M, Moore J, Maiman DJ. Comparison of Head-Neck Responses in Frontal Impacts Using Restrained Human Surrogates. Paper presented at: Annals of Advances in Automotive Medicine/Annual Scientific Conference2011.
14. Viano DC, Culver CC. *Performance of a Shoulder Belt and Knee Restraint in Barrier Crash Simulations.* SAE Technical Paper;1979. 0148-7191.
15. Daniel RP, Yost CD. *Knee Bolster Parametric Study.* SAE Technical Paper;1988. 0148-7191.
16. Shaw C, Lessley D, Ash J, Crandall J, Parent D. Response Comparison for the Hybrid Iii, Thor Mod Kit with Sd-3 Shoulder, and Pmhs in a Simulated Frontal Crash. Paper presented at: 23rd ESV Conference, Paper2013.
17. Shaw G, Parent D, Purtsezov S, Crandall J, Törnvall F. Torso Deformation in Frontal Sled Tests: Comparision between Thor Nt, Thor Nt with the Chalmers Sd-1 Shoulder, and Pmhs. Paper presented at: International IRCOBI Conference on the Biomechanics of Impact2010.
18. Shaw G, Parent D, Purtsezov S, Lessley D, Crandall J, Kent R, Guillemot H, Ridella SA, Takhounts E, Martin P. Impact Response of Restrained Pmhs in Frontal Sled Tests: Skeletal Deformation Patterns under Seat Belt Loading. *Stapp Car Crash Journal.* 2009;53:1.
19. Cheng R, Yang K-H, Levine RS, King AI. *Dynamic Impact Loading of the Femur under Passive Restrained Condition.* SAE Technical Paper;1984. 0148-7191.
20. Crandall JR, Kuhlmann TP, Pilkey WD. Air and Knee Bolster Restraint System: Laboratory Sled Tests with Human Cadavers and the Hybrid Iii Dummy. *Journal of Trauma and Acute Care Surgery.* 1995;38(4):517-520.
21. Forman J, Lessley D, Shaw CG, Evans J. Thoracic Response of Belted Pmhs, the Hybrid Iii, and the Thor-Nt Mid-Sized Male Surrogates in Low Speed, Frontal Crashes. *Stapp car crash journal.* 2006;50:191.

22. Kent R, Lessley D, Shaw G, Crandall J. The Utility of Hybrid Iii and Thor Chest Deflection for Discriminating between Standard and Force-Limiting Belt Systems. *Stapp car crash journal.* 2003;47:267.
23. Kent R, Shaw G, Lessley D, Crandall J, Kallieris D, Svensson M. Comparison of Belted Hybrid Iii, Thor, and Cadaver Thoracic Responses in Oblique Frontal and Full Frontal Sled Tests. Paper presented at: SAE 2003 World Congress; March 3-6, 2003; Detroit, Michigan.
24. Kent RW, Crandall JR, Bolton JR, Duma SM. Comparison and Evaluation of Contemporary Restraint Systems in the Driver and Front-Passenger Environments. *Proceedings of the Institution of Mechanical Engineers, Part D: Journal of Automobile Engineering.* 2001;215(11):1147-1159.
25. Rupp JD, Miller CS, Reed MP, Madura NH, Ritchie NL, Schneider LW. Characterization of Knee Impacts in Frontal Crashes. Paper presented at: Proceedings of the 22nd Enhanced Safety of Vehicles Conference2007; Lyon, France.
26. Janovicz D, Fischer B. *Final Report of New Car Assessment Program Frontal Impact Testing of 2012 Toyota Camry Lee 4-Dr Sedan.* Washington, DC: USDOT; December 16, 2011 2011.
27. NHTSA. *Laboratory Test Procedure for New Car Assessment Program (Ncap)- Frontal Impact Testing*. Washington, DC: U.S. Department of Transportation; 2012.
28. SAE. *Instrumentation for Impact Test.* Warrendale, PA: Society of Automotive Engineers;1995.
29. Naik S. *Final Report of New Car Assessment Program Testing of a 2005 Toyota Camry Le.* Washington, DC: U.S. Department of Transportation,; March 11, 2005 2005.
30. Mahadevan K, Agrawal HN, Tekelly JP. Knee Bolster Analysis of a Thermoplastic Instrument Panel with Damage Mechanics Material Law. *Stapp Car Crash J.* 1994;38:1-9.

Appendix

Table A2.1: Material response of the rigid polyurethane foams at all loading rates.

Test ID	CSR (psi)	Loading Rate (mm/s)	Yield Force (N)	Yield Deflection (mm)	Initial Stiffness (N/mm)	Secondary Stiffness (N/mm)
FC-19 psi-S1	19	1	385.0	14.9	26.2	5.4
FC-19 psi-F1	19	100	522.8	13.8	38.5	4.2
FC-19 psi-FF2	19	1000	446.1	13.6	33.4	3.8
FC-24 psi-S1	24	1	457.0	14.1	33.9	5.9
FC-24 psi-F1	24	100	572.8	13.5	43.0	5.6
FC-24 psi-FF1	24	1000	497.5	15.6	32.3	8.2
FC-27 psi-S1	27	1	697.6	13.8	52.7	14.5
FC-27 psi-F1	27	100	652.0	15.0	44.6	13.6
FC-27 psi-FF1	27	1000	717.5	15.4	47.1	13.8
FC-65 psi-S1	65	1	959.6	13.1	74.5	12.9
FC-65 psi-S2	65	1	969.0	12.9	76.1	12.7
FC-65 psi-F1	65	100	1331.6	13.1	103.0	17.4
FC-65 psi-F2	65	100	1054.4	12.5	85.4	20.6
FC-65 psi-FF1	65	1000	1405.3	13.2	107.9	15.1
FC-65 psi-FF2	65	1000	1410.3	13.0	109.7	14.9
FC-90 psi-S1	90	1	2150.5	13.3	164.7	24.5
FC-90 psi-S2	90	1	2138.1	13.1	165.6	27.8
FC-90 psi-F1	90	100	2542.6	13.5	191.5	36.1
FC-90 psi-F2	90	100	1958.3	13.3	149.5	20.6
FC-90 psi-FF1	90	1000	2698.0	13.1	211.0	29.3
FC-90 psi-FF2	90	1000	2532.0	12.9	199.9	31.6
FC-142 psi-S1	142	1	2709.1	13.4	204.7	40.2
FC-142 psi-S2	142	1	2530.6	13.5	190.1	37.5
FC-142 psi-F1	142	100	2772.9	13.3	212.4	38.2
FC-142 psi-F3	142	100	2830.9	13.3	216.7	42.9
FC-142 psi-FF1	142	1000	2615.4	12.7	208.6	29.0
FC-142 psi-FF2	142	1000	2633.3	12.6	211.8	37.0
FC-237 psi-S1	237	1	5610.9	13.0	436.7	93.5
FC-237 psi-S2	237	1	5457.8	14.1	392.0	92.9
FC-237 psi-F1	237	100	5801.0	13.4	440.7	93.2
FC-237 psi-F2	237	100	6400.0	13.5	482.9	107.1
FC-237 psi-FF1	237	1000	6705.8	13.6	499.8	107.0
FC-237 psi-FF2	237	1000	6143.7	13.9	449.1	90.7

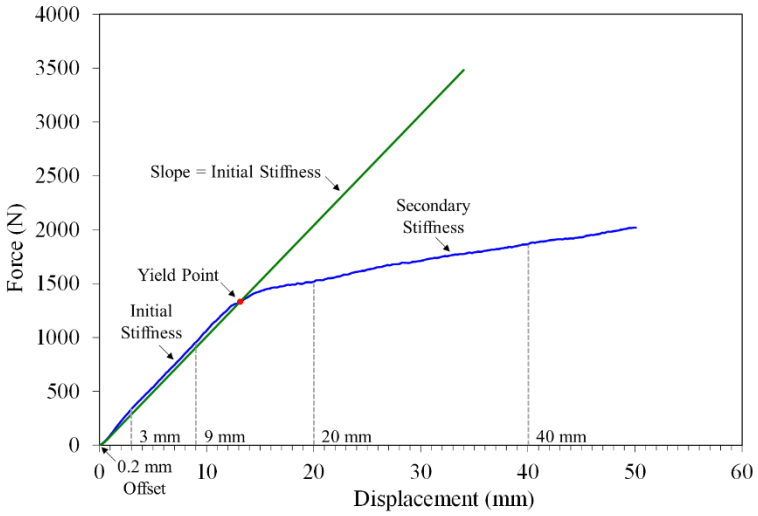

Figure A2.1: Methodology for determining initial stiffness, secondary stiffness, and yield point.

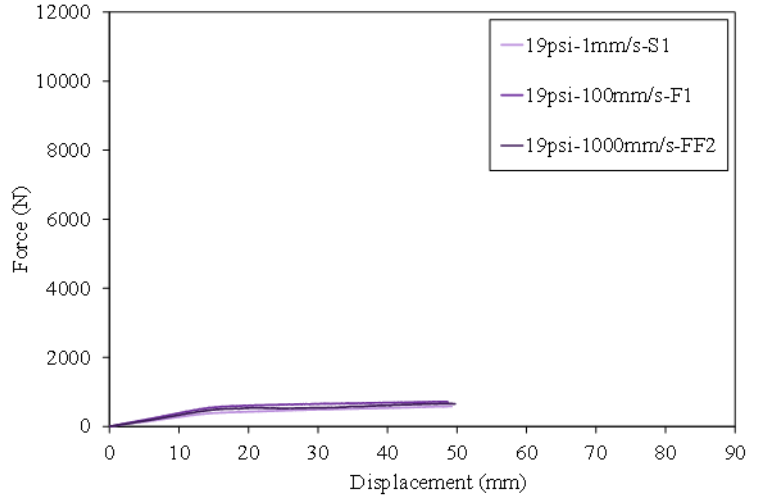

Figure A2.2: Force-displacement curves for the 19 psi foam at all loading rates.

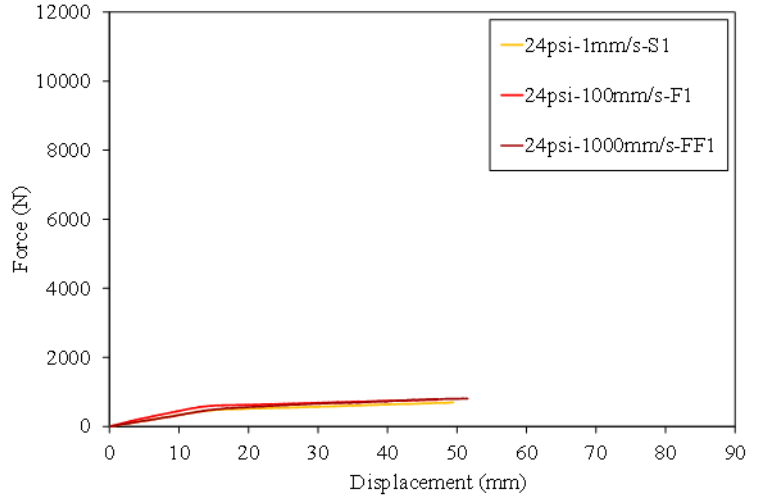

Figure A2.3: Force-displacement curves for the 24 psi foam at all loading rates.

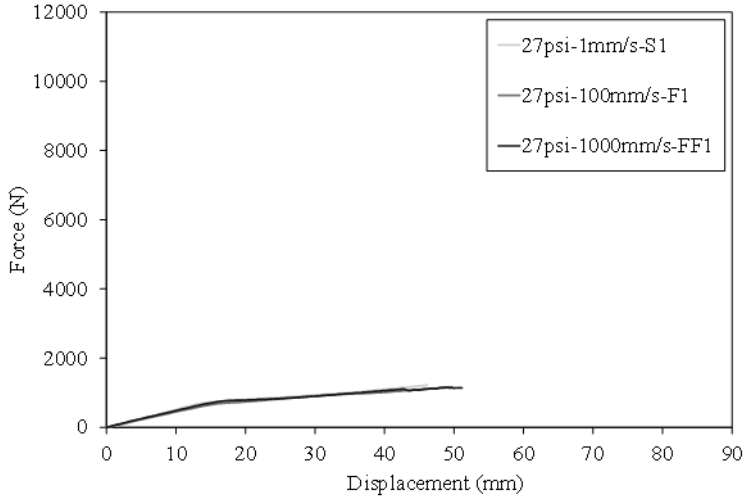

Figure A2.4: Force-displacement curves for the 27 psi foam at all loading rates.

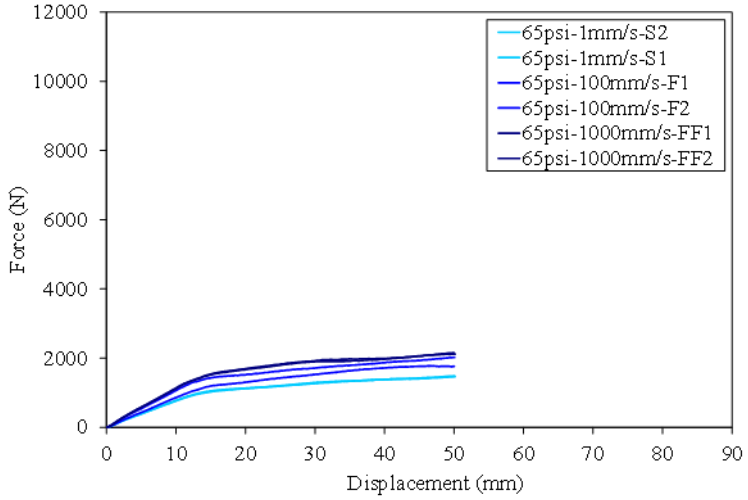

Figure A2.5: Force-displacement curves for the 65 psi foam at all loading rates.

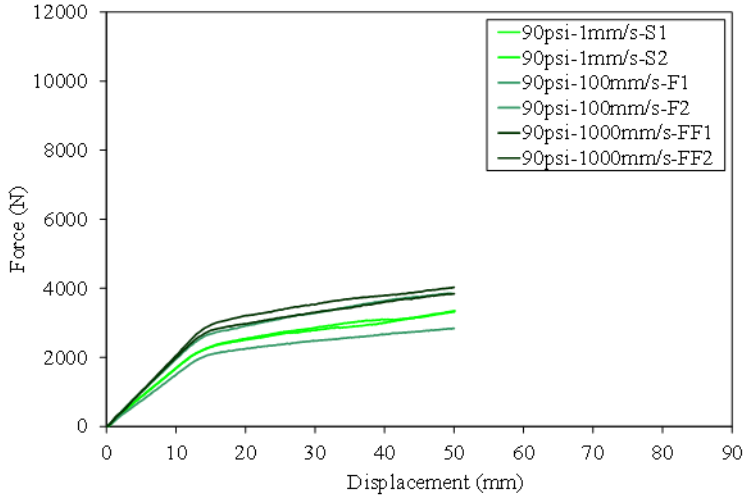

Figure A2.6: Force-displacement curves for the 90 psi foam at all loading rates.

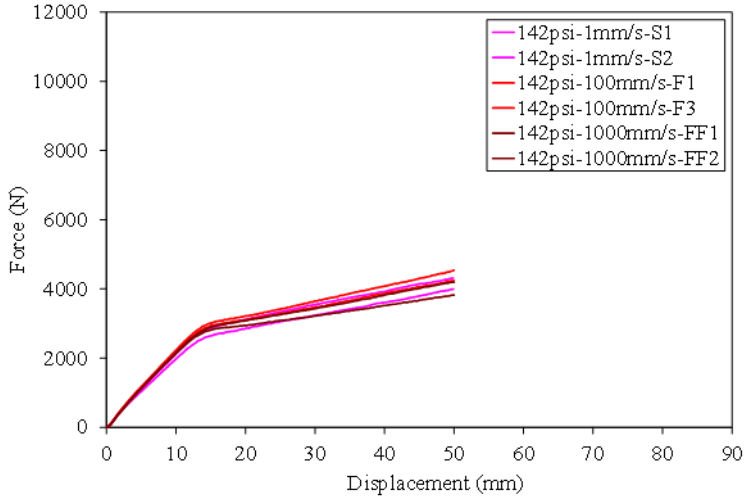

Figure A2.7: Force-displacement curves for the 142 psi foam at all loading rates.

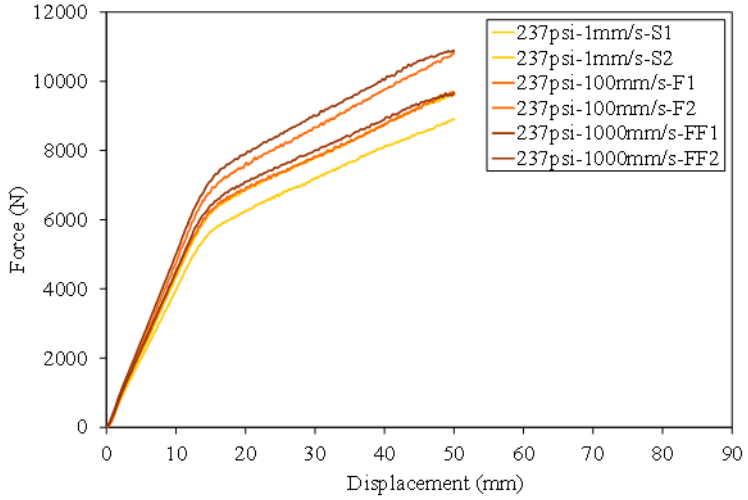

Figure A2.8: Force-displacement curves for the 237 psi foam at all loading rates.

Biomechanical Responses of Human Surrogates under Various Frontal Loading Conditions with an Emphasis on Thoracic Response and Injury Tolerance

Devon Albert

Preliminary Examination submitted to the faculty of the Virginia Polytechnic Institute and State University in partial fulfillment of the requirements for the degree of

Doctor of Philosophy
In
Biomedical Engineering

Andrew R. Kemper
Amanda M. Agnew
H. Clay Gabler
Warren N. Hardy
Joel D. Stitzel

4/19/2018
Blacksburg, VA

Keywords: Hybrid III, THOR, PMHS, knee bolster, knee bolster airbag, frontal motor vehicle collision, thoracic injury criterion, rib

TABLE OF CONTENTS

LIST OF FIGURES

LIST OF TABLES

CHAPTER 3: OCCUPANT KINEMATICS OF THE HYBRID III, THOR-M, AND POST-MORTEM HUMAN SURROGATES UNDER VARIOUS RESTRAINT CONDITIONS IN FULL-SCALE FRONTAL SLED TESTS

Select contents published in:

Albert DL, Beeman SM, Kemper AR, "Occupant Kinematics of the Hybrid III, THOR-M, and Postmortem Human Surrogates under Various Restraint Conditions in Full-Scale Frontal Sled Tests," *Traffic Injury Prevention*, 19(sup1), ppS50-S58, 2018.

Introduction

Frontal crashes accounted for about 60% of all fatalities and 55% of all non-fatal injuries due to motor vehicle collisions in 2014 [1]. This amounted to 10,813 fatalities and 937,000 injuries that were the result of frontal crashes despite advances in vehicle safety [1]. The Test device for Human Occupant Restraint (THOR-M) was developed to be a more biofidelic anthropomorphic test device (ATD) than the Hybrid III (HIII), which is currently the standard ATD in frontal crash testing. The THOR-M was designed to be more anatomically-correct than the HIII in the neck, shoulder, spine, rib cage, abdomen, and pelvis. In addition, improvements were made to produce more biofidelic kinematics [2]. For example, the THOR-M neck was designed to be more compliant than the HIII neck [3,4], and the shoulder was designed to mimic the protraction and elevation of a human shoulder [5]. The design of the rib cage, including the downward slant of the ribs, was intended to better reflect actual human anatomy and thereby produce more biofidelic chest responses during loading from safety restraints [6].

A large body of research is available that examines different aspects of the biofidelity of the THOR-M and its earlier design iterations (generically termed "THOR" in this chapter) in pure frontal crash scenarios. The authors are not aware of any studies that compare the kinematics of the THOR-M and HIII to post-mortem human surrogates (PMHSs) in an effort to evaluate the comparative biofidelity of the ATDs. Although several studies have examined the kinematics of matched frontal sled tests between PMHSs, the HIII, and earlier iterations of the THOR [7-9], modifications introduced in the THOR-M since these studies were performed have the potential to change occupant kinematics. These modifications include an increase in neck compliance, changes in the clavicle design to accommodate clavicle load cells, new thoracic deflection instrumentation, and a reduction in femur stiffness [10]. In addition these studies only evaluated the surrogate responses under one safety restraint condition. It is possible that the sensitivity of the THOR to changes in restraint condition differs from that of the HIII and PMHS. Rangarajan *et al.* (1998) and Forman *et al.* (2008) both examined the sensitivities of the HIII and THOR to different restraint conditions. PMHS tests were later performed to match the ATD tests reported by Forman *et al.* (2008); however, a direct comparison was never performed between the ATD and PMHS kinematics [13]. In these previous studies only the comparative sensitivities of each ATD were

reported rather than which ATD exhibited a more biofidelic response for each restraint condition. Additionally, the effect of different lower extremity restraints was not assessed in these studies.

Knee bolster airbags (KBABs) have been introduced into the vehicle fleet with the intention of reducing lower extremity, chest, and head injuries. KBABs are projected to limit the forward excursion of the knee and pelvis, and consequently decrease the forward excursions of the head and chest as compared to standard knee bolsters (KBs) [14]. The reduction of forward head and chest movements is anticipated to decrease interaction with the seatbelt, SWAB, and other vehicle components which have the potential to cause injuries. The greater compliance of an airbag relative to a rigid bolster is expected to reduce lower extremity injuries. However, the efficacy of KBABs remains untested outside of computational modeling analyses [15-17] and real-world crash comparisons [18,19], which both have limitations.

With the planned incorporation of the THOR-M into crash test safety ratings [2,20], it is imperative to fully assess the THOR-M's biofidelity over a variety of safety restraint conditions, including KBABS. Therefore, the purpose of this study was to compare the occupant kinematics of the HIII, THOR-M, and PMHS during full-scale frontal sled tests under three safety restraint conditions: knee bolster (KB), knee bolster and steering wheel airbag (KB/SWAB), and knee bolster airbag and steering wheel airbag (KBAB/SWAB).

Methods

A total of 20 full-scale frontal sled tests were performed using the HIII, THOR-M, and PMHSs to quantify and compare occupant kinematics under three safety restraint conditions: KB, KB/SWAB, and KBAB/SWAB. The sled tests were designed to simulate the 2005 Toyota Camry (KB/SWAB) and 2012 Toyota Camry (KBAB/SWAB) frontal New Car Assessment Program (NCAP) full-scale crash tests [21,22]. All tests were performed on a 1.4 MN ServoSled^{TM} system (Seattle Safety LLC, Kent, WA) with a custom designed sled buck (Figure 3.1) and employed the vehicle acceleration pulse of the 2012 Toyota Camry NCAP test (ΔV = 56 kph, peak acceleration = 470 m/s^2) (Figure 3.2). The sled buck was designed to match the interior of a 2013 Toyota Camry SE. Specifically, the locations and geometries of the B-pillar, D-ring, retractor, knee bolster, steering column and wheel, and seat on the sled buck were in accordance with

measurements taken within the interior of the 2013 Toyota Camry SE. New 2013 Toyota Camry vehicle components, including a three-point, U.S. driver side seatbelt (with a pretensioner, 4kN load limiter, retractor, and buckle), seat, steering wheel, steering column, and steering wheel airbag were employed for each test. The initiation of the pretensioner and deployment of the dual-stage airbag (when applicable) were synchronous, with both events occurring 10 ms after the initiation of sled acceleration. The timing of these events were compared to the 2012 Toyota Camry NCAP test onboard Event Data Recorder (EDR) to ensure approximate alignment with the NCAP test.

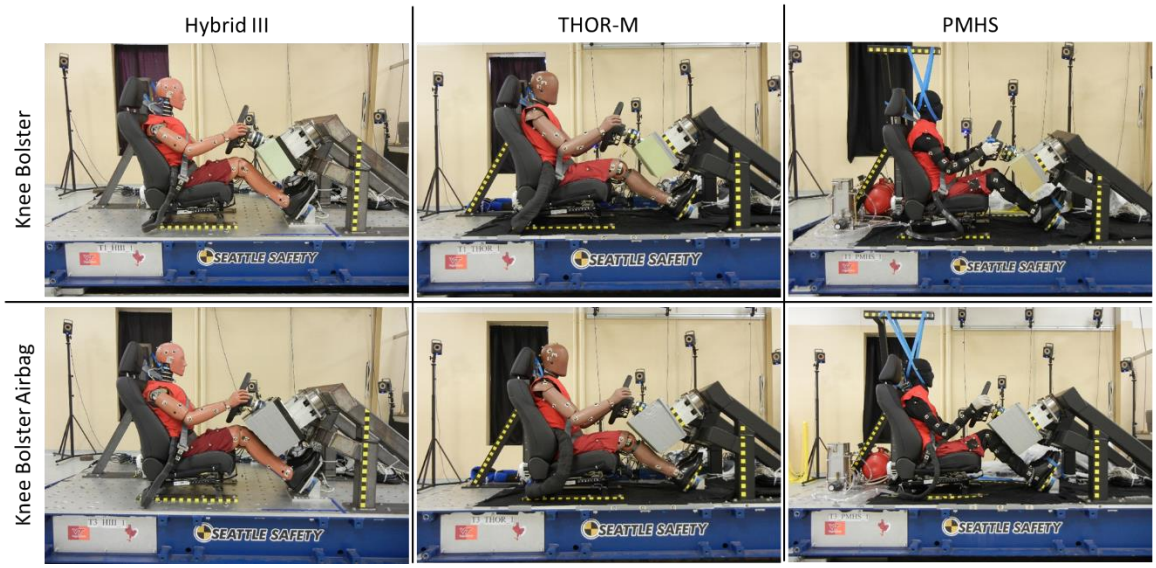

Figure 3.1: The sled test setup for the KB and KBAB conditions for all surrogates.

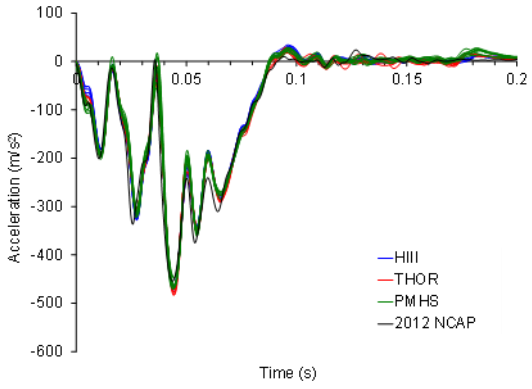

Figure 3.2: Sled pulses for all sled tests and the vehicle acceleration from the 2012 Toyota Camry NCAP test.

Six tests each were performed with the HIII and THOR-M ATDs, while a total of eight PMHS tests were performed. For the ATD tests, two tests were performed for each of the three safety restraint conditions per ATD. For the PMHSs, two tests were in the KB condition and three tests each were performed in the KB/SWAB and KBAB/SWAB conditions. Each PMHS was used for only a single test. Demographic information for the approximately 50th percentile male PMHSs are provided in Table 3.1.

Table 3.1: PMHS demographics.

Surrogate	**Age (years)**	**Weight (kg)**	**Height (cm)**
PMHS-KB-1	72	62.6	173.0
PMHS-KB-2	63	70.1	181.6
PMHS-KB/SWAB-1	57	59.0	167.0
PMHS-KB/SWAB-2	88	79.5	180.5
PMHS-KB/SWAB-3	67	68.0	182.9
PMHS-KBAB/SWAB-1	80	81.8	187.0
PMHS-KBAB/SWAB-2	71	72.6	190.0
PMHS-KBAB/SWAB-3	78	77.3	169.6
50th Percentile Male [23]	-	76.7	175.1

Surrogate Positioning

Positioning of the surrogates and vehicle components (i.e. seat track, seat back, steering column, seat belt, and knee bolster) were guided by the NCAP Test Procedure Document [24] and the NCAP Report for the 2012 Toyota Camry [21]. These specifications were readily applied for all tests involving the HIII. Due to variations in geometry between the HIII, the THOR-M, and PMHSs, techniques and measurements were adapted to ensure appropriate, repeatable positioning for each surrogate type. To elaborate, it was deemed critical to have consistent offset distances between the surrogate and the test buck structure or vehicle components (i.e., knee and knee bolster, chest and steering hub, and nose to rim) for all tests to preserve the interaction of the surrogates with the vehicle components and safety restraint systems (Tables 3.2 - 3.4) [9]. Minor adjustments were made to the seat track position, seat back angle, steering column telescoping position, and belt D-ring detent to address the differences in anthropometry.

All surrogates were positioned such that they were centered (left to right) in the seat with their feet on the foot plates and hands on the steering wheel. The mid-sagittal plane of the surrogate was coincident with the centerline of the seat and headrest. The torso rested against the seatback, and the thighs rested on the seat cushion. The feet were placed centered (left to right) on their respective foot plates with the heels near the bottom of the foot plates. The left and right arms were positioned such that the palm of the hands were in contact with the steering wheel at the rim's horizontal centerline. The thumbs were placed over the steering wheel, and a 0.25 in. wide strip of masking tape was used to tape each thumb of the HIII and THOR-M to the steering wheel, wrapping around the thumb and steering wheel only once. For the PMHS tests, masking tape was wrapped around the thumb and/or hand and steering wheel, using only the necessary number of passes to keep the hand in place prior to the test. It should be noted that prior to positioning the HIII and THOR-M for each test, all joints were set to 1g, barely restraining the weight of the limb when it was extended horizontally.

In positioning the THOR-M, a concerted effort was made to match the positioning measurements of the HIII tests. However, differences in the design of the two ATDs necessitated concessions in some positional measurements, while others perceived to be more critical to the interaction between the ATD and the restraint system or test buck were preserved. Positioning was executed in a systematic manner, starting with the knee to bolster offset, followed by the chest and head offsets. The THOR-M's spine was adjusted at the junction between the thoracic and lumbar regions so that the ATD assumed a "slouched" (leaning forward by 9°) posture. The THOR-M "slouched" position was deemed more similar to the posture of the HIII. The adjusted spine posture and a more vertical seat back angle helped account for the shallower chest depth of the THOR-M, as compared to the HIII, and allowed the offset between the chest and the steering hub to be consistent with those used in the HIII tests. The offset distance between the nose and steering wheel rim was still larger for the THOR-M tests than the HIII tests, an artifact of the noticeably different facial contours, as the THOR-M head lacks a nose.

As with positioning the THOR-M, differences in anthropometry of the PMHSs required some adjustments to the NCAP positioning specifications while preserving those critical to the interaction of the PMHSs with the restraint system and test buck. The same systematic approach

was employed to meet the lower extremity, chest, and head offsets from the vehicle components. Given the lack of resting muscle tone, it was necessary to support the head-and-neck to maintain the desired initial position. The head was supported in an upright, forward-facing position using masking tape and a rigid overhead support structure. Tape was also used at the knees, when necessary, to prevent rotation at the hip joints, maintaining alignment of the hip, knee, and ankle joints in the sagittal plane. Any tape used to facilitate the initial position of the PMHSs was cut slightly prior to the start of each test to ensure that it tore free and did not impede the kinematics of the PMHS during the test.

Table 3.2: Positioning measurements for HIII tests.

Measurement	2012 Toyota Camry NCAP Report	HIII					
		KB		KB/SWAB		KBAB/SWAB	
		Test 1	Test 2	Test 1	Test 2	Test 1	Test 2
Striker to H-Point	315 mm	345 mm	341 mm	337.5 mm	336 mm	348.5 mm	341 mm
Striker to Knee	616 mm	647 mm	647 mm	651 mm	645 mm	648 mm	644 mm
Nose to Rim	425 mm	420 mm	420 mm	422 mm	421 mm	421 mm	420 mm
Chest to Steering Hub	323 mm	340 mm	340 mm	340 mm	341 mm	340 mm	340 mm
Knee to Dash – Left	168 mm	179 mm	180 mm	177 mm	180 mm	99 mm	101 mm
Knee to Dash – Right	140 mm	180 mm	181 mm	180 mm	176 mm	100 mm	100 mm
Knee to Knee	350 mm	278 mm	280 mm	281 mm	277 mm	281 mm	282 mm
Head Angle (from vert)	*N/A*	5.2 º	5.6 º	6.5 º	5.6 º	6.0 º	5.9 º
Arm Angle – Left	*N/A*	28.0 º	28.7 º	25.7 º	25.2 º	25.6 º	27.0 º
Arm Angle – Right	*N/A*	27.7 º	27.3 º	26.0 º	25.2 º	30.4 º	29.9 º
Forearm Angle – Left	*N/A*	22.3 º	20.0 º	19.0 º	20.2 º	20.8 º	18.7 º
Forearm Angle – Right	*N/A*	21.9 º	18.4 º	21.3 º	21.4 º	22.0 º	26.9 º
Pelvis Angle – Left	22.6 º	13.2 º	12.7 º	12.3 º	13.1 º	14.2 º	13.7 º
Pelvis Angle – Right	*N/A*	15.3 º	16.8 º	15.9 º	14.1 º	16.9 º	18.2 º
Tibia Angle – Left	41.6 º	35.8 º	36.5 º	38.0 º	38.2 º	37.2 º	36.1 º
Tibia Angle – Right	*N/A*	36.3 º	34.6 º	36.6 º	38.9 º	35.7 º	36.3 º
Shoulder Belt Angle	*N/A*	26.6 º	24.7 º	27.6 º	27.1 º	27.3 º	26.5 º
Seat Back Angle	3.5 º	5.4 º	5.1 º	5.7 º	6.5 º	5.4 º	6.1 º

Table 3.3: Positioning measurements for THOR-M tests.

Measurement	2012 Toyota Camry NCAP Report	THOR-M					
		KB		KB/SWAB		KBAB/SWAB	
		Test 1	Test 2	Test 1	Test 2	Test 1	Test 2
Striker to H-Point	315 mm	326 mm	329.5 mm	327 mm	323.5 mm	325.5 mm	320.5 mm
Striker to Knee	616 mm	667 mm	661 mm	666 mm	665 mm	670 mm	666 mm
Nose to Rim	425 mm	450 mm	450 mm	450 mm	450 mm	450 mm	451 mm
Chest to Steering Hub	323 mm	340 mm	341 mm	340 mm	340 mm	340 mm	340 mm
Knee to Dash – Left	168 mm	179 mm	179 mm	176 mm	175 mm	100 mm	97.5 mm
Knee to Dash – Right	140 mm	176 mm	181 mm	175 mm	174 mm	100 mm	99 mm
Knee to Knee	350 mm	223.5 mm	225 mm	213.5 mm	222 mm	218 mm	220.5 mm
Head Angle (from vert)	*N/A*	6.8 º	7.1 º	8.6 º	8.2 º	5.8 º	7.0 º
Arm Angle – Left	*N/A*	45.1 º	46.3 º	41.0 º	41.1 º	45.1 º	41.8 º
Arm Angle – Right	*N/A*	48.0 º	41.3 º	48.0 º	48.3 º	43.5 º	42.3 º
Forearm Angle – Left	*N/A*	30.7 º	32.6 º	32.2 º	33.8 º	31.2 º	32.8 º
Forearm Angle – Right	*N/A*	28.3 º	30.0 º	34.5 º	36.7 º	28.6 º	30.7 º
Pelvis Angle – Left	22.6 º	8.9 º	9.1 º	8.6 º	8.2 º	6.8 º	8.2 º
Pelvis Angle – Right	*N/A*	9.0 º	6.6 º	8.5 º	11.0 º	7.5 º	9.7 º
Tibia Angle – Left	41.6 º	32.3 º	30.9 º	33.9 º	32.4 º	33.0 º	32.5 º
Tibia Angle – Right	*N/A*	31.7 º	29.9 º	33.1 º	31.9 º	31.8 º	31.7 º
Shoulder Belt Angle	*N/A*	20.9 º	24.7 º	25.4 º	25.8 º	24.3 º	25.1 º
Seat Back Angle	3.5 º	3.0 º	3.1 º	3.2 º	3.1 º	2.7 º	2.5 º

Note: The length of the Hybrid III nose (~20-25 mm) accounts for the majority of the difference in the nose to rim distance between the Hybrid III and THOR-M.

Table 3.4: Positioning measurements for PMHS tests.

Measurement	2012 Toyota Camry NCAP Report	PMHS							
		KB		KB/SWAB			KBAB/SWAB		
		Test 1	Test 2	Test 1	Test 2	Test 3	Test 1	Test 2	Test 3
Striker to H-Point	315 mm	345 mm	350 mm	350 mm	335 mm	348 mm	363 mm	352 mm	331 mm
Striker to Knee	616 mm	670 mm	642 mm	663 mm	625 mm	637 mm	628 mm	636 mm	651 mm
Nose to Rim	425 mm	422 mm	416 mm	418 mm	420 mm	413 mm	405 mm	420 mm	403 mm
Chest to Steering Hub	323 mm	353 mm	356 mm	350 mm	348 mm	348 mm	354 mm	361 mm	342 mm
Knee to Dash – Left	168 mm	138 mm	123 mm	125 mm	125 mm	142 mm	60 mm	81 mm	47 mm
Knee to Dash – Right	140 mm	139 mm	134 mm	125 mm	116 mm	120 mm	62 mm	79 mm	49 mm
Knee to Knee	350 mm	240 mm	215 mm	245 mm	235 mm	227 mm	230 mm	220 mm	245 mm
Head Angle (from vert)	*N/A*	*N/A*	*N/A*	*N/A*	*N/A*	*N/A*	*N/A*	*N/A*	*N/A*
Arm Angle – Left	*N/A*	52.7 º	47.7 º	55.9 º	55.6 º	58.7 º	56.5 º	58.1 º	48.0 º
Arm Angle – Right	*N/A*	56.8 º	44.5 º	56.0 º	51.2 º	45.8 º	55.8 º	58.3 º	46.1 º
Forearm Angle – Left	*N/A*	23.2 º	48.6 º	31.5 º	36.0 º	45.7 º	33.5 º	37.5 º	38.8 º
Forearm Angle – Right	*N/A*	33.3 º	48.8 º	30.0 º	36.5 º	42.8 º	36.0 º	42.1 º	43.1 º
Pelvis Angle – Left	22.6 º	16.5 º	20.0 º	21.0 º	18.9 º	23.7 º	23.9 º	22.6 º	20.7 º
Pelvis Angle – Right	*N/A*	18.6 º	22.9 º	21.0 º	23.0 º	21.6 º	19.6 º	26.7 º	17.0 º
Tibia Angle – Left	41.6 º	43.7 º	44.5 º	44.1 º	42.0 º	41.4 º	43.8 º	45.4 º	44.8 º
Tibia Angle – Right	*N/A*	40.3 º	43.3 º	43.2 º	43.9 º	42.8 º	41.6 º	41.6 º	43.4 º
Shoulder Belt Angle	*N/A*	24.0 º	27.4 º	26.5 º	27.0 º	24.3 º	21.0 º	28.0 º	29.2 º
Seat Back Angle	3.5 º	2.8 º	0.3 º	5.1 º	3.6 º	4.2 º	0.3 º	1.2 º	5.3 º

Foam KB/KBAB Surrogates

The KB and KBAB were simulated using 65 psi and 19 psi rigid polyurethane foams, respectively. The right and left KBs and KBABs were independent foam blocks, located on either side of the steering column, and were replaced for each test. The geometries for the KB and KBAB foams during the HIII tests were reported by Albert *et al.* (2016) and Chapter 2 [25]. The knee to KB offset and the dimensions of the KB foam were maintained for all tests. For the KBAB foam, a consistent offset was maintained between the foam and shank for the entire length of the shank for all tests. This was achieved by slightly varying the dimensions of the KBAB foam for each surrogate to account for differences in lower extremity lengths and angles. When positioning subjects for the KBAB/SWAB tests, lower extremity offsets were first confirmed to be in accordance with those specified for the KB. Subsequently, the exact geometry of the KBAB foam was determined for each individual test to achieve the desired offset.

Instrumentation

A Vicon motion analysis system, consisting of 16 MX-T20 high speed motion tracking cameras (Figure 3.3), was used to capture test buck and subject kinematics. While the exact arrangement of markers varied between surrogate types, approximately 50 retroreflective markers were strategically placed on each surrogate to quantify the position of key anatomical landmarks (Table 3.5). Markers were adhered to the ATDs using double sided tape, while markers were affixed to the PMHSs using a combination of double sided tape, rigid attachment with bone screws, and rigid attachment via mounting plates. Bone screws were used to attach the right and left head CG markers, right and left shoulder (lateral humeral head) markers, and right and left greater trochanter markers. A metal plate with 4 markers was attached to the superior-posterior aspect of the head using two bone screws. Metal plates, one per leg with four markers each, were mounted to custom brackets that were rigidly fixed to the femurs using zip ties and tightened in place using noninvasive set screws. These set screws were used to push against the outside of the bone, thereby removing any slack from the zip ties, creating a rigid attachment to the bone. All 3D position data were captured at 1000Hz and reconstructed with a minimum criterion of two cameras to triangulate the position of the markers. Marker trajectories were converted to the reference frame of the test buck, then to the SAE J211 sign convention [26].

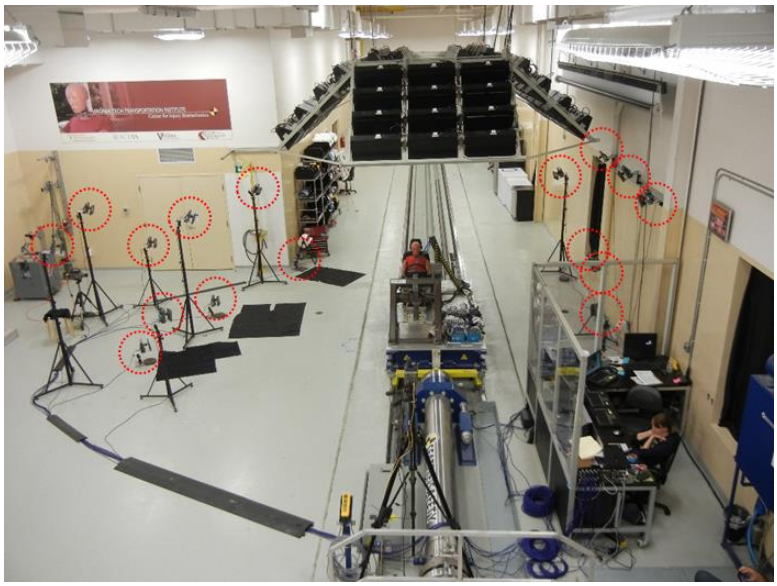

Figure 3.3: Motion capture setup with cameras circled in red.

Table 3.5: Number of Vicon markers on each surrogate.

Body Region	Surrogate		
	HIII	THOR-M	PMHS
Left & Right Lower Extremity	22	24	24
Left & Right Upper Extremity	18	20	20
Head	9	9	6
Total	49	53	50

Regions of interest for comparing excursions included the CG of the head, as well as the shoulder, hip, knee, and ankle, bilaterally. The head CG was calculated as the average of the right and left markers positioned in line with the CG of the ATD and PMHS heads. The shoulder locations were defined as the markers located on the shoulder joints of the HIII, the markers on the lateral aspect of the arm in line with the shoulders for the THOR-M, and the markers rigidly attached to the lateral aspect of the humeral heads for the PMHSs. The hip locations were defined as the markers located near the external inlet for the H-point tool of the HIII and THOR, and the greater trochanter marker for the PMHS. The knee and ankle locations were defined as the lateral knee and lateral ankle markers, respectively, for all subjects.

The surrogates and test buck were instrumented with a number of sensors. Both ATDs were instrumented with six degree of freedom sensor blocks at the head, chest, and pelvis that recorded linear accelerations and angular rates (Table 3.6). For the PMHS, analogous instrumentation was located at the head, T4, and sacrum. For the PMHS, the accelerometers and angular rate sensors were rigidly attached to the skeleton. First, the sensors were directly mounted to metal cubes. Then, these metal cubes were affixed to metal plates, which were rigidly attached the head, T4, and sacrum using bone screws. The PMHS head accelerometer assemblies were mounted to the posterior aspect of the head in line with the mid-sagittal plane. Therefore, it was necessary to transform the PMHS head accelerations to the head CG using rigid body dynamics to facilitate comparisons between surrogates. The head CG was assumed to be at the intersection of the line connecting the left and right anterior-superior insertion point of the helix of the ear with the mid-sagittal plane [27,28]. The horizontal and vertical distances between the accelerometer block and the head CG were determined for each PMHS from pictures taken before the sled test. The accelerometers and angular rate sensors at each location for each surrogate were oriented along the x, y, and z axes according to the SAE J211 sign convention [26]. Two belt load cells (3255, Denton, Rochester Hills, MI) were used to measure the lap belt and shoulder belt forces during each test. All data were collected at 20 kHz (TDAS Pro & G5, DTS, Seal Beach, CA) and filtered using channel frequency classes (CFCs) from SAE J211 [26] (Table 3.7).

Table 3.6: Accelerometer and angular rate sensor information for all surrogates.

Signal Type	**Surrogate**		
	HIII	**THOR-M**	**PMHS**
Head Accelerometers	7264B-2000, Endevco[†]	7264C-2000, Endevco	6DX PRO, DTS[‡]
Head Angular Rate Sensors	ARS PRO-18K, DTS	ARS PRO-8K, DTS	6DX PRO, DTS
Thorax Accelerometers	7264B-2000, Endevco	7264C-2000, Endevco	6DX PRO, DTS
Thorax Angular Rate Senosrs	ARS PRO-18K, DTS	ARS PRO-8K, DTS	6DX PRO, DTS
Pelvis Accelerometers	7264B-2000, Endevco	7264C-2000, Endevco	7264C-2000, Endevco
Pelvis Angular Rate Sensors	ARS PRO-18K, DTS	ARS PRO-8K, DTS	ARS PRO-18K, DTS

[†] Endevco, San Juan Capistrano, CA

[‡] DTS, Seal Beach, CA

Table 3.7: CFCs used to filter each signal type for all surrogates.

Signal Type	Surrogate		
	HIII	**THOR-M**	**PMHS**
Head Linear Accelerations	600	600	180
Head Angular Velocities	100	100	60
Thorax Linear Accelerations	180	180	180
Thorax Angular Velocities	60	60	60
Pelvis Linear Accelerations	180	180	180†
Pelvis Angular Velocities	60	60	60‡
Shoulder Belt Forces	180	180	180
Lab Belt Forces	180	180	180

† PMHS-KB/SWAB-1 was filtered at CFC 60 to eliminate excess noise

‡ PMHS-KB-2 was filtered at CFC 30 to eliminate excess noise

Data Analysis

Trajectories, linear accelerations, and angular velocities were compared qualitatively and quantitatively between test conditions and between subject types. Trajectories were normalized to their respective initial positions. Then, the peaks, peak timing, and overall time histories were compared for the trajectories, accelerations, and angular velocities. Comparisons were made between parameters of interest, including the forward (x) and vertical (z) excursions and linear accelerations as well as the angular velocities in the x, y, and z directions. The similarities in time histories between surrogates were evaluated using ISO/TS 18571 (referred to as ISO throughout) [29] by comparing the PMHS response to the HIII and THOR-M, and the HIII response to the THOR-M within each restraint condition.

The ISO rating was developed to compare computational model results (comparison curves) to experimental test results (reference curves), and components of the overall rating are calculated according to the reference curve. Therefore, how a set of curves are assigned to the reference and comparison categories can influence the resulting ISO scores. In order to maintain consistency between individual comparisons, the PMHS responses were considered the reference except in the case of between ATD comparisons, where the HIII responses were considered the reference. The ISO rating metric was also used to compare trajectory and acceleration time histories between the KB condition (reference) and the KB/SWAB condition (comparison) and between the KB/SWAB (reference) condition and the KBAB/SWAB condition (comparison) for each surrogate type.

The ISO rating metric was also designed to compare only one comparison curve to one reference curve. Therefore, a characteristic average was calculated using the method described in Lessley *et al.* (2004). The time of peak absolute magnitude was the characteristic time used to align the signals. However, some signals with multiple extrema did not have analogous absolute peaks. For these cases, the most defined analogous peaks were used to determine the characteristic time (see Figure 3.4 for representative curves). Average curves were only calculated to 0.15s or the maximum time point where data was available for all tests for each body region and parameter of interest, if data was not available for 0.15s. After 0.15s, the sled moved out of the motion capture volume and excursion data was mostly unavailable. Furthermore, peak accelerations and angular velocities occurred before this time point. If a motion capture marker for a region of interest was obstructed during a test before reaching peak excursion, the data from that test for that body region was not included in the analysis except for the PMHS head and shoulders, which did not peak within the capture volume. Before the ISO score was calculated, the average curves were truncated to an interval of evaluation using the algorithm employed by CORA with the parameter values listed in Table 3.8 [31]. The ISO scores were calculated based on the written standard, and included a window for the dynamic time warping algorithm that was 10% of the length of the curves before any phase shifting was applied.

Head injury risk was evaluated for all surrogates. The risk of sustaining an AIS3+ head injury was calculated for all conditions and surrogates using the Head Injury Criterion (HIC) (Equation 1) [32] and its corresponding risk function (Equation 2). The risk of sustaining an AIS3+ head injury was also calculated using the brain injury criterion (BrIC) (Equation 3) [33] and its corresponding risk function (Equation 4). Each PMHS was dissected after the sled test to record and categorize the occurrence of facial fractures. The observed injuries were used as a basis to evaluate the accuracy of the calculated injury risks.

Table 3.8: CORA parameter values used for the truncation algorithm.

CORA Parameter	Value
A_THRES	0.015
B_THRES	0.075
A_EVAL	0
B_DELTA_END	0 (disabled)
Y_NORM	extremum

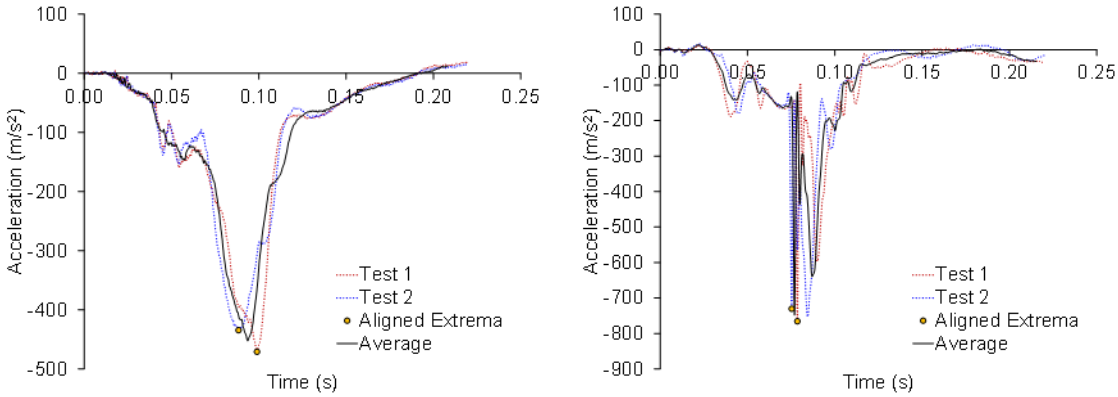

Figure 3.4: Example characteristic averages for head acceleration data where the absolute maximums were chosen to align the signals (left) and the distinct head strikes were chosen to align the signals (right).

Equation 1 $$HIC_{15} = \left|(t_2 - t_1)\left[\frac{1}{(t_2-t_1)}\int_{t_1}^{t_2} a(t)dt\right]^{2.5}\right|_{max}$$

Equation 2 $$p(AIS \geq 3) = \Phi\left[\frac{\ln(HIC_{15}) - 7.45231}{0.73998}\right]$$

Equation 3 $$BrIC = \sqrt{\left(\frac{\max(|\omega_x|)}{66.25}\right)^2 + \left(\frac{\max(|\omega_y|)}{56.45}\right)^2 + \left(\frac{\max(|\omega_z|)}{42.87}\right)^2}$$

Equation 4 $$p(AIS \geq 3) = 1 - e^{-\left(\frac{BrIC}{0.987}\right)^{2.84}}$$

Results

Head Kinematics

The comparative biofidelities of the HIII and THOR-M head kinematics varied between data type. The THOR-M experienced greater forward head excursions than the PMHSs regardless of restraint condition, while the magnitudes of the HIII forward excursions were more similar to the PMHS excursions (Figure A3.1, Table A3.1). When the head excursions of each ATD were quantitatively compared to the PMHSs, the average ISO scores for the THOR-M (0.688) were slightly lower than

those for the HIII (0.699) (Table 3.10, Table A3.15, Table A3.16). However, the THOR-M appeared to be more biofidelic in terms of head accelerations and angular rates (Figure A3.11 - Figure A3.15). The THOR-M forward head accelerations were more similar to the PMHS head accelerations, while the HIII had greater forward head accelerations than the other surrogates. The THOR-M also produced head angular rates that were more similar to the PMHS response since the HIII angular rates were out of phase compared to the other two surrogates. Consequently, the THOR-M had a higher average ISO score for the head accelerations and angular rates (0.585) than the HIII (0.422) when each ATD was compared to the PMHS response (Table 3.12, Table A3.17 - Table A3.21). When the ISO scores for all head kinematic data were averaged for each ATD, the THOR-M's score (0.614) was higher than the HIII's score (0.501), indicating that the THOR-M had more biofidelic head kinematics.

The most notable difference between the ATD and PMHS head kinematics was observed in the vertical head excursions. Both of the ATDs produced defined peaks in the vertical direction. However, the PMHS excursions for the KB condition only exhibited slight peaks that were subsequently followed by a cessation in forward motion. For the SWAB conditions, PMHS vertical head excursions increased without peaking until the end of the available capture time.

The head kinematics were more influenced by the addition of the SWAB than the KBAB. For all surrogates, the head accelerations were higher for the KB condition than the SWAB conditions due to the head striking the steering wheel/hub. The KB condition also had the greatest forward head excursions for all surrogates. Substantial differences between the head excursions, accelerations, and angular rates were not observed between the KB/SWAB and KBAB/SWAB conditions.

Shoulder/Thorax Kinematics

Each surrogate produced different shoulder kinematics. The THOR-M experienced the greatest peak forward excursions across all conditions for both shoulders. The PMHSs had greater forward excursions than the HIII for the KB condition, but were more similar to the HIII for the SWAB conditions. Both the THOR-M and the PMHSs exhibited differences between the left and right shoulder excursions, while the HIII did not. Additionally, marked differences were observed

between the ATDs and PMHSs in shoulder vertical excursions. The ATD shoulders moved downward, peaked, and began to move back up, while the PMHS shoulders generally moved upward through the last available time point. Accordingly, the ISO comparisons between the HIII and THOR-M had much higher scores than the comparisons between the ATDs and PMHS. The average ISO scores for the shoulder excursions were very similar between the HIII/PMHS (0.469) and THOR/PMHS (0.454) comparisons, indicating comparable biofidelity despite notable kinematic differences and the THOR-M's "improved" shoulder design.

The thorax accelerations and angular rates were qualitatively more similar between surrogates than the shoulder excursions. The PMHSs experienced more variability in forward thorax accelerations than the ATDs, but the peak timing and magnitude of these responses were similar on average for all surrogates (Figure A3.16). In the z direction, the PMHS thorax experienced the highest accelerations, and the THOR-M experienced the lowest (Figure A3.17). The z acceleration time history for one test (THOR-KB/SWAB-2) was not included in the analysis due to an equipment malfunction. For the angular velocities, the x and z responses were low in magnitude with some differences in timing and magnitude between surrogates, resulting in poor ISO scores when the ATDs were compared to the PMHSs (Figure A3.18 - Figure A3.20, Table 3.11 - Table 3.12, Table A3.5 - Table A3.7, Table A3.19 - Table A3.21). However, the two ATDs had comparable average ISO scores for the accelerations and angular velocities in all directions (HIII average: 0.450, THOR-M average: 0.484), indicating comparable biofidelity in thorax kinematics.

When comparing between conditions, differences in thoracic kinematics were not readily observed due to the addition of a KBAB, but differences were observed due to the addition of a SWAB. The KB condition had greater shoulder forward excursions than the SWAB conditions for all surrogates. This was reflected in the between-condition ISO comparisons where the scores comparing the SWAB conditions were mostly higher than the scores comparing the KB (no SWAB) condition to the KB/SWAB for all surrogates. The HIII experienced a distinct decrease in thoracic accelerations with the addition of a SWAB, but the THOR-M and PMHSs experienced little to no decrease.

Pelvis/Hip Kinematics

The hip markers were often obstructed during the tests, especially for the PMHSs, as a result of the seatbelt, clothing, and the seat. Therefore, several trajectories had to be excluded from the analysis because the markers were obstructed before peak excursion, including: left PMHS-KB/SWAB-2, right PMHS-KB-2, right PMHS-KB/SWAB-2, right PMHS-KBAB/SWAB-2, and right PMHS-KBAB/SWAB-3. Despite these losses, at least one trajectory was present for each condition for the PMHSs.

The hip excursions were more similar across surrogates than the pelvis accelerations. All surrogates showed similar peak magnitudes and timing for the hip excursions (Figure A3.5 - Figure A3.6). The main differences between surrogates resulted from differences in kinematics between the left and right sides. In the forward direction, both the PMHSs and the THOR-M experienced higher peak excursions on the right than the left. However, the HIII had higher peak excursions on the left than the right. For the ATDs, these left/right differences were also observed in the vertical excursions. Interestingly, the left/right differences observed in the hip trajectories were not captured in the x and z pelvic angular velocities, which were low in magnitude for all surrogates. The THOR-M had the highest forward accelerations, but the lowest vertical accelerations relative to the other surrogates (Figure A3.21 - Figure A3.22). Other timing and magnitude differences were observed between surrogates for each condition and acceleration direction, but these differences were not generalizable into trends. The average ISO scores of the pelvis/hip kinematics for each ATD/PMHS comparison were extremely similar (HIII average: 0.547, THOR-M average: 0.546). The HIII/PMHS pelvis acceleration and angular velocity comparisons yielded a slightly higher average ISO score (0.540) than the THOR/PMHS comparisons (0.478). However, the THOR/PMHS hip trajectory comparisons yielded a slightly higher average score (0.631) than the HIII/PMHS comparisons (0.556). Therefore, it cannot be concluded that one ATD has a definitively more biofidelic hip/pelvis response than the other.

The implementation of a KBAB affected pelvis and hip kinematics. For all surrogates, both the left and right hips had lower peak forward excursions for the KBAB/SWAB condition than the conditions involving a KB. All surrogates also had lower forward and vertical accelerations for the KBAB condition as compared to the KB conditions.

Knee Kinematics

The THOR-M had different knee kinematics compared to the other two surrogates. Primarily, the THOR-M had higher peak forward and vertical knee excursions than the other surrogates across all conditions. The HIII trajectories tended to be more similar to the PMHS trajectories in terms of magnitude. Consequently, the HIII had a much higher average ISO score (0.735) than the THOR-M (0.389) when each ATD was compared to the PMHS knee excursions for all conditions in both directions. Therefore, the HIII was more biofidelic than the THOR-M in terms of knee kinematics. One trajectory, right PMHS-KBAB/SWAB-3, was excluded from the knee kinematic analysis because the lateral knee marker was obstructed before reaching peak excursion.

Similar to the hips, the left and right knees experienced the lowest peak forward excursion for the KBAB/SWAB condition compared to the conditions involving KBs for all surrogates. Therefore, the KBAB was successful at reducing both knee and hip forward excursions.

Ankle Kinematics

The left and right ankles had the smallest forward and vertical excursions of all of the body regions. Little displacement at the ankle joint occurred for all surrogates and conditions because the feet remained stationary on the foot supports while the shank rotated in the sagittal plane about the ankle joint. As such, there was little difference between surrogates and conditions, and no trends were observed.

Global Kinematics

When considering the ISO scores for the excursions, accelerations, and angular rates for all body regions, the HIII and THOR-M were comparable in terms of biofidelity. The average ISO scores for the HIII/PMHS and THOR-M/PMHS comparisons were 0.527 and 0.518, respectively. The HIII had slightly higher scores than the THOR-M for the excursions (HIII average: 0.574; THOR-M average: 0.520). However, the THOR-M had slightly higher scores for the accelerations and angular rates (HIII average: 0.471; THOR-M average: 0.516).

Seatbelt Loads

The shoulder belt responses were consistent between surrogates and conditions due to the load limiter, whereas the lap belt response varied (Figure A3.26 - Figure A3.27). The HIII had the highest lap belt force for all conditions compared to the other surrogates. Whether the PMHS or THOR-M had the lowest lap belt forces depended on the restraint condition. The addition of a SWAB produced little difference in lap belt magnitude, but the addition of a KBAB decreased lap belt forces for all surrogates.

Head Injury Risk

The majority of tests predicted less than a 50% risk of AIS3+ head injury and no PMHS head or facial fractures were observed (Table 3.13). Two tests had a greater than 50% risk of AIS3+ injury from BrIC: HIII-KB-1 and PMHS-KB-2. In fact, BrIC predicted a greater injury risk for all tests compared to HIC. Both injury risk criteria predicted a higher injury risk for the KB condition compared to the SWAB conditions. This was a result of the head strike to the steering rim/hub in the KB conditions. The HIII had the highest predicted injury risks from HIC, while the PMHSs had the lowest. Conversely, the PMHSs had the highest predicted injury risks from BrIC with the exception of the KB condition, where the HIII had the highest predicted values.

Table 3.9: ISO scores for between condition trajectory comparisons in the forward (x) and vertical (z) directions.

Location	Surrogate	KB to KB/SWAB				KB/SWAB to KBAB/SWAB			
		X		Z		X		Z	
		Left	Right	Left	Right	Left	Right	Left	Right
Head	HIII	0.929		0.799		0.978		0.967	
	THOR	0.860		0.720		0.994		0.879	
	PMHS	0.820		0.413		0.954		0.737	
Shoulder	HIII	0.976	0.957	0.921	0.906	0.988	0.965	0.914	0.948
	THOR	0.858	0.888	0.604	0.892	0.860	0.979	0.566	0.694
	PMHS	0.752	0.750	0.385	0.547	0.948	0.890	0.729	0.441
Hip	HIII	0.989	0.970	0.964	0.903	0.746	0.679	0.730	0.711
	THOR	0.966	0.970	0.960	0.855	0.600	0.666	0.606	0.793
	PMHS	0.805	0.755	0.276	0.437	0.639	0.556	0.367	0.516
Knee	HIII	0.967	0.951	0.943	0.876	0.488	0.529	0.368	0.431
	THOR	0.940	0.968	0.933	0.891	0.597	0.590	0.668	0.709
	PMHS	0.777	0.839	0.735	0.827	0.551	0.664	0.509	0.609
Ankle	HIII	0.776	0.596	0.595	0.670	0.816	0.561	0.458	0.689
	THOR	0.906	0.861	0.376	0.324	0.905	0.812	0.653	0.290
	PMHS	0.845	0.756	0.695	0.673	0.825	0.757	0.380	0.377

Note: Green, yellow, orange, and red shading refer to excellent, good, fair, and poor ISO scores, respectively.

Table 3.10: ISO scores for between surrogate trajectory comparisons in the forward (x) and vertical (z) directions.

Location	Condition	PMHS to HIII				PMHS to THOR				HIII to THOR			
		X		Z		X		Z		X		Z	
		Left	Right	Left	Right	Left	Right	Left	Right	Left	Right	Left	Right
Head	KB	0.939		0.635		0.933		0.563		0.857		0.704	
	KB/SWAB	0.934		0.292		0.905		0.278		0.974		0.788	
	KBAB/SWAB	0.956		0.436		0.976		0.473		0.936		0.659	
Shoulder	KB	0.800	0.720	0.063	0.068	0.796	0.803	0.303	0.094	0.587	0.525	0.412	0.489
	KB/SWAB	0.957	0.879	0.134	0.086	0.671	0.664	0.149	0.083	0.708	0.573	0.668	0.473
	KBAB/SWAB	0.918	0.752	0.134	0.120	0.762	0.855	0.131	0.143	0.818	0.578	0.267	0.445
Hip	KB	0.708	0.603	0.120	0.377	0.607	0.512	0.237	0.788	0.835	0.684	0.706	0.362
	KB/SWAB	0.886	0.709	0.327	0.323	0.803	0.678	0.478	0.743	0.917	0.594	0.735	0.339
	KBAB/SWAB	0.780	0.729	0.747	0.366	0.836	0.533	0.722	0.632	0.966	0.659	0.613	0.345
Knee	KB	0.717	0.600	0.600	0.493	0.489	0.402	0.238	0.237	0.694	0.755	0.384	0.457
	KB/SWAB	0.940	0.785	0.750	0.688	0.674	0.516	0.296	0.237	0.721	0.674	0.368	0.319
	KBAB/SWAB	0.939	0.898	0.725	0.686	0.581	0.506	0.259	0.231	0.578	0.582	0.273	0.257
Ankle	KB	0.747	0.784	0.409	0.304	0.678	0.677	0.405	0.372	0.757	0.731	0.485	0.505
	KB/SWAB	0.653	0.586	0.355	0.330	0.809	0.808	0.169	0.259	0.691	0.634	0.305	0.258
	KBAB/SWAB	0.589	0.630	0.131	0.179	0.729	0.774	0.212	0.363	0.677	0.700	0.200	0.421

Note: Green, yellow, orange, and red shading refer to excellent, good, fair, and poor ISO scores, respectively.

Table 3.11: ISO scores for between condition comparisons for linear accelerations (aX, aZ) and angular velocities (wX, wY, wZ).

Location	Surrogate	KB to KB/SWAB					KB/SWAB to KBAB/SWAB				
		aX	aZ	wX	wY	wZ	aX	aZ	wX	wY	wZ
Head	HIII	0.589	0.747	0.752	0.418	0.488	0.815	0.797	0.635	0.904	0.478
	THOR	0.587	0.778	0.286	0.376	0.334	0.839	0.823	0.808	0.924	0.755
	PMHS	0.621	0.667	0.330	0.495	0.464	0.686	0.657	0.629	0.840	0.706
Thorax	HIII	0.816	0.742	0.727	0.855	0.694	0.878	0.633	0.740	0.947	0.267
	THOR	0.752	0.600	0.575	0.854	0.487	0.850	0.612	0.777	0.879	0.663
	PMHS	0.550	0.732	0.442	0.756	0.214	0.697	0.787	0.521	0.828	0.607
Pelvis	HIII	0.927	0.914	0.600	0.847	0.792	0.758	0.860	0.547	0.763	0.327
	THOR	0.962	0.854	0.349	0.816	0.508	0.712	0.729	0.497	0.680	0.582
	PMHS	0.773	0.792	0.333	0.671	0.424	0.755	0.682	0.532	0.682	0.322

Note: Green, yellow, orange, and red shading refer to excellent, good, fair, and poor ISO scores, respectively.

Table 3.12: ISO scores for between surrogate comparisons for linear accelerations (aX, aZ) and angular velocities (wX, wY, wZ).

Location	Condition	PMHS to HIII					PMHS to THOR					HIII to THOR				
		aX	aZ	wX	wY	wZ	aX	aZ	wX	wY	wZ	aX	aZ	wX	wY	wZ
Head	KB	0.491	0.620	0.522	0.382	0.431	0.695	0.730	0.437	0.580	0.294	0.714	0.728	0.596	0.683	0.331
	KB/SWAB	0.502	0.610	0.264	0.318	0.194	0.700	0.600	0.730	0.701	0.318	0.649	0.729	0.306	0.540	0.101
	KBAB/SWAB	0.512	0.704	0.216	0.343	0.223	0.567	0.749	0.588	0.687	0.394	0.641	0.800	0.153	0.488	0.244
Thorax	KB	0.505	0.532	0.359	0.564	0.208	0.561	0.349	0.249	0.599	0.428	0.828	0.472	0.555	0.767	0.240
	KB/SWAB	0.809	0.473	0.489	0.496	0.197	0.767	0.284	0.552	0.506	0.324	0.841	0.374	0.409	0.877	0.114
	KBAB/SWAB	0.642	0.593	0.377	0.352	0.151	0.649	0.521	0.428	0.455	0.582	0.895	0.444	0.400	0.895	0.168
Pelvis	KB	0.628	0.674	0.200	0.655	0.412	0.628	0.580	0.332	0.598	0.330	0.816	0.606	0.279	0.846	0.565
	KB/SWAB	0.711	0.706	0.450	0.656	0.436	0.696	0.522	0.234	0.677	0.342	0.800	0.570	0.156	0.771	0.217
	KBAB/SWAB	0.875	0.579	0.332	0.322	0.457	0.808	0.492	0.157	0.558	0.216	0.775	0.519	0.216	0.613	0.178

Note: Green, yellow, orange, and red shading refer to excellent, good, fair, and poor ISO scores, respectively.

Table 3.13: Probability of an AIS3+ head injury for each surrogate and the observed PMHS injuries.

Test	P(HIC_{15})	P(BrIC)	PMHS Observed Injury
HIII-KB-1	0.265	**0.733**	PMHS-KB-1: None PMHS-KB-2: None
HIII-KB-2	0.227	0.421	
HIII-KB/SWAB-1	0.000	0.139	PMHS-KB/SWAB-1: None PMHS-KB/SWAB-2: None PMHS-KB/SWAB-3: None
HIII-KB/SWAB-2	0.001	0.075	
HIII-KBAB/SWAB-1	0.003	0.123	PMHS-KBAB/SWAB-1: None PMHS-KBAB/SWAB-2: None PMHS-KBAB/SWAB-3: None
HIII-KBAB/SWAB-2	0.003	0.094	
THOR-KB-1	0.029	0.397	PMHS-KB-1: None PMHS-KB-2: None
THOR-KB-2	0.016	0.417	
THOR-KB/SWAB-1	0.000	0.143	PMHS-KB/SWAB-1: None PMHS-KB/SWAB-2: None PMHS-KB/SWAB-3: None
THOR-KB/SWAB-2	0.000	0.150	
THOR-KBAB/SWAB-1	0.000	0.145	PMHS-KBAB/SWAB-1: None PMHS-KBAB/SWAB-2: None PMHS-KBAB/SWAB-3: None
THOR-KBAB/SWAB-2	0.000	0.133	
PMHS-KB-1	0.003	0.330	PMHS-KB-1: None
PMHS-KB-2	0.043	**0.622**	PMHS-KB-2: None
PMHS-KB/SWAB-1	0.000	0.227	PMHS-KB/SWAB-1: None
PMHS-KB/SWAB-2	0.000	0.146	PMHS-KB/SWAB-2: None
PMHS-KB/SWAB-3	0.000	0.465	PMHS-KB/SWAB-3: None
PMHS-KBAB/SWAB-1	0.000	0.294	PMHS-KBAB/SWAB-1: None
PMHS-KBAB/SWAB-2	0.000	0.381	PMHS-KBAB/SWAB-2: None
PMHS-KBAB/SWAB-3	0.000	0.106	PMHS-KBAB/SWAB-3: None

Note: Boldface font indicates a calculated risk greater than 50% (0.500).

Discussion

The knee excursions for all surrogates were sensitive to the change in restraint condition from KB to KBAB. Specifically, KBABs were effective at reducing forward knee excursion. Interestingly, the KBAB also reduced the amount of upward knee excursion that each surrogate experienced. This is a natural consequence of a reduction in forward knee excursion because a greater forward knee excursion with a relatively fixed foot will increase the amount of knee flexion and, thereby,

the amount of vertical knee excursion. However, real-world KBABs and the KBAB foam surrogates used in this test series are capable of extending over the top of the knee, which can limit vertical knee excursions while transmitting loads to the shank. In fact, Weaver *et al.* (2013) reported a significantly higher incidence of proximal tibia and fibula fractures as well foot and ankle fractures associated with KBABs in their analysis of the effect of KBABs on injury using real-world crash comparisons. In another study of real-world crashes Patel *et al.* (2013) reported non-significant increases in these same fractures for occupants exposed to KBABs. Further research is needed to compare lower extremity loads between these surrogates and conditions. However, the results of this study demonstrate a possible injury mechanism for these real-world observations, involving increased shank loading due to the shank being pinned between the KBAB and floor pan.

The THOR-M's lower biofidelity in terms of knee kinematics was likely a result of the THOR-M's femur design. The THOR-M's femur was longer than the HIII femur, which changed the initial joint angles and influenced the kinematics of the THOR-M compared to the other surrogates. Furthermore, the THOR-M femur incorporated a deformable, stroking element [10], which could influence KB and KBAB interactions as well as lap belt forces.

The differences in thorax/shoulder and pelvis/hip kinematics between surrogates suggests that each surrogate interacted differently with the belt system. The THOR-M and PMHS had similar rotational kinematics outside of the sagittal plane as demonstrated by the thoracic angular accelerations and left/right excursion differences for the shoulders and hips. Conversely, the HIII showed little thoracic rotation outside of the sagittal plane and experienced left/right relative hip movement opposite the other two surrogates. These kinematics imply that the THOR-M was interacting with the shoulder belt in a more biofidelic manner than the HIII. Furthermore, each surrogate experienced different trends in pelvis acceleration and lap belt forces, indicating the surrogates interacted differently with the lap belt. The differences in pelvis shape and abdominal properties between surrogates likely caused some of these differences in lap belt interaction.

The greater peak forward shoulder excursions and delayed vertical and forward shoulder excursions experienced by the THOR-M in comparison to the HIII may be a result of differences

in chest and shoulder design between the THOR-M and HIII. Specifically, the THOR-M shoulder was designed to be more biofidelic by adding range of motion through protraction, and the thorax was modified to have a more anatomically correct design via clavicle shape, rib number, rib slant, and left/right decoupling. However, the similarity between the THOR-M and HIII thoracic accelerations indicate that the differences in excursions at the shoulder were not the result of gross movement of the thorax and were likely a result of protraction of the THOR-M shoulder.

The main difference in shoulder kinematics between surrogates was that the PMHS vertical trajectories indicated upward movement over the course of the test, whereas the ATDs exhibited downward shoulder movement. The upward shoulder excursions may be partially attributed to marker placement. Markers were originally placed on both the acromion and the humeral head of each PMHS. However, the SWAB often obstructed the acromion markers so the humeral head markers were used to calculate shoulder trajectories. The humeral head is meant to be an approximation of the shoulder joint center for sagittal plane motion. However, motion of the upper arm in the frontal plane, as was observed in the tests, will vertically displace the marker a greater distance than the shoulder joint itself elevates. However, additional video analysis also revealed that true shoulder elevation corresponding to the upward motion of the arm may also have contributed to the vertical displacement of the humeral head marker.

Differences in surrogate neck compliance introduced substantial deviations in head kinematics between surrogates. The greater forward head accelerations experienced by the HIII were likely a result of its stiffer neck, while the comparatively more compliant THOR-M neck produced greater head excursions. The PMHS necks were the most compliant, producing very different head kinematics compared to the ATDs. Both ATDs rebounded after reaching peak vertical excursion during all conditions, while the PMHS head exhibited a slight rebound during the KB condition before coming to rest on the steering wheel. During the SWAB conditions, the heads of the PMHSs sank into the airbags and continued to slide down the bags until the sled moved out of the capture volume, resulting in no peak vertical excursion. Therefore, ISO comparisons between the ATD and PMHS vertical excursions did not yield high scores.

Yoganandan *et al.* (2011) compared the head kinematics of a previous iteration of the THOR to the HIII and PMHS responses at low, medium, and high velocities under belted conditions. They reported that the THOR had higher biofidelity compared to the HIII, especially at lower severities, while the biofidelity of the HIII was acceptable at medium and high velocities. The current high velocity study found that the THOR-M had greater peak forward excursions than the other surrogates. This may be a result of the change in neck compliance between previous iterations of the THOR and the THOR-M. Despite these differences in forward excursions, the current study also found that the THOR-M had a more biofidelic head response when all head kinematic data was considered.

The ISO objective rating metric has several limitations. First, the metric is calculated over a user-defined interval of evaluation. The interval of evaluation is intended to restrict the evaluated curves to the meaningful signal, excluding baseline data before and after the test that could inflate the similarity score. Therefore, what data is included in the interval could influence the calculated scores. In an effort to minimize such influence, an established truncation algorithm presented as part of the CORA metric [31] was employed to determine the interval of evaluation for the data in this study. Second, the ISO metric is sensitive to noise in the evaluated curves, the presence of which could deflate the similarity scores. Noise was present in some of the acceleration data evaluated in this study, which could have led to reduced scores. However, an effort was made to maintain consistent CFCs within a type of signal to prevent any biases that would result from differences in filtering. Third, a study comparing expert opinion to the results of objective rating metrics found that the shape and phase scores from the ISO metric were not significantly different from expert opinion [34]. However, a significant difference between the ISO magnitude score and expert opinion was reported, which could be considered a limitation of the metric.

When averaging the ISO scores, all signal types and directions were equally weighted. However, certain signals or directions may be considered more important when examining frontal biofidelity. Additionally, low magnitude signals with a lower signal to noise ratio can deflate average scores, if weighted equally with higher magnitude signals. For example, low scores were observed for the x and z angular rates and ankle excursions for both surrogates due to the low magnitude of these responses. The ankle was mostly constrained, resulting in little motion. Additionally, motion out

of the sagittal plane was usually lower in magnitude than the in-plane motion. These low scoring parameters were hypothesized to influence the overall findings. Excluding the ankle excursions, x and z angular rates, or all of these parameters from the average ISO scores for each ATD slightly increased the scores, but still resulted in little difference in biofidelity between the ATDs (Figure A3.28). Limiting the average ISO scores to include only trajectories and accelerations in the forward direction led to the most substantial increase in average ISO score, but still there was little change in the difference between the HIII and THOR-M ISO scores.

This study was also limited by its small sample size for each condition. Although the ATDs offered highly repeatable responses, the responses of the PMHSs varied within condition due to variability in anthropometry between subjects. Including more PMHSs in each condition would have decreased the influence of each individual on the results. Furthermore, the limitations of motion capture increase as the complexities of the test setup and sled buck design increase due to a decrease in the lines of sight between the motion capture cameras and the markers. This was most evident at the hip, where trajectory data was lost for four out of eight tests on the right side and one of eight tests on the left due to marker obfuscation. Due to these losses, samples sizes within conditions were further reduced. The worst case was the KB/SWAB condition for the right hip, which had only one trajectory that could be compared to the other surrogates and conditions.

In the field of impact biomechanics, it is common practice to scale or normalize the biomechanical responses of individual PMHSs to that of a standard subject that an ATD is designed to represent, e.g., a 50th percentile male, in order to make direct comparisons between surrogate types. This is because differences in size, shape, and inertial properties can result in large differences in the measured biomechanical response. However, the PMHS response data in the current study was not normalized to a 50th percentile subject for several reasons. First, the relationship between the physical characteristics of a subject, e.g., mass and/or stature, and the corresponding biomechanical response to a stimulus must be established in order to predict the response of a standard subject based on the measured response of a non-standard subject [35]. Several techniques have been developed to normalize PMHS impact/reaction force, linear acceleration, and deflection data to a specific subject demographic based on total subject mass, effective mass, and/or a characteristic length [35-37]. However, each of these normalizing techniques were

derived based on the boundary conditions specific to particular experimental setups, which were generally limited to interactions with one loading surface along one loading direction, and consequently cannot be ubiquitously applied to all PMHS impact response data. Since the boundary conditions used in the current study are considerably more complex than those used to derive the currently published normalizing techniques, it is unclear if and how the physical characteristics of a subject correlate to the corresponding biomechanical response under such complex loading conditions. Therefore, it would not be appropriate to apply any of these normalizing techniques to the current linear acceleration data. Second, to the authors' knowledge there are currently no established techniques for normalizing trajectory or angular rate data for belted, frontal, PMHS sled tests. Finally, the mass and stature of the PMHSs used in the current study were intentionally selected to be approximately the same as a 50th percentile male to minimize the differences in the measured biomechanical response due to differences in size, shape, or inertial properties. The masses of the PMHSs were within +/-10% of a 50th male on average (max=23%, min=-1%), and only two subjects had masses greater than +/-11% of a 50th male (PMHS-KB-1=18%, PMHS-KB-2=23%). The statures of the PMHSs were within +/-4% of a 50th male on average (max=5%, min=-9%). Given the relatively small differences in mass and stature between the PMHSs and a 50th percentile male, it is not expected that normalizing the current data would have a considerable influence on the measured responses or observed trends.

The results of this study are specific to the test conditions and restraint conditions used. It is possible that different results would be obtained by using different offsets between the surrogates and the vehicle components, by reproducing a different vehicle interior, or by simulating the conditions of an out of position occupant. Different results may also be obtained using alternate safety restraint conditions. The timing of the belt pretensioner and airbag deployment used in this test were chosen based on the 2012 Toyota Camry NCAP test and may not be representative of other vehicle makes and model years. Additionally, the target KB stiffness was representative of a sedan, and results may differ with other bolster types and stiffnesses. Future research should be conducted under different test conditions and restraint conditions to further evaluate the comparative biofidelity of the HIII and THOR-M occupant kinematics.

Conclusions

Overall, this study evaluated differences in occupant kinematics for the HIII, THOR-M, and PMHS for three safety restraint conditions: KB, KB/SWAB, and KBAB/SWAB. All surrogates showed some degree of sensitivity to changes in restraint condition. For example, the use of a KBAB decreased the pelvis accelerations and the forward excursions of the knees and hips for all surrogates. However, these trends were not observed for the thorax, shoulders, and head, which showed more sensitivity to the presence of a SWAB. The results of the objective rating analysis indicated that the HIII and THOR-M had comparable overall biofidelity scores. The THOR-M slightly out-performed the HIII for the acceleration and angular velocity data. However, the HIII scored slightly better than the THOR-M for the excursion data. The most notable difference in biofidelity was for the knee excursions, where the HIII had a much higher average ISO score. This study only evaluated the biofidelity of the HIII and THOR with regard to occupant kinematics. However, future work will evaluate the biofidelity of the ATDs in terms of lower extremity loading, thoracic response, and neck loading.

References

1. NHTSA. *Traffic Safety Facts 2014: A Compilation of Motor Vehicle Crash Data Form the Fatality Analysis Reporting System and the General Estimates System*. Washington, DC: Transportation USDo; 2014.
2. Federal Register. *Part V. National Highway Traffic Safety Administration Consumer Information: New Car Assessment Program*. U.S. Department of Transportation; 2015.
3. Hoofman M, van Ratingen MR, Wismans J. Evaluation of the Dynamic and Kinematic Performance of the Thor Dummy: Neck Performance. Proceedings of the International Research Council on the Biomechanics of Injury conference (IRCOBI); September 16-18, 1998.
4. White RP, Zhoa Y, Rangarajan N, Haffner M. Development of an Instrumented Biofidelic Neck for the Nhtsa Advanced Frontal Test Dummy. Paper presented at: The 15th International Technical Conference on the Enhanced Safety of Vehicles; May, 1996; Melbourne, Australia.
5. Törnvall FV, Holmqvist K, Davidsson J, Svensson MY, Håland Y, Öhrn H. A New Thor Shoulder Design: A Comparison with Volunteers, the Hybrid Iii, and Thor Nt. *Traffic injury prevention.* 2007;8(2):205-215.
6. Kent R, Shaw G, Lessley D, Crandall J, Kallieris D, Svensson M. Comparison of Belted Hybrid Iii, Thor, and Cadaver Thoracic Responses in Oblique Frontal and Full Frontal Sled Tests. Paper presented at: SAE 2003 World Congress; March 3-6, 2003; Detroit, Michigan.
7. Forman J, Lessley D, Shaw CG, Evans J. Thoracic Response of Belted Pmhs, the Hybrid Iii, and the Thor-Nt Mid-Sized Male Surrogates in Low Speed, Frontal Crashes. *Stapp car crash journal.* 2006;50:191.
8. Shaw G, Crandall J, Butcher J. Biofidelity Evaluation of the Thor Advanced Frontal Crash Test Dummy. Proceedings of the International Research Council on the Biomechanics of Injury (IRCOBI) Conference; September 20-22, 2000; Montpellier, France.
9. Yoganandan N, Pintar F, Schlick M, Moore J, Maiman D. Comparison of Head–Neck Responses in Frontal Impacts Using Restrained Human Surrogates. Proceedings of the 55th Annals of Advances in Automotive Medicine/Annual Scientific Conference; October 3-5, 2011; Paris, France.

10. Ridella S, Parent D. Modifications to Improve the Durability, Usability, and Biofidelity of the Thor-Nt Dummy. The 22nd International Technical Conference on the Enhanced Safety of Vehicles; June 13-15, 2011; Washington, DC.
11. Rangarajan N, Shams T, McDonald J, White R, Oester J, Hjerpe E, Haffner MP. Response of Thor in Frontal Sled Testing in Different Restraint Conditions. Proceedings of the International Research Council on the Biomechanics of Injury (IRCOBI) conference; September 16-18, 1998.
12. Forman J, Michaelson J, Kent R, Kuppa S, Bostrom O. Occupant Restraint in the Rear Seat: Atd Responses to Standard and Pre-Tensioning, Force-Limiting Belt Restraints. *Ann Adv Automot Med.* 2008;52:141-154.
13. Forman J, Lopez-Valdes F, Lessley D, Kindig M, Kent R, Ridella S, Bostrom O. Rear Seat Occupant Safety: An Investigation of a Progressive Force-Limiting, Pretensioning 3-Point Belt System Using Adult Pmhs in Frontal Sled Tests. *Stapp car crash journal.* 2009;53:49.
14. Roychoudhury RS, Conlee JK, Best M, Schenck D. Blow-Molded Plastic Active Knee Bolsters. Paper presented at: SAE World Congress 2004; March 8-11, 2004; Detroit, Michigan.
15. Danelson KA, Golman AJ, Kemper AR, Gayzik FS, Gabler HC, Duma SM, Stitzel JD. Finite Element Comparison of Human and Hybrid Iii Responses in a Frontal Impact. *Accident Analysis & Prevention.* 2015;85:125-156.
16. Nie B, Crandall JR, Panzer MB. Computational Investigation of the Effects of Knee Airbag Design on the Interaction with Occupant Lower Extremity in Frontal and Oblique Impacts. *Traffic injury prevention.* 2016;18(2):207-215.
17. Ye X, Panzer MB, Shaw G, Crandall JR. Driver Lower Extremity Response to out of Position Knee Airbag Deployment. Proceedings of the International Research Council on the Biomechanics of Injury (IRCOBI) conference; September 10-12, 2014; Berlin, Germany.
18. Patel V, Griffin R, Eberhardt AW, McGwin G. The Association between Knee Airbag Deployment and Knee–Thigh–Hip Fracture Injury Risk in Motor Vehicle Collisions: A Matched Cohort Study. *Accident Analysis & Prevention.* 2013;50:964-967.

19. Weaver AA, Loftis KL, Stitzel JD. Investigation of the Safety Effects of Knee Bolster Air Bag Deployment in Similar Real-World Crash Comparisons. *Traffic injury prevention.* 2013;14(2):168-180.
20. Humanetics. Euro Ncap Adopts Thor-50m [press release]. 2016. Available at: http://www.humaneticsatd.com/about-us/press-releases/euro-ncap-adopts-thor-50m. Accessed April 1, 2017.
21. Janovicz D, Fischer B. *Final Report of New Car Assessment Program Frontal Impact Testing of 2012 Toyota Camry Lee 4-Dr Sedan.* Washington, DC: USDOT; December 16, 2011 2011.
22. Naik S. *Final Report of New Car Assessment Program Testing of a 2005 Toyota Camry Le*. Washington, DC: U.S. Department of Transportation,; March 11, 2005 2005.
23. Schneider L. Development of Anthropometrically Based Design Specifications for an Advanced Adult Anthropomorphic Dummy Family, Volume 1. Final Report. 1983.
24. NHTSA. *Laboratory Test Procedure for New Car Assessment Program (Ncap)- Frontal Impact Testing*. Washington, DC: U.S. Department of Transportation; 2012.
25. Albert DL, Beeman SM, McNally C, Kemper AR. Evaluation of Rigid Polyurethane Foam as a Surrogate Material for Knee Bolsters and Knee Bolster Airbags in Full Scale Frontal Sled Tests. Short Communications from Aaam's 60th Annual Scientific Conference. *Traffic Injury Prevention.* 2016/09/12 2016;17(sup1):205-208.
26. SAE. *Instrumentation for Impact Test.* Warrendale, PA: Society of Automotive Engineers;1995.
27. Vital J, Senegas J. Anatomical Bases of the Study of the Constraints to Which the Cervical Spine Is Subject in the Sagittal Plane a Study of the Center of Gravity of the Head. *Surgical and Radiologic Anatomy.* 1986;8(3):169-173.
28. Walker LB, Harris EH, Pontius UR. *Mass, Volume, Center of Mass, and Mass Moment of Inertia of Head and Head and Neck of Human Body.* SAE Technical Paper;1973. 0148-7191.
29. ISO. Road Vehicles - Objective Rating Metric for Non-Ambiguous Signals. ISO/TS 18571. 2014.
30. Lessley D, Crandall J, Shaw G, Kent R, Funk J. *A Normalization Technique for Developing Corridors from Individual Subject Responses.* SAE Technical Paper;2004. 0148-7191.

31. Thunert C. Cora Release 3.6 User's Manual. GNS mbH, Germany; 2012.
32. Federal Register. *Part Ii. National Highway Traffic Safety Administration Consumer Information: New Car Assessment Program*. U.S. Department of Transportation; 2008.
33. Takhounts EG, Craig MJ, Moorhouse K, McFadden J, Hasija V. Development of Brain Injury Criteria (Bric). *Stapp car crash journal.* 2013;57:243.
34. Davis ML. *Development and Full Body Validation of a 5th Percentile Female Finite Element Model*. Winston-Salem, North Carolina: School of Biomedical Engineering & Sciences, Virginia Tech - Wake Forest University; 2017.
35. Mertz HJ. *A Procedure for Normalizing Impact Response Data.* SAE Technical Paper;1984. 0148-7191.
36. Eppinger RH, Marcus JH, Morgan RM. *Development of Dummy and Injury Index for Nhtsa's Thoracic Side Impact Protection Research Program.* SAE Technical Paper;1984. 0148-7191.
37. ISO. Road Vehicles -- Anthropomorphic Side Impact Dummy -- Lateral Impact Response Requirements to Assess the Biofidelity of the Dummy. ISO/TR 9790. 1999.

Appendix

Table A3.1: Peak forward (x) excursions (m) for the head, shoulders, hips, knees, and ankles for all tests.

Surrogate	Condition	Test	Head	Shoulders		Hips		Knees		Ankles	
				Left	Right	Left	Right	Left	Right	Left	Right
HIII	KB	1	0.523	0.364	0.360	0.134	0.120	0.099	0.100	0.020	0.017
		2	0.533	0.365	0.368	0.135	0.123	0.096	0.106	0.018	0.022
	KB/SWAB	1	0.478	0.335	0.323	0.132	0.112	0.089	0.096	0.017	0.016
		2	0.477	0.345	0.331	0.140	0.116	0.096	0.092	0.018	0.015
	KBAB/SWAB	1	0.476	0.327	0.322	0.112	0.092	0.058	0.054	0.018	0.020
		2	0.463	0.321	0.311	0.114	0.094	0.063	0.064	0.020	0.022
THOR-M	KB	1	0.560	0.497	0.505	0.150	0.152	0.116	0.102	0.017	0.019
		2	0.578	0.504	0.515	0.150	0.167	0.115	0.113	0.018	0.019
	KB/SWAB	1	0.480	0.427	0.466	0.153	0.168	0.115	0.110	0.017	0.019
		2	0.480	0.429	0.461	0.144	0.147	0.111	0.105	0.018	0.019
	KBAB/SWAB	1	0.470	0.346	0.464	0.110	0.133	0.086	0.082	0.012	0.012
		2	0.495	0.395	0.437	0.105	0.108	0.085	0.080	0.016	0.016
PMHS	KB	1	0.549	0.439	0.448	0.135	0.130	0.096	0.087	0.032	0.030
		2	0.530	0.409	0.414	0.141	-	0.097	0.086	0.026	0.020
	KB/SWAB	1	0.411	0.373	0.342	0.141	0.134	0.093	0.089	0.027	0.031
		2	0.455	0.367	0.427	-	-	0.104	0.097	0.024	0.026
		3	0.431	0.248	0.316	0.134	0.152	0.085	0.082	0.024	0.021
	KBAB/SWAB	1	0.431	0.295	0.383	0.092	0.090	0.057	0.051	0.022	0.018
		2	0.521	0.302	0.438	0.123	-	0.064	0.059	0.015	0.017
		3	0.424	0.346	0.362	0.095	-	0.055	-	0.014	0.016

Table A3.2: Peak vertical (z) excursions (m) for the head, shoulders, hips, knees, and ankles for all tests.

Surrogate	Condition	Test	Head	Shoulders		Hips		Knees		Ankles	
				Left	Right	Left	Right	Left	Right	Left	Right
HIII	KB	1	0.207	0.075	0.084	0.036	0.025	-0.068	-0.068	0.017	0.009
		2	0.196	0.089	0.104	0.037	0.025	-0.069	-0.070	0.013	0.015
	KB/SWAB	1	0.179	0.070	0.078	0.036	0.022	-0.065	-0.064	0.023	0.025
		2	0.180	0.071	0.081	0.036	0.026	-0.071	-0.061	0.022	0.017
	KBAB/SWAB	1	0.191	0.064	0.070	0.033	0.025	-0.036	-0.035	0.023	0.025
		2	0.185	0.069	0.075	0.029	0.019	-0.037	-0.035	0.025	0.018
THOR-M	KB	1	0.240	0.047	0.108	0.030	0.038	-0.102	-0.091	0.001	0.004
		2	0.242	0.070	0.131	0.034	0.063	-0.101	-0.100	0.009	0.006
	KB/SWAB	1	0.201	0.041	0.115	0.031	0.073	-0.097	-0.092	0.001	0.001
		2	0.204	0.061	0.111	0.034	0.048	-0.097	-0.093	0.002	0.002
	KBAB/SWAB	1	0.216	0.042	0.099	0.032	0.068	-0.093	-0.088	0.001	0.006
		2	0.199	0.028	0.062	0.029	0.031	-0.084	-0.084	0.005	0.011
PMHS	KB	1	0.191	-0.026	-0.076	0.015	0.041	-0.075	-0.065	0.024	0.032
		2	0.144	-0.107	-0.058	0.012	-	-0.062	-0.060	0.016	0.027
	KB/SWAB	1	0.103	-0.132	-0.076	0.020	0.030	-0.064	-0.063	0.000	0.019
		2	0.125	-0.132	-0.144	-	-	-0.075	-0.072	0.006	0.019
		3	0.216	-0.097	-0.148	0.017	0.097	-0.065	-0.055	0.010	0.021
	KBAB/SWAB	1	0.165	-0.091	-0.103	0.004	0.052	-0.041	-0.037	0.009	0.006
		2	0.249	-0.071	-0.060	0.033	-	-0.047	-0.037	0.011	0.013
		3	0.160	-0.124	-0.138	0.061	-	-0.035	-	0.008	0.004

Table A3.3: Peak x accelerations (m/s^2) for the head, chest, and pelvis for all tests.

Surrogate	Condition	Test	Head	Chest	Pelvis
HIII	KB	1	-1915	-468	-584
		2	-1822	-460	-608
	KB/SWAB	1	-369	-350	-584
		2	-408	-356	-548
	KBAB/SWAB	1	-471	-314	-401
		2	-434	-345	-387
THOR-M	KB	1	-924	-350	-718
		2	-856	-340	-707
	KB/SWAB	1	-284	-354	-733
		2	-290	-354	-711
	KBAB/SWAB	1	-296	-331	-438
		2	-292	-334	-475
PMHS	KB	1	-766	-246	-408
		2	-753	-399	-380
	KB/SWAB	1	-253	-551	-689
		2	-301	-347	-497
		3	-361	-274	-544
	KBAB/SWAB	1	-217	-242	-408
		2	-320	-387	-440
		3	-260	-315	-407

Table A3.4: Peak z accelerations (m/s^2) for the head, chest, and pelvis for all tests.

Surrogate	Condition	Test	Head	Chest	Pelvis
HIII	KB	1	784	176	-360
		2	679	145	-361
	KB/SWAB	1	169	58	-351
		2	198	59	-355
	KBAB/SWAB	1	231	112	-287
		2	203	107	-285
THOR-M	KB	1	543	-83	-257
		2	539	118	-282
	KB/SWAB	1	237	-71	-236
		2	217	N/A	-254
	KBAB/SWAB	1	258	77	-152
		2	270	81	-150
PMHS	KB	1	388	280	-551
		2	522	326	-590
	KB/SWAB	1	246	149	-563
		2	189	266	-374
		3	161	167	-430
	KBAB/SWAB	1	282	193	-259
		2	284	206	-367
		3	326	156	-268

Table A3.5: Peak x angular velocities (rad/s) for the head, chest, and pelvis for all tests.

Surrogate	Condition	Test	Head	Chest	Pelvis
HIII	KB	1	-7.6	2.6	-1.9
		2	10.2	2.8	2.3
	KB/SWAB	1	4.4	2.3	-2.0
		2	5.7	-2.5	-2.0
	KBAB/SWAB	1	-2.4	1.9	-1.8
		2	4.6	2.5	-2.4
THOR-M	KB	1	8.2	3.9	1.7
		2	-8.5	1.2	-1.8
	KB/SWAB	1	11.7	4.7	1.9
		2	10.8	5.1	2.2
	KBAB/SWAB	1	9.4	4.4	3.0
		2	8.1	4.3	2.4
PMHS	KB	1	-5.7	6.3	3.7
		2	-11.5	-3.9	4.0
	KB/SWAB	1	10.5	4.6	-8.5
		2	-8.0	6.1	-3.4
		3	13.6	5.3	2.0
	KBAB/SWAB	1	-9.7	-5.6	-2.9
		2	12.5	-6.5	3.3
		3	-9.4	4.9	1.7

Table A3.6: Peak y angular velocities (rad/s) for the head, chest, and pelvis for all tests.

Surrogate	Condition	Test	Head	Chest	Pelvis
HIII	KB	1	-61.0	-22.7	-17.5
		2	-60.5	-23.4	-15.5
	KB/SWAB	1	-28.7	-18.7	-12.5
		2	-21.7	-19.2	-14.8
	KBAB/SWAB	1	-28.1	-19.3	-10.4
		2	-24.0	-19.4	-10.2
THOR-M	KB	1	-41.3	-19.3	-13.0
		2	-42.9	-21.0	-14.2
	KB/SWAB	1	-23.2	-17.1	-12.2
		2	-22.5	-17.5	-11.7
	KBAB/SWAB	1	-24.7	-15.8	-9.1
		2	-23.8	-17.3	-10.2
PMHS	KB	1	-30.3	-25.4	-17.5
		2	-36.8	-23.3	-27.1
	KB/SWAB	1	-31.0	-17.1	-11.9
		2	-27.3	-11.6	-17.6
		3	-38.0	-16.1	-12.6
	KBAB/SWAB	1	-33.4	-12.5	-11.7
		2	-36.3	-13.6	-11.1
		3	-22.3	-15.2	-13.8

Table A3.7: Peak z angular velocities (rad/s) for the head, chest, and pelvis for all tests.

Surrogate	Condition	Test	Head	Chest	Pelvis
HIII	KB	1	2.5	3.3	-2.9
		2	-7.8	3.0	-2.1
	KB/SWAB	1	3.1	2.5	-1.4
		2	4.1	2.8	1.5
	KBAB/SWAB	1	3.0	2.1	1.7
		2	5.9	5.6	1.9
THOR-M	KB	1	9.8	-4.5	-1.6
		2	8.3	4.1	-2.1
	KB/SWAB	1	-10.6	-5.1	-1.7
		2	-12.6	-5.6	-2.1
	KBAB/SWAB	1	-9.9	-5.4	-2.6
		2	10.0	-6.0	-1.8
PMHS	KB	1	-19.9	5.5	-3.4
		2	-30.3	-5.1	-
	KB/SWAB	1	-9.4	-4.0	-12.7
		2	5.6	-2.8	-6.9
		3	19.4	-4.5	2.5
	KBAB/SWAB	1	-13.0	-5.0	-3.3
		2	15.6	-6.9	-4.7
		3	7.8	3.0	3.1

Table A3.8: Detailed ISO scores for the between condition comparisons of forward (x) excursions.

Location	Surrogate	Reference	Comparison	Phase	Magnitude	Slope	Corridor	Overall
Head	HIII	KB	KB/SWAB	0.904	0.962	0.887	0.946	0.929
		KB/SWAB	KBAB/SWAB	0.934	0.995	0.961	1.000	0.978
	THOR	KB	KB/SWAB	0.915	0.841	0.912	0.817	0.860
		KB/SWAB	KBAB/SWAB	0.993	0.998	0.979	1.000	0.994
	PMHS	KB	KB/SWAB	0.978	0.786	0.853	0.740	0.820
		KB/SWAB	KBAB/SWAB	0.924	0.969	0.905	0.987	0.954
L Shoulder	HIII	KB	KB/SWAB	0.992	0.978	0.929	0.991	0.976
		KB/SWAB	KBAB/SWAB	0.996	0.981	0.966	0.998	0.988
	THOR	KB	KB/SWAB	0.892	0.828	0.914	0.828	0.858
		KB/SWAB	KBAB/SWAB	0.790	0.863	0.931	0.859	0.860
	PMHS	KB	KB/SWAB	0.682	0.730	0.877	0.735	0.752
		KB/SWAB	KBAB/SWAB	0.891	0.986	0.904	0.980	0.948
R Shoulder	HIII	KB	KB/SWAB	0.980	0.963	0.914	0.963	0.957
		KB/SWAB	KBAB/SWAB	0.904	0.989	0.952	0.990	0.965
	THOR	KB	KB/SWAB	0.802	0.908	0.900	0.914	0.888
		KB/SWAB	KBAB/SWAB	0.972	0.984	0.944	0.998	0.979
	PMHS	KB	KB/SWAB	0.635	0.776	0.833	0.754	0.750
		KB/SWAB	KBAB/SWAB	0.862	0.931	0.914	0.872	0.890
L Hip	HIII	KB	KB/SWAB	0.992	0.998	0.956	1.000	0.989
		KB/SWAB	KBAB/SWAB	0.816	0.825	0.862	0.614	0.746
	THOR	KB	KB/SWAB	0.926	0.997	0.927	0.991	0.966
		KB/SWAB	KBAB/SWAB	0.711	0.581	0.809	0.450	0.600
	PMHS	KB	KB/SWAB	0.753	0.949	0.820	0.752	0.805
		KB/SWAB	KBAB/SWAB	0.741	0.704	0.807	0.472	0.639
R Hip	HIII	KB	KB/SWAB	0.988	0.981	0.889	0.996	0.970
		KB/SWAB	KBAB/SWAB	0.707	0.768	0.749	0.586	0.679
	THOR	KB	KB/SWAB	0.951	0.995	0.919	0.994	0.970
		KB/SWAB	KBAB/SWAB	0.818	0.654	0.805	0.526	0.666
	PMHS	KB	KB/SWAB	0.730	0.910	0.819	0.658	0.755
		KB/SWAB	KBAB/SWAB	0.706	0.514	0.762	0.398	0.556
L Knee	HIII	KB	KB/SWAB	1.000	0.980	0.910	0.973	0.967
		KB/SWAB	KBAB/SWAB	0.711	0.407	0.717	0.301	0.488
	THOR	KB	KB/SWAB	0.903	0.992	0.891	0.957	0.940
		KB/SWAB	KBAB/SWAB	0.727	0.620	0.751	0.445	0.597
	PMHS	KB	KB/SWAB	0.737	0.923	0.769	0.728	0.777
		KB/SWAB	KBAB/SWAB	0.737	0.495	0.776	0.373	0.551
R Knee	HIII	KB	KB/SWAB	0.958	0.977	0.899	0.961	0.951
		KB/SWAB	KBAB/SWAB	0.715	0.464	0.729	0.369	0.529

	THOR	KB	KB/SWAB	0.966	0.997	0.879	1.000	0.968
		KB/SWAB	KBAB/SWAB	0.720	0.598	0.741	0.445	0.590
	PMHS	KB	KB/SWAB	0.858	0.967	0.789	0.790	0.839
		KB/SWAB	KBAB/SWAB	0.846	0.645	0.756	0.536	0.664
L Ankle	HIII	KB	KB/SWAB	0.941	0.936	0.747	0.628	0.776
		KB/SWAB	KBAB/SWAB	0.970	0.901	0.689	0.760	0.816
	THOR	KB	KB/SWAB	1.000	0.938	0.798	0.896	0.906
		KB/SWAB	KBAB/SWAB	1.000	0.928	0.783	0.907	0.905
	PMHS	KB	KB/SWAB	0.989	0.881	0.782	0.788	0.845
		KB/SWAB	KBAB/SWAB	1.000	0.847	0.697	0.791	0.825
R Ankle	HIII	KB	KB/SWAB	0.857	0.745	0.606	0.387	0.596
		KB/SWAB	KBAB/SWAB	0.877	0.691	0.588	0.324	0.561
	THOR	KB	KB/SWAB	0.964	0.849	0.735	0.880	0.861
		KB/SWAB	KBAB/SWAB	0.948	0.906	0.714	0.744	0.812
	PMHS	KB	KB/SWAB	0.948	0.819	0.628	0.692	0.756
		KB/SWAB	KBAB/SWAB	0.966	0.737	0.658	0.713	0.757

Note: Green, yellow, orange, and red shading refer to excellent, good, fair, and poor ISO scores, respectively.

Table A3.9: Detailed ISO scores for the between condition comparisons of vertical (z) excursions.

Location	Surrogate	Reference	Comparison	Phase	Magnitude	Slope	Corridor	Overall
Head	HIII	KB	KB/SWAB	0.617	0.946	0.810	0.812	0.799
		KB/SWAB	KBAB/SWAB	0.925	0.982	0.940	0.993	0.967
	THOR	KB	KB/SWAB	0.473	0.858	0.773	0.747	0.720
		KB/SWAB	KBAB/SWAB	0.626	0.982	0.874	0.957	0.879
	PMHS	KB	KB/SWAB	0.000	0.680	0.652	0.366	0.413
		KB/SWAB	KBAB/SWAB	0.751	0.723	0.687	0.763	0.737
L Shoulder	HIII	KB	KB/SWAB	0.995	0.934	0.879	0.898	0.921
		KB/SWAB	KBAB/SWAB	0.851	0.976	0.862	0.941	0.914
	THOR	KB	KB/SWAB	0.409	0.789	0.646	0.586	0.604
		KB/SWAB	KBAB/SWAB	0.460	0.583	0.619	0.584	0.566
	PMHS	KB	KB/SWAB	0.000	0.169	0.548	0.604	0.385
		KB/SWAB	KBAB/SWAB	0.905	0.683	0.698	0.678	0.729
R Shoulder	HIII	KB	KB/SWAB	0.958	0.923	0.909	0.871	0.906
		KB/SWAB	KBAB/SWAB	0.962	0.966	0.904	0.953	0.948
	THOR	KB	KB/SWAB	0.787	0.985	0.889	0.900	0.892
		KB/SWAB	KBAB/SWAB	0.553	0.785	0.745	0.693	0.694
	PMHS	KB	KB/SWAB	0.691	0.379	0.190	0.737	0.547
		KB/SWAB	KBAB/SWAB	0.060	0.000	0.637	0.755	0.441
L Hip	HIII	KB	KB/SWAB	0.973	0.994	0.854	1.000	0.964
		KB/SWAB	KBAB/SWAB	0.593	0.934	0.734	0.694	0.730
	THOR	KB	KB/SWAB	0.979	0.990	0.859	0.987	0.960
		KB/SWAB	KBAB/SWAB	0.514	0.890	0.615	0.506	0.606
	PMHS	KB	KB/SWAB	0.380	0.395	0.065	0.269	0.276
		KB/SWAB	KBAB/SWAB	0.894	0.000	0.464	0.238	0.367
R Hip	HIII	KB	KB/SWAB	0.957	0.922	0.758	0.938	0.903
		KB/SWAB	KBAB/SWAB	0.596	0.903	0.666	0.695	0.711
	THOR	KB	KB/SWAB	0.975	0.919	0.810	0.787	0.855
		KB/SWAB	KBAB/SWAB	0.747	0.930	0.698	0.796	0.793
	PMHS	KB	KB/SWAB	0.708	0.449	0.363	0.331	0.437
		KB/SWAB	KBAB/SWAB	0.405	0.705	0.464	0.503	0.516
L Knee	HIII	KB	KB/SWAB	0.992	0.981	0.844	0.948	0.943
		KB/SWAB	KBAB/SWAB	0.806	0.093	0.633	0.154	0.368
	THOR	KB	KB/SWAB	0.963	0.946	0.822	0.967	0.933
		KB/SWAB	KBAB/SWAB	0.828	0.722	0.579	0.606	0.668
	PMHS	KB	KB/SWAB	0.688	0.885	0.768	0.668	0.735
		KB/SWAB	KBAB/SWAB	0.649	0.440	0.799	0.329	0.509
R Knee	HIII	KB	KB/SWAB	0.910	0.935	0.779	0.878	0.876
		KB/SWAB	KBAB/SWAB	0.779	0.248	0.688	0.219	0.431

	THOR	KB	KB/SWAB	0.911	0.928	0.767	0.924	0.891
		KB/SWAB	KBAB/SWAB	0.815	0.777	0.581	0.687	0.709
	PMHS	KB	KB/SWAB	0.833	0.950	0.830	0.760	0.827
		KB/SWAB	KBAB/SWAB	0.783	0.523	0.765	0.487	0.609
L Ankle	HIII	KB	KB/SWAB	0.929	0.515	0.565	0.484	0.595
		KB/SWAB	KBAB/SWAB	1.000	0.000	0.462	0.414	0.458
	THOR	KB	KB/SWAB	0.712	0.000	0.286	0.440	0.376
		KB/SWAB	KBAB/SWAB	1.000	0.283	0.647	0.667	0.653
	PMHS	KB	KB/SWAB	0.943	0.521	0.659	0.675	0.695
		KB/SWAB	KBAB/SWAB	0.646	0.000	0.436	0.410	0.380
R Ankle	HIII	KB	KB/SWAB	0.918	0.541	0.544	0.672	0.670
		KB/SWAB	KBAB/SWAB	0.914	0.528	0.611	0.696	0.689
	THOR	KB	KB/SWAB	0.780	0.000	0.313	0.265	0.324
		KB/SWAB	KBAB/SWAB	0.000	0.000	0.393	0.530	0.290
	PMHS	KB	KB/SWAB	0.941	0.611	0.618	0.598	0.673
		KB/SWAB	KBAB/SWAB	0.615	0.000	0.527	0.372	0.377

Note: Green, yellow, orange, and red shading refer to excellent, good, fair, and poor ISO scores, respectively.

Table A3.10: Detailed ISO scores for the between condition comparisons of forward (x) linear accelerations.

Location	Surrogate	Reference	Comparison	Phase	Magnitude	Slope	Corridor	Overall
Head	HIII	KB	KB/SWAB	0.650	0.142	0.478	0.836	0.589
		KB/SWAB	KBAB/SWAB	0.981	0.916	0.462	0.859	0.815
	THOR	KB	KB/SWAB	0.445	0.549	0.480	0.730	0.587
		KB/SWAB	KBAB/SWAB	0.953	0.939	0.461	0.921	0.839
	PMHS	KB	KB/SWAB	0.473	0.649	0.491	0.747	0.621
		KB/SWAB	KBAB/SWAB	0.922	0.759	0.392	0.678	0.686
Thorax	HIII	KB	KB/SWAB	0.953	0.857	0.574	0.847	0.816
		KB/SWAB	KBAB/SWAB	0.990	0.940	0.625	0.917	0.878
	THOR	KB	KB/SWAB	0.922	0.846	0.463	0.765	0.752
		KB/SWAB	KBAB/SWAB	0.960	0.926	0.586	0.888	0.850
	PMHS	KB	KB/SWAB	0.821	0.441	0.478	0.505	0.550
		KB/SWAB	KBAB/SWAB	0.963	0.747	0.510	0.633	0.697
Pelvis	HIII	KB	KB/SWAB	0.957	0.962	0.745	0.986	0.927
		KB/SWAB	KBAB/SWAB	0.993	0.800	0.593	0.701	0.758
	THOR	KB	KB/SWAB	0.986	0.985	0.846	0.996	0.962
		KB/SWAB	KBAB/SWAB	0.972	0.695	0.545	0.673	0.712
	PMHS	KB	KB/SWAB	0.975	0.820	0.465	0.802	0.773
		KB/SWAB	KBAB/SWAB	0.932	0.830	0.496	0.760	0.755

Note: Green, yellow, orange, and red shading refer to excellent, good, fair, and poor ISO scores, respectively.

Table A3.11: Detailed ISO scores for the between condition comparisons of vertical (z) linear accelerations.

Location	Surrogate	Reference	Comparison	Phase	Magnitude	Slope	Corridor	Overall
Head	HIII	KB	KB/SWAB	0.918	0.598	0.502	0.859	0.747
		KB/SWAB	KBAB/SWAB	0.978	0.889	0.504	0.807	0.797
	THOR	KB	KB/SWAB	0.917	0.780	0.486	0.853	0.778
		KB/SWAB	KBAB/SWAB	0.931	0.941	0.526	0.859	0.823
	PMHS	KB	KB/SWAB	0.869	0.558	0.498	0.704	0.667
		KB/SWAB	KBAB/SWAB	0.953	0.686	0.359	0.643	0.657
Thorax	HIII	KB	KB/SWAB	0.986	0.492	0.575	0.829	0.742
		KB/SWAB	KBAB/SWAB	0.980	0.546	0.441	0.599	0.633
	THOR	KB	KB/SWAB	0.954	0.608	0.156	0.642	0.600
		KB/SWAB	KBAB/SWAB	0.899	0.596	0.404	0.580	0.612
	PMHS	KB	KB/SWAB	0.905	0.713	0.466	0.788	0.732
		KB/SWAB	KBAB/SWAB	0.982	0.864	0.522	0.783	0.787
Pelvis	HIII	KB	KB/SWAB	0.940	0.974	0.692	0.981	0.914
		KB/SWAB	KBAB/SWAB	0.988	0.899	0.684	0.863	0.860
	THOR	KB	KB/SWAB	0.977	0.877	0.609	0.904	0.854
		KB/SWAB	KBAB/SWAB	0.959	0.719	0.521	0.723	0.729
	PMHS	KB	KB/SWAB	0.993	0.814	0.569	0.791	0.792
		KB/SWAB	KBAB/SWAB	0.772	0.746	0.521	0.686	0.682

Note: Green, yellow, orange, and red shading refer to excellent, good, fair, and poor ISO scores, respectively.

Table A3.12: Detailed ISO scores for the between condition comparisons of x angular velocities.

Location	Surrogate	Reference	Comparison	Phase	Magnitude	Slope	Corridor	Overall
Head	HIII	KB	KB/SWAB	0.903	0.775	0.596	0.743	0.752
		KB/SWAB	KBAB/SWAB	0.935	0.550	0.549	0.571	0.635
	THOR	KB	KB/SWAB	0.362	0.000	0.284	0.392	0.286
		KB/SWAB	KBAB/SWAB	0.884	0.881	0.664	0.807	0.808
	PMHS	KB	KB/SWAB	0.719	0.000	0.518	0.206	0.330
		KB/SWAB	KBAB/SWAB	0.955	0.539	0.755	0.447	0.629
Thorax	HIII	KB	KB/SWAB	0.983	0.704	0.586	0.681	0.727
		KB/SWAB	KBAB/SWAB	0.927	0.756	0.594	0.711	0.740
	THOR	KB	KB/SWAB	0.941	0.473	0.376	0.544	0.575
		KB/SWAB	KBAB/SWAB	0.784	0.953	0.694	0.728	0.777
	PMHS	KB	KB/SWAB	0.921	0.182	0.459	0.323	0.442
		KB/SWAB	KBAB/SWAB	0.929	0.257	0.526	0.447	0.521
Pelvis	HIII	KB	KB/SWAB	0.983	0.373	0.619	0.512	0.600
		KB/SWAB	KBAB/SWAB	0.980	0.339	0.413	0.500	0.547
	THOR	KB	KB/SWAB	0.355	0.475	0.259	0.329	0.349
		KB/SWAB	KBAB/SWAB	0.835	0.272	0.496	0.440	0.497
	PMHS	KB	KB/SWAB	0.000	0.529	0.335	0.401	0.333
		KB/SWAB	KBAB/SWAB	0.817	0.545	0.378	0.460	0.532

Note: Green, yellow, orange, and red shading refer to excellent, good, fair, and poor ISO scores, respectively.

Table A3.13: Detailed ISO scores for the between condition comparisons of y angular velocities.

Location	Surrogate	Reference	Comparison	Phase	Magnitude	Slope	Corridor	Overall
Head	HIII	KB	KB/SWAB	0.000	0.213	0.435	0.720	0.418
		KB/SWAB	KBAB/SWAB	0.962	0.946	0.818	0.897	0.904
	THOR	KB	KB/SWAB	0.000	0.366	0.485	0.514	0.376
		KB/SWAB	KBAB/SWAB	0.956	0.974	0.894	0.898	0.924
	PMHS	KB	KB/SWAB	0.379	0.700	0.627	0.385	0.495
		KB/SWAB	KBAB/SWAB	0.951	0.873	0.784	0.795	0.840
Thorax	HIII	KB	KB/SWAB	0.988	0.798	0.825	0.832	0.855
		KB/SWAB	KBAB/SWAB	0.977	0.987	0.853	0.959	0.947
	THOR	KB	KB/SWAB	0.918	0.886	0.823	0.821	0.854
		KB/SWAB	KBAB/SWAB	0.985	0.915	0.746	0.875	0.879
	PMHS	KB	KB/SWAB	0.927	0.714	0.645	0.747	0.756
		KB/SWAB	KBAB/SWAB	0.950	0.871	0.672	0.824	0.828
Pelvis	HIII	KB	KB/SWAB	0.952	0.823	0.824	0.819	0.847
		KB/SWAB	KBAB/SWAB	0.963	0.742	0.632	0.738	0.763
	THOR	KB	KB/SWAB	0.941	0.804	0.823	0.756	0.816
		KB/SWAB	KBAB/SWAB	0.872	0.671	0.494	0.682	0.680
	PMHS	KB	KB/SWAB	0.718	0.563	0.739	0.668	0.671
		KB/SWAB	KBAB/SWAB	0.740	0.710	0.652	0.655	0.682

Note: Green, yellow, orange, and red shading refer to excellent, good, fair, and poor ISO scores, respectively.

Table A3.14: Detailed ISO scores for the between condition comparisons of z angular velocities.

Location	Surrogate	Reference	Comparison	Phase	Magnitude	Slope	Corridor	Overall
Head	HIII	KB	KB/SWAB	0.384	0.428	0.524	0.552	0.488
		KB/SWAB	KBAB/SWAB	0.796	0.292	0.340	0.481	0.478
	THOR	KB	KB/SWAB	0.732	0.000	0.404	0.268	0.334
		KB/SWAB	KBAB/SWAB	0.787	0.945	0.709	0.666	0.755
	PMHS	KB	KB/SWAB	0.483	0.110	0.602	0.563	0.464
		KB/SWAB	KBAB/SWAB	0.961	0.835	0.604	0.565	0.706
Thorax	HIII	KB	KB/SWAB	0.997	0.548	0.598	0.664	0.694
		KB/SWAB	KBAB/SWAB	0.000	0.449	0.277	0.304	0.267
	THOR	KB	KB/SWAB	0.848	0.455	0.429	0.350	0.487
		KB/SWAB	KBAB/SWAB	0.871	0.639	0.646	0.579	0.663
	PMHS	KB	KB/SWAB	0.000	0.000	0.375	0.348	0.214
		KB/SWAB	KBAB/SWAB	0.887	0.621	0.531	0.498	0.607
Pelvis	HIII	KB	KB/SWAB	0.986	0.717	0.691	0.782	0.792
		KB/SWAB	KBAB/SWAB	0.437	0.323	0.425	0.224	0.327
	THOR	KB	KB/SWAB	0.900	0.214	0.363	0.531	0.508
		KB/SWAB	KBAB/SWAB	0.909	0.497	0.450	0.527	0.582
	PMHS	KB	KB/SWAB	0.600	0.588	0.133	0.400	0.424
		KB/SWAB	KBAB/SWAB	0.027	0.173	0.489	0.459	0.322

Note: Green, yellow, orange, and red shading refer to excellent, good, fair, and poor ISO scores, respectively.

Table A3.15: Detailed ISO scores for the between surrogate comparisons of forward (x) excursions.

Location	Condition	Reference	Comparison	Phase	Magnitude	Slope	Corridor	Overall
Head	KB	PMHS	HIII	0.963	0.966	0.874	0.947	0.939
		PMHS	THOR	0.850	0.969	0.927	0.960	0.933
		HIII	THOR	0.815	0.895	0.887	0.845	0.857
	KB/SWAB	PMHS	HIII	0.931	0.952	0.879	0.954	0.934
		PMHS	THOR	0.913	0.911	0.912	0.894	0.905
		HIII	THOR	0.982	0.987	0.932	0.986	0.974
	KBAB/SWAB	PMHS	HIII	0.927	0.986	0.892	0.987	0.956
		PMHS	THOR	0.982	0.973	0.936	0.996	0.976
		HIII	THOR	0.912	0.962	0.915	0.945	0.936
L Shoulder	KB	PMHS	HIII	0.613	0.854	0.895	0.820	0.800
		PMHS	THOR	0.967	0.773	0.829	0.704	0.796
		HIII	THOR	0.596	0.439	0.774	0.564	0.587
	KB/SWAB	PMHS	HIII	0.923	0.984	0.935	0.972	0.957
		PMHS	THOR	0.765	0.601	0.836	0.577	0.671
		HIII	THOR	0.672	0.679	0.877	0.658	0.708
	KBAB/SWAB	PMHS	HIII	0.818	0.989	0.893	0.945	0.918
		PMHS	THOR	0.927	0.784	0.813	0.642	0.762
		HIII	THOR	0.885	0.833	0.876	0.747	0.818
R Shoulder	KB	PMHS	HIII	0.774	0.736	0.747	0.671	0.720
		PMHS	THOR	0.821	0.794	0.849	0.775	0.803
		HIII	THOR	0.635	0.321	0.708	0.480	0.525
	KB/SWAB	PMHS	HIII	0.878	0.939	0.918	0.830	0.879
		PMHS	THOR	0.704	0.640	0.817	0.579	0.664
		HIII	THOR	0.845	0.401	0.784	0.418	0.573
	KBAB/SWAB	PMHS	HIII	0.905	0.730	0.888	0.619	0.752
		PMHS	THOR	0.865	0.889	0.864	0.829	0.855
		HIII	THOR	0.798	0.424	0.789	0.439	0.578
L Hip	KB	PMHS	HIII	0.565	0.941	0.815	0.611	0.708
		PMHS	THOR	0.422	0.832	0.763	0.509	0.607
		HIII	THOR	0.855	0.922	0.885	0.756	0.835
	KB/SWAB	PMHS	HIII	0.787	0.993	0.891	0.880	0.886
		PMHS	THOR	0.722	0.947	0.881	0.733	0.803
		HIII	THOR	0.937	0.956	0.912	0.891	0.917
	KBAB/SWAB	PMHS	HIII	0.721	0.957	0.849	0.687	0.780
		PMHS	THOR	0.770	0.982	0.856	0.785	0.836
		HIII	THOR	0.950	0.986	0.933	0.981	0.966
R Hip	KB	PMHS	HIII	0.360	0.905	0.726	0.512	0.603
		PMHS	THOR	0.360	0.623	0.703	0.436	0.512

		HIII	THOR	0.996	0.676	0.819	0.463	0.684
	KB/SWAB	PMHS	HIII	0.626	0.851	0.802	0.633	0.709
		PMHS	THOR	0.551	0.851	0.783	0.602	0.678
		HIII	THOR	0.940	0.522	0.818	0.346	0.594
	KBAB/SWAB	PMHS	HIII	0.602	0.978	0.755	0.654	0.729
		PMHS	THOR	0.440	0.587	0.760	0.438	0.533
		HIII	THOR	0.809	0.742	0.812	0.467	0.659
L Knee	KB	PMHS	HIII	0.642	0.895	0.752	0.649	0.717
		PMHS	THOR	0.368	0.488	0.674	0.458	0.489
		HIII	THOR	0.729	0.777	0.818	0.573	0.694
	KB/SWAB	PMHS	HIII	0.912	0.995	0.882	0.954	0.940
		PMHS	THOR	0.748	0.757	0.817	0.523	0.674
		HIII	THOR	0.834	0.784	0.845	0.572	0.721
	KBAB/SWAB	PMHS	HIII	0.962	0.992	0.799	0.970	0.939
		PMHS	THOR	0.778	0.642	0.745	0.370	0.581
		HIII	THOR	0.829	0.649	0.766	0.324	0.578
R Knee	KB	PMHS	HIII	0.618	0.683	0.702	0.499	0.600
		PMHS	THOR	0.300	0.276	0.614	0.410	0.402
		HIII	THOR	0.764	0.872	0.753	0.692	0.755
	KB/SWAB	PMHS	HIII	0.794	0.899	0.720	0.756	0.785
		PMHS	THOR	0.511	0.508	0.674	0.444	0.516
		HIII	THOR	0.746	0.766	0.737	0.562	0.674
	KBAB/SWAB	PMHS	HIII	0.910	0.970	0.810	0.900	0.898
		PMHS	THOR	0.604	0.523	0.770	0.317	0.506
		HIII	THOR	0.711	0.691	0.789	0.358	0.582
L Ankle	KB	PMHS	HIII	0.985	0.784	0.724	0.622	0.747
		PMHS	THOR	0.989	0.580	0.734	0.543	0.678
		HIII	THOR	0.993	0.745	0.742	0.653	0.757
	KB/SWAB	PMHS	HIII	0.959	0.538	0.574	0.596	0.653
		PMHS	THOR	0.984	0.781	0.754	0.764	0.809
		HIII	THOR	0.944	0.657	0.619	0.617	0.691
	KBAB/SWAB	PMHS	HIII	0.905	0.495	0.409	0.567	0.589
		PMHS	THOR	0.958	0.774	0.736	0.589	0.729
		HIII	THOR	0.963	0.643	0.689	0.545	0.677
R Ankle	KB	PMHS	HIII	0.901	0.883	0.639	0.748	0.784
		PMHS	THOR	0.889	0.654	0.569	0.637	0.677
		HIII	THOR	0.952	0.724	0.624	0.677	0.731
	KB/SWAB	PMHS	HIII	0.927	0.442	0.602	0.479	0.586
		PMHS	THOR	0.996	0.819	0.740	0.743	0.808
		HIII	THOR	0.897	0.697	0.554	0.513	0.634
	KBAB/SWAB	PMHS	HIII	0.980	0.595	0.641	0.466	0.630

		PMHS	THOR	0.972	0.845	0.700	0.675	0.774
		HIII	THOR	0.956	0.688	0.761	0.547	0.700

Note: Green, yellow, orange, and red shading refer to excellent, good, fair, and poor ISO scores, respectively.

Table A3.16: Detailed ISO scores for the between surrogate comparisons of vertical (z) excursions.

Location	Condition	Reference	Comparison	Phase	Magnitude	Slope	Corridor	Overall
Head	KB	PMHS	HIII	0.502	0.880	0.604	0.594	0.635
		PMHS	THOR	0.886	0.523	0.675	0.366	0.563
		HIII	THOR	0.643	0.752	0.810	0.657	0.704
	KB/SWAB	PMHS	HIII	0.000	0.445	0.567	0.225	0.292
		PMHS	THOR	0.000	0.448	0.608	0.168	0.278
		HIII	THOR	0.518	0.877	0.857	0.845	0.788
	KBAB/SWAB	PMHS	HIII	0.000	0.829	0.643	0.355	0.436
		PMHS	THOR	0.000	0.954	0.771	0.318	0.473
		HIII	THOR	0.088	0.803	0.797	0.804	0.659
L Shoulder	KB	PMHS	HIII	0.000	0.000	0.000	0.157	0.063
		PMHS	THOR	1.000	0.000	0.202	0.158	0.303
		HIII	THOR	0.000	0.356	0.535	0.585	0.412
	KB/SWAB	PMHS	HIII	0.000	0.000	0.557	0.056	0.134
		PMHS	THOR	0.000	0.000	0.585	0.079	0.149
		HIII	THOR	0.957	0.648	0.754	0.491	0.668
	KBAB/SWAB	PMHS	HIII	0.000	0.000	0.401	0.136	0.134
		PMHS	THOR	0.000	0.000	0.267	0.195	0.131
		HIII	THOR	0.000	0.022	0.579	0.366	0.267
R Shoulder	KB	PMHS	HIII	0.000	0.000	0.000	0.170	0.068
		PMHS	THOR	0.000	0.000	0.000	0.234	0.094
		HIII	THOR	0.117	0.884	0.826	0.310	0.489
	KB/SWAB	PMHS	HIII	0.000	0.000	0.180	0.125	0.086
		PMHS	THOR	0.037	0.000	0.000	0.190	0.083
		HIII	THOR	0.253	0.716	0.789	0.304	0.473
	KBAB/SWAB	PMHS	HIII	0.000	0.000	0.177	0.211	0.120
		PMHS	THOR	0.000	0.000	0.066	0.324	0.143
		HIII	THOR	0.000	0.836	0.811	0.288	0.445
L Hip	KB	PMHS	HIII	0.396	0.000	0.000	0.101	0.120
		PMHS	THOR	0.627	0.000	0.000	0.278	0.237
		HIII	THOR	0.964	0.742	0.726	0.550	0.706
	KB/SWAB	PMHS	HIII	0.648	0.000	0.556	0.216	0.327
		PMHS	THOR	0.734	0.242	0.609	0.404	0.478
		HIII	THOR	0.986	0.798	0.703	0.593	0.735
	KBAB/SWAB	PMHS	HIII	0.768	0.926	0.537	0.752	0.747
		PMHS	THOR	0.784	0.892	0.528	0.702	0.722
		HIII	THOR	0.680	0.702	0.485	0.600	0.613
R Hip	KB	PMHS	HIII	0.947	0.022	0.517	0.199	0.377

		PMHS	THOR	0.992	0.905	0.473	0.786	0.788
		HIII	THOR	0.931	0.000	0.642	0.119	0.362
	KB/SWAB	PMHS	HIII	0.672	0.000	0.566	0.188	0.323
		PMHS	THOR	0.737	0.915	0.590	0.735	0.743
		HIII	THOR	0.953	0.000	0.506	0.117	0.339
	KBAB/SWAB	PMHS	HIII	0.475	0.024	0.580	0.376	0.366
		PMHS	THOR	0.426	0.952	0.640	0.571	0.632
		HIII	THOR	0.988	0.000	0.437	0.149	0.345
L Knee	KB	PMHS	HIII	0.533	0.694	0.604	0.584	0.600
		PMHS	THOR	0.257	0.000	0.513	0.209	0.238
		HIII	THOR	0.702	0.097	0.722	0.200	0.384
	KB/SWAB	PMHS	HIII	0.875	0.868	0.679	0.664	0.750
		PMHS	THOR	0.589	0.000	0.519	0.187	0.296
		HIII	THOR	0.640	0.113	0.641	0.222	0.368
	KBAB/SWAB	PMHS	HIII	0.654	0.968	0.700	0.650	0.725
		PMHS	THOR	0.392	0.000	0.590	0.156	0.259
		HIII	THOR	0.778	0.000	0.391	0.098	0.273
R Knee	KB	PMHS	HIII	0.452	0.473	0.571	0.485	0.493
		PMHS	THOR	0.257	0.000	0.530	0.200	0.237
		HIII	THOR	0.853	0.319	0.688	0.211	0.457
	KB/SWAB	PMHS	HIII	0.689	0.814	0.658	0.639	0.688
		PMHS	THOR	0.374	0.000	0.444	0.184	0.237
		HIII	THOR	0.652	0.000	0.616	0.163	0.319
	KBAB/SWAB	PMHS	HIII	0.640	0.976	0.720	0.548	0.686
		PMHS	THOR	0.296	0.000	0.584	0.138	0.231
		HIII	THOR	0.681	0.000	0.418	0.092	0.257
L Ankle	KB	PMHS	HIII	0.826	0.000	0.585	0.316	0.409
		PMHS	THOR	0.826	0.000	0.510	0.344	0.405
		HIII	THOR	0.770	0.251	0.394	0.504	0.485
	KB/SWAB	PMHS	HIII	0.842	0.000	0.347	0.294	0.355
		PMHS	THOR	0.000	0.000	0.164	0.341	0.169
		HIII	THOR	0.000	0.000	0.250	0.637	0.305
	KBAB/SWAB	PMHS	HIII	0.176	0.000	0.332	0.074	0.131
		PMHS	THOR	0.000	0.042	0.262	0.378	0.212
		HIII	THOR	0.000	0.000	0.370	0.316	0.200
R Ankle	KB	PMHS	HIII	0.703	0.000	0.456	0.182	0.304
		PMHS	THOR	0.924	0.000	0.517	0.210	0.372
		HIII	THOR	0.836	0.452	0.488	0.374	0.505
	KB/SWAB	PMHS	HIII	1.000	0.000	0.507	0.070	0.330
		PMHS	THOR	0.623	0.000	0.285	0.192	0.259
		HIII	THOR	0.151	0.000	0.263	0.438	0.258

	KBAB/SWAB	PMHS	HIII	0.453	0.000	0.323	0.060	0.179
		PMHS	THOR	0.933	0.000	0.422	0.231	0.363
		HIII	THOR	0.961	0.000	0.500	0.322	0.421

Note: Green, yellow, orange, and red shading refer to excellent, good, fair, and poor ISO scores, respectively.

Table A3.17: Detailed ISO scores for the between surrogate comparisons of forward (x) linear accelerations.

Location	Condition	Reference	Comparison	Phase	Magnitude	Slope	Corridor	Overall
Head	KB	PMHS	HIII	0.612	0.449	0.072	0.660	0.491
		PMHS	THOR	0.973	0.559	0.460	0.741	0.695
		HIII	THOR	0.839	0.532	0.527	0.837	0.714
	KB/SWAB	PMHS	HIII	0.398	0.809	0.198	0.553	0.502
		PMHS	THOR	0.729	0.957	0.299	0.757	0.700
		HIII	THOR	0.701	0.752	0.410	0.690	0.649
	KBAB/SWAB	PMHS	HIII	0.678	0.507	0.282	0.546	0.512
		PMHS	THOR	0.689	0.775	0.229	0.571	0.567
		HIII	THOR	0.639	0.787	0.302	0.740	0.641
Thorax	KB	PMHS	HIII	0.913	0.412	0.321	0.441	0.505
		PMHS	THOR	1.000	0.330	0.469	0.503	0.561
		HIII	THOR	0.968	0.911	0.550	0.855	0.828
	KB/SWAB	PMHS	HIII	0.944	0.947	0.513	0.821	0.809
		PMHS	THOR	0.884	0.927	0.420	0.801	0.767
		HIII	THOR	0.965	0.951	0.509	0.890	0.841
	KBAB/SWAB	PMHS	HIII	0.974	0.677	0.395	0.582	0.642
		PMHS	THOR	0.983	0.672	0.471	0.561	0.649
		HIII	THOR	0.990	0.973	0.579	0.966	0.895
Pelvis	KB	PMHS	HIII	0.819	0.622	0.311	0.694	0.628
		PMHS	THOR	0.789	0.614	0.339	0.698	0.628
		HIII	THOR	0.951	0.896	0.532	0.851	0.816
	KB/SWAB	PMHS	HIII	0.746	0.871	0.422	0.757	0.711
		PMHS	THOR	0.734	0.862	0.398	0.743	0.696
		HIII	THOR	0.903	0.929	0.501	0.834	0.800
	KBAB/SWAB	PMHS	HIII	0.972	0.934	0.594	0.937	0.875
		PMHS	THOR	0.894	0.920	0.531	0.848	0.808
		HIII	THOR	0.864	0.945	0.506	0.780	0.775

Note: Green, yellow, orange, and red shading refer to excellent, good, fair, and poor ISO scores, respectively.

Table A3.18: Detailed ISO scores for the between surrogate comparisons of vertical (z) linear accelerations.

Location	Condition	Reference	Comparison	Phase	Magnitude	Slope	Corridor	Overall
Head	KB	PMHS	HIII	0.752	0.704	0.155	0.745	0.620
		PMHS	THOR	0.896	0.760	0.454	0.770	0.730
		HIII	THOR	0.831	0.734	0.426	0.824	0.728
	KB/SWAB	PMHS	HIII	0.937	0.551	0.398	0.584	0.610
		PMHS	THOR	0.860	0.627	0.371	0.572	0.600
		HIII	THOR	0.974	0.875	0.390	0.702	0.729
	KBAB/SWAB	PMHS	HIII	0.967	0.644	0.458	0.725	0.704
		PMHS	THOR	0.959	0.796	0.455	0.768	0.749
		HIII	THOR	0.958	0.910	0.464	0.835	0.800
Thorax	KB	PMHS	HIII	0.655	0.333	0.456	0.607	0.532
		PMHS	THOR	0.130	0.067	0.520	0.513	0.349
		HIII	THOR	0.834	0.184	0.441	0.450	0.472
	KB/SWAB	PMHS	HIII	0.814	0.005	0.524	0.510	0.473
		PMHS	THOR	0.170	0.123	0.256	0.436	0.284
		HIII	THOR	0.940	0.206	0.000	0.361	0.374
	KBAB/SWAB	PMHS	HIII	0.809	0.562	0.474	0.560	0.593
		PMHS	THOR	0.603	0.380	0.492	0.565	0.521
		HIII	THOR	0.920	0.103	0.493	0.351	0.444
Pelvis	KB	PMHS	HIII	0.738	0.698	0.533	0.699	0.674
		PMHS	THOR	0.574	0.510	0.561	0.629	0.580
		HIII	THOR	0.664	0.660	0.517	0.596	0.606
	KB/SWAB	PMHS	HIII	0.678	0.885	0.590	0.689	0.706
		PMHS	THOR	0.344	0.563	0.592	0.556	0.522
		HIII	THOR	0.645	0.544	0.535	0.563	0.570
	KBAB/SWAB	PMHS	HIII	0.576	0.768	0.482	0.535	0.579
		PMHS	THOR	0.398	0.470	0.546	0.523	0.492
		HIII	THOR	0.801	0.270	0.541	0.490	0.519

Note: Green, yellow, orange, and red shading refer to excellent, good, fair, and poor ISO scores, respectively.

Table A3.19: Detailed ISO scores for the between surrogate comparisons of x angular velocities.

Location	Condition	Reference	Comparison	Phase	Magnitude	Slope	Corridor	Overall
Head	KB	PMHS	HIII	0.711	0.296	0.497	0.553	0.522
		PMHS	THOR	0.944	0.000	0.451	0.396	0.437
		HIII	THOR	0.797	0.544	0.610	0.514	0.596
	KB/SWAB	PMHS	HIII	0.257	0.000	0.553	0.255	0.264
		PMHS	THOR	0.894	0.765	0.733	0.629	0.730
		HIII	THOR	0.381	0.056	0.405	0.344	0.306
	KBAB/SWAB	PMHS	HIII	0.000	0.000	0.475	0.302	0.216
		PMHS	THOR	0.951	0.250	0.599	0.571	0.588
		HIII	THOR	0.000	0.000	0.073	0.345	0.153
Thorax	KB	PMHS	HIII	0.587	0.055	0.520	0.318	0.359
		PMHS	THOR	0.098	0.063	0.501	0.291	0.249
		HIII	THOR	0.677	0.670	0.405	0.512	0.555
	KB/SWAB	PMHS	HIII	0.672	0.341	0.525	0.454	0.489
		PMHS	THOR	0.933	0.432	0.552	0.422	0.552
		HIII	THOR	0.580	0.174	0.493	0.400	0.409
	KBAB/SWAB	PMHS	HIII	0.603	0.000	0.525	0.379	0.377
		PMHS	THOR	0.938	0.004	0.467	0.366	0.428
		HIII	THOR	0.477	0.226	0.367	0.466	0.400
Pelvis	KB	PMHS	HIII	0.000	0.028	0.262	0.356	0.200
		PMHS	THOR	0.494	0.000	0.436	0.366	0.332
		HIII	THOR	0.241	0.000	0.460	0.348	0.279
	KB/SWAB	PMHS	HIII	0.983	0.052	0.442	0.387	0.450
		PMHS	THOR	0.000	0.286	0.355	0.266	0.234
		HIII	THOR	0.000	0.000	0.271	0.255	0.156
	KBAB/SWAB	PMHS	HIII	0.792	0.000	0.399	0.235	0.332
		PMHS	THOR	0.000	0.090	0.258	0.219	0.157
		HIII	THOR	0.241	0.000	0.361	0.239	0.216

Note: Green, yellow, orange, and red shading refer to excellent, good, fair, and poor ISO scores, respectively.

Table A3.20: Detailed ISO scores for the between surrogate comparisons of y angular velocities.

Location	Condition	Reference	Comparison	Phase	Magnitude	Slope	Corridor	Overall
Head	KB	PMHS	HIII	0.671	0.404	0.000	0.418	0.382
		PMHS	THOR	0.932	0.554	0.392	0.511	0.580
		HIII	THOR	0.798	0.593	0.609	0.708	0.683
	KB/SWAB	PMHS	HIII	0.419	0.103	0.550	0.259	0.318
		PMHS	THOR	0.915	0.706	0.749	0.569	0.701
		HIII	THOR	0.600	0.642	0.706	0.377	0.540
	KBAB/SWAB	PMHS	HIII	0.778	0.000	0.346	0.296	0.343
		PMHS	THOR	0.938	0.607	0.647	0.623	0.687
		HIII	THOR	0.550	0.517	0.645	0.364	0.488
Thorax	KB	PMHS	HIII	0.973	0.249	0.595	0.502	0.564
		PMHS	THOR	0.857	0.445	0.549	0.573	0.599
		HIII	THOR	0.876	0.782	0.752	0.713	0.767
	KB/SWAB	PMHS	HIII	0.677	0.621	0.535	0.323	0.496
		PMHS	THOR	0.821	0.586	0.419	0.352	0.506
		HIII	THOR	0.958	0.887	0.785	0.878	0.877
	KBAB/SWAB	PMHS	HIII	0.615	0.389	0.380	0.189	0.352
		PMHS	THOR	0.716	0.498	0.407	0.327	0.455
		HIII	THOR	0.924	0.883	0.877	0.895	0.895
Pelvis	KB	PMHS	HIII	0.928	0.610	0.694	0.522	0.655
		PMHS	THOR	0.888	0.422	0.566	0.558	0.598
		HIII	THOR	0.985	0.913	0.714	0.809	0.846
	KB/SWAB	PMHS	HIII	0.669	0.743	0.733	0.568	0.656
		PMHS	THOR	0.757	0.728	0.672	0.614	0.677
		HIII	THOR	0.959	0.700	0.783	0.707	0.771
	KBAB/SWAB	PMHS	HIII	0.497	0.094	0.490	0.264	0.322
		PMHS	THOR	0.758	0.417	0.582	0.516	0.558
		HIII	THOR	0.757	0.712	0.492	0.553	0.613

Note: Green, yellow, orange, and red shading refer to excellent, good, fair, and poor ISO scores, respectively.

Table A3.21: Detailed ISO scores for the between surrogate comparisons of z angular velocities.

Location	Condition	Reference	Comparison	Phase	Magnitude	Slope	Corridor	Overall
Head	KB	PMHS	HIII	0.677	0.000	0.587	0.445	0.431
		PMHS	THOR	0.000	0.000	0.469	0.499	0.294
		HIII	THOR	0.767	0.000	0.332	0.279	0.331
	KB/SWAB	PMHS	HIII	0.000	0.000	0.494	0.238	0.194
		PMHS	THOR	0.447	0.514	0.311	0.159	0.318
		HIII	THOR	0.169	0.000	0.000	0.169	0.101
	KBAB/SWAB	PMHS	HIII	0.000	0.000	0.488	0.315	0.223
		PMHS	THOR	0.353	0.524	0.533	0.280	0.394
		HIII	THOR	0.586	0.000	0.162	0.237	0.244
Thorax	KB	PMHS	HIII	0.000	0.000	0.439	0.301	0.208
		PMHS	THOR	0.590	0.382	0.505	0.332	0.428
		HIII	THOR	0.354	0.000	0.219	0.313	0.240
	KB/SWAB	PMHS	HIII	0.000	0.000	0.372	0.306	0.197
		PMHS	THOR	0.866	0.000	0.262	0.246	0.324
		HIII	THOR	0.037	0.000	0.000	0.266	0.114
	KBAB/SWAB	PMHS	HIII	0.000	0.000	0.232	0.260	0.151
		PMHS	THOR	0.986	0.627	0.308	0.494	0.582
		HIII	THOR	0.000	0.000	0.312	0.263	0.168
Pelvis	KB	PMHS	HIII	0.887	0.000	0.506	0.334	0.412
		PMHS	THOR	0.584	0.000	0.545	0.260	0.330
		HIII	THOR	0.633	0.728	0.499	0.482	0.565
	KB/SWAB	PMHS	HIII	0.667	0.000	0.466	0.523	0.436
		PMHS	THOR	0.124	0.000	0.495	0.546	0.342
		HIII	THOR	0.000	0.261	0.318	0.254	0.217
	KBAB/SWAB	PMHS	HIII	0.835	0.000	0.481	0.484	0.457
		PMHS	THOR	0.000	0.131	0.454	0.246	0.216
		HIII	THOR	0.000	0.000	0.123	0.384	0.178

Note: Green, yellow, orange, and red shading refer to excellent, good, fair, and poor ISO scores, respectively.

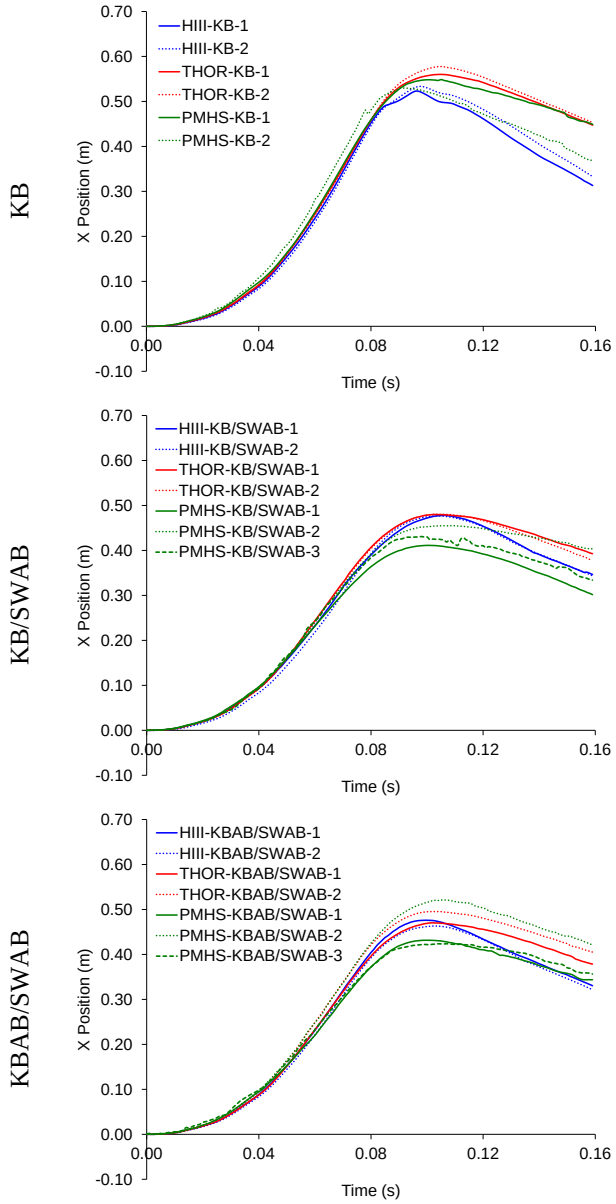

Figure A3.1: Forward (x) head excursions for all conditions.

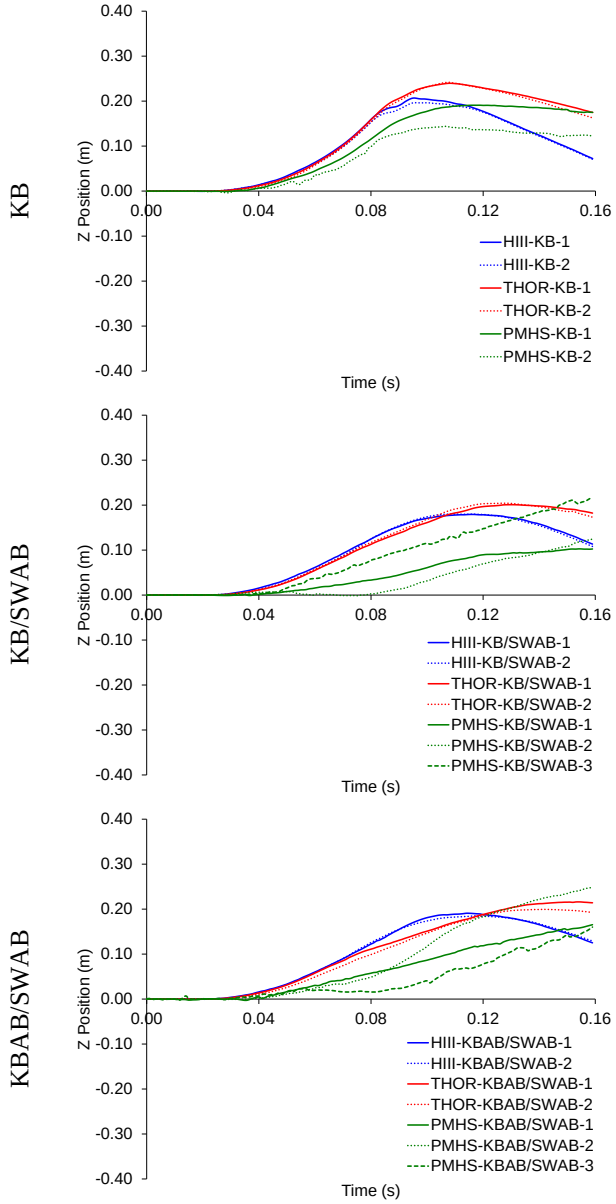

Figure A3.2: Vertical (z) head excursions for all conditions.

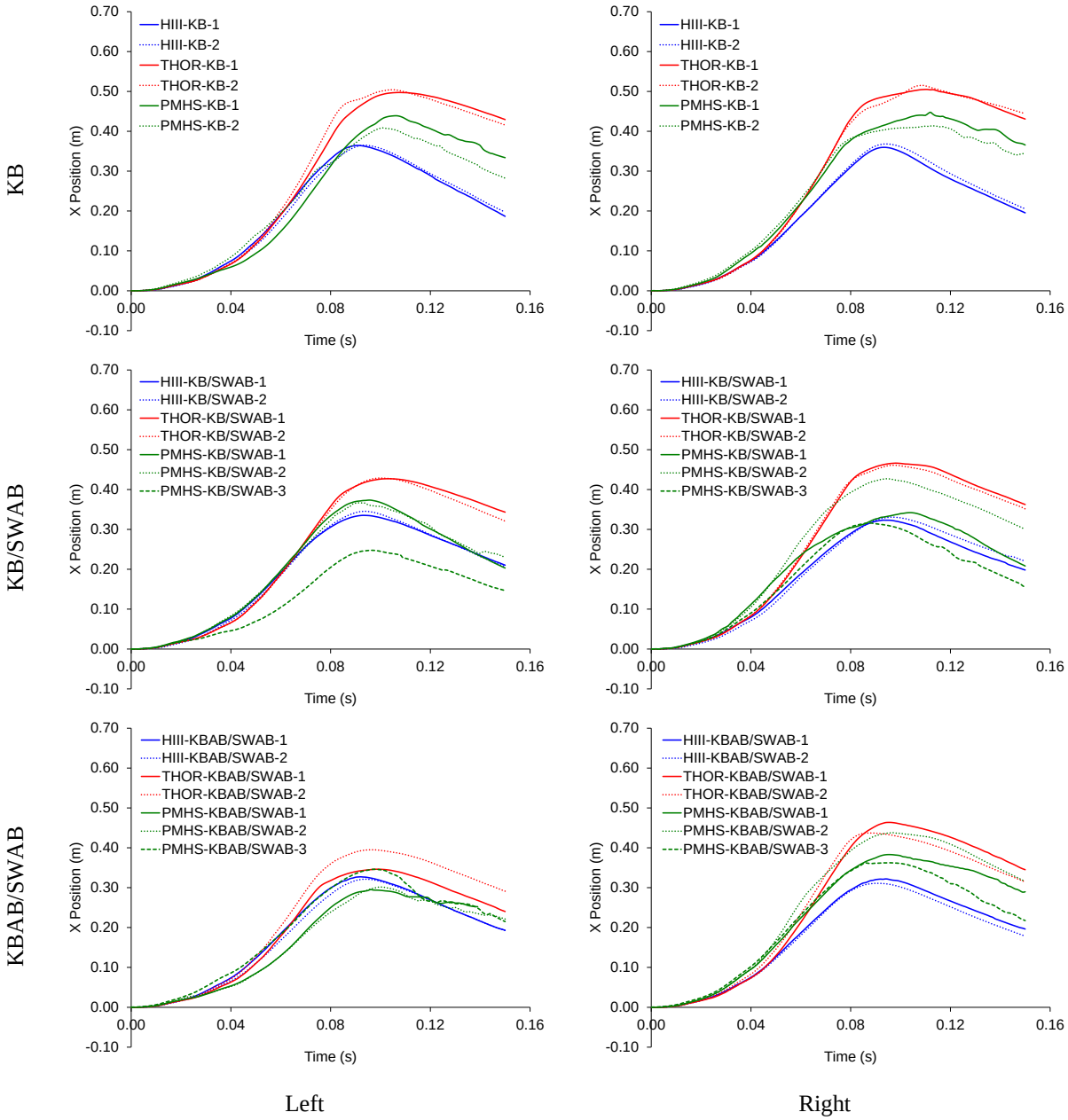

Figure A3.3: Forward (x) shoulder excursions for all conditions.

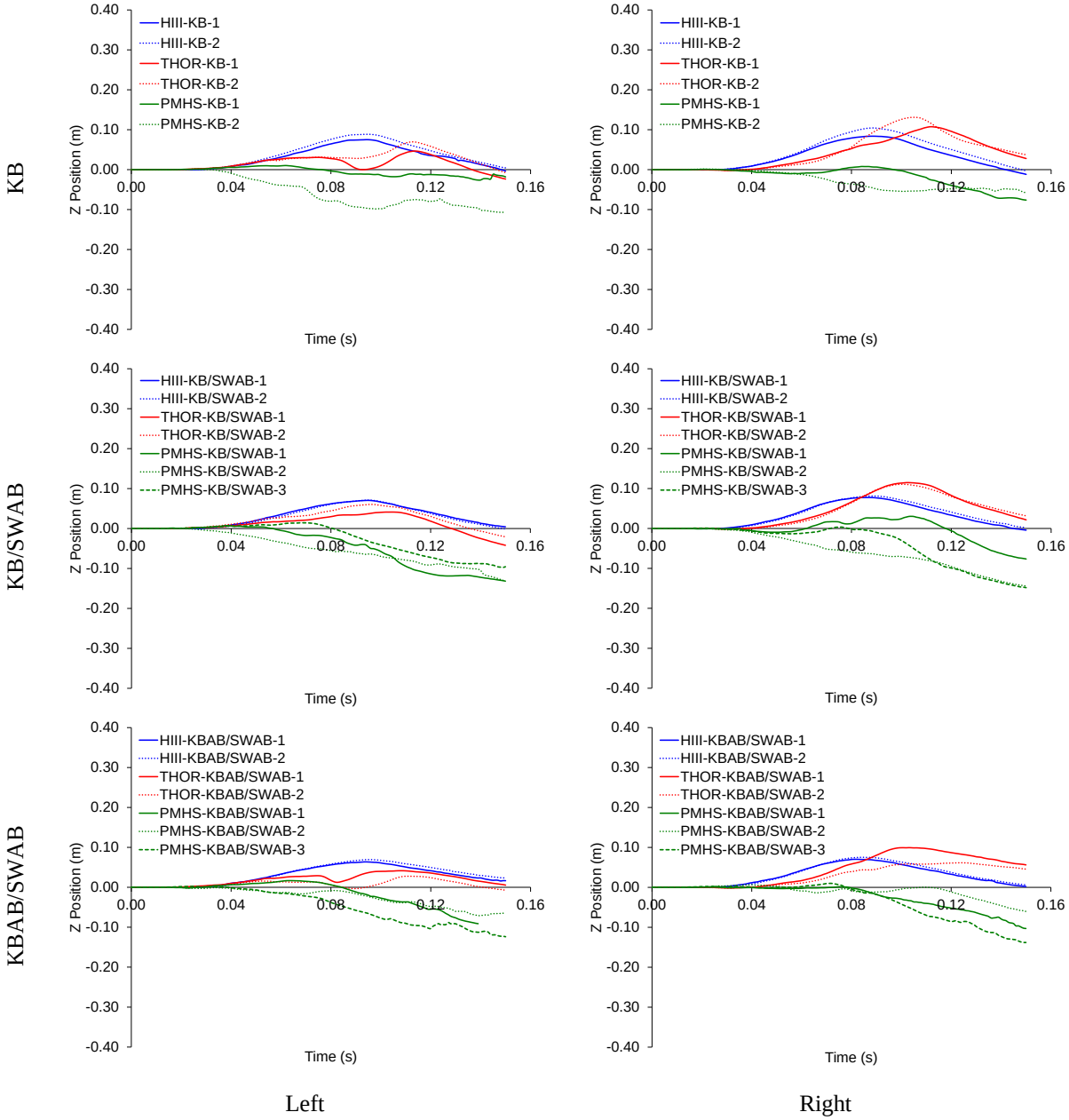

Figure A3.4: Vertical (z) shoulder excursions for all conditions.

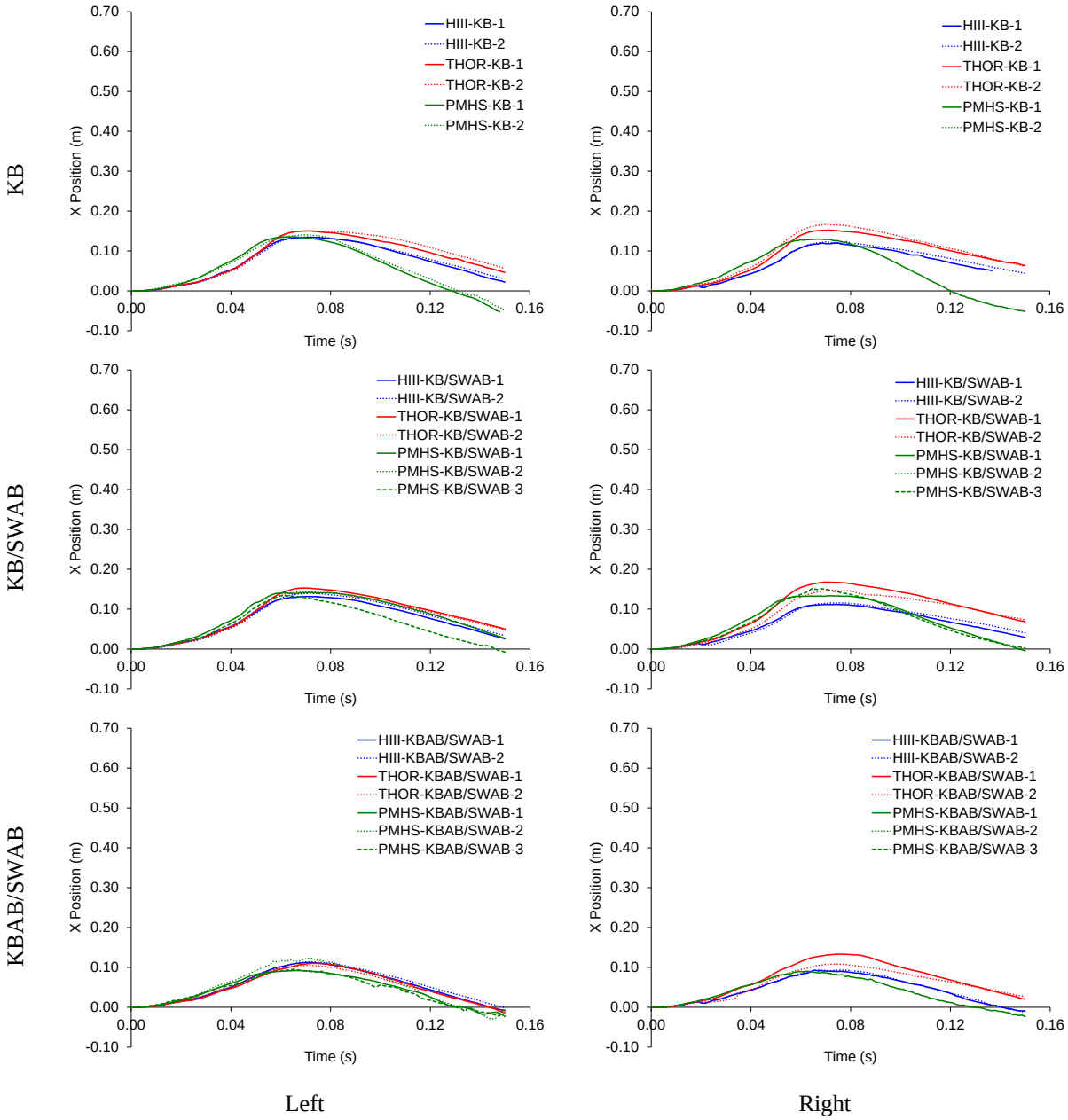

Figure A3.5: Forward (x) hip excursions for all conditions.

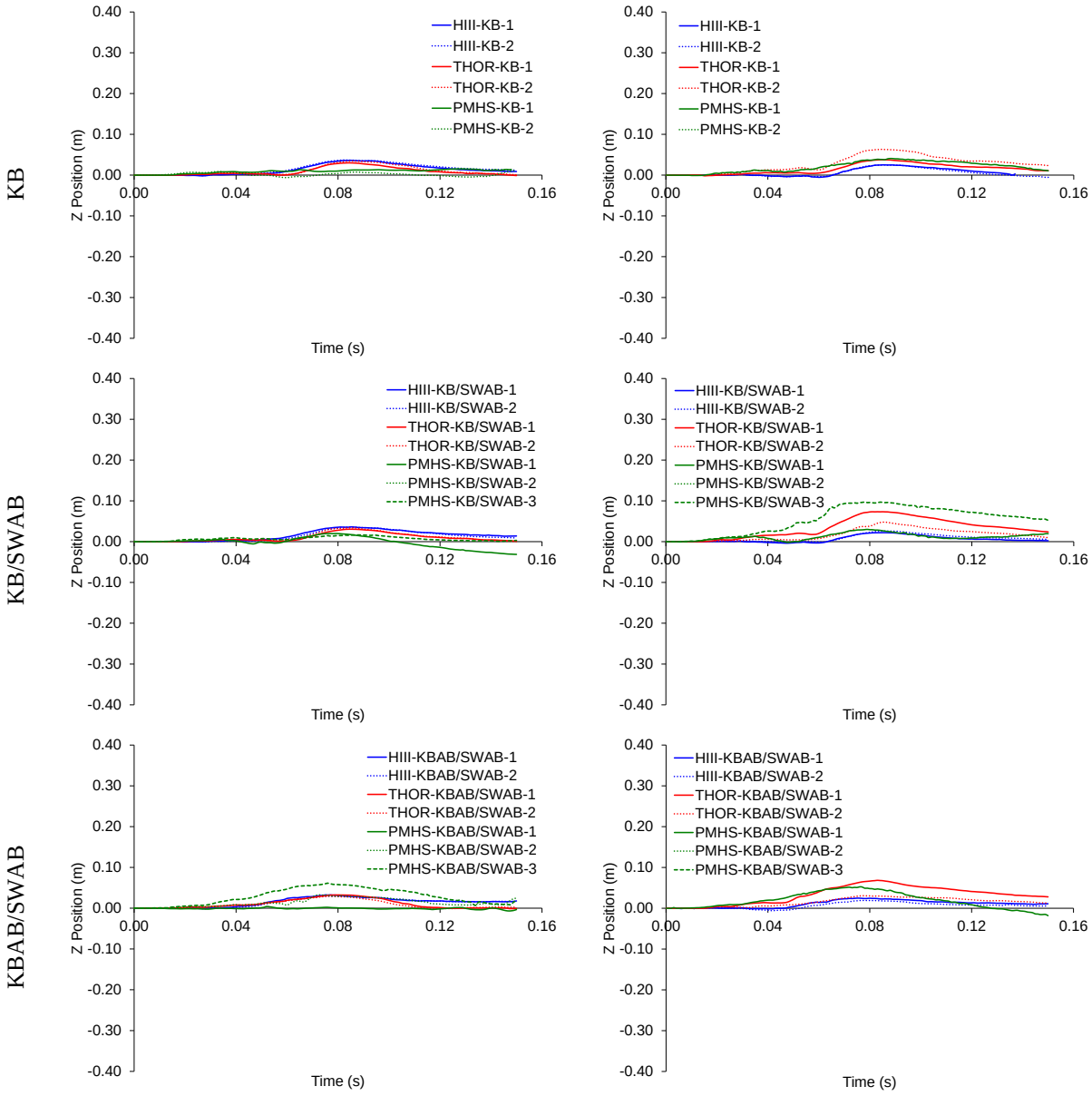

Figure A3.6: Vertical (z) hip excursions for all conditions.

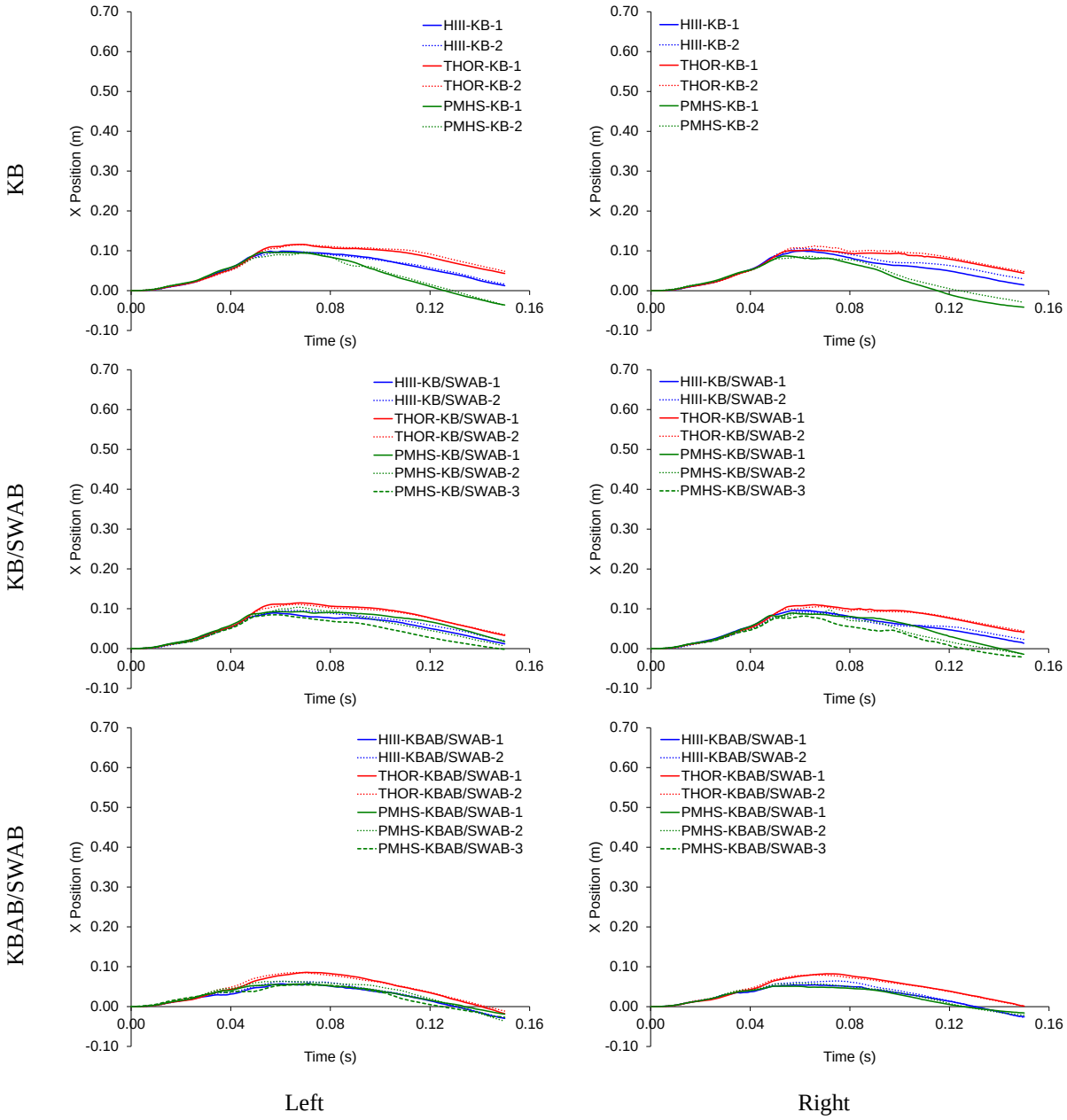

Figure A3.7: Forward (x) knee excursions for all conditions.

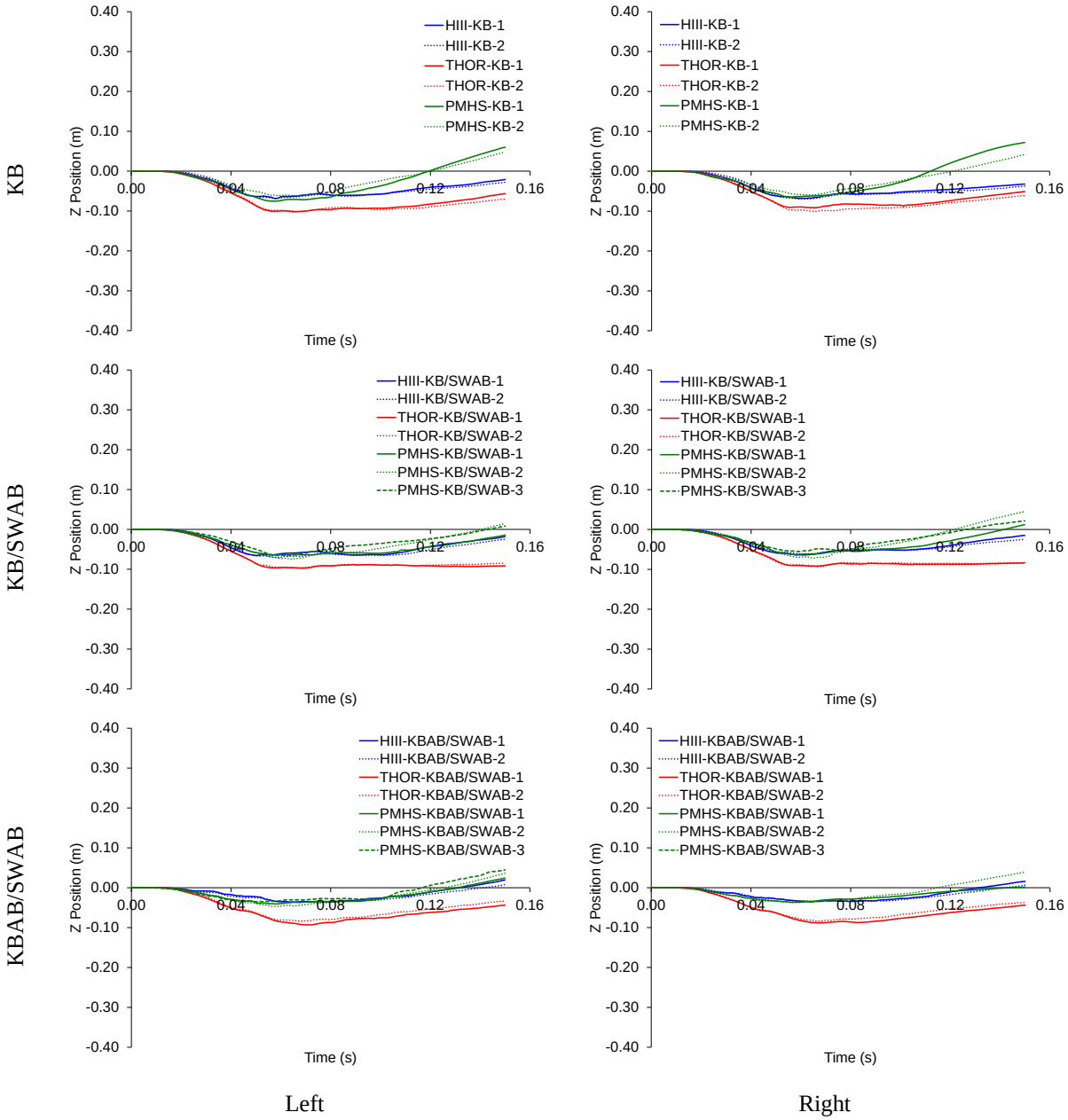

Figure A3.8: Vertical (z) knee excursions for all conditions.

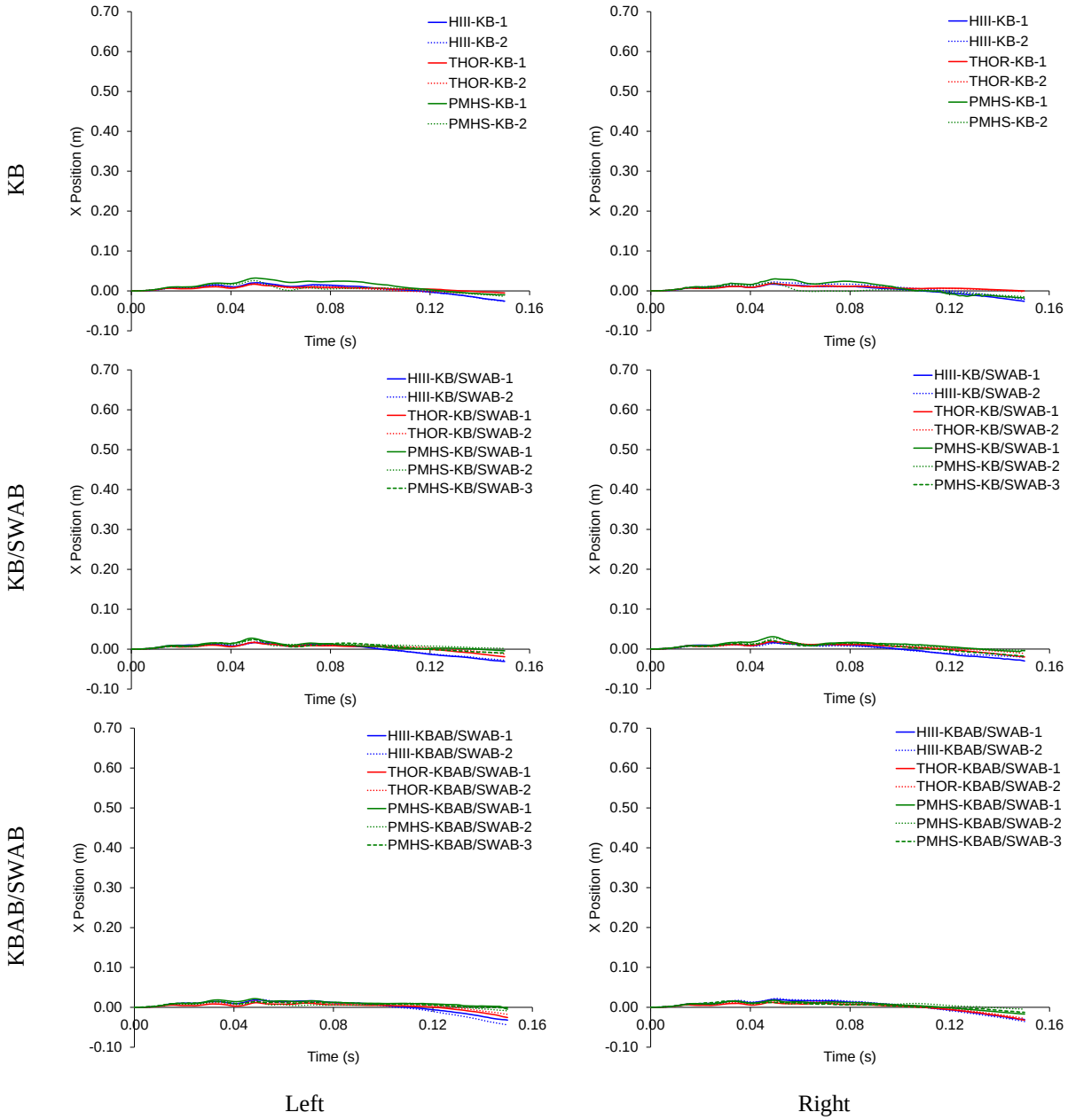

Figure A3.9: Forward (x) ankle excursions for all conditions.

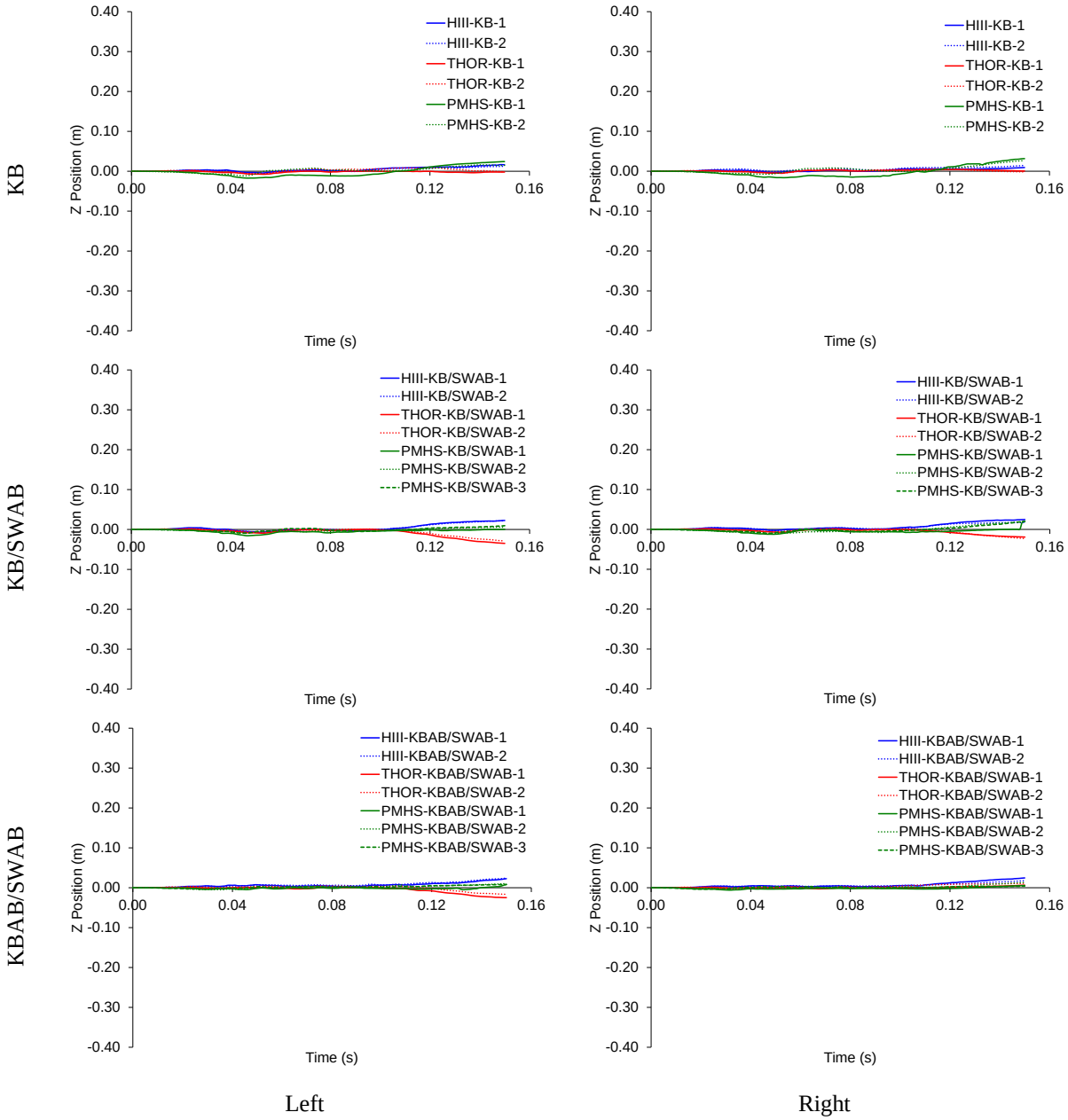

Figure A3.10: Vertical (z) ankle excursions for all conditions.

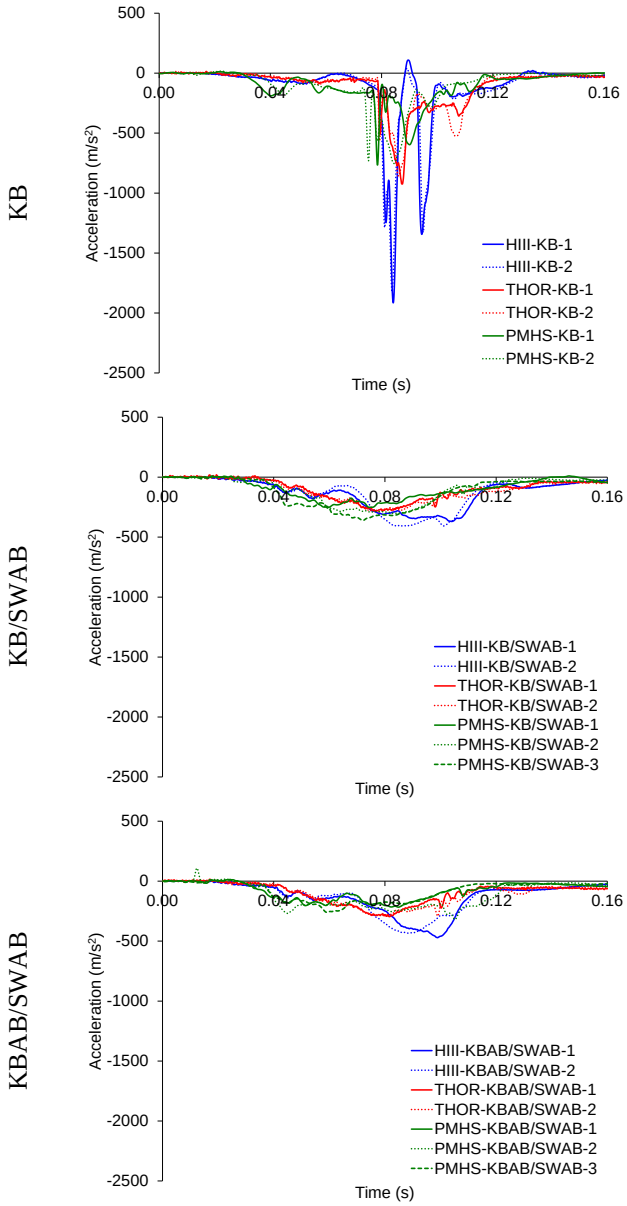

Figure A3.11: Forward (x) head accelerations for all conditions.

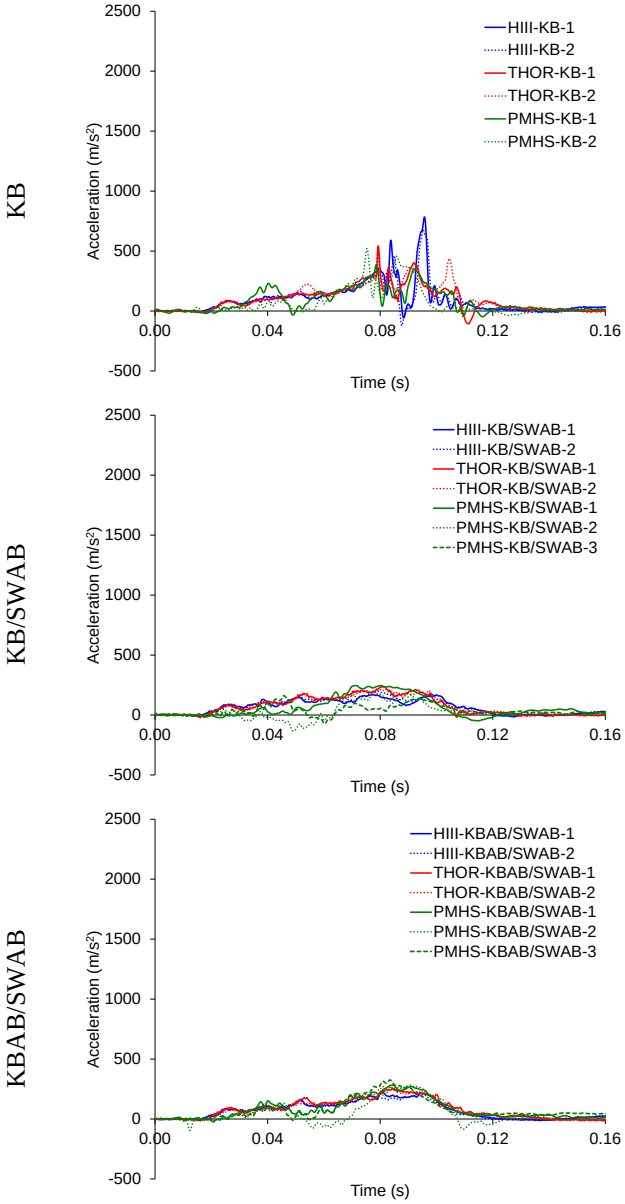

Figure A3.12: Vertical (z) head accelerations for all conditions.

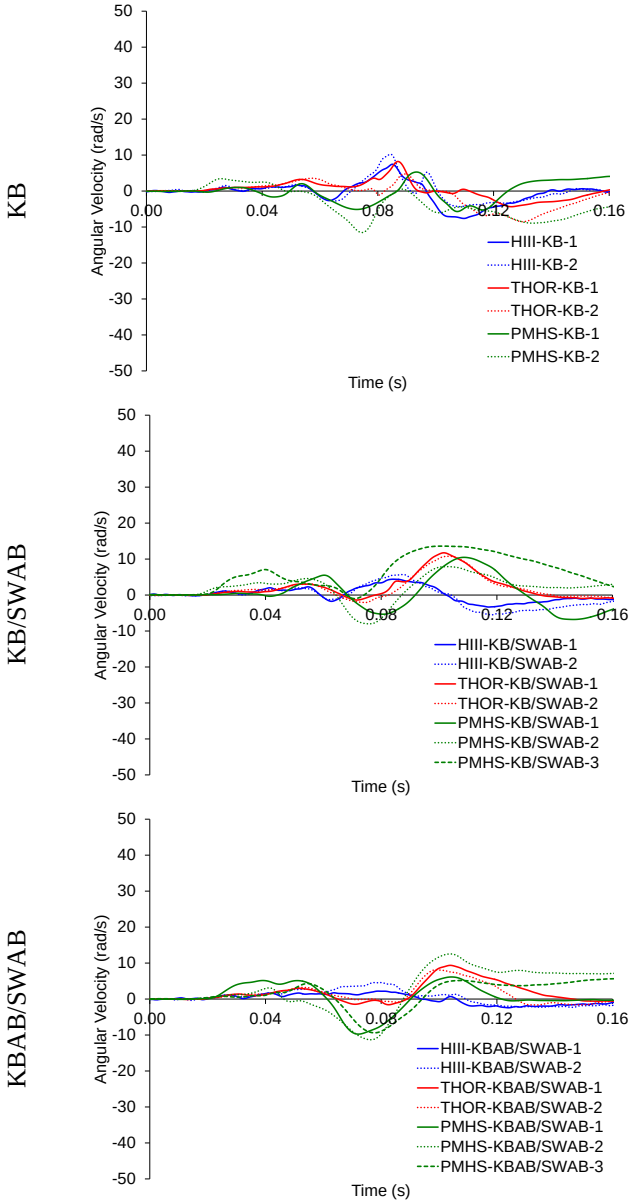

Figure A3.13: Head (x) angular velocities for all conditions.

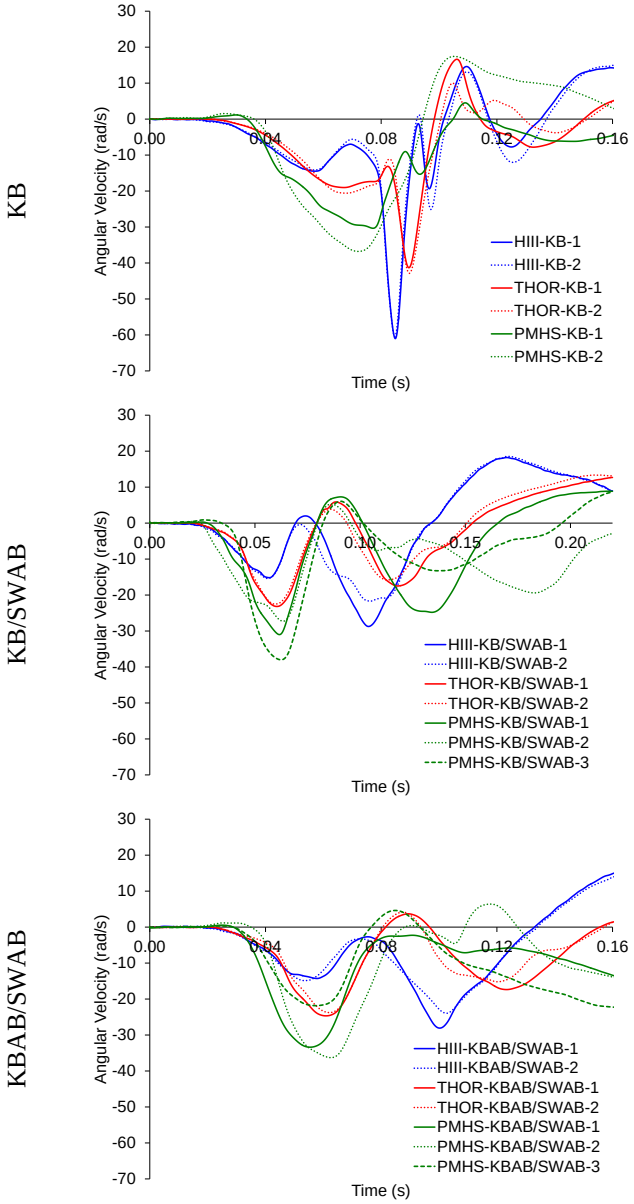

Figure A3.14: Head (y) angular velocities for all conditions.

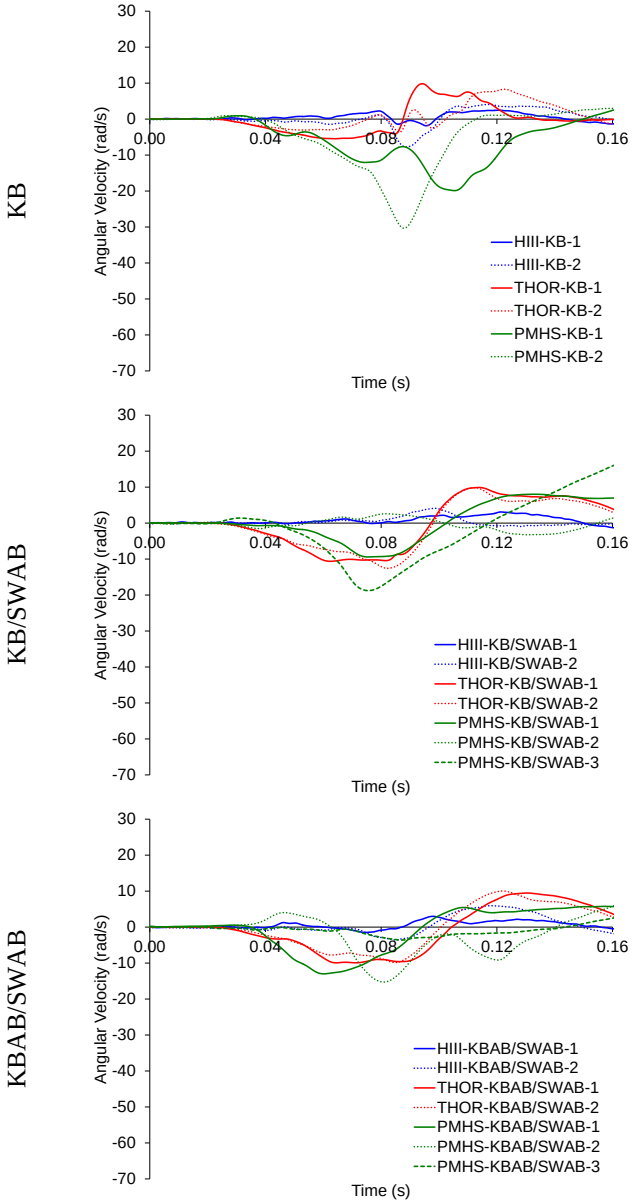

Figure A3.15: Head (z) angular velocities for all conditions.

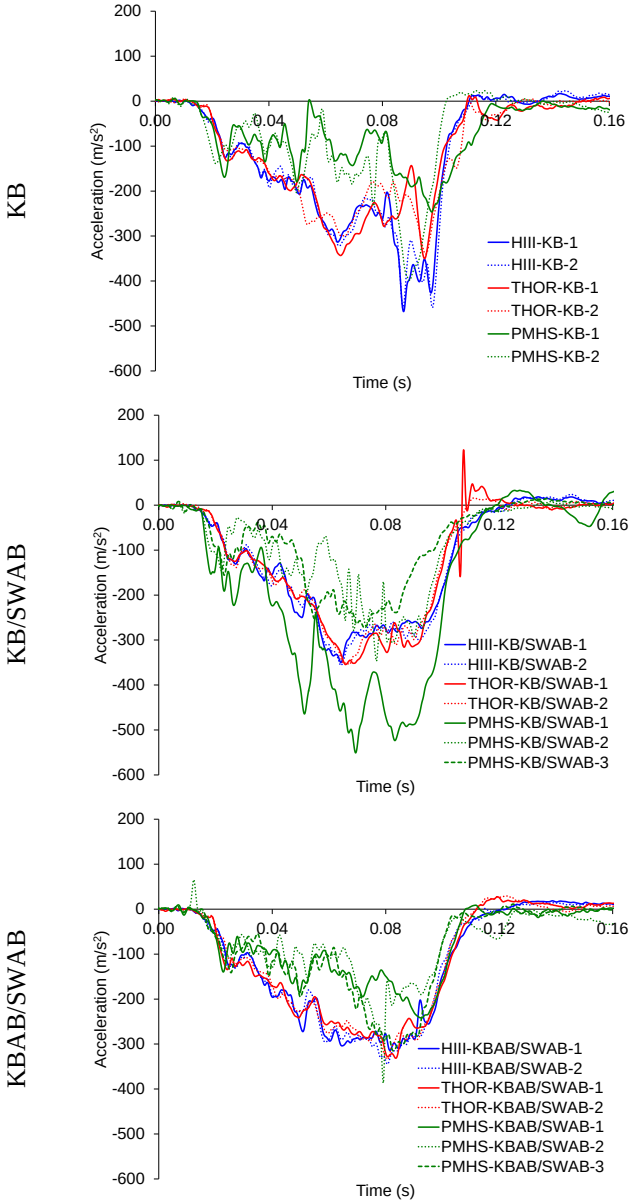

Figure A3.16: Forward (x) chest accelerations for all conditions.

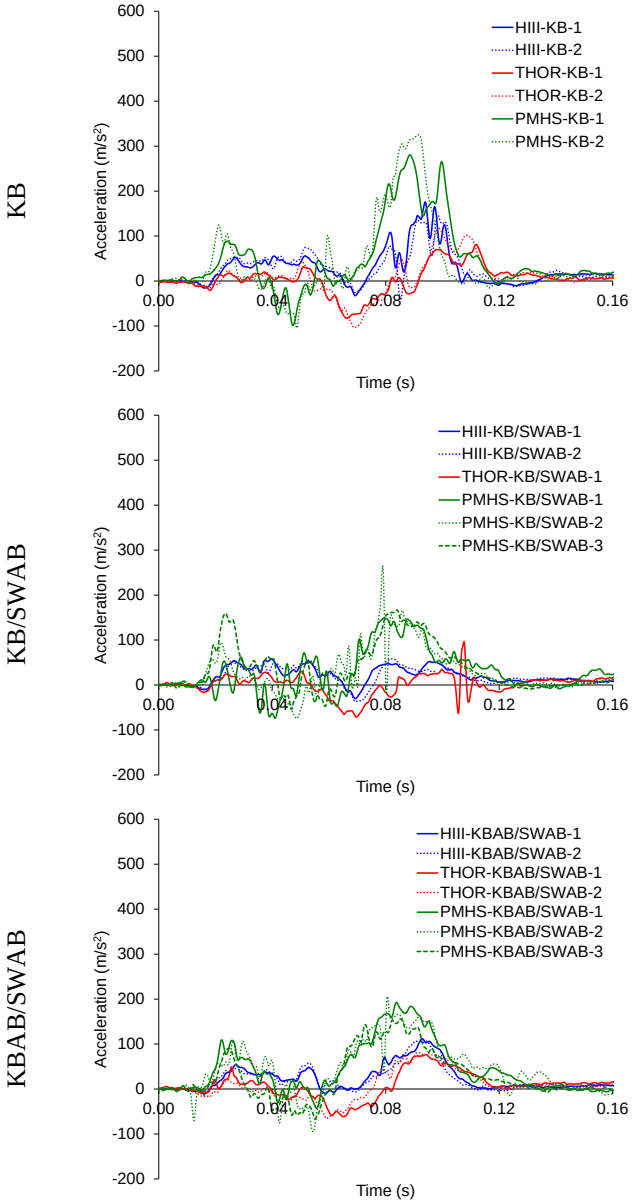

Figure A3.17: Vertical (z) chest accelerations for all conditions.

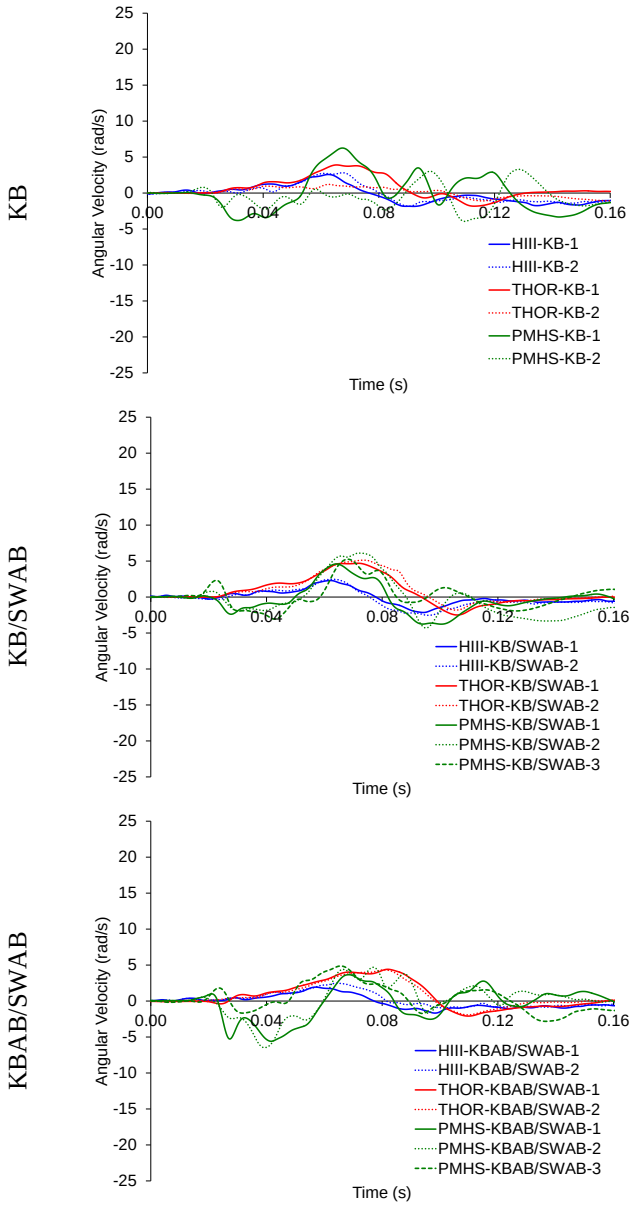

Figure A3.18: Chest (x) angular velocities for all conditions.

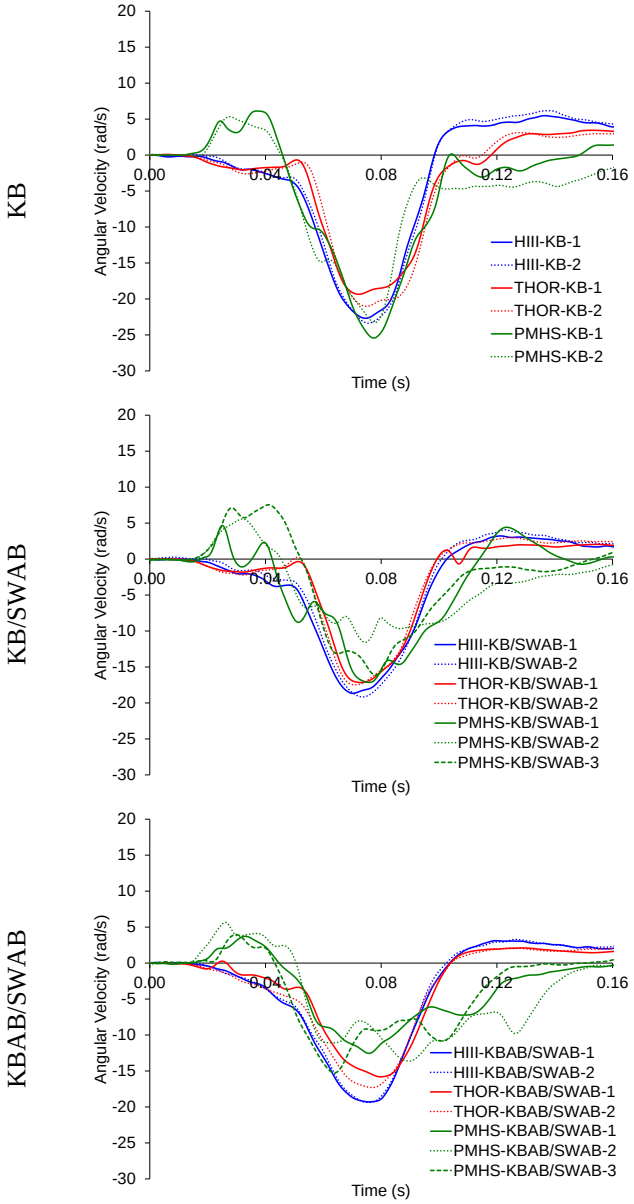

Figure A3.19: Chest (y) angular velocities for all conditions.

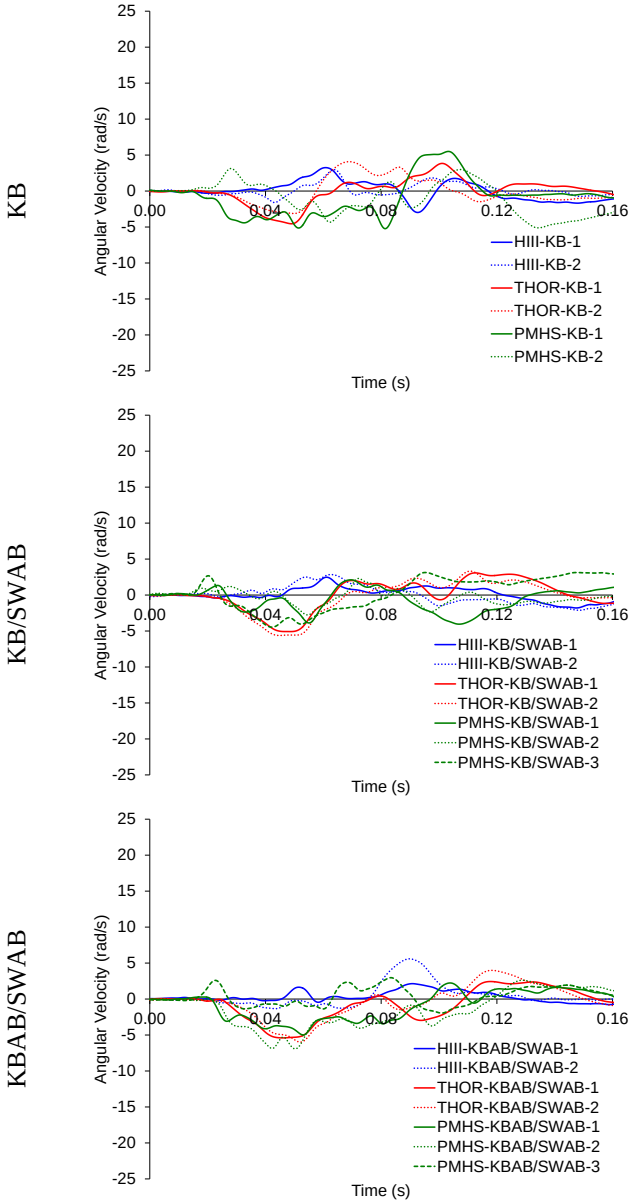

Figure A3.20: Chest (z) angular velocities for all conditions.

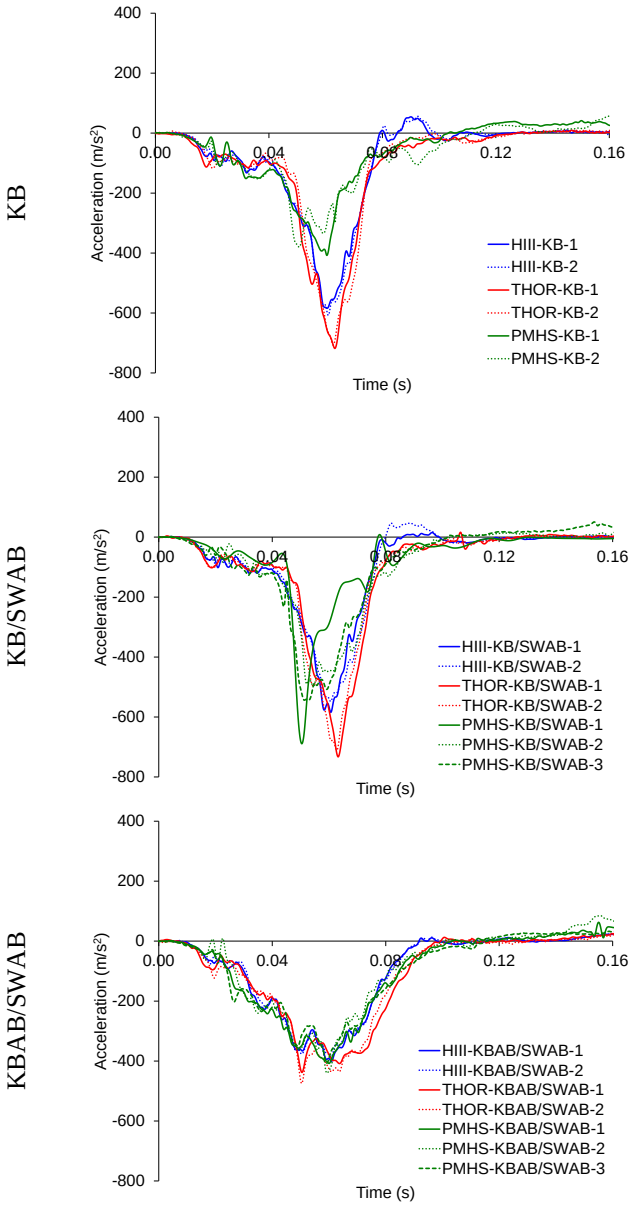

Figure A3.21: Forward (x) pelvis accelerations for all conditions.

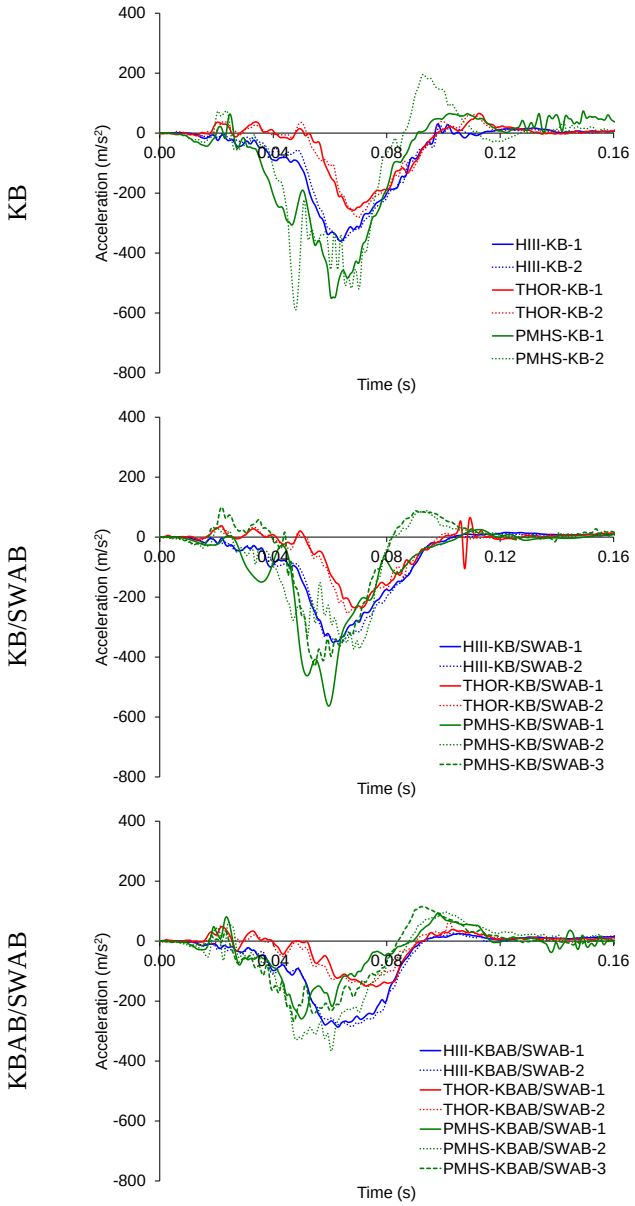

Figure A3.22: Vertical (z) pelvis accelerations for all conditions.

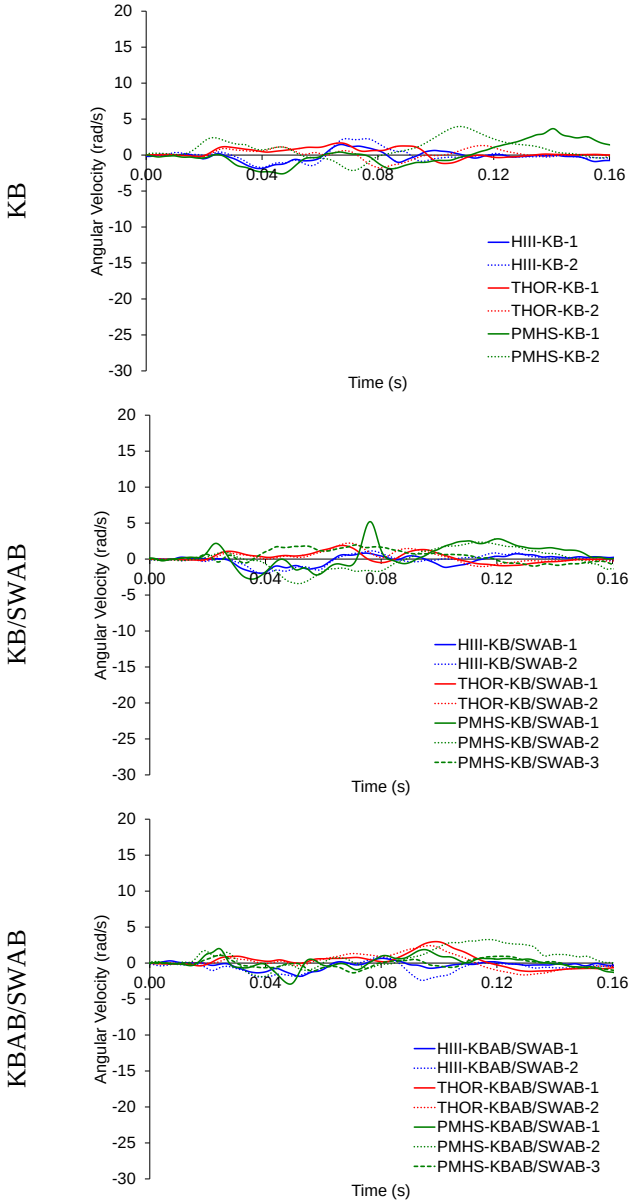

Figure A3.23: Pelvis (x) angular velocities for all conditions.

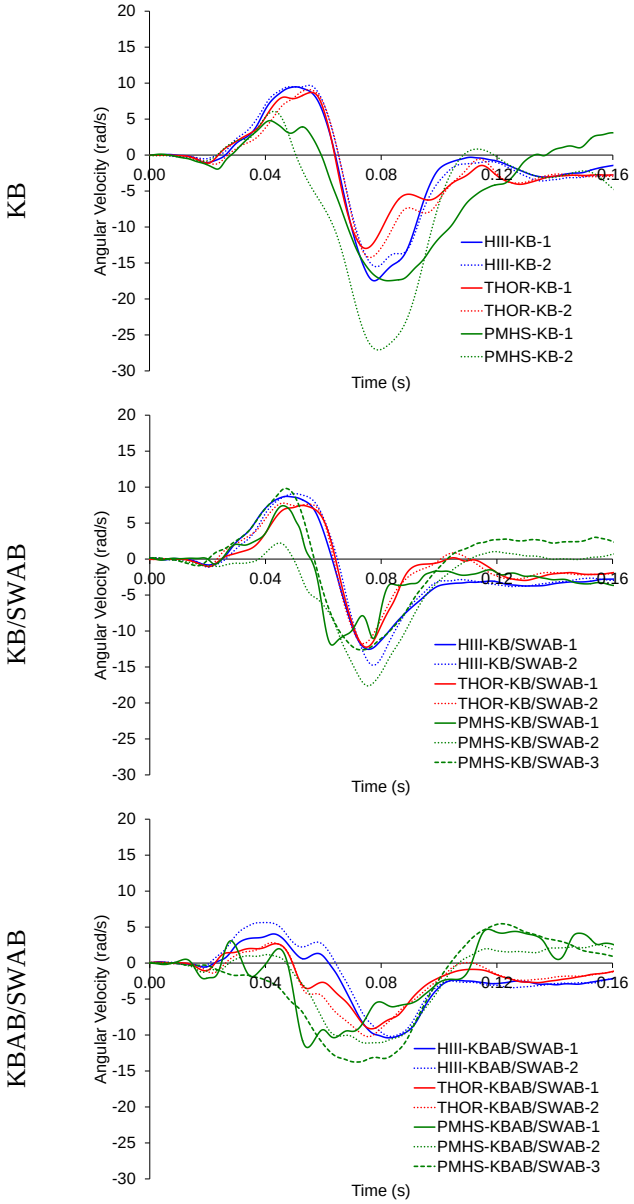

Figure A3.24: Pelvis (y) angular velocities for all conditions.

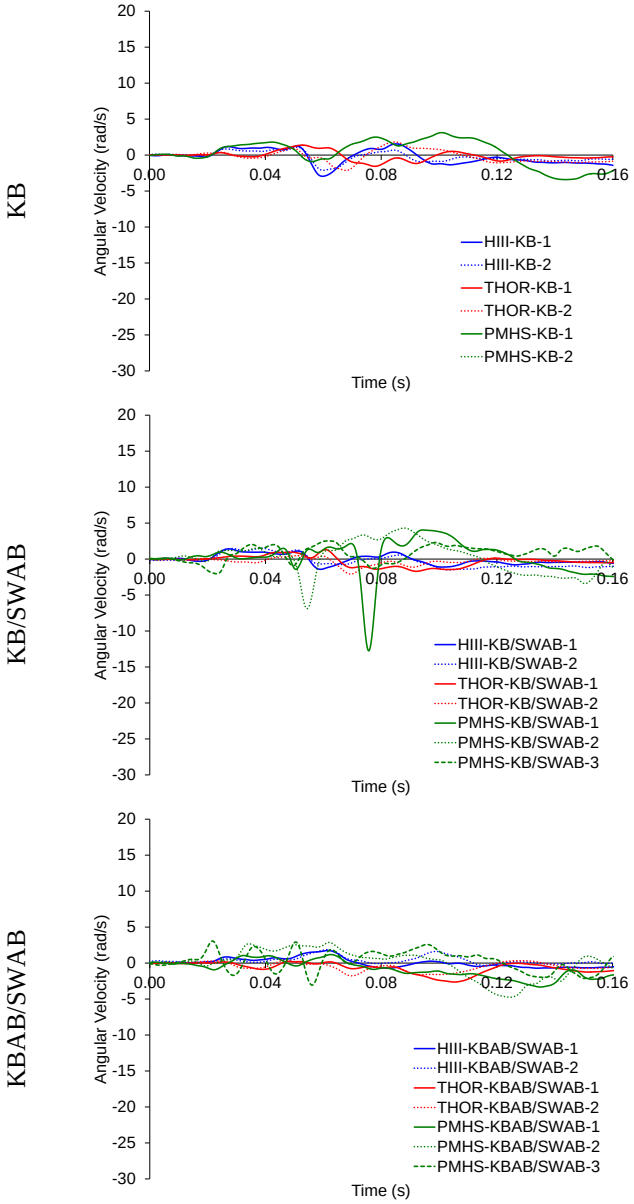

Figure A3.25: Pelvis (z) angular velocities for all conditions.

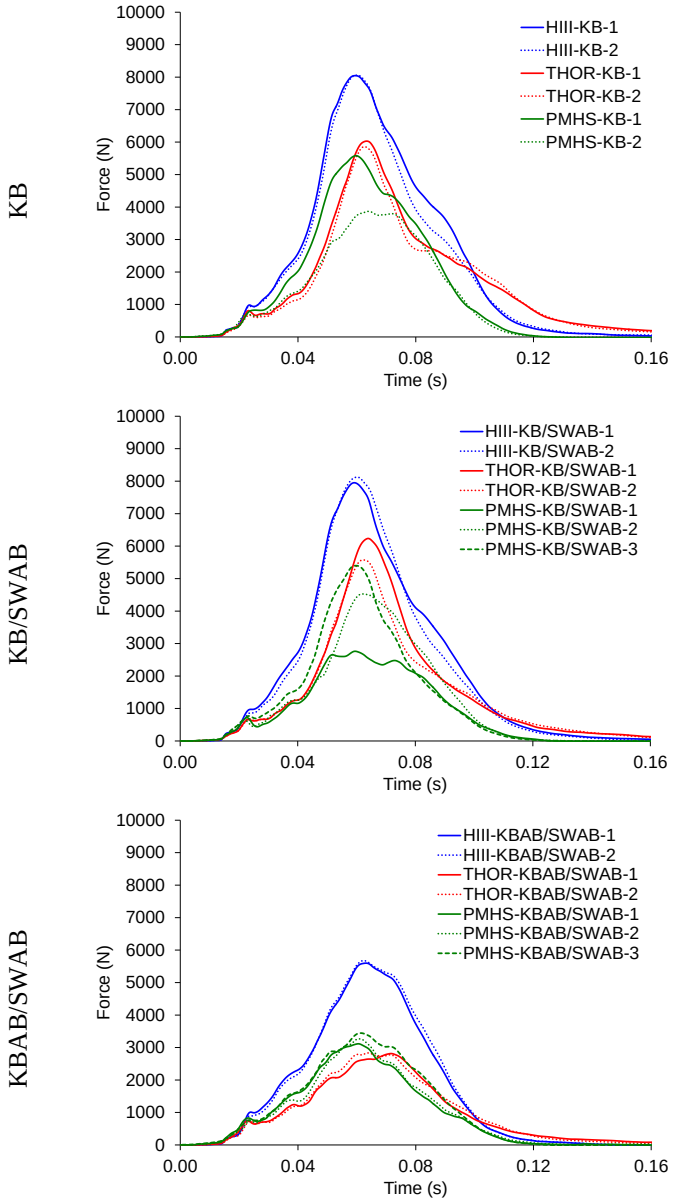

Figure A3.26: Lap belt forces for all conditions.

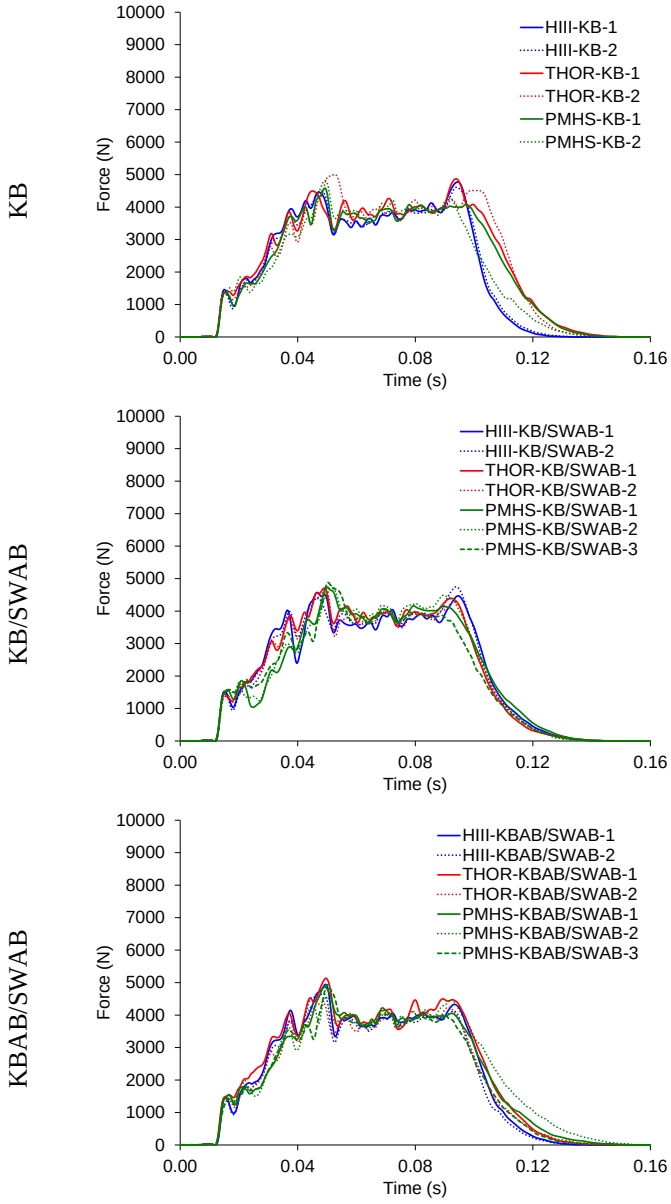

Figure A3.27: Shoulder belt forces for all conditions.

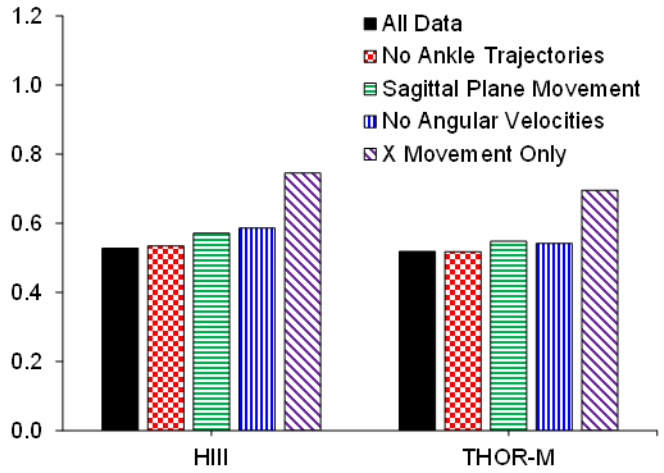

Figure A3.28: Sensitivity analysis of average ISO scores for the HIII/PMHS and THOR-M/PMHS comparisons.

Biomechanical Responses of Human Surrogates under Various Frontal Loading Conditions with an Emphasis on Thoracic Response and Injury Tolerance

Devon Albert

Preliminary Examination submitted to the faculty of the Virginia Polytechnic Institute and State University in partial fulfillment of the requirements for the degree of

Doctor of Philosophy
In
Biomedical Engineering

Andrew R. Kemper
Amanda M. Agnew
H. Clay Gabler
Warren N. Hardy
Joel D. Stitzel

4/19/2018
Blacksburg, VA

Keywords: Hybrid III, THOR, PMHS, knee bolster, knee bolster airbag, frontal motor vehicle collision, thoracic injury criterion, rib

TABLE OF CONTENTS

LIST OF FIGURES

LIST OF TABLES

CHAPTER 4: LOWER EXTREMITY RESPONSES OF THE HYBRID III, THOR-M, AND POST-MORTEM HUMAN SURROGATES UNDER VARIOUS RESTRAINT CONDITIONS IN FULL-SCALE FRONTAL SLED TESTS

Proposed Authors:

Albert DL, Beeman SM, Hardy WN, Kemper AR

Introduction

The lower extremity is the most frequently injured body region in frontal motor vehicle collisions (MVCs) with knee-thigh-hip (KTH) injuries accounting for approximately 55% of all lower extremity injuries [1]. It is estimated that the instrument panel and knee bolster (KB) are the source of 87% of KTH injuries and 5% of lower leg injuries [2]. Knee bolster airbags (KBABs) have been introduced into the vehicle fleet in an attempt to mitigate lower extremity injuries. Specifically, it is hypothesized that KBABs will distribute loads over a wider area of the knee than KBs and absorb energy over a longer duration of time, reducing the force on the lower extremity and mitigating KTH injuries [3]. Additionally, the decreased rigidity of KBABs compared to KBs may reduce tibia, fibula, ankle, and foot injuries by preventing the lower leg from being pinned between the bolster and floor pan [3].

Previous studies that have attempted to evaluate the capacity of KBABs to mitigate lower extremity injuries have employed finite element modeling (FEM) and real-world crash comparisons. Weaver *et al.* (2013) compared similar MVCs from the Crash Injury Research and Engineering Network (CIREN) database that did and did not involve a KBAB deployment [4]. They found that significantly fewer femur fractures were observed for collisions with KBAB deployments. However, they also observed a significant increase in proximal tibia and fibula fractures with KBAB deployments. Using a combination of the CIREN and National Automotive Sampling System-Crashworthiness Data System (NASS-CDS) databases, Patel *et al.* (2013) observed non-significant decreases in hip and femur fractures and non-significant increases in tibia, fibula, and foot fractures for collisions involving KBABs [5]. For the FEM studies, Kitagawa *et al.* (2005) observed a slight decrease in peak femur force and an increase in the duration of femur force when the Total Human Model for Safety (THUMS) was exposed to a KBAB compared to a standard KB [6]. In contrast, Nie *et al.* (2016) observed an increase in femur axial forces and femur bending moments when THUMS was exposed to a KBAB deployment in a frontal crash mode [7]. Nie *et al.* (2016) also reported a decrease in tibia axial forces and bending moments with KBAB deployments. Finally, Danelson *et al.* (2015) investigated the effect of KBABs using both the THUMS and a Hybrid III (HIII) FEM and found that femur forces were increased in THUMS, but decreased in the HIII with the use of a KBAB [8].

The inconsistent findings between previous studies regarding the efficacy of KBABs at mitigating lower extremity injuries may be the result of many factors. The real-world crash comparisons were limited by small sample sizes, especially for collisions involving KBABs, because of their relatively recent introduction into a limited number of new vehicles. Additionally, the comparisons did not represent direct comparisons between collisions involving KBs and KBABs due to differences in crash features (e.g., ΔV and principal direction of force), occupant demographics, and occupant compartment design, which may vary between vehicle models, makes, and years. The FEM studies were limited by a lack of validation data since full-scale laboratory sled tests involving KBABs have yet to be conducted. The models also employed different vehicle environments and restraint systems, which may have influenced the different outcomes.

The limitations and disparity of findings observed in previous studies evaluating the efficacy of KBABs demonstrates the need for highly controlled laboratory sled tests to determine whether KBABs mitigate lower extremity injuries. Furthermore, it is important to evaluate the lower extremity biofidelity of the current frontal anthropomorphic test devices (ATDs), i.e., the HIII and the Test device for Human Occupant Restraint (THOR-M), under this relatively new restraint condition. In order to evaluate ATD biofidelity, ATD lower extremity loads must be compared to PMHS lower extremity loads. Previous studies have measured loads in PMHS lower extremities by implanting load cells into the long bones [9-13]. However, this invasive approach could alter the kinematic and kinetic responses of the lower extremity. A previous study developed a preliminary method for measuring lower extremity loads/moments during underbody blast using strain gages arrays (bone cells) attached to the bones [14]. This approach is less invasive, but has not yet been validated under loading typical of a MVC.

The purpose of this study was two-fold. The first objective was to measure and validate PMHS lower extremity loads and moments using bone cells during full-scale frontal sled tests. The second objective was to compare the lower extremity responses of the HIII, THOR-M, and PMHSs during full-scale frontal sled tests under three safety restraint conditions: knee bolster (KB), knee bolster and steering wheel airbag (KB/SWAB), and knee bolster airbag and steering wheel airbag (KBAB/SWAB).

Methods

A total of 20 full-scale frontal sled tests were performed using the HIII, THOR-M, and PMHSs to quantify and compare lower extremity forces and moments under three safety restraint conditions: KB, KB/SWAB, and KBAB/SWAB. Six tests each were performed with the HIII and THOR-M ATDs, while a total of eight PMHS tests were performed. For the ATD tests, two tests were performed for each of the three safety restraint conditions per ATD. For the PMHSs, two tests were performed in the KB condition and three tests each were performed in the KB/SWAB and KBAB/SWAB conditions. Each PMHS was used for only a single test. Detailed methodology for the sled tests was described in Chapter 3. In brief, the sled tests were designed to simulate the 2005 Toyota Camry (KB/SWAB) and 2012 Toyota Camry (KBAB/SWAB) frontal New Car Assessment Program (NCAP) full-scale crash tests [15,16]. All tests were performed on a 1.4 MN ServoSled^{TM} system (Seattle Safety LLC, Kent, WA) with a custom sled buck designed to match the interior of a 2013 Toyota Camry SE. New 2013 Toyota Camry vehicle components, including a three-point, U.S. driver side seatbelt (with a pretensioner, 4kN load limiter, retractor, and buckle), seat, steering wheel, steering column, and steering wheel airbag were used for each test. The KB and KBABs were simulated using 65 and 19 psi rigid polyurethane foams, respectively. The vehicle acceleration pulse of the 2012 Toyota Camry NCAP test (ΔV = 56 kph, peak acceleration = 470 m/s^2) was employed for each test.

Positioning of the surrogates and vehicle components (i.e. seat track, seat back, steering column, seat belt, and KB) were guided by the NCAP Test Procedure Document [17] and the NCAP Report for the 2012 Toyota Camry [15]. Detailed positioning information and knee bolster geometry were provided in Chapters 3 and 2, respectively. Notably, the offsets between the surrogate and vehicle components were maintained across tests in order to ensure valid comparisons between conditions and surrogates.

Instrumentation

All surrogates were instrumented to collect lower extremity forces and moments. The ATDs were instrumented with 6 axis load cells in the left and right femurs, 5 axis load cells in the left and right upper tibias, and 5 axis load cells in the left and right lower tibias (see detailed instrumentation information in Table 4.1 and Table A4.1). The PMHSs were instrumented with bone cells, i.e.,

strain gages in bridge configurations, to quantify axial forces (Fz) and anterior-posterior (AP) bending moments (My) for the mid-femur and distal tibia (Figure 4.1). Four two-axis strain gages were arranged at equidistant locations around the circumference of each bone with the gage vertical centerlines aligned with the main axis of the bone in order to measure the axial forces (Figure 4.2). In order to measure the bending moments, two pairs of single-axis strain gages were positioned on the anterior and posterior aspects of the bone several centimeters apart such that the centerlines of the anterior and posterior gages were approximately aligned (Figure 4.3).

Table 4.1: ATD lower extremity load cell instrumentation.

ATD	Load Cell Location	Model	Company	Company Location
HIII	L/R Femur	1914A	Denton	Rochester Hills, MI
	L/R Upper Tibia	3643	Denton	Rochester Hills, MI
	L/R Lower Tibia	3644FL	Denton	Rochester Hills, MI
THOR-M	L/R Femur	W5071010S1	Humanetics	Plymouth, MI
	L/R Upper Tibia	10390JI4	Humanetics	Plymouth, MI
	L/R Lower Tibia	10391JI4	Humanetics	Plymouth, MI

A detailed procedure was followed to apply the strain gages to the PMHS tibias and femurs. The soft tissue and periosteum were removed from the mid-shaft of both femurs and the distal shaft of both tibias. The exposed bone was cleaned with isopropyl alcohol and dried with acetone. A catalyst (M-Bond 200 Catalyst, Vishay Micro-Measurement, Shelton, CT) was applied to the bone and the back of each strain gage before the gage was adhered to the bone. The adhesive (M-Bond 200 Adhesive, Vishay Micro-Measurement, Shelton, CT) was applied to the gage. Then the gage was positioned on the bone and held in place with pressure for several minutes. A protective coating (M-Coat-D Adhesive, Vishay Micro-Measurement, Shelton, CT) was applied to the top of the gage and the bone immediately surrounding the bone in order to seal the gage against fluids.

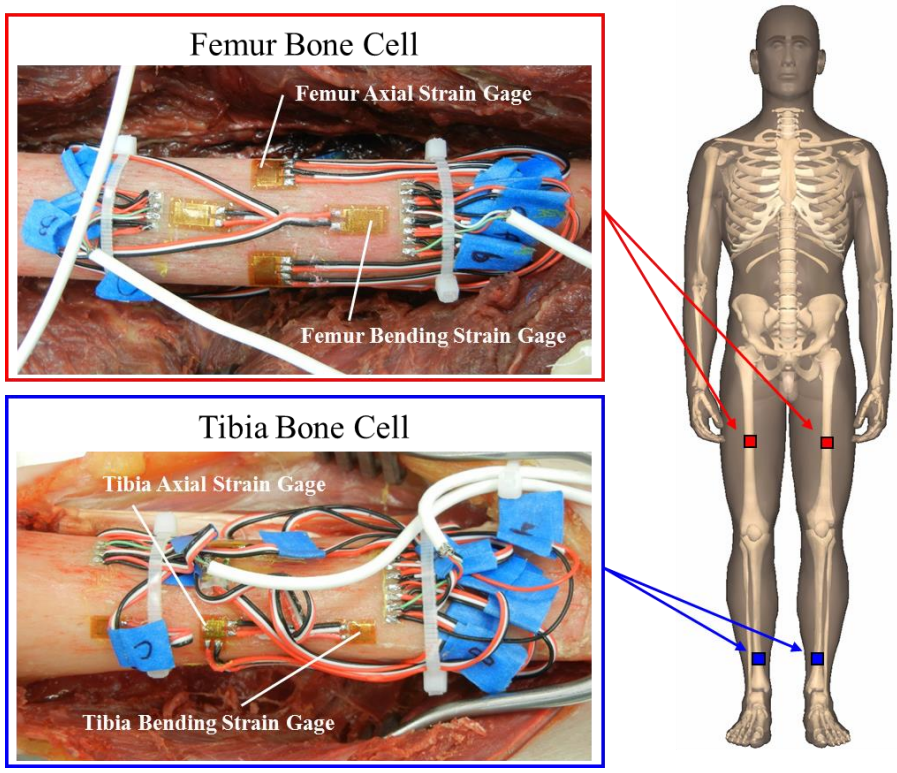

Figure 4.1: PMHS lower extremity instrumentation.

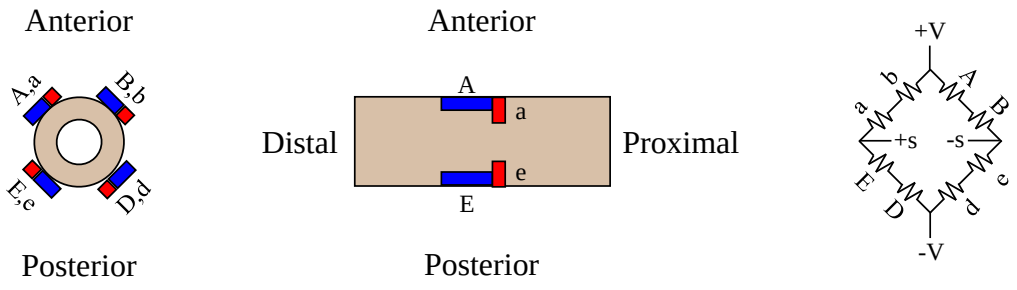

Figure 4.2: PMHS axial force bone cell configuration.

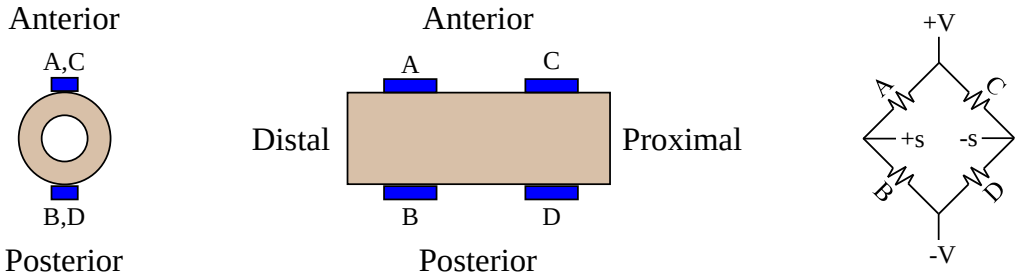

Figure 4.3: PMHS bending moment bone cell configuration.

The voltage outputs of the axial and bending bridge configurations (bone cells) were converted to axial forces and bending moments for each PMHS via a calibration procedure completed after gage application and before the sled test. The calibration procedure involved manipulating the lower extremity, imposing axial forces or bending moments on the tibia and femur, while recording these loads using a uniaxial load cell held at the heel or knee. The load cell output was plotted against the bone cell output, and a linear trend line was fit to the data (Figure 4.4). The slope of the trend line was used as a calibration factor to convert the bone cell outputs (mV) to the axial forces and bending moments. Applying a bending moment to the bone produced some axial output with an approximately linear relationship between axial and bending output. This relationship was not accounted for in the calibration of the axial bone cell data. Therefore, the reported axial forces for the lower extremity were not the pure axial forces and are influenced by the bending moment experienced by the bone.

Sled buck reaction forces and moments were also collected for each surrogate (Table A4.2). The left and right knee bolsters were each instrumented with a 6 axis load cell (2513TF, Endevco, San Juan Capistrano, CA), and the left and right foot pedals were each instrumented with a 3 axis load cell (5768, Endevco, San Juan Capistrano, CA). The load cells were compensated for crosstalk, and were inertially compensated using accelerations from sets of three uniaxial accelerometers (7264-2000, Endevco, San Juan Capistrano, CA) mounted to the same reaction plates as the load cells.

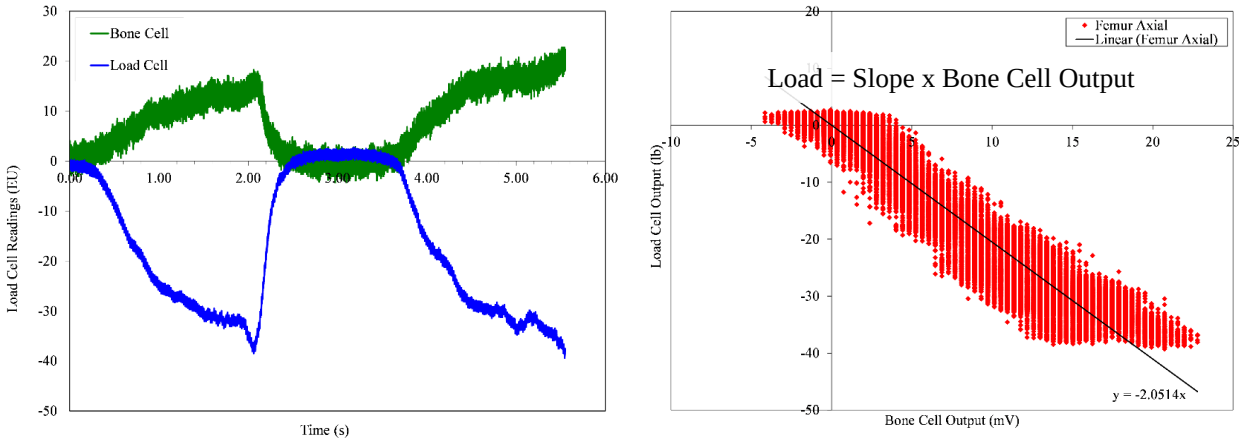

Figure 4.4: Output from a bone cell and load cell during calibration (left) and the trend line used to determine the calibration factor to convert bone cell output to a load (right).

All data was collected at 20 kHz. Sled buck reaction forces and moments were filtered at SAE channel filter class (CFC) 60 [18]. PMHS and ATD lower extremity forces and moments were filtered at CFC 600 except for the HIII right femur axial force data, which were filtered at CFC 180 to minimize noise spikes.

Data Analysis

In order to assess the validity of the axial forces obtained from the PMHS lower extremity bone cells, the ratio between the lower extremity forces and the sled buck reaction forces was calculated for all surrogates. Due to the complexity of the loading on the femur and tibia, analogous lower extremity moment/reaction moment ratios could not be calculated. Axial femur load was divided by the component of the resultant x and z knee bolster reaction load that was aligned with the axial femur. Axial tibia load was divided by the component of the foot support reaction load that was aligned with the axial tibia. Ratios were calculated for the times of maximum lower extremity load and maximum reaction load for each test. Both times were used because the maximum lower extremity force and reaction force did not occur at the same time for all tests. The angles between the axial loading axes of the lower extremities and their corresponding reaction loads were determined from high speed video stills at the approximate time of peak knee excursion. The time of peak knee excursion approximately corresponded with the times of peak lower extremity and reaction loads. The ratios were compared across surrogates to determine whether there were substantial differences between the PMHSs and the ATDs.

The lower extremity force and moment time histories were qualitatively compared between test conditions and between subject types. The location of the bone cells on the PMHS tibias was closest to the location of the lower tibia load cells in the ATDs. Therefore, the ATD lower tibia axial forces and bending moments were compared to the PMHS tibia axial forces and bending moments. The femur bone cells were located toward the middle of the diaphysis for the PMHSs, while the ATD femur load cells were located toward the distal end of the femur.

Lower extremity injury risk was evaluated for the HIII and THOR-M. The risk of sustaining an AIS2+ femur injury was calculated for all tests for both ATDs using Equation 1 from [1]. The

Tibia Index (TI) (Equation 2) [19] was calculated for the HIII upper and lower tibia. The risk of sustaining an AIS2+ tibia injury was calculated for the THOR using three injury criteria (Equations 3 - 6) [1]: Revised Tibia Index (RTI), proximal tibia force ($F_{z,UTibia}$), and distal tibia force ($F_{z,LTibia}$). Each PMHS was dissected after the sled test to record and categorize the occurrence of lower extremity injuries. The observed injuries were used as a basis to evaluate the accuracy of the calculated injury risks.

Equation 1 $$p(AIS2+) = \frac{1}{1+e^{5.7949-0.5196F_z}}$$

Equation 2 $$TI = \frac{F_{z,compressive}}{35.9} + \frac{M_{Resultant}}{225}$$

Equation 3 $$RTI = \frac{F_{z,compressive}}{12} + \frac{M_{Resultant}}{240}$$

Equation 4 $$p(AIS2+) = 1 - e^{-e^{\left[\frac{\ln(RTI)-0.2468}{0.2728}\right]}}$$

Equation 5 $$p(AIS2+) = \frac{1}{1+e^{4.572-0.670F_{z,LTibia}}}$$

Equation 6 $$p(AIS2+) = \frac{1}{1+e^{5.6654-0.8189F_{z,UTibia}}}$$

Results

All data could not be collected for the THOR-M and PMHS tests. For the THOR-M, the left upper tibia AP bending moment (My) was not functional. For the PMHS, six forces and moments were not reported due to malfunctioning strain gages or the inability to obtain a linear calibration factor. The unreported PMHS data included: PMHS-KB-2 right axial femur force, PMHS-KB-2 left femur AP bending moment, PMHS-KB-2 right femur AP bending moment, PMHS-KB-2 right tibia axial force, PMHS-KB/SWAB-1 left femur axial force, and PMHS-KB/SWAB-3 right femur axial force.

Lower Extremity to Reaction Force Ratios

When comparing the femur axial force to the bolster resultant force, all surrogates showed similar trends. The HIII had the best alignment between the time of maximum femur force and maximum bolster force with a difference of only 1 ms on average (Figure A4.1). The THOR-M and PMHS had less alignment in these times with an average difference of 6 ms for both surrogates (Figures A4.2 – A4.5, Table A4.3, Table A4.4). The maximum bolster resultant force was caused by the

surrogate arm hitting the foam or bolster support structure late in the event for three tests: THOR-KBAB-1 (left and right), THOR-KBAB-2 (left and right), and PMHS-KB-1 (right). For these tests, the maximum resultant force was adjusted to be the maximum before arm contact. PMHS-KB-1 had a large difference between the times of maximum right femur force and maximum right bolster force with the maximum femur force occurring after bolster loading. This inflated the femur to bolster force ratio at the time of maximum femur force, leading to a higher average ratio for the PMHS compared to the ATDs. Excluding this test from the average produced similar average ratios across all surrogates with the PMHS average falling between the HIII and THOR-M averages (Table 4.2). Looking at the time of maximum bolster force, the average ratios were even more similar between surrogates with the PMHS average still falling between the two ATDs (Table 4.3).

For the comparisons between the tibia axial force and the foot support force, the PMHSs showed different results compared to the ATDs. The THOR-M had the best alignment between the time of maximum tibia force and maximum foot support force with an average difference of 1 ms (Figure A4.7). The HIII and PMHS had average differences of 5 and 4 ms, respectively (Figure A4.6, Figures A4.8 – A4.10). Regardless of the time point of interest, the PMHS had lower average tibia to foot support force ratios than the ATDs (Table A4.4, Table 4.4, Table 4.5).

Table 4.2: Average femur to bolster force ratios for all surrogates at the time of maximum femur force.

Surrogate	**Restraint Condition**		
	KB & KB/SWAB	**KBAB/SWAB**	**All**
HIII	-0.54	-0.66	-0.58
THOR	-0.65	-0.84	-0.71
PMHS	-0.51	-0.76	-0.63

Note: PMHS-KB-1 right femur was excluded from averages.

Table 4.3: Average femur to bolster force ratios for all surrogates at the time of maximum bolster force.

Surrogate	**Restraint Condition**		
	KB & KB/SWAB	**KBAB/SWAB**	**All**
HIII	-0.51	-0.60	-0.54
THOR	-0.45	-0.52	-0.47
PMHS	-0.44	-0.62	-0.53

Table 4.4: Average tibia to foot support force ratios for all surrogates at the time of maximum tibia force.

Surrogate	Restraint Condition		
	KB & KB/SWAB	KBAB/SWAB	All
HIII	0.74	0.80	0.76
THOR	1.02	0.91	0.98
PMHS	0.60	0.44	0.54

Table 4.5: Average tibia to foot support force ratios for all surrogates at the time of maximum foot support force.

Surrogate	Restraint Condition		
	KB & KB/SWAB	KBAB/SWAB	All
HIII	0.66	0.79	0.70
THOR	0.85	0.84	0.84
PMHS	0.37	0.33	0.36

Comparisons between Surrogates

The bolster support and foot support reaction forces had similar peak timing, but differences in magnitudes across surrogates (Figure 4.5 and Figure 4.6). For the bolster reaction forces, trends varied depending on the restraint condition. The THOR-M had the greatest bolster reaction forces for the two KB conditions. For the KB only condition, the PMHS had the lowest forces. However, the HIII and PMHS had comparable forces for the KB/SWAB condition. All surrogates had similar peak magnitudes for the KBAB/SWAB conditions if the short duration spike late in the loading event (caused by the THOR-M upper extremity striking the foam/bolster support structure) was not considered. For the foot support forces, the PMHS had lower peak magnitudes compared to the ATDs, whereas the ATDs were comparable in magnitude.

Femur axial forces and AP bending moments were more similar between the ATDs than between the ATDs and PMHSs (Figure 4.7 and Figure 4.8). For the axial femur forces, all surrogates had similar peak timing and similarly shaped time history curves, except for PMHS-KB-1. The THOR-M had the highest axial femur forces for all conditions, while the PMHSs had the lowest peak forces on average for all conditions. The differences between the PMHSs and other surrogates were more pronounced for the KB condition. Specifically, the PMHSs had lower axial forces for the KB condition, indicating that the PMHS did not load the KB as much as the ATDs. The PMHS

peak forces were only slightly less than the HIII for the KBAB condition. For the femur AP bending moments, the ATDs had similarly shaped time histories and similar peak timing. The HIII had higher peaks than the THOR-M for all conditions. Compared to the ATDs, the PMHSs had more variability in femur AP moment. PMHS peak magnitudes varied between being less than or greater than the ATDs, depending on the test. For the KBAB condition, the average peak magnitudes were less for the PMHSs than the ATDs. For the two KB conditions, all PMHS tests showed a sharp positive increase at the time of contact with the KB. This roughly coincided with an increase in ATD AP moments.

Lower tibia axial force and AP bending moment time histories had similar timing across all surrogates; however, differences in magnitude were observed (Figure 4.9 and Figure 4.10). For the axial forces, the PMHS time histories had a similar shape compared to the ATDs for most tests, but the PMHS tests were much lower in magnitude. In particular, PMHS-KBAB/SWAB-2 experienced negligible left tibia axial forces. For all of the ATD tests, the THOR-M had a slightly higher magnitude than the HIII. For the lower tibia AP bending moments, the PMHS responses were most similar to the ATD responses for the KBAB condition. For the KB conditions, the PMHSs experienced much more variability in AP bending moments, resulting in peak magnitudes greater or less than the ATD peak magnitudes depending upon the test. Some PMHS tests showed a sharp positive increase in bending moment that corresponded to contact between the shank and the KB.

The ATDs had similar femur shear forces (Fx, Fy) (Figure A4.11, Figure A4.12), but exhibited differences in moments about the x and z-axes (Mx, Mz) (Figure A4.14, Figure A4.16). For the AP shear forces (Fx), both ATDs had similar time histories in terms of shape and magnitude. For the medial-lateral (ML) shear forces (Fy), both ATDs experienced negligible loads compared to the femur loads in other directions. Regarding the femur moments about the x-axis (Mx), the ATDs were most similar for the KBAB/SWAB condition in terms of both magnitude and shape. However, there were clear differences in peak timing and magnitude for the KB and KB/SWAB conditions. Specifically, the HIII peaked earlier with a higher magnitude. Both ATDs exhibited differences in the shape of the Mx time history curves between the left and right sides. For the moments about the z-axis, the ATDs exhibited differences in the shape of the time history curves

for all conditions. Furthermore, the THOR-M had higher magnitudes for the SWAB conditions and had more differences between the left and right sides for all conditions. However, the magnitudes were low for both ATDs.

Similar to what was observed for the femur, the ATDs had similar tibia shear forces (Fx, Fy) (Figure A4.17, Figure A4.18, Figure A4.22, and Figure A4.23), but experienced differences in tibia moments about the x-axis (Mx) (Figure A4.20, Figure A4.25). For the upper and lower tibia AP shear forces (Fx), minimal differences were observed between the HIII and THOR-M. The only notable difference was for the upper tibia where the HIII had greater peak magnitudes than the THOR-M for the KBAB/SWAB condition. The loading profiles for the upper and lower tibia AP shear forces were generally opposite in polarity for both ATDs. For example, the upper tibia experienced mostly negative loading for the KBAB/SWAB condition, while the lower tibia experienced mostly positive loading. For the upper and lower tibia ML shear forces (Fy), both ATDs experienced negligible forces with little difference between the upper and lower tibia. For the upper and lower tibia moments about the x-axis, the ATDs exhibited differences in peak magnitude and timing. The THOR-M had slightly higher peak moments than the HIII, except for the right upper tibia KB conditions, where the ATDs were similar in magnitude. For both ATDs, the upper tibia moments were greater than the lower tibia moments.

The ATDs were both instrumented to quantify upper tibia axial forces and AP bending moments (Figure A4.19, Figure A4.21), which did not have PMHS analogs since the PMHSs were instrumented at locations that corresponded more closely to the lower tibia load cells in the ATDs. For the upper tibia axial forces, both ATDs had very similar time histories in terms of shape and magnitude for all conditions. The THOR-M had lower axial forces at the upper tibia compared to the lower tibia. However, there was little difference in magnitude between the upper and lower axial tibia forces for the HIII. For the right upper tibia AP bending moments, the THOR-M had higher peak forces than the HIII. Upper tibia AP bending moments were not collected for the THOR-M on the left side. The HIII showed little difference in peak AP bending moment between the upper and lower tibia. However, the THOR-M exhibited differences in peak AP bending moment between the upper and lower tibia, depending upon the restraint condition. For both KB

conditions, the THOR-M upper tibia had greater AP bending moments than the lower tibia, while the opposite was observed for the KBAB/SWAB condition.

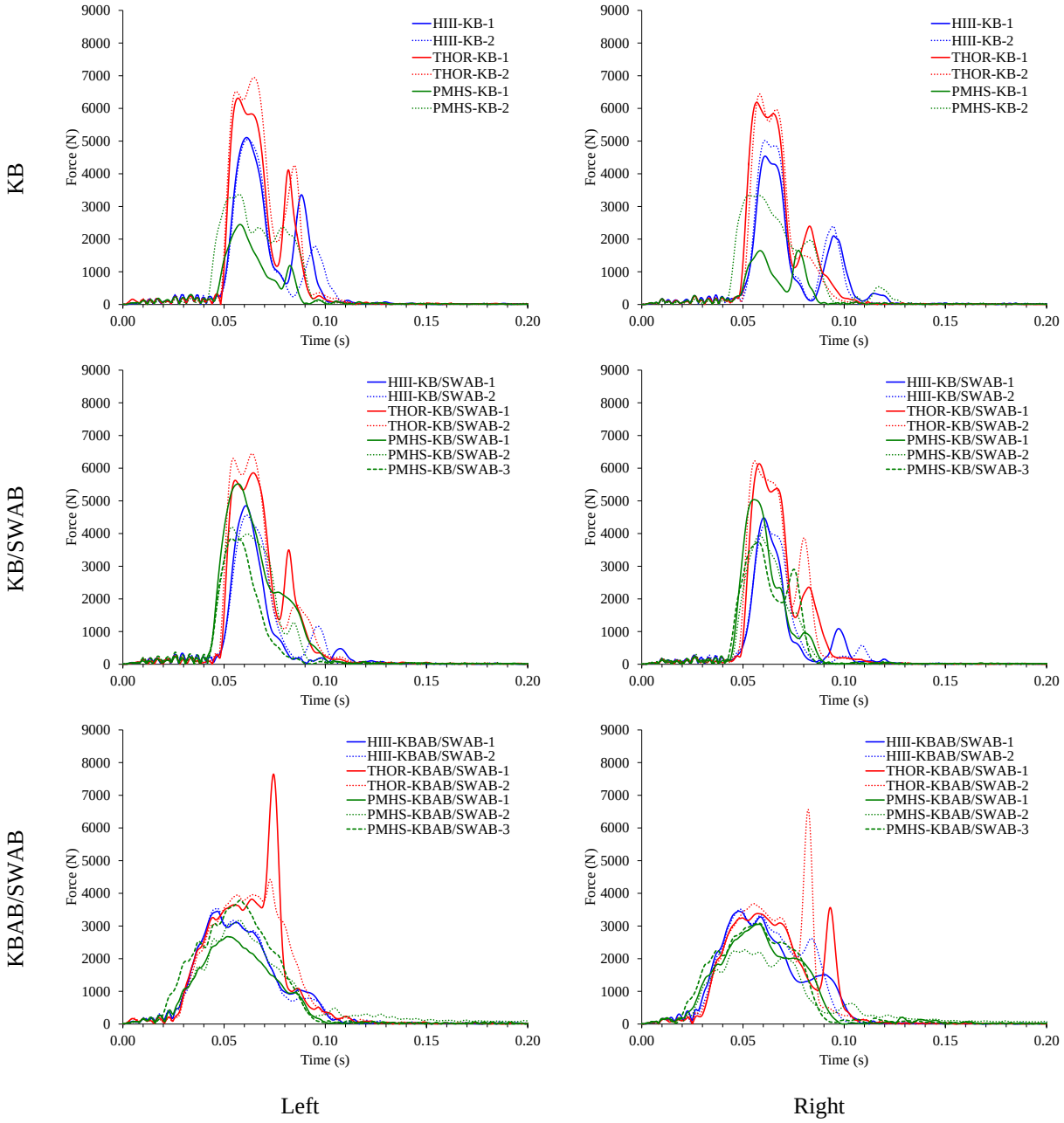

Figure 4.5: Resultant (Fx, Fz) knee bolster reactions forces for all surrogates and conditions.

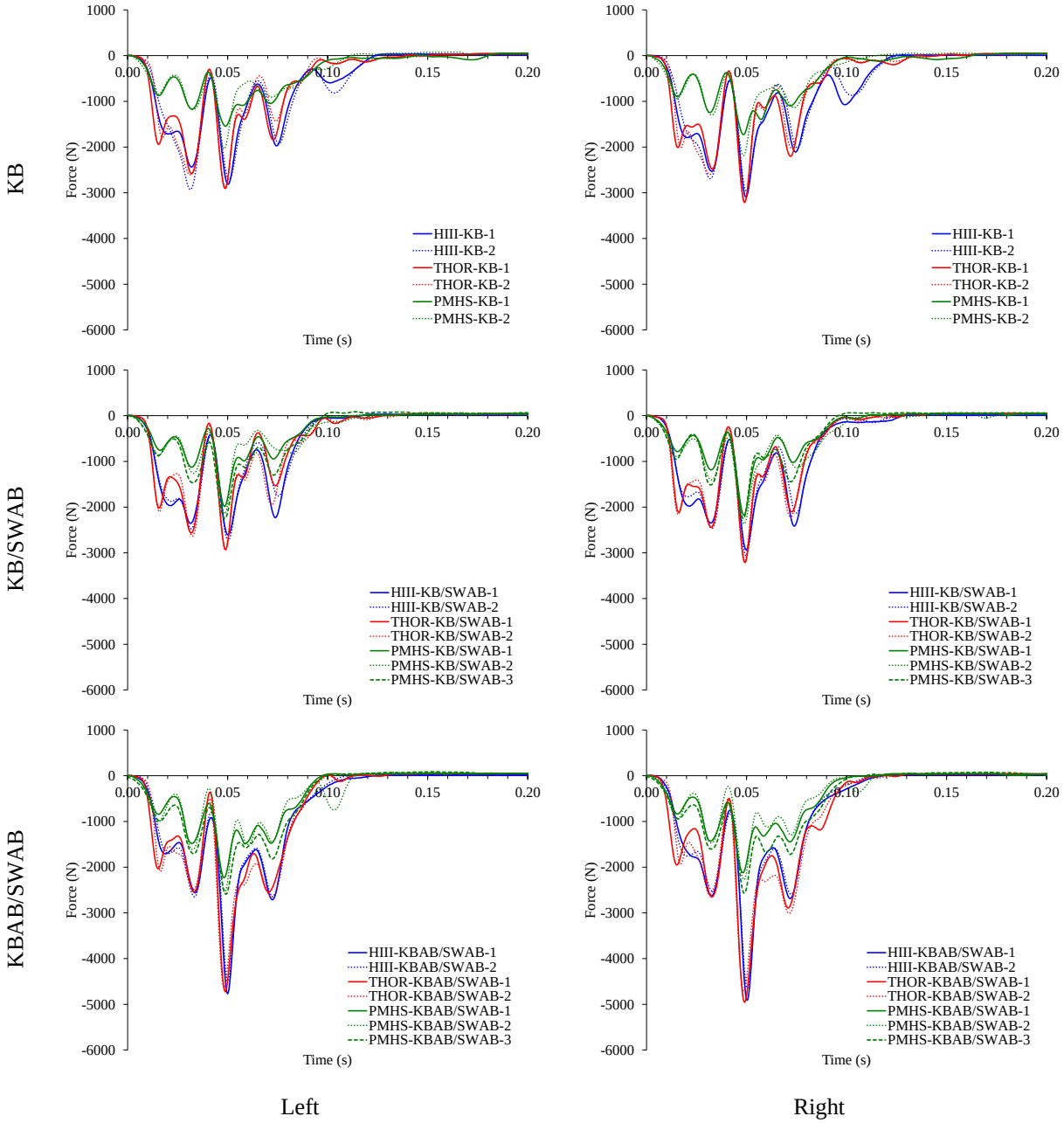

Figure 4.6: Foot support reaction forces for all surrogates and conditions.

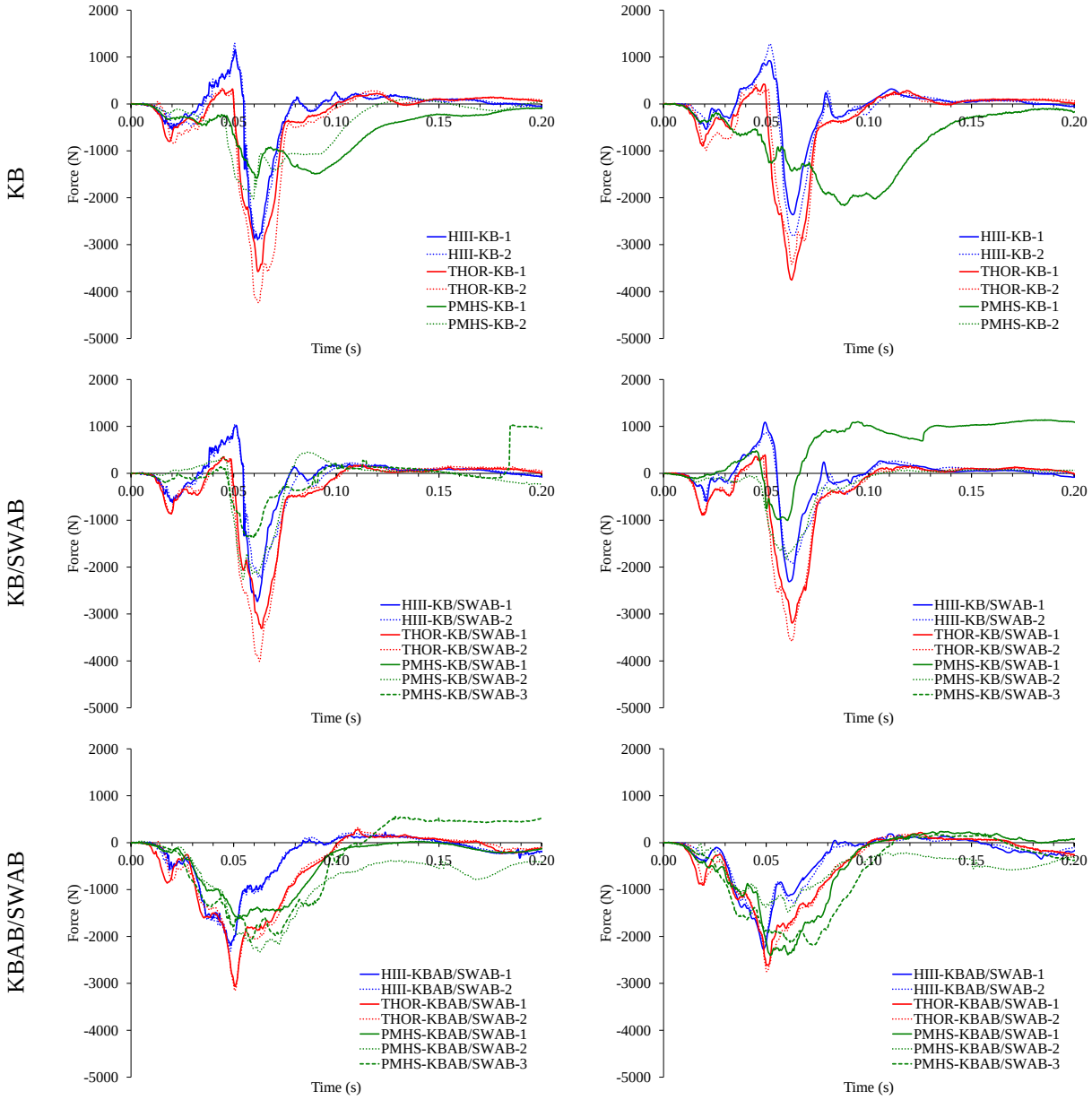

Figure 4.7: Femur axial forces (Fz) for all surrogates and conditions.
Note: Forward knee movement and rearward pelvis movement are positive.

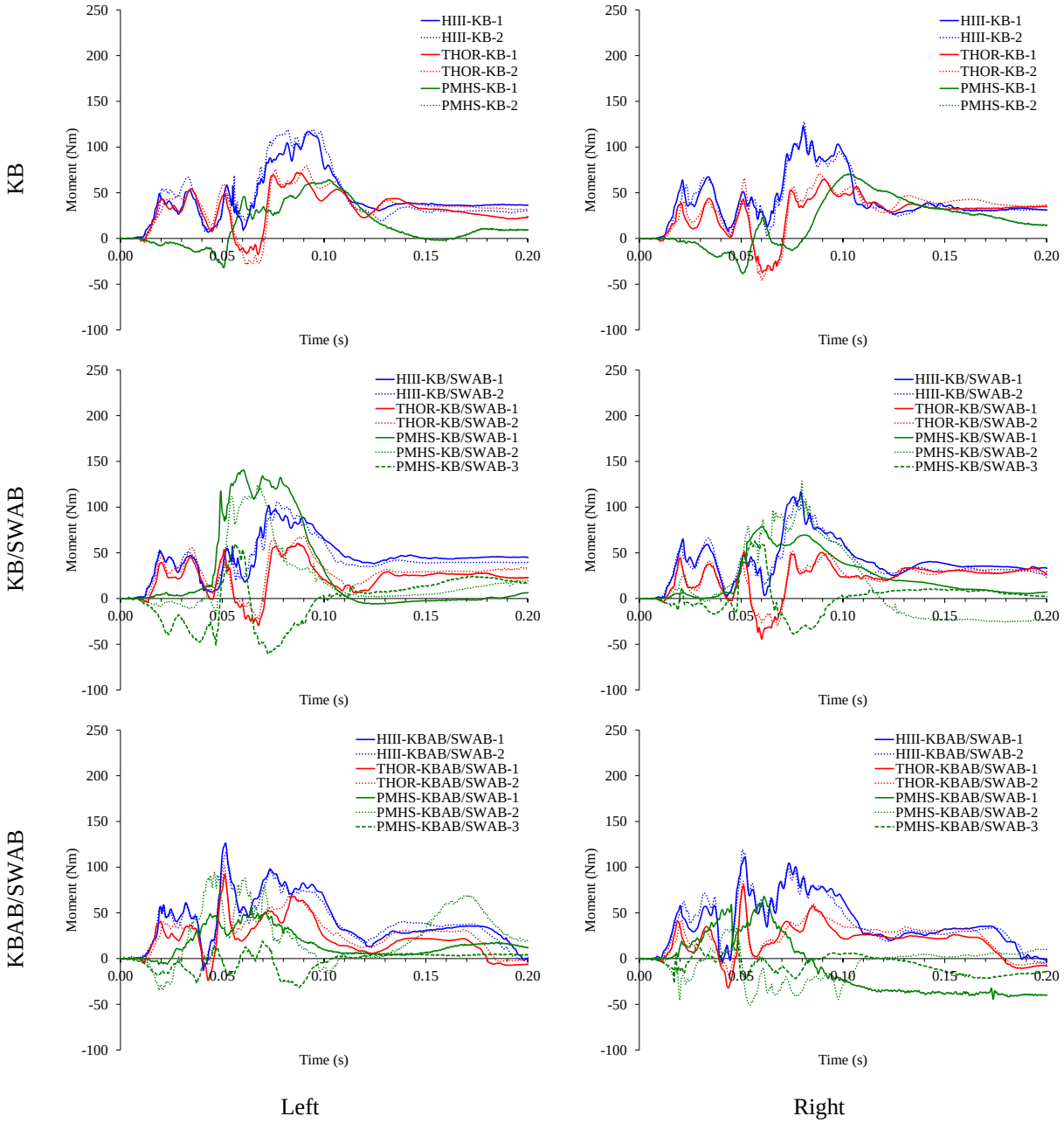

Figure 4.8: Femur AP bending moments (My) for all surrogates and conditions.
Note: Upward knee movement relative to the upper femur is positive

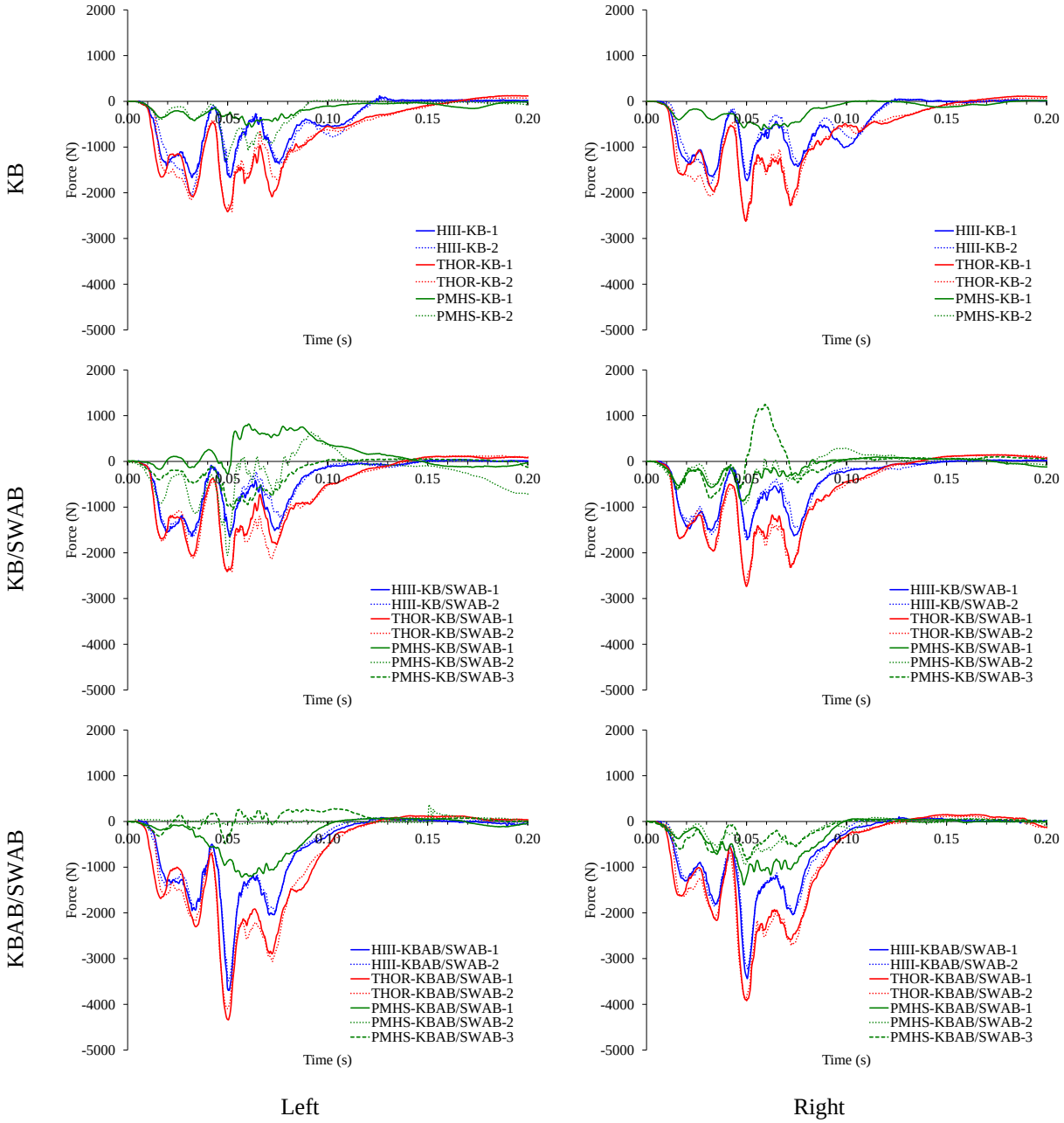

Figure 4.9: Lower tibia axial forces (Fz) for all surrogates and conditions.
Note: Downward ankle movement and upward knee movement are positive.

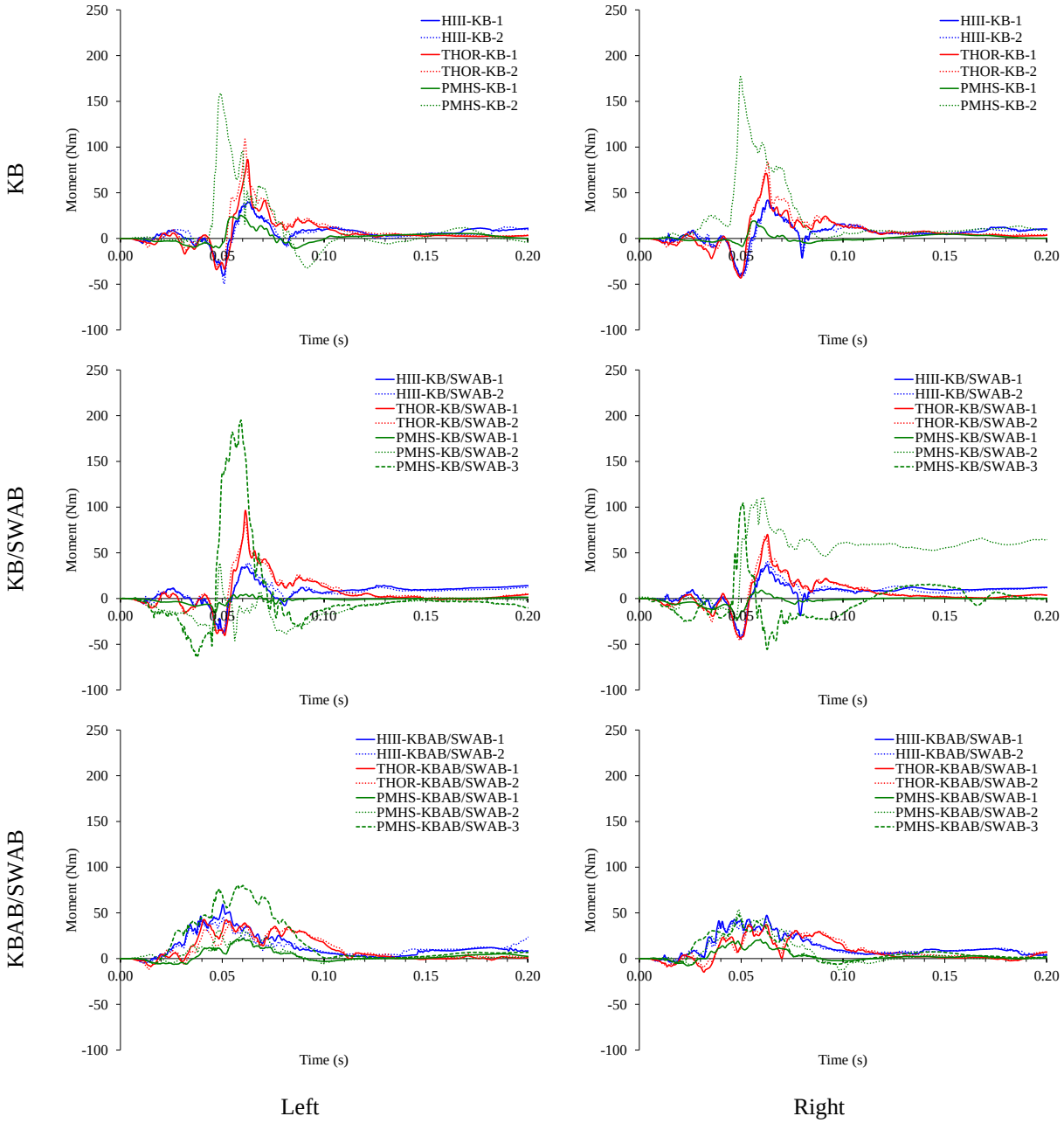

Figure 4.10: Lower tibia AP bending moments (My) for all surrogates and conditions. Note: Forward ankle movement and rearward knee movement are positive.

Comparisons between Conditions

Differences in the bolster support forces and foot support forces were observed between restraint conditions. For the bolster support forces, all surrogates had an earlier onset of loading for the KBAB/SWAB condition compared to the KB conditions, which resulted in a longer duration of

loading. If the peaks resulting from upper extremity contact with the foam/bolster support are excluded, both ATDs experienced a decrease in peak force for the KBAB/SWAB condition compared to the two KB conditions. For the PMHS, the KB/SWAB condition had the highest magnitude, while the KB and KBAB/SWAB conditions had more similar, lower peak magnitudes. For the foot support forces, the ATDs experienced greater forces for the KBAB/SWAB condition compared to the two KB conditions, while the PMHSs had slightly higher magnitudes for the two SWAB conditions compared to the KB condition.

Out of all of the femur forces and moments, the femur axial forces showed the most sensitivity to restraint condition. All surrogates had a longer duration of axial femur loading for the KBAB/SWAB condition compared to the two KB conditions. The THOR-M experienced a decrease in loading for the KBAB/SWAB condition compared to the KB conditions. The HIII also experienced a slight decrease for the KBAB/SWAB condition relative to the KB/SWAB condition. However, the PMHSs exhibited no notable change in magnitude between restraint conditions. Neither femur shear force (Fx, Fy) demonstrated a sensitivity to restraint condition in terms of peak timing or magnitude for either ATD. The femur moments about the x-axis showed some sensitivity to changes in restraint condition; however, the changes were small and inconsistent between the left and right sides of each ATD. The ATDs did exhibit a difference in peak timing between the KB and KBAB conditions for the AP bending moments (My). The KBAB/SWAB condition resulted in earlier peak timing than the two KB conditions, but no appreciable difference in magnitude. The variability in the PMHS time histories made it difficult to detect trends in peak timing and magnitude between conditions for the AP bending moments. For the moments about the z-axis, little difference was observed between conditions for both ATDs.

The effect of restraint condition on the tibia forces and moments varied with each surrogate. For the axial lower tibia forces, the ATDs had greater peak forces for the KBAB/SWAB condition compared to the KB conditions, while the PMHS showed little difference between conditions. Despite some changes in magnitude, the duration of loading was consistent between conditions for all surrogates. The same trends in magnitude were observed for the ATD upper tibia forces, where the KBAB/SWAB had greater peak forces than the KB conditions. Changes between conditions for the upper and lower tibia AP shear forces were less pronounced. Both the upper and lower tibia

AP shear forces time histories exhibited shape differences between the KBAB/SWAB and KB conditions. Furthermore, the HIII experienced a slight increase in magnitude for the KBAB/SWAB condition at the upper tibia, while the THOR-M did not. At the lower tibia, both ATDs had slightly lower magnitudes for the KBAB/SWAB condition compared to the KB conditions. The upper and lower tibia ML shear forces did not show a sensitivity to restraint condition. For the upper and lower tibia moments about the x-axis, both ATDs experienced slightly higher peak moments for the KBAB/SWAB condition compared to the KB conditions except for the HIII's right tibia, which experienced comparable peak moments across all conditions. Conversely, both ATDs had a decreased upper tibia AP bending moment for the KBAB/SWAB condition. This trend was not as prominent at the lower tibia, where the THOR-M experienced a slight decrease in magnitude for the KBAB/SWAB condition, but the HIII showed little difference in magnitude across conditions. The lower tibia AP bending moments were highly variable for the PMHSs so it was difficult to discern any changes between conditions.

Injury Risk

No femur injuries were observed from the PMHS tests, and none of the ATD tests predicted more than a 3% risk of an AIS2+ femur injury (Table 4.6). The THOR-M predicted a slightly higher risk of injury than the HIII for all conditions. Both ATDs predicted a slightly higher risk of injury for the two KB conditions compared to the KBAB/SWAB condition.

No AIS2+ tibia injuries were observed from the PMHS tests, and none of the ATD tests predicted an appreciable risk of an AIS2+ tibia injury (Table 4.7 - Table 4.9). The only tibia injury observed in the PMHS tests was a left tibia posterior endplate fracture (AIS1) for PMHS-KB-2 (Figure 4.11). Two injury thresholds have been proposed for the tibia index: 1.0 [19] and 1.3 (ECE R94). The highest tibia index observed for the HIII tests was 0.5224, which was still well below either of the proposed thresholds. Therefore, the predicted likelihood of a tibia fracture was low. The analogous RTI injury metric, proposed for the THOR-M, has a corresponding injury risk curve that predicts the risk of an AIS2+ tibia injury. The predicted risk of an AIS2+ injury based on RTI was less than 15% for all THOR-M tests. The risk of an AIS2+ tibia injury was also computed for the THOR-M using the upper and lower axial tibia forces. The predicted injury risks from this criterion were all under 16%.

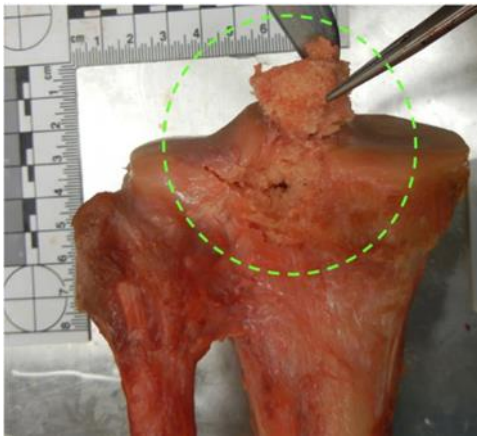

Figure 4.11: Left tibia posterior endplate fracture (AIS1).

Injury prediction results varied with restraint condition for both ATDs. The HIII tibia index for the upper tibia was higher for the KB conditions compared to the KBAB/SWAB condition. However, the opposite was true for the lower tibia, where the tibia index values were highest for the KBAB/SWAB condition. Similar trends in injury prediction were observed for the HIII and THOR-M upper tibia. The THOR-M RTI also resulted in a higher injury risk for the KB conditions at the upper tibia. However, there was little difference observed in predicted injury risk between conditions for the THOR-M lower tibia. The THOR-M injury risks from the axial tibia force were higher for the KBAB/SWAB condition compared to the KB conditions for both the upper and lower tibia.

Table 4.6: Probability of an AIS2+ femur injury for the HIII and THOR-M.

Test	Left	Right
HIII-KB-1	0.013	0.010
HIII-KB-2	0.014	0.013
HIII-KB/SWAB-1	0.012	0.010
HIII-KB/SWAB-2	0.010	0.008
HIII-KBAB/SWAB-1	0.010	0.010
HIII-KBAB/SWAB-2	0.010	0.010
THOR-KB-1	0.019	0.021
THOR-KB-2	0.027	0.018
THOR-KB/SWAB-1	0.017	0.016
THOR-KB/SWAB-2	0.024	0.019
THOR-KBAB/SWAB-1	0.015	0.012
THOR-KBAB/SWAB-2	0.015	0.013

Table 4.7: Tibia index for the HIII upper and lower tibia.

Test	Upper Tibia		Lower Tibia	
	Left	**Right**	**Left**	**Right**
HIII-KB-1	0.481	0.434	0.226	0.230
HIII-KB-2	0.522	0.468	0.269	0.227
HIII-KB/SWAB-1	0.423	0.384	0.213	0.237
HIII-KB/SWAB-2	0.411	0.420	0.215	0.237
HIII-KBAB/SWAB-1	0.268	0.219	0.369	0.281
HIII-KBAB/SWAB-2	0.253	0.249	0.304	0.257

Table 4.8: Revised tibia index (RTI), probability of an AIS2+ injury based on RTI, and probability of an AIS2+ injury based on axial tibia force for the THOR-M upper tibia.

Test	RTI		P(RTI)		P(Fz)	
	Left	**Right**	**Left**	**Right**	**Left**	**Right**
THOR-KB-1		0.708		0.108	0.011	0.013
THOR-KB-2		0.771		0.144	0.014	0.013
THOR-KB/SWAB-1		0.699		0.103	0.013	0.013
THOR-KB/SWAB-2		0.711		0.110	0.014	0.013
THOR-KBAB/SWAB-1		0.558		0.047	0.053	0.043
THOR-KBAB/SWAB-2		0.512		0.034	0.047	0.040

Note: Left RTI and P(RTI) could not be calculated due to the missing data from the left upper tibia load cell.

Table 4.9: Revised tibia index (RTI), probability of an AIS2+ injury based on RTI, and probability of an AIS2+ injury based on axial tibia force for the THOR-M lower tibia.

Test	RTI		P(RTI)		P(Fz)	
	Left	Right	Left	Right	Left	Right
THOR-KB-1	0.478	0.413	0.027	0.016	0.050	0.056
THOR-KB-2	0.584	0.449	0.055	0.021	0.050	0.057
THOR-KB/SWAB-1	0.511	0.407	0.034	0.015	0.049	0.061
THOR-KB/SWAB-2	0.484	0.418	0.028	0.017	0.049	0.058
THOR-KBAB/SWAB-1	0.516	0.427	0.035	0.018	0.159	0.125
THOR-KBAB/SWAB-2	0.445	0.387	0.021	0.012	0.138	0.121

Discussion

The ratios of lower extremity to support forces between surrogates were compared to indicate whether the PMHS bone cells produced reasonable forces. The ratio of femur axial force to bolster support force was comparable across surrogates, indicating that the PMHS femur axial bone cells were providing reasonable force measurements. However, the ratio of tibia axial force to foot support force was much lower for the PMHS than the ATDs. There are three possible explanations for the mismatch between the PMHS and ATD tibia axial forces ratios. First, load sharing occurs

between the tibia and fibula in a PMHS that would not be present in an ATD. This load sharing would result in a decreased tibia force in the PMHS relative to the ATDs. Funk *et al.* (2004) performed quasi-static shank compression tests with different orientations of the foot (inversion, eversion, neutral) and ankle (plantarflexion, dorsiflexion, neutral). Load cells were implanted in the tibia and fibula to measure how much load each bone bore. For the current study, the percent load sharing of the fibula was averaged from the Funk *et al.* (2004) tests involving a neutral foot orientation and a dorsiflexed or neutral ankle because these conditions most represented the position of the PMHS foot during the sled tests. The resulting average indicated that the fibula bore 6.8% of the load, while the tibia bore 93.2%. These numbers were used to compensate the PMHS axial tibia force to foot support force ratios (Table 4.10, Table 4.11). The compensation produced a small increase in the PMHS ratios; however, the PMHS ratios were still much lower than those of the ATDs. Measuring the foot support in only one direction (parallel to the main axis of the load cell) may have also contributed to the discrepancy in ratios. It is possible that the PMHSs exerted more force perpendicular to the load cell's sensing axis than the ATDs. Since the load cell did not measure shear forces, this force would not be accounted for in the ratios. Some support for this theory can be seen in the alignment of the surrogate tibiae with the foot support load cell. The angle between the load sensing axis of the tibia and foot support load cell was much higher for the HIII than the THOR-M. The better aligned forces for the THOR-M would theoretically result in a higher ratio compared to the HIII, which was borne out in the data. However, the average PMHS angle was between that of the HIII and THOR-M so the difference in angle does not fully explain why the PMHS ratios were much lower than the ATDs. The final explanation for the lower PMHS ratios is that there may have been an issue with the calibration procedure for the tibia bone cells, and the resulting calibration factor was inaccurate. This could be the result of many factors, including uncompensated cross-talk between axial force and bending moment. This limitation will be discussed in more depth later in this chapter.

Table 4.10: Load sharing compensated average tibia to foot support force ratios for all surrogates at the time of maximum tibia force.

Surrogate	Restraint Condition		
	KB & KB/SWAB	KBAB/SWAB	All
HIII	0.74	0.80	0.76
THOR	1.02	0.91	0.98
PMHS	0.64	0.48	0.58

Table 4.11: Load sharing compensated average tibia to foot support force ratios for all surrogates at the time of maximum foot support force.

Surrogate	Restraint Condition		
	KB & KB/SWAB	KBAB/SWAB	All
HIII	0.66	0.79	0.70
THOR	0.85	0.84	0.84
PMHS	0.40	0.35	0.38

Because the PMHS femur moments, tibia forces, and tibia moments could not be quantitatively validated, the biofidelity of the ATD lower extremity forces could not be validated using the PMHS data. However, the time histories were still qualitatively compared between surrogates and conditions. The trends observed in the axial femur and tibia forces between conditions were also observed in the bolster and foot support reaction forces for all surrogates, indicating the PMHS forces were able to reasonably represent trends in the data. Furthermore, the shapes of the PMHS tibia axial force time histories were very similar to those of the ATDs, despite the differences in magnitude. However, one test (PMHS-KBAB/SWAB-2) had a particularly low left tibia axial force. The calibration factor for this force was not unusually low, but it is still possible there was an issue with the calibration of this bone cell. It is also possible that this gage was malfunctioning due to exposure to body fluids, direct pressure on the gage, or a loose connection.

The results of this study support some of the findings of previous FEM studies that assessed the effect of KBABs on lower extremity loads. Kitagawa *et al.* (2005) reported a decrease in axial femur force and an increase in the duration of femur loading with a KBAB. In the current study, a decrease in axial femur force was observed in the ATDs for the KBAB/SWAB condition, and an increased duration of loading was observed in all surrogates. The decrease in femur force for the KBAB conditions was much more pronounced for the THOR-M, whereas the HIII experienced

only a slight decrease. This is an interesting difference since Danelson *et al.* (2015) reported a decrease in axial femur force for the THUMS model, but an increase in femur force using a HIII model when both were exposed to a KBAB deployment. Nie *et al.* (2016) reported both an increase in axial femur force and femur bending moments when the THUMS model experienced KBAB deployment. However, neither of these trends were observed in the current study, as little difference in magnitude was observed between conditions for the femur AP bending moments. Nie *et al.* (2016) also reported that both tibia axial force and AP bending moment decreased when a KBAB deployment occurred. Contrasting with these results, both ATDs experienced an increase axial tibia force for the KBAB condition in the current study. For the lower tibia AP bending moments, little difference was observed between conditions. However, both ATDs did experience a decrease in upper tibia AP bending moments for the KBAB/SWAB condition, partially agreeing with the results of Nie *et al.* (2016). The discrepancies between the current study and Nie *et al.* (2016) could be attributed to differences in vehicle geometry, occupant seating position, and differences in restraint system. Specifically, Nie *et al.* (2016) reported that the belt system modeled in the study was very aggressive and influenced some of the results.

All ATD injury metrics correctly predicted the lack of AIS2+ injuries that were observed in the PMHS tests. Although no injuries were predicted, the trends in injury prediction between conditions can be compared to injury outcomes from studies that analyzed real-world crash data. Weaver *et al.* (2013) reported a significant decrease in femur fractures for crashes that involved a KBAB deployment, while Patel *et al.* (2013) reported a non-significant decrease in femur fractures. The current study supported those findings, as both ATDs predicted decreased femur injury risks for the KBAB condition compared to the KB conditions. Both real-world studies also reported increases in tibia, fibula, and foot fractures in crashes involving KBABs [4,5]. For Weaver *et al.* (2013), these increases were significant and specifically affected the proximal tibia, proximal fibula, foot, and ankle. In the current study, the tibia index for the HIII reported an increase in injury risk at the lower tibia for the KBAB/SWAB condition. The RTI metric for the THOR-M produced little difference in injury risk prediction across conditions. However, the upper tibia exhibited a decrease in injury risk for the KBAB/SWAB condition for both ATDs using these same metrics. This discrepancy between upper and lower tibia injury prediction was likely a result of the AP bending moment, which decreased at the upper tibia for the KBAB/SWAB condition and

did not vary between conditions for at the lower tibia. Lending support to this theory, the THOR-M's tibia axial force injury metric predicted an increased injury risk for the KBAB/SWAB condition at both the upper and lower tibia. The trends in injury risk observed in this study provide some support to the findings of the real-world crash studies. The injury risk results also indicate that axial force through the shank, possibly from the KBAB pinning the shank between itself and the foot pedals, is likely causing the tibia and fibula fractures observed in the literature. It should be noted that the differences in injury risk observed in this study were small. It is possible that more injurious conditions could increase or decrease the differences in injury risk.

Based off of the results of the real-world crash studies and calculated lower extremity injury risks, KBABs may decrease the risk of femur injuries, but may also increase the risk of tibia, fibula, foot, and ankle injuries. Despite having similar AIS scores, these injuries have different prognoses that may render the inclusion of KBABs unfavorable in terms of injury outcome. For example, tibia shaft fractures have a higher rate of non-union than femur shaft fractures [20]. Additionally, previous research has shown that occupants who experienced foot and ankle fractures during MVCs had higher costs of hospitalization and rehabilitation, higher rates of rehospitalization within one year of injury, and decreased functional capacity up to one year after injury compared to occupants who sustained lower extremity injuries that did not involve the foot or ankle [21]. Consequently, sustaining femur shaft fractures from a KB may result in better injury outcomes than sustaining tibia, foot, and ankle injuries from a KBAB. However, the impact of KBABs on the injury risks of other body regions, e.g., the thorax, must also be considered when evaluating the influence of KBABs on occupant injury risk.

A major limitation of this study was the calibration procedure used to convert the bone cell output to lower extremity forces and moments. The lower extremity manipulations and loading used to gather calibration data were performed on the whole PMHS before each sled test and were not as controlled as a normal calibration procedure for a load cell, which could result in inaccurate calibrations. Furthermore, potential cross-talk between the axial and bending bone cells was not compensated. It is known that the natural curvature of the tibia can produce a bending moment when the bone is exposed to pure axial loading [12]. This could have influenced the calibration factor and, consequently, the measured PMHS femur and tibia loads, since the femur also has some

natural curvature. Future work will include performing a more controlled calibration on the PMHS tibiae and femora bone cells used in the sled tests to obtain a more accurate calibration factor and allow for cross-talk compensation. This calibration will then be applied to the PMHS data presented in this study so that the PMHS data can confidently be used to assess the biofidelity of the ATD lower extremity responses.

Finally, the results of this study were specific to the experimental conditions of the study. Changes to the sled pulse, surrogate positioning, sled buck geometry, restraint conditions, etc. could all result in different outcomes.

Conclusions

This study compared the lower extremity responses of the HIII, THOR-M, and PMHSs under three safety restraint conditions. PMHS lower extremity forces and moments were measured using arrays of strain gages. This study was able to validate the PMHS axial femur forces, but not the femur moments, tibia axial forces, or tibia moments. The ATDs generally experienced similar lower extremity forces and moments for a given test condition. The PMHS femur axial forces were similar to the ATDs, but slightly lower in magnitude for the KB conditions. The tibia axial force time histories were similar in shape to the ATDs, but were much lower in magnitude for all conditions. The PMHS AP bending moments showed more variability in peak timing and magnitude so trends were difficult to observe. The use of a KBAB decreased femur forces and increased tibia forces for the ATDs, but affected the tibia moments differently depending on the surrogate and location on the tibia. The predicted ATD lower extremity injury risks partially supported the findings of real-world crash analyses: KBABs decreased the risk of femur injury. However, the effect of KBABs on tibia injury prediction varied with surrogate, injury metric, and location on the tibia. Future work will perform a more controlled calibration on the PMHS bone cells so that the ATD lower extremity responses can be assessed using validated PMHS data.

References

1. Kuppa S, Wang J, Haffner M, Eppinger R. Lower Extremity Injuries and Associated Injury Criteria. Paper presented at: 17th International Technical Conference on the Enhanced Safety of Vehicles2001.
2. Austin RA. *Lower Extremitty Injuries and Intrusion in Frontal Crashes.* Washington, DC: NHTSA; March 2012 2012.
3. Roychoudhury RS, Conlee JK, Best M, Schenck D. *Blow-Molded Plastic Active Knee Bolsters.* SAE Technical Paper;2004. 0148-7191.
4. Weaver AA, Loftis KL, Stitzel JD. Investigation of the Safety Effects of Knee Bolster Air Bag Deployment in Similar Real-World Crash Comparisons. *Traffic injury prevention.* 2013;14(2):168-180.
5. Patel V, Griffin R, Eberhardt AW, McGwin G. The Association between Knee Airbag Deployment and Knee–Thigh–Hip Fracture Injury Risk in Motor Vehicle Collisions: A Matched Cohort Study. *Accident Analysis & Prevention.* 2013;50:964-967.
6. Kitagawa Y, Hasegawa J, Yasuki T, Iwamoto M, Miki K. A Study of Knee Joint Kinematics and Mechanics Using a Human Fe Model. *Stapp car crash journal.* 2005;49:117.
7. Nie B, Crandall JR, Panzer MB. Computational Investigation of the Effects of Knee Airbag Design on the Interaction with Occupant Lower Extremity in Frontal and Oblique Impacts. *Traffic injury prevention.* 2016;18(2):207-215.
8. Danelson KA, Golman AJ, Kemper AR, Gayzik FS, Gabler HC, Duma SM, Stitzel JD. Finite Element Comparison of Human and Hybrid Iii Responses in a Frontal Impact. *Accident Analysis & Prevention.* 2015;85:125-156.
9. Cheng R, Yang K-H, Levine RS, King AI. *Dynamic Impact Loading of the Femur under Passive Restrained Condition.* SAE Technical Paper;1984. 0148-7191.
10. Dean-El I, Boyse D, Hariharan P, Kargus R, Atkinson P, Anseth S, Rill B, Jain R, Safley C. *Implantation Design Guidelines for Instrumenting the Cadaveric Lower Extremity to Transduce Femur Loads and Tibial Forces and Moments.* SAE Technical Paper;2003. 0148-7191.

11. Donnelly BR, Roberts DP. *Comparison of Cadaver and Hybrid Iii Dummy Response to Axial Impacts of the Femur*. SAE Technical Paper;1987. 0148-7191.
12. Funk JR, Rudd RW, Kerrigan JR, Crandall JR. The Effect of Tibial Curvature and Fibular Loading on the Tibia Index. *Traffic injury prevention.* 2004;5(2):164-172.
13. Funk JR, Rudd RW, Srinivasan SC, King RJ, Crandall JR, Petit PY. *Methodology for Measuring Tibial and Fibular Loads in a Cadaver*. SAE Technical Paper;2002. 0148-7191.
14. Danelson KA, Kemper AR, Mason MJ, Tegtmeyer M, Swiatkowski SA, Bolte IV JH, Hardy WN. *Comparison of Atd to Pmhs Response in the under-Body Blast Environment.* SAE Technical Paper;2015.
15. Janovicz D, Fischer B. *Final Report of New Car Assessment Program Frontal Impact Testing of 2012 Toyota Camry Lee 4-Dr Sedan.* Washington, DC: USDOT; December 16, 2011 2011.
16. Naik S. *Final Report of New Car Assessment Program Testing of a 2005 Toyota Camry Le*. Washington, DC: U.S. Department of Transportation,; March 11, 2005 2005.
17. NHTSA. *Laboratory Test Procedure for New Car Assessment Program (Ncap)- Frontal Impact Testing*. Washington, DC: U.S. Department of Transportation; 2012.
18. SAE. *Instrumentation for Impact Test.* Warrendale, PA: Society of Automotive Engineers;1995.
19. Mertz HJ. Anthropomorphic Test Devices. In: Nahum AM, Melvin JW, eds. *Accidental Injury: Biomechanics and Prevention*. New York: Springer-Verlag; 1993.
20. Tzioupis C, Giannoudis PV. Prevalence of Long-Bone Non-Unions. *Injury.* 2007;38:S3-S9.
21. Read KM, Kufera JA, Dischinger PC, Kerns TJ, Ho SM, Burgess AR, Burch CA. Life-Altering Outcomes after Lower Extremity Injury Sustained in Motor Vehicle Crashes. *Journal of Trauma and Acute Care Surgery.* 2004;57(4):815-823.

Appendix

Table A4.1: Surrogate movements associated with positive lower extremity forces and moments.

Load Cell Location	Data Channel	Surrogate Movement	Polarity
Femur	Fx	Knee upward, upper femur downward	Positive
	Fy	Knee rightward, upper femur leftward	Positive
	Fz	Knee forward, pelvis rearward	Positive
	Mx	Knee leftward, hold upper femur in place	Positive
	My	Knee upward, hold upper femur in place	Positive
	Mz	Tibia leftward, hold pelvis in place	Positive
Upper Tibia	Fx	Tibia forward, femur rearward	Positive
	Fy	Tibia downward, femur leftward	Positive
	Fz	Tibia downward, femur upward	Positive
	Mx	Ankle leftward, hold knee in place	Positive
	My	Ankle forward, bottom of knee rearward	Positive
Lower Tibia	Fx	Ankle forward, knee rearward	Positive
	Fy	Ankle downward, knee leftward	Positive
	Fz	Ankle downward, knee upward	Positive
	Mx	Ankle leftward, hold knee in place	Positive
	My	Ankle forward, bottom of knee rearward	Positive

Table A4.2: Reaction load cell polarities.

Load Cell Location	Data Channel	Surrogate Movement	Polarity
L/R Bolster Support	Fx	Compression	Positive
	Fy	Right	Positive
	Fz	Backward, up	Positive
	Mx	Left up, right down	Positive
	My	Top back, bottom forward	Positive
	Mz	Left down and back, right up and forward	Positive
L/R Foot Support	Fx	Compression	Positive
	My	Top up and back, bottom down and forward	Positive
	Mz	Left up and back, right down and forward	Positive

Table A4.3: Femur force to bolster force ratios for all tests at the times of maximum femur force and maximum bolster force.

Test	Max Femur Force		Max Bolster Force	
	Left	Right	Left	Right
HIII-KB-1	-0.57	-0.54	-0.55	-0.48
HIII-KB-2	-0.58	-0.58	-0.58	-0.52
HIII-KB/SWAB-1	-0.57	-0.53	-0.54	-0.50
HIII-KB/SWAB-2	-0.52	-0.47	-0.46	-0.44
HIII-KBAB/SWAB-1	-0.68	-0.66	-0.59	-0.63
HIII-KBAB/SWAB-2	-0.69	-0.61	-0.58	-0.61
THOR-KB-1	-0.66	-0.69	-0.36	-0.39
THOR-KB-2	-0.67	-0.63	-0.51	-0.39
THOR-KB/SWAB-1	-0.59	-0.62	-0.56	-0.41
THOR-KB/SWAB-2	-0.66	-0.66	-0.58	-0.42
THOR-KBAB/SWAB-1	-0.87	-0.81	-0.48	-0.53
THOR-KBAB/SWAB-2	-0.88	-0.80	-0.50	-0.57
PMHS-KB-1	-0.78	-50.12	-0.56	-0.59
PMHS-KB-2	-0.65		-0.56	
PMHS-KB/SWAB-1		-0.23		-0.20
PMHS-KB/SWAB-2	-0.55	-0.48	-0.51	-0.40
PMHS-KB/SWAB-3	-0.37		-0.29	
PMHS-KBAB/SWAB-1	-0.61	-0.84	-0.60	-0.74
PMHS-KBAB/SWAB-2	-0.86	-0.74	-0.65	-0.57
PMHS-KBAB/SWAB-3	-0.56	-0.94	-0.55	-0.63

Table A4.4: Tibia force to foot support force ratios for all tests at the times of maximum tibia force and maximum foot support force.

Test	Max Femur Force		Max Bolster Force	
	Left	Right	Left	Right
HIII-KB-1	0.80	0.67	0.67	0.65
HIII-KB-2	0.83	0.78	0.80	0.61
HIII-KB/SWAB-1	0.73	0.66	0.66	0.59
HIII-KB/SWAB-2	0.78	0.66	0.65	0.63
HIII-KBAB/SWAB-1	0.81	0.78	0.81	0.77
HIII-KBAB/SWAB-2	0.81	0.79	0.81	0.76
THOR-KB-1	0.94	0.88	0.84	0.84
THOR-KB-2	1.35	0.90	0.84	0.84
THOR-KB/SWAB-1	0.90	0.93	0.84	0.87
THOR-KB/SWAB-2	1.36	0.91	0.85	0.86
THOR-KBAB/SWAB-1	0.94	0.90	0.87	0.82
THOR-KBAB/SWAB-2	0.92	0.86	0.85	0.82
PMHS-KB-1	0.68	0.48	0.21	0.35
PMHS-KB-2	0.71		0.58	
PMHS-KB/SWAB-1	0.17	0.44	0.09	0.42
PMHS-KB/SWAB-2	1.14	0.44	0.72	0.43
PMHS-KB/SWAB-3	0.77	0.57	0.36	0.22
PMHS-KBAB/SWAB-1	1.00	0.65	0.46	0.62
PMHS-KBAB/SWAB-2	0.05	0.40	0.03	0.37
PMHS-KBAB/SWAB-3	0.20	0.37	0.20	0.30

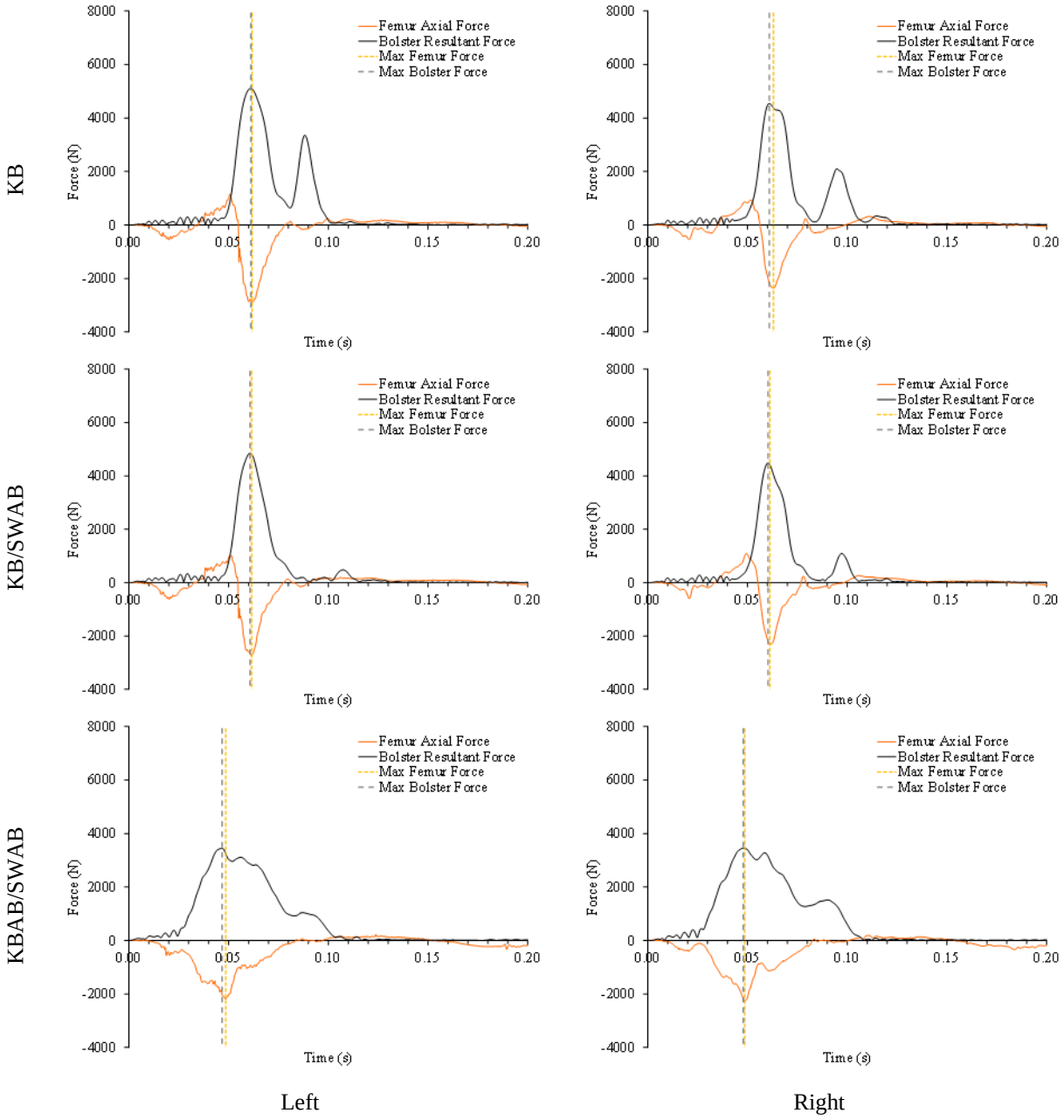

Figure A4.1: Exemplar HIII femur axial force (Fz) and bolster resultant force (Fx, Fz) timing comparisons for each condition.
Note: Axial femur tension is positive.

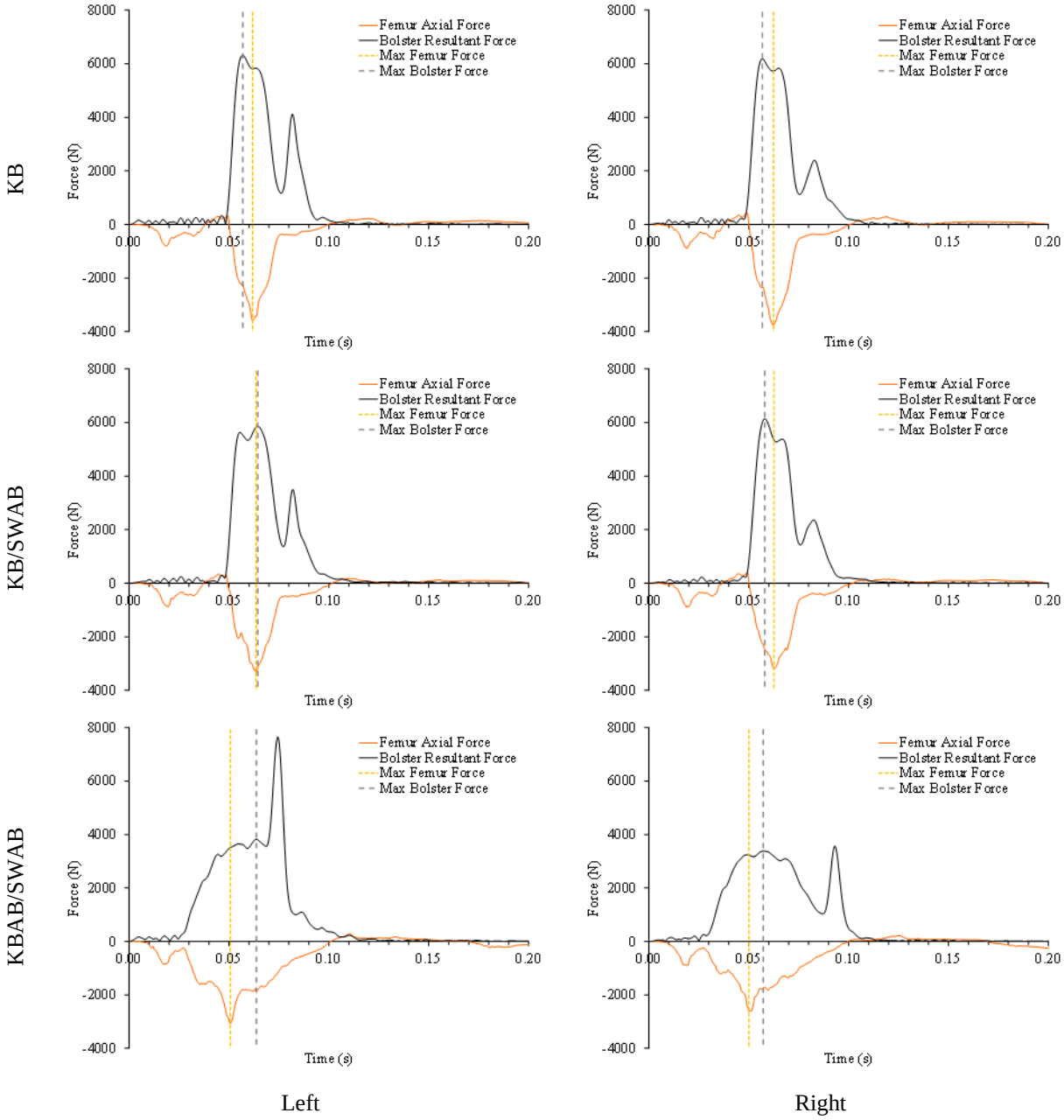

Figure A4.2: Exemplar THOR-M femur axial force (Fz) and bolster resultant force (Fx, Fz) timing comparisons for each condition.
Note: Axial femur tension is positive.

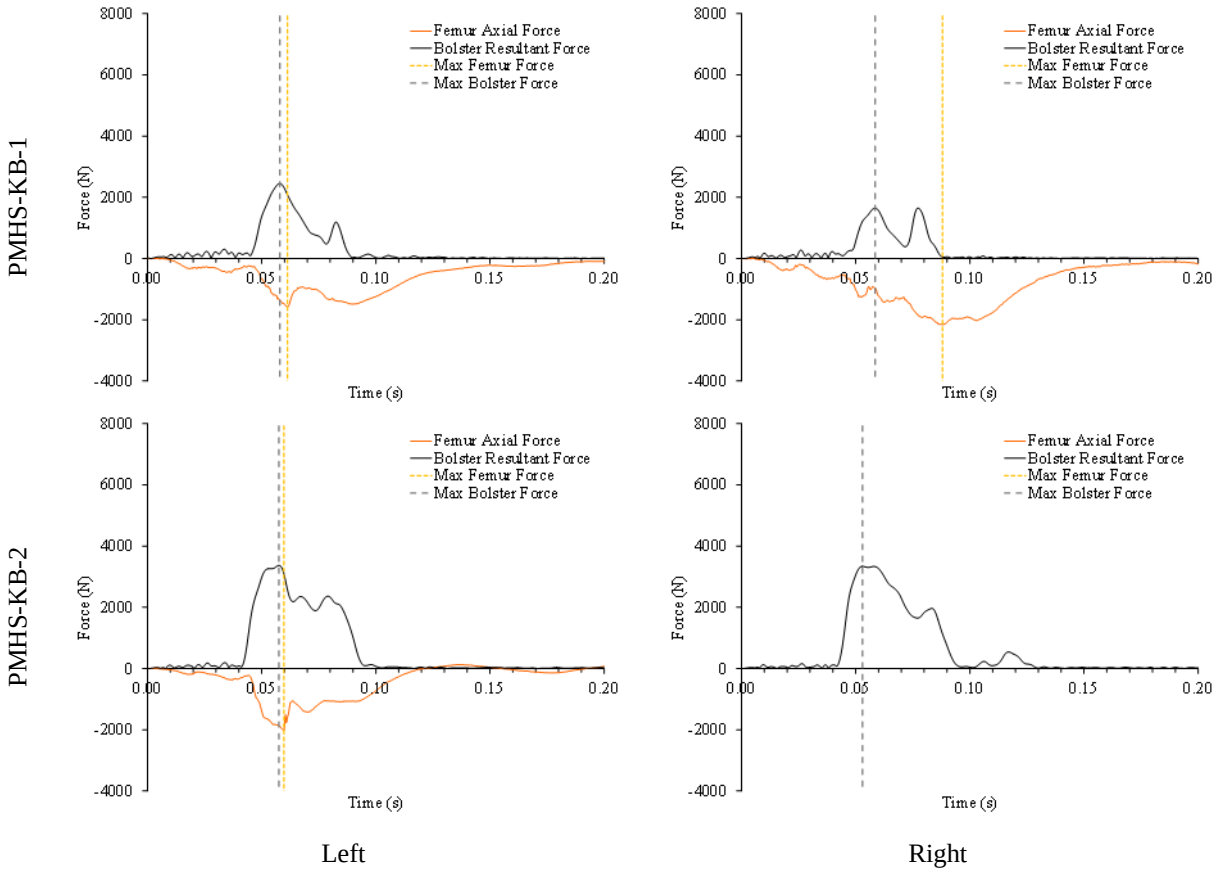

Figure A4.3: PMHS femur axial force (Fz) and bolster resultant force (Fx, Fz) timing comparisons for each KB test.
Note: Axial femur tension is positive.

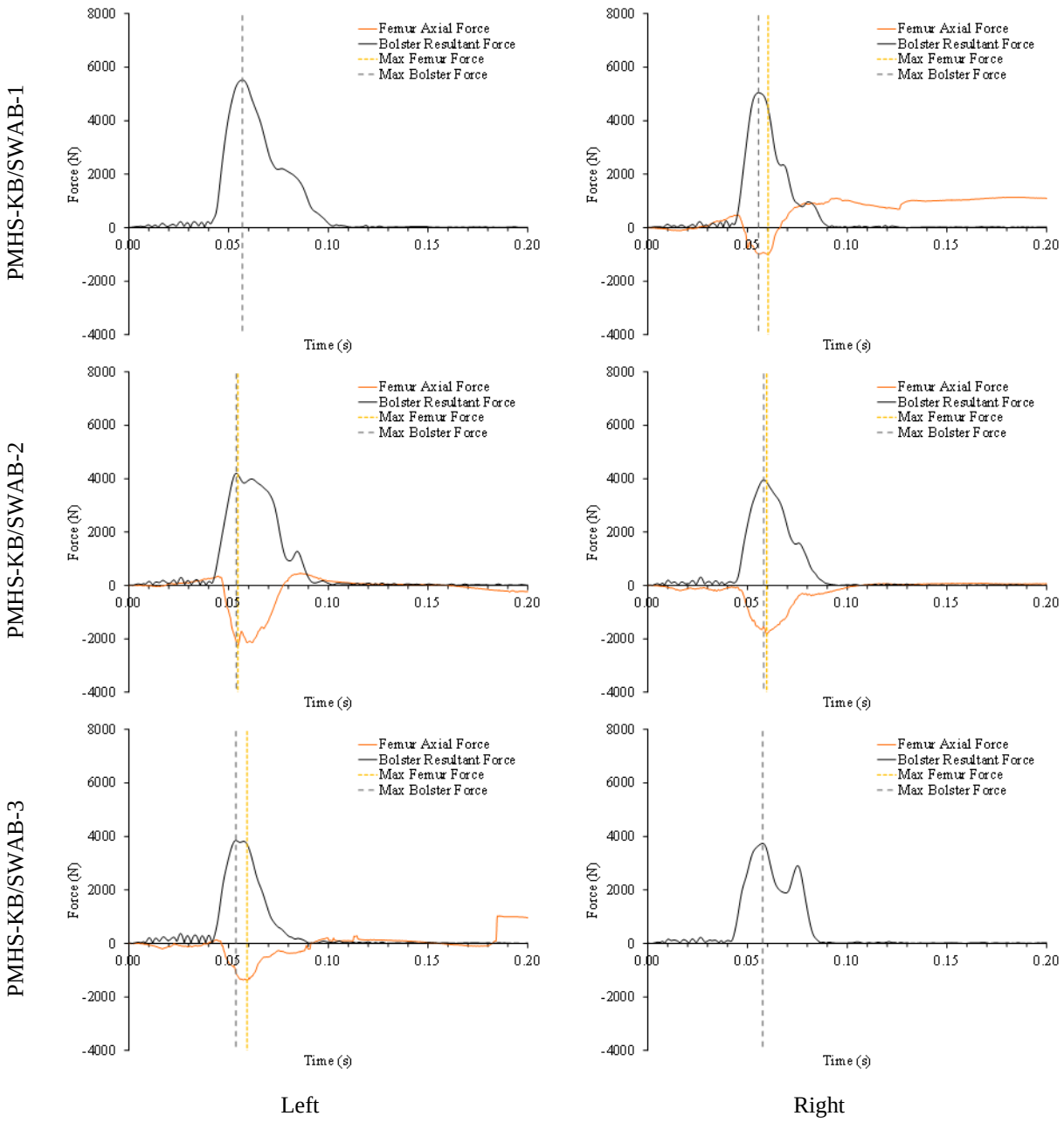

Figure A4.4: PMHS femur axial force (Fz) and bolster resultant force (Fx, Fz) timing comparisons for each KB/SWAB test.
Note: Axial femur tension is positive.

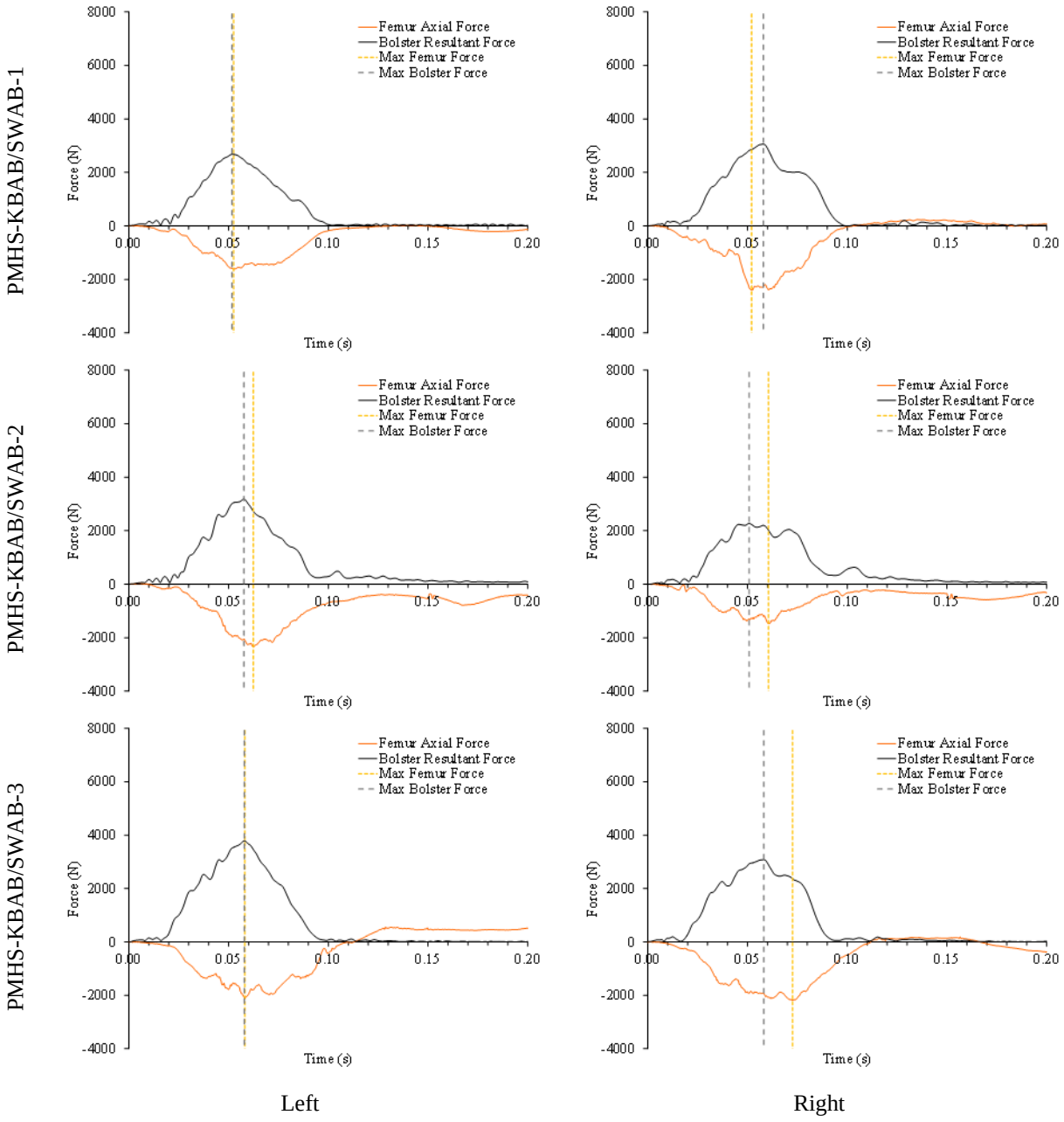

Figure A4.5: PMHS femur axial force (Fz) and bolster resultant force (Fx, Fz) timing comparisons for each KBAB/SWAB test.
Note: Axial femur tension is positive.

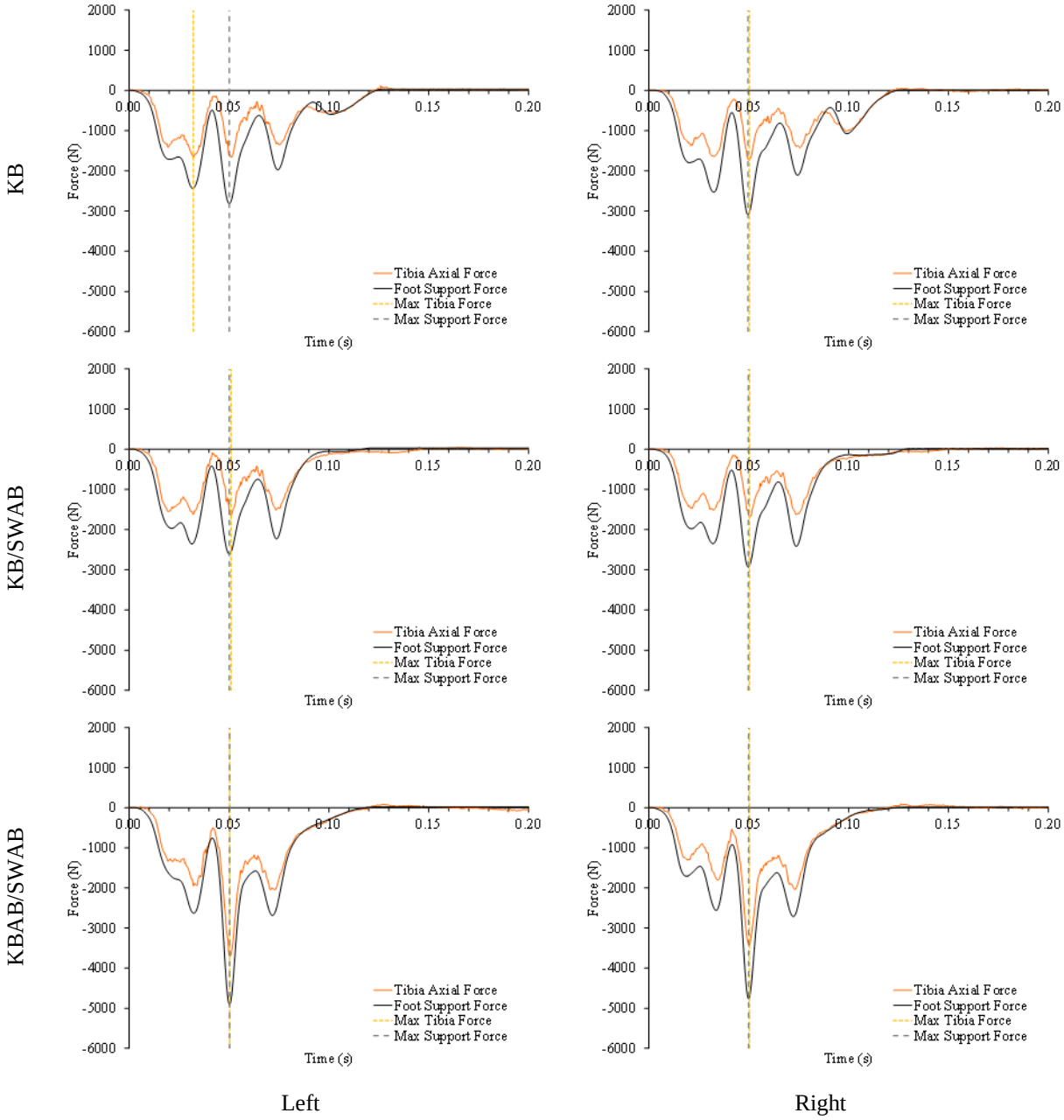

Figure A4.6: Exemplar HIII tibia axial force (Fz) and foot support force timing comparisons for each condition.
Note: Axial tibia tension is positive and foot support tension is positive.

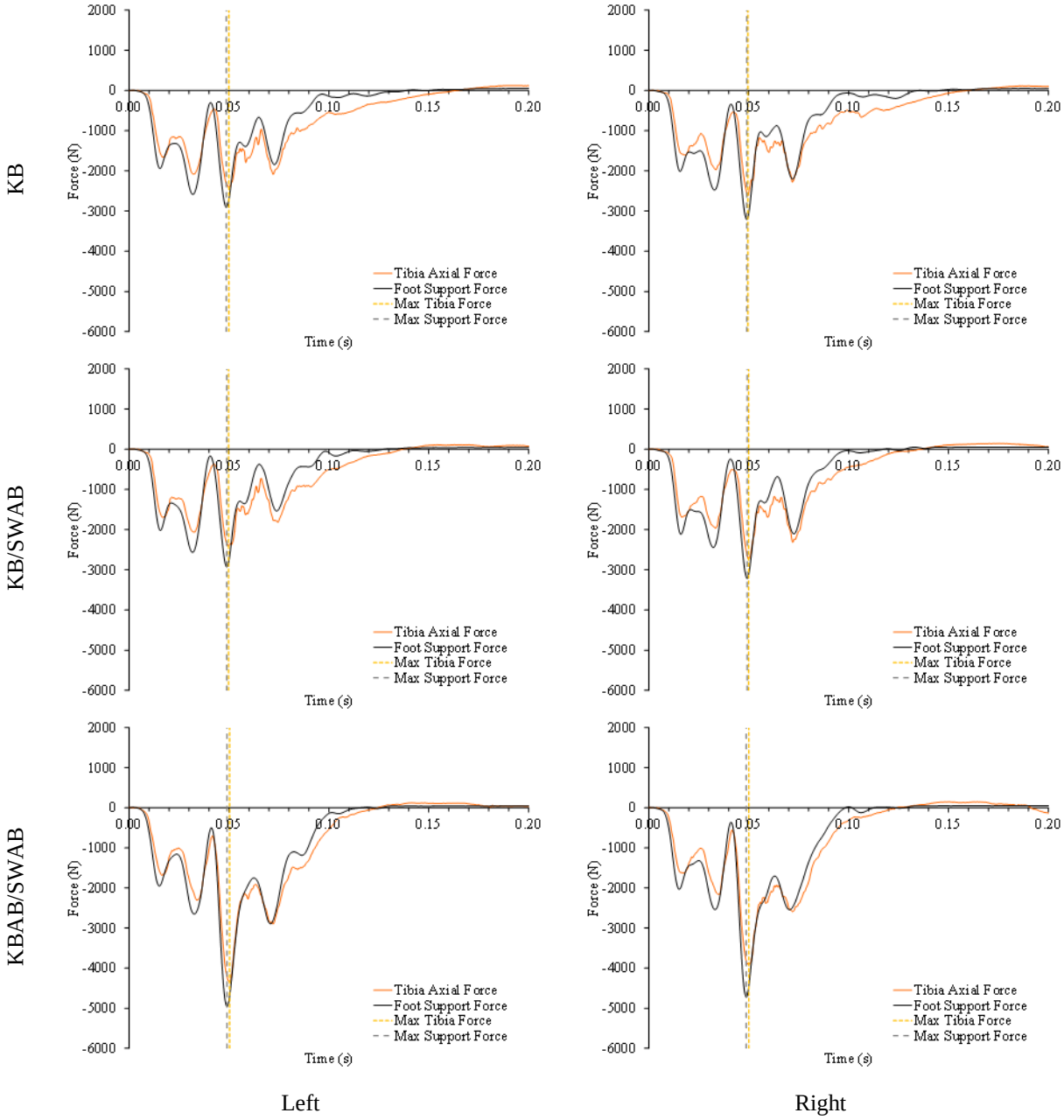

Figure A4.7: Exemplar THOR-M tibia axial force (Fz) and foot support force timing comparisons for each condition.
Note: Axial tibia tension is positive and foot support tension is positive.

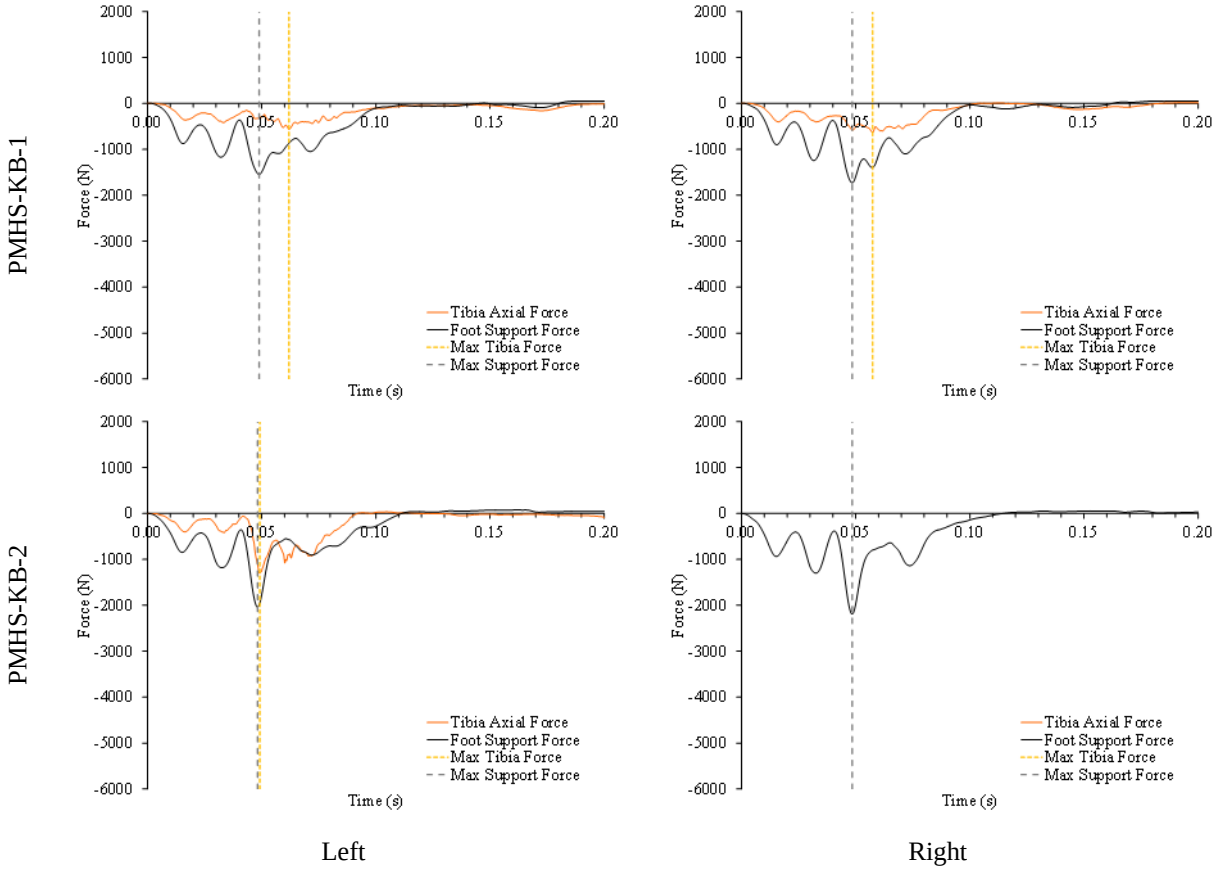

Figure A4.8: PMHS tibia axial force (Fz) and foot support force timing comparisons for each KB test.
Note: Axial tibia tension is positive and foot support tension is positive.

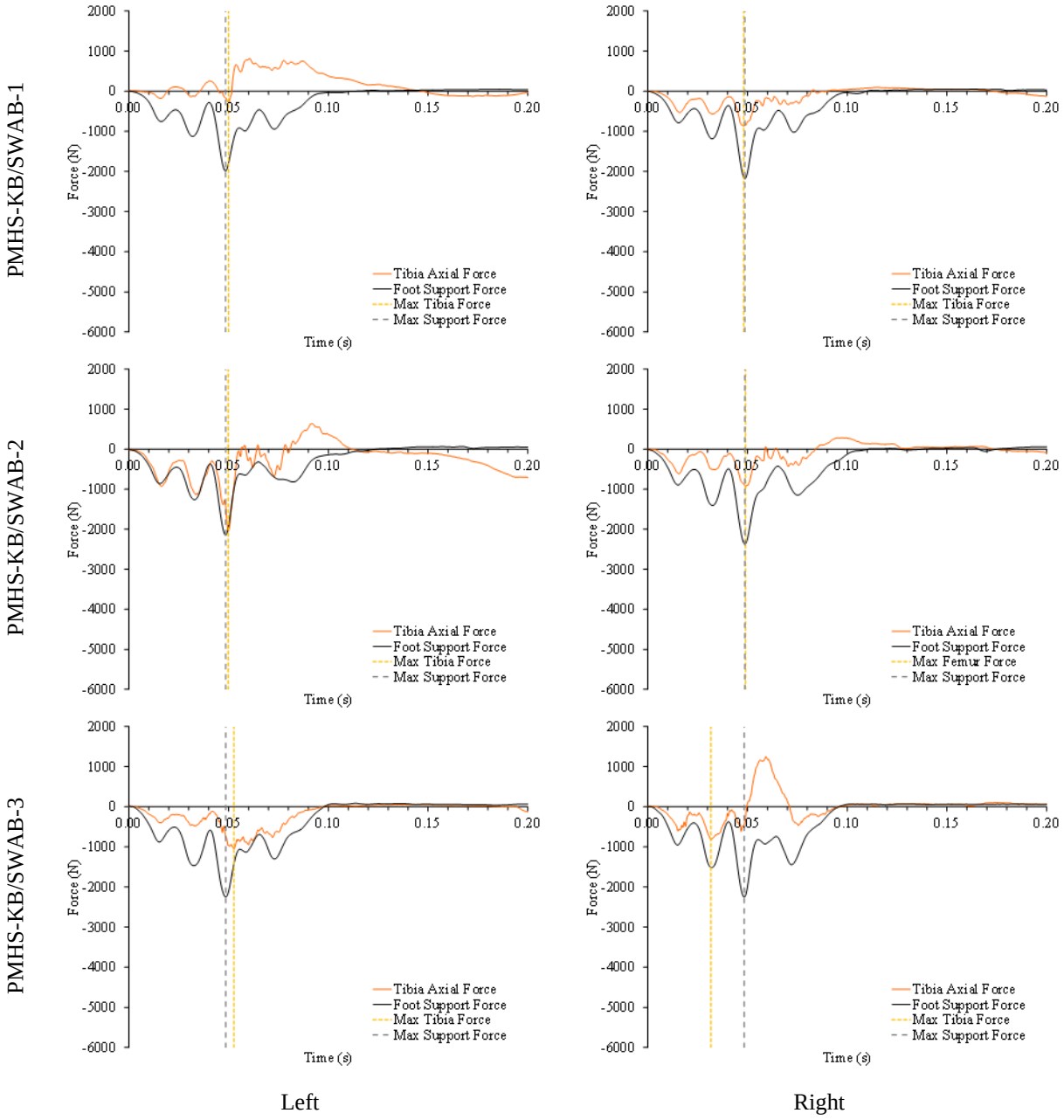

Figure A4.9: PMHS tibia axial force (Fz) and foot support force timing comparisons for each KB/SWAB test.
Note: Axial tibia tension is positive and foot support tension is positive.

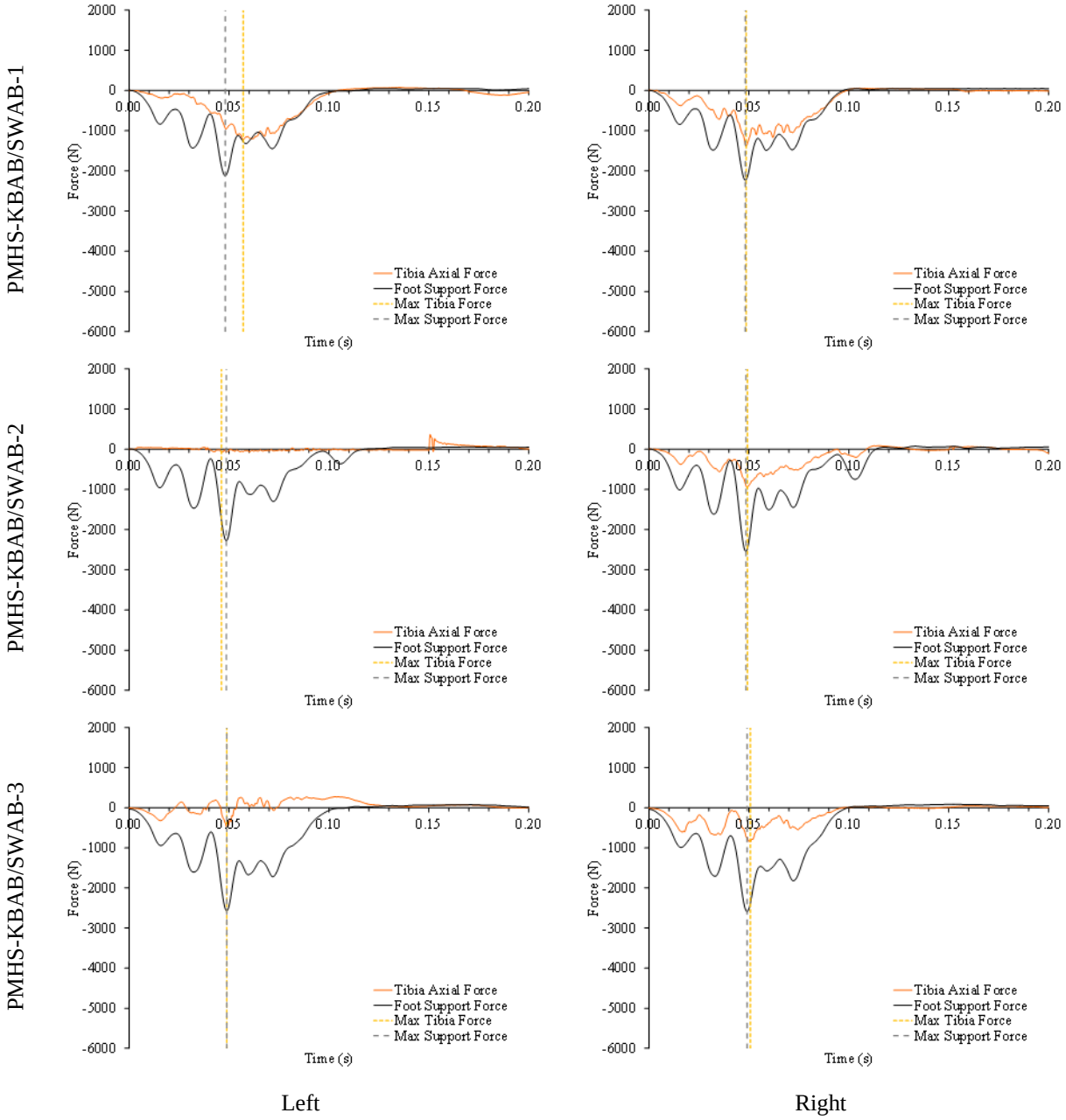

Figure A4.10: PMHS tibia axial force (Fz) and foot support force timing comparisons for each KBAB/SWAB test.
Note: Axial tibia tension is positive and foot support tension is positive.

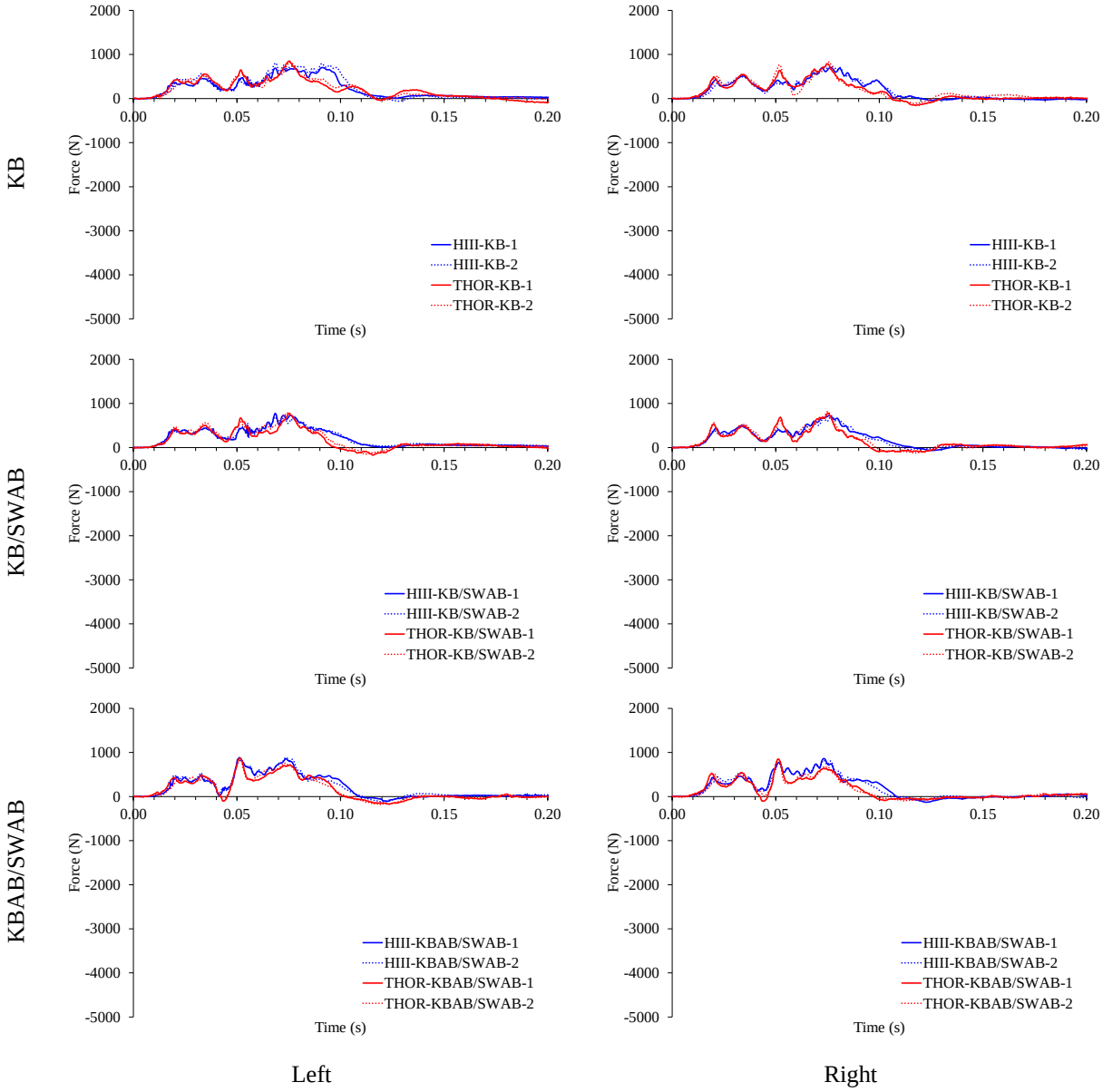

Figure A4.11: Femur AP shear forces (Fx) for the HIII and THOR-M for all conditions. Note Upward knee movement and downward upper femur movement are positive.

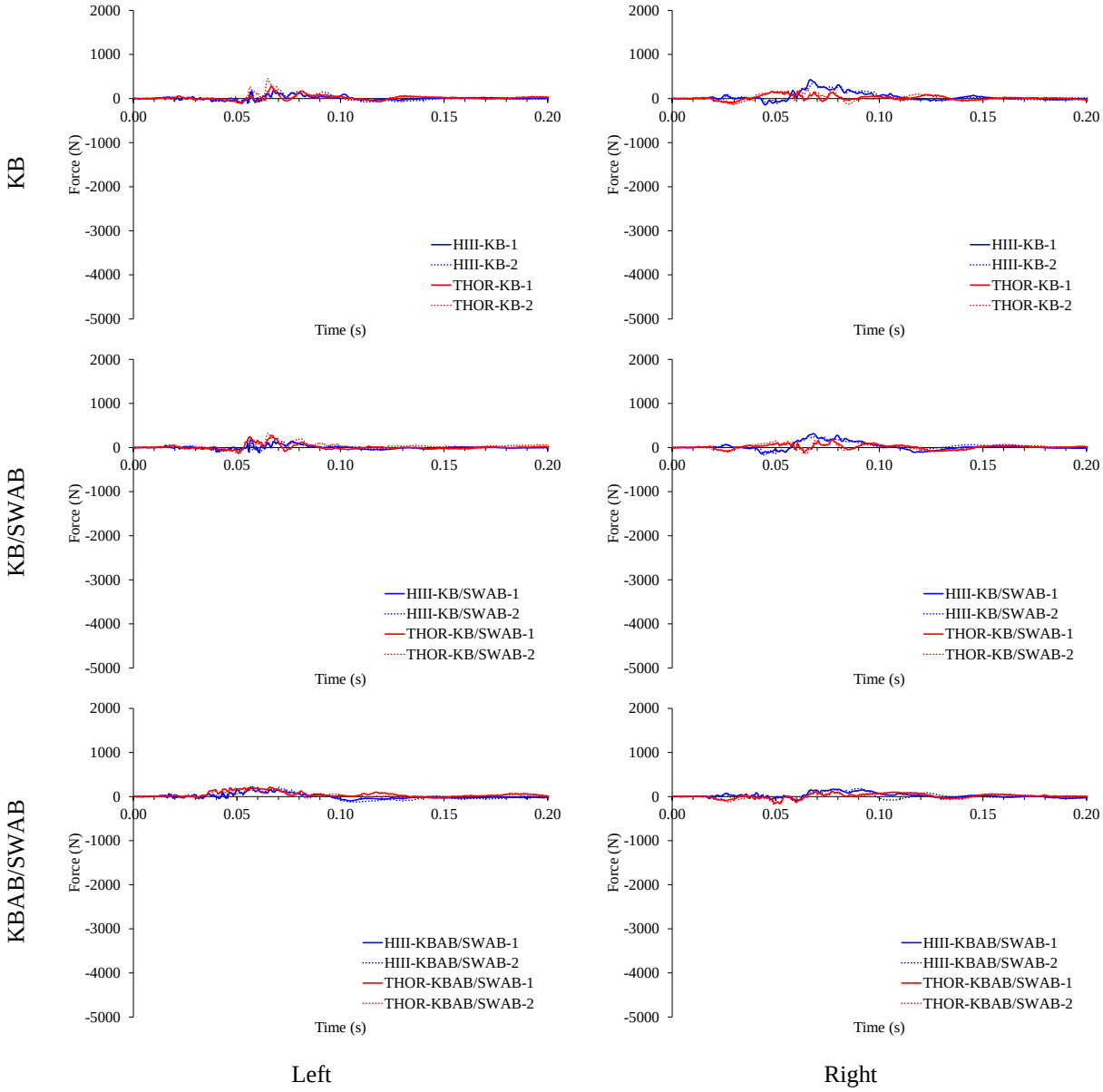

Figure A4.12: Femur ML shear forces (Fy) for the HIII and THOR-M for all conditions. Note: Rightward knee movement and leftward upper femur movement are positive.

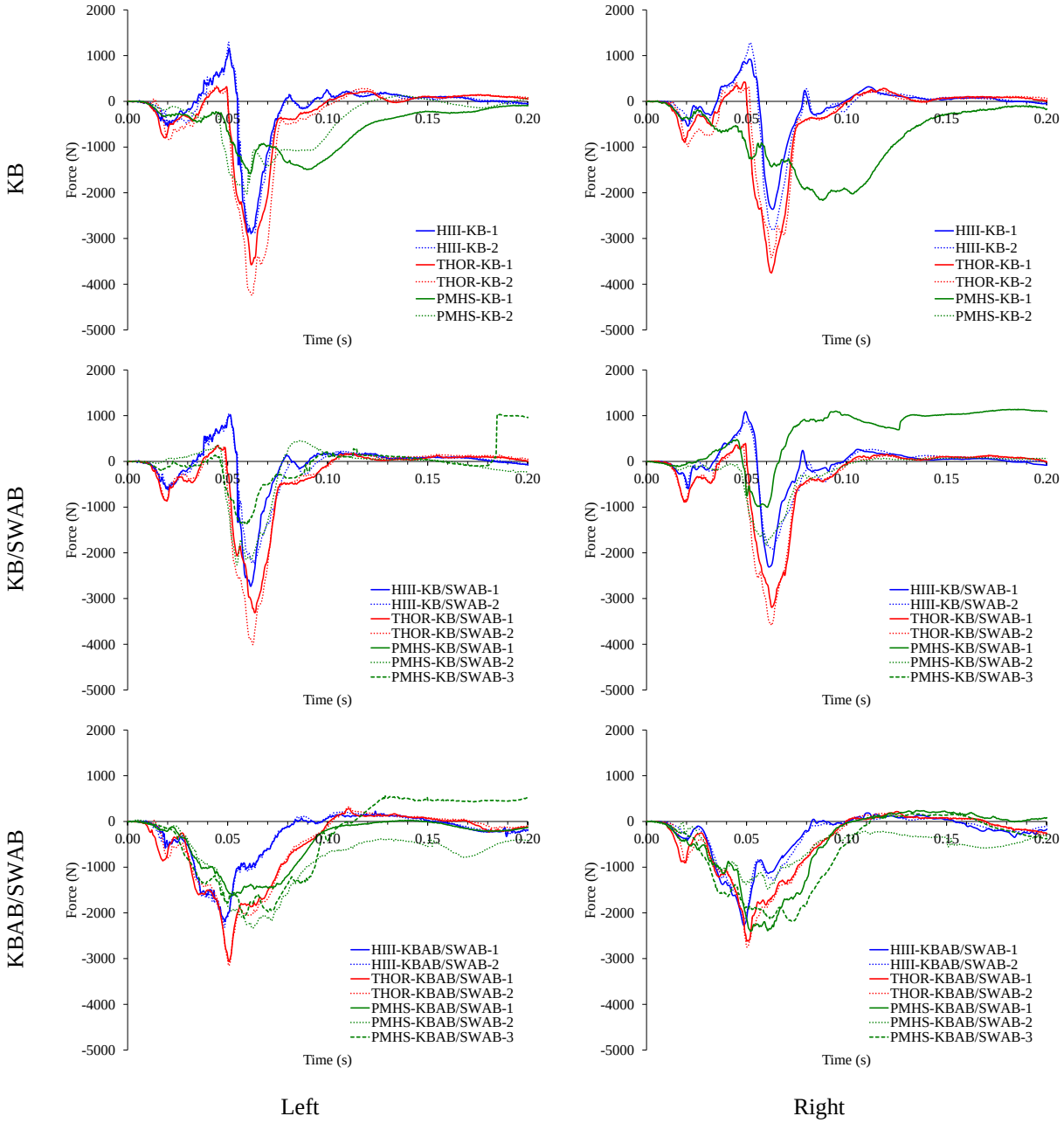

Figure A4.13: Femur axial forces (Fz) for all surrogates and conditions.
Note: Forward knee movement and rearward pelvis movement are positive.

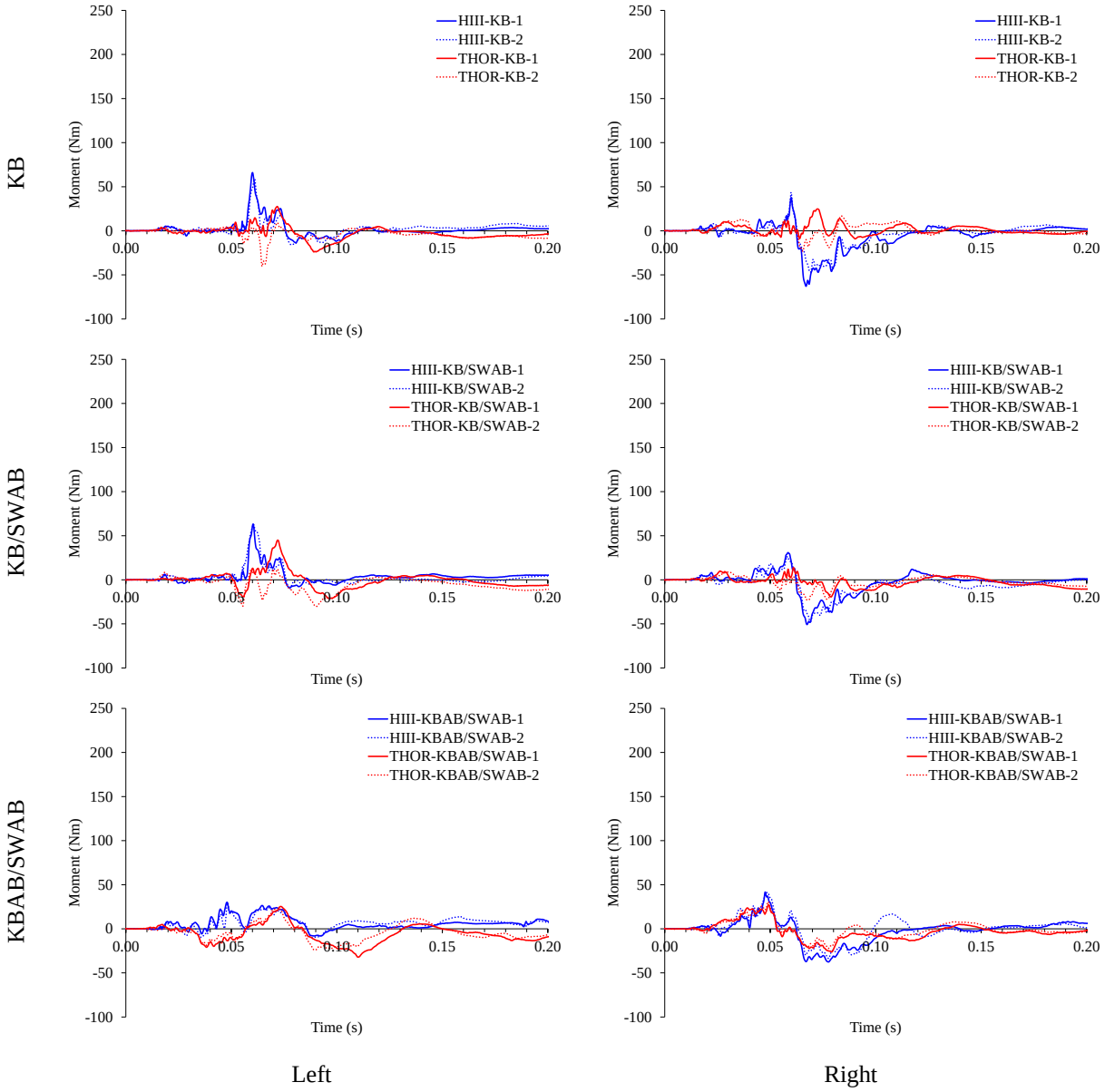

Figure A4.14: Femur moments about the x-axis (Mx) for the HIII and THOR-M for all conditions.
Note: Leftward knee movement relative to the upper femur is positive.

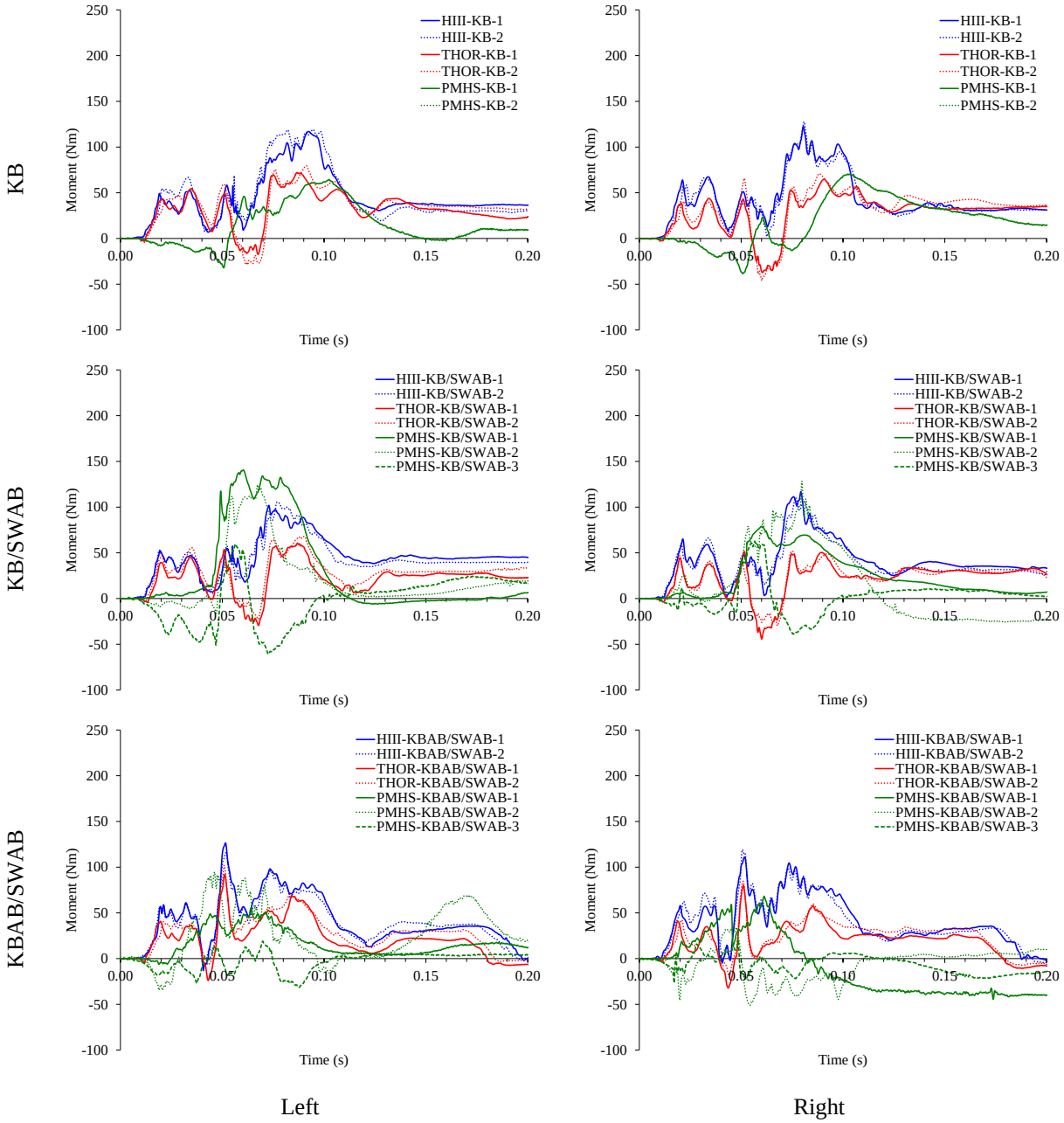

Figure A4.15: Femur AP bending moments (My) for all surrogates and conditions. Note: Upward knee movement relative to the upper femur is positive.

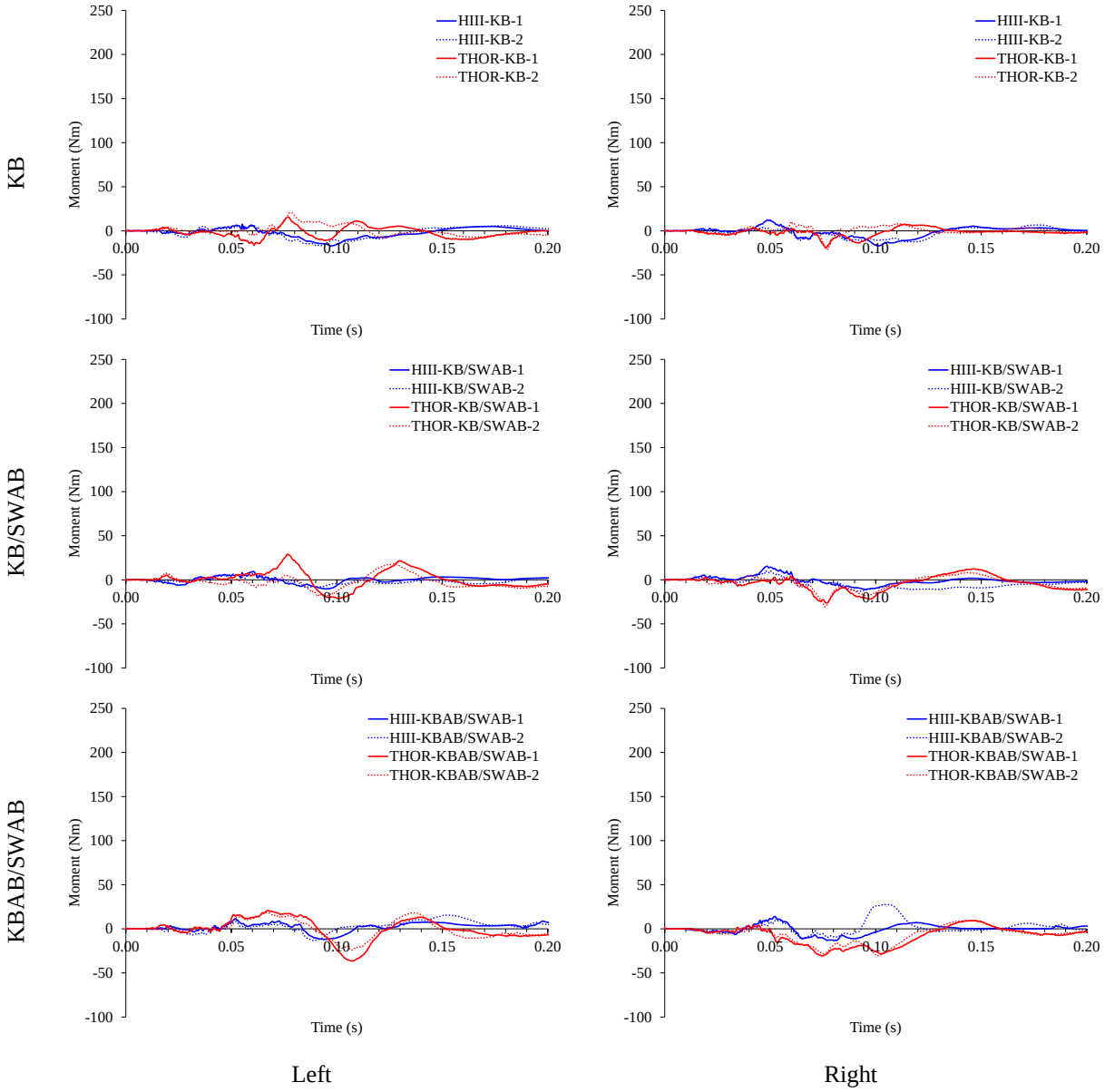

Figure A4.16: Femur moments about the z-axis (Mz) for the HIII and THOR-M for all conditions.
Note: Leftward tibia movement relative to the pelvis is positive.

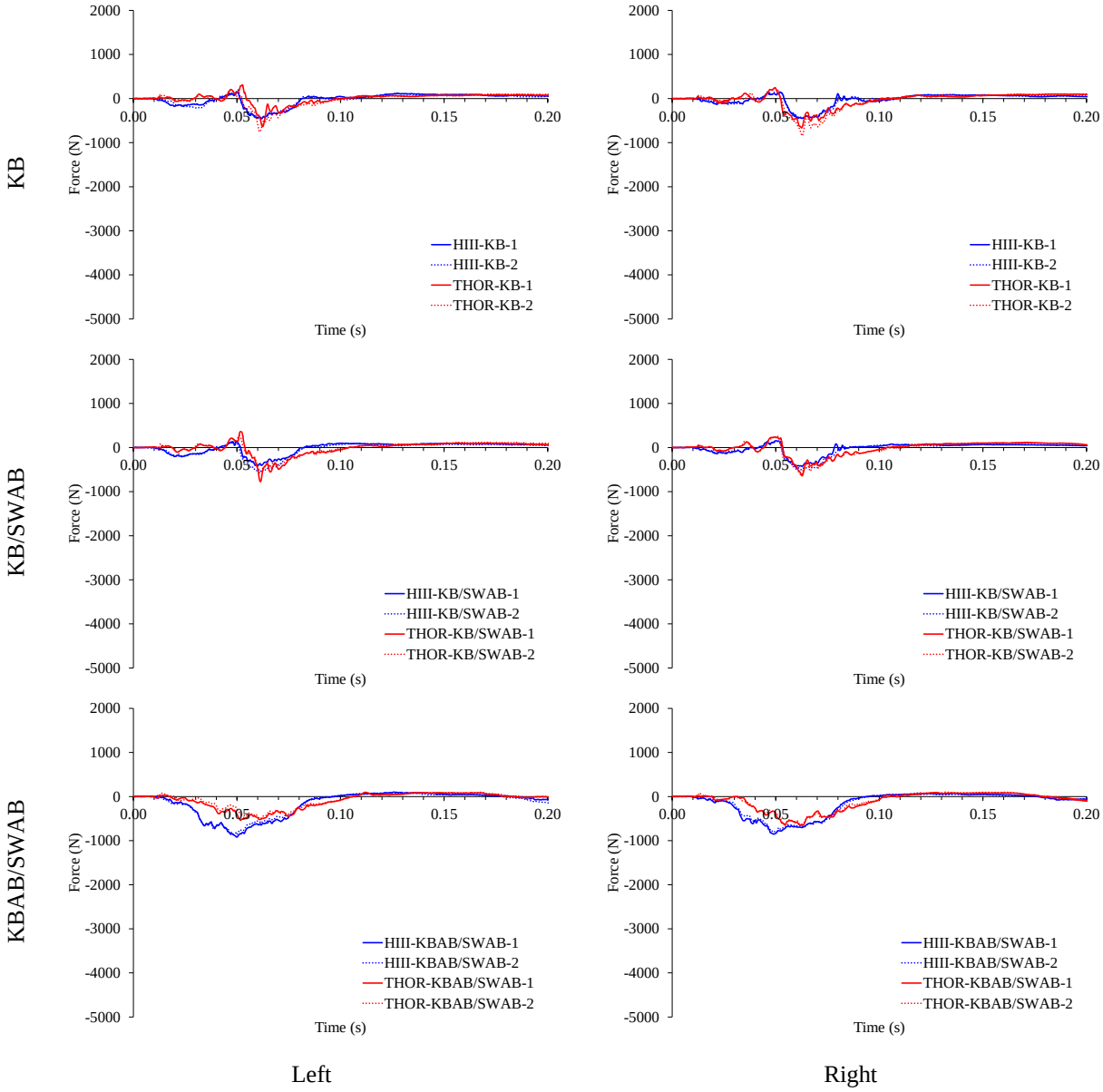

Figure A4.17: Upper tibia AP shear forces (Fx) for the HIII and THOR-M for all conditions. Note: Forward tibia movement and rearward femur movement are positive.

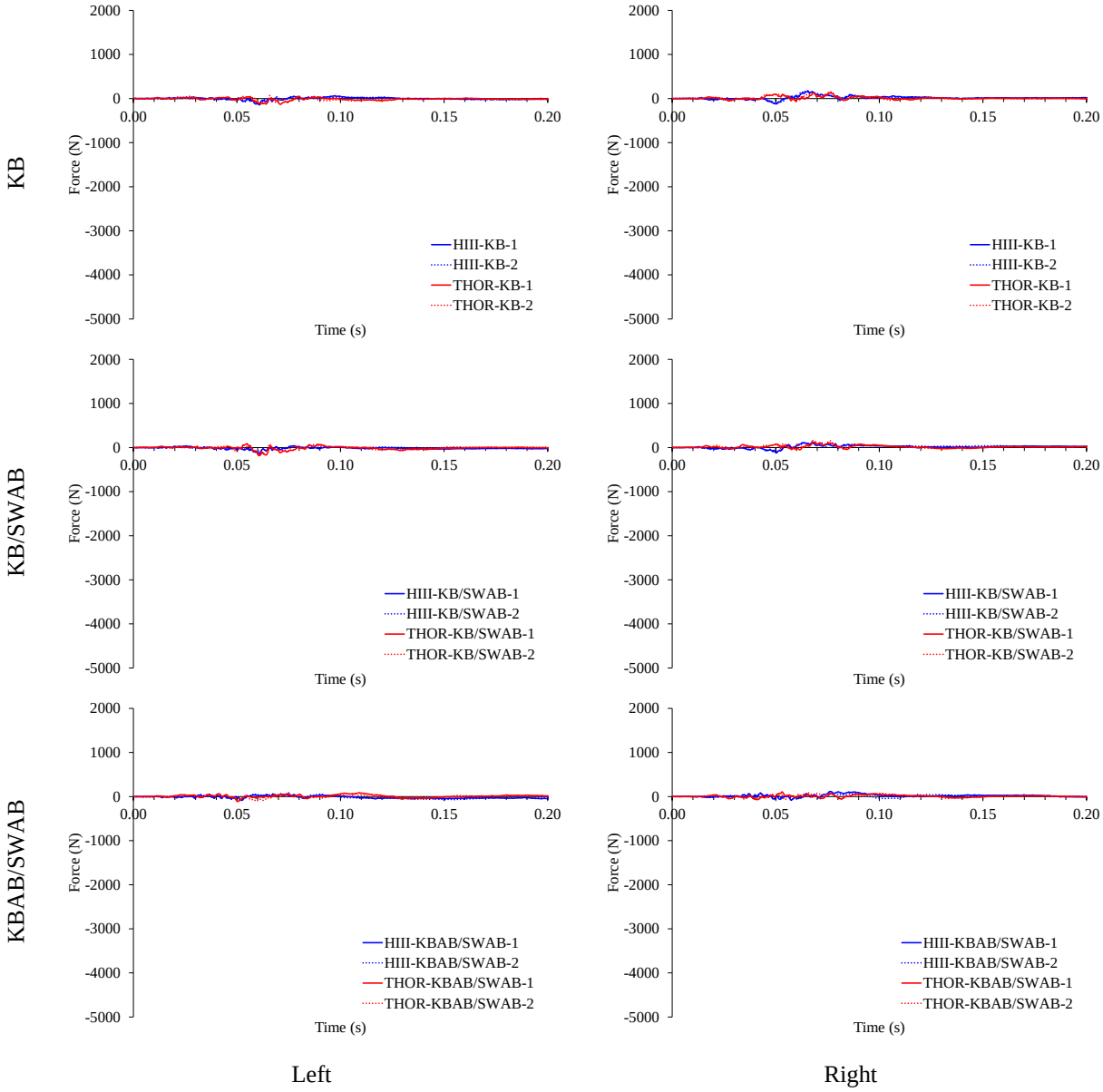

Figure A4.18: Upper tibia ML shear forces (Fy) for the HIII and THOR-M for all conditions. Note: Downward tibia movement and leftward femur movement are positive.

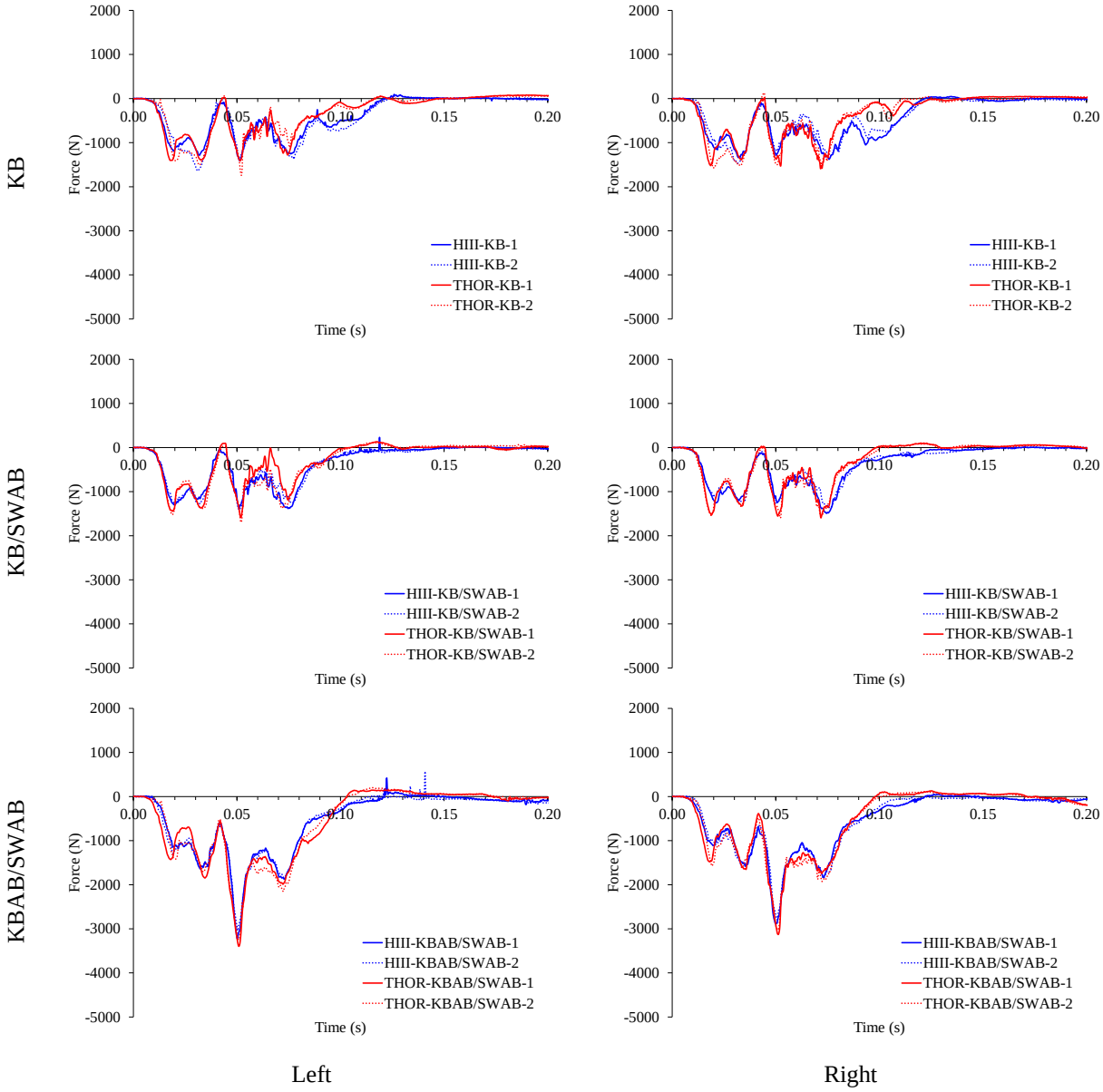

Figure A4.19: Upper tibia axial forces (Fz) for the HIII and THOR-M for all conditions. Note: Downward tibia movement and upward femur movement are positive.

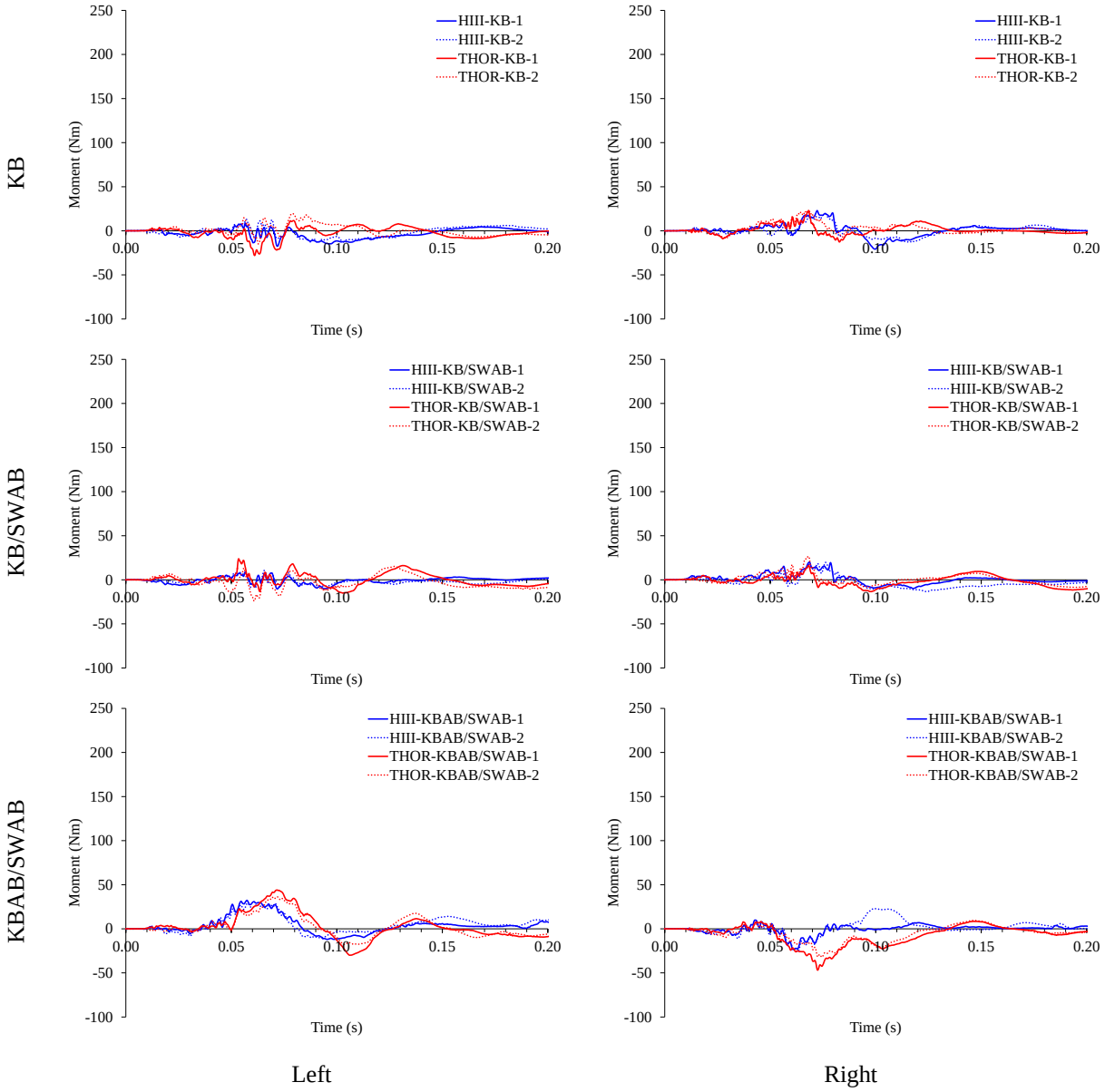

Figure A4.20: Upper tibia moments about the x-axis (Mx) for the HIII and THOR-M for all conditions.
Note: Leftward ankle movement relative to the knee is positive.

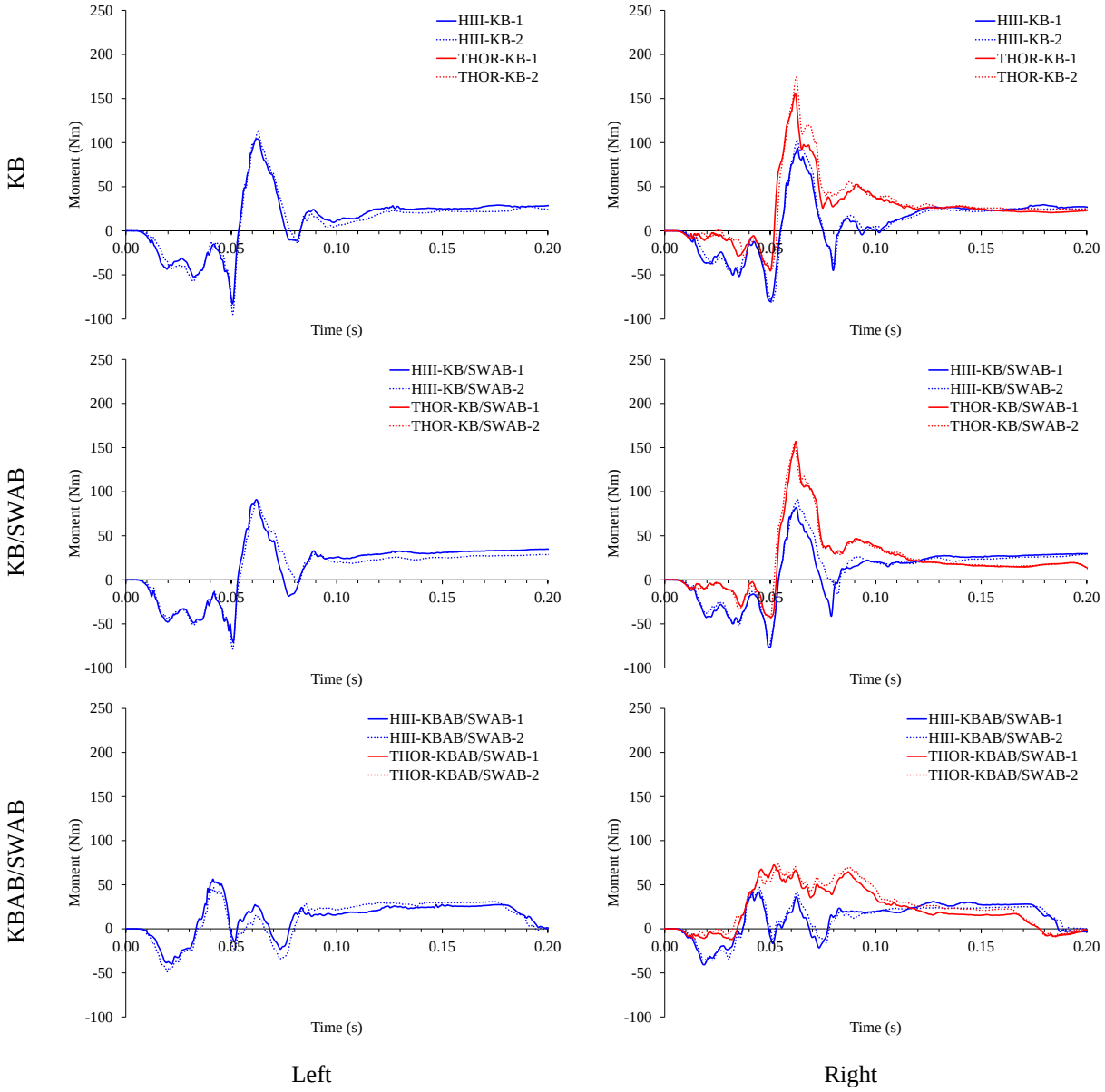

Figure A4.21: Upper tibia AP bending moments (My) for the HIII and THOR-M for all conditions.
Note: Forward ankle movement and rearward knee movement are positive.

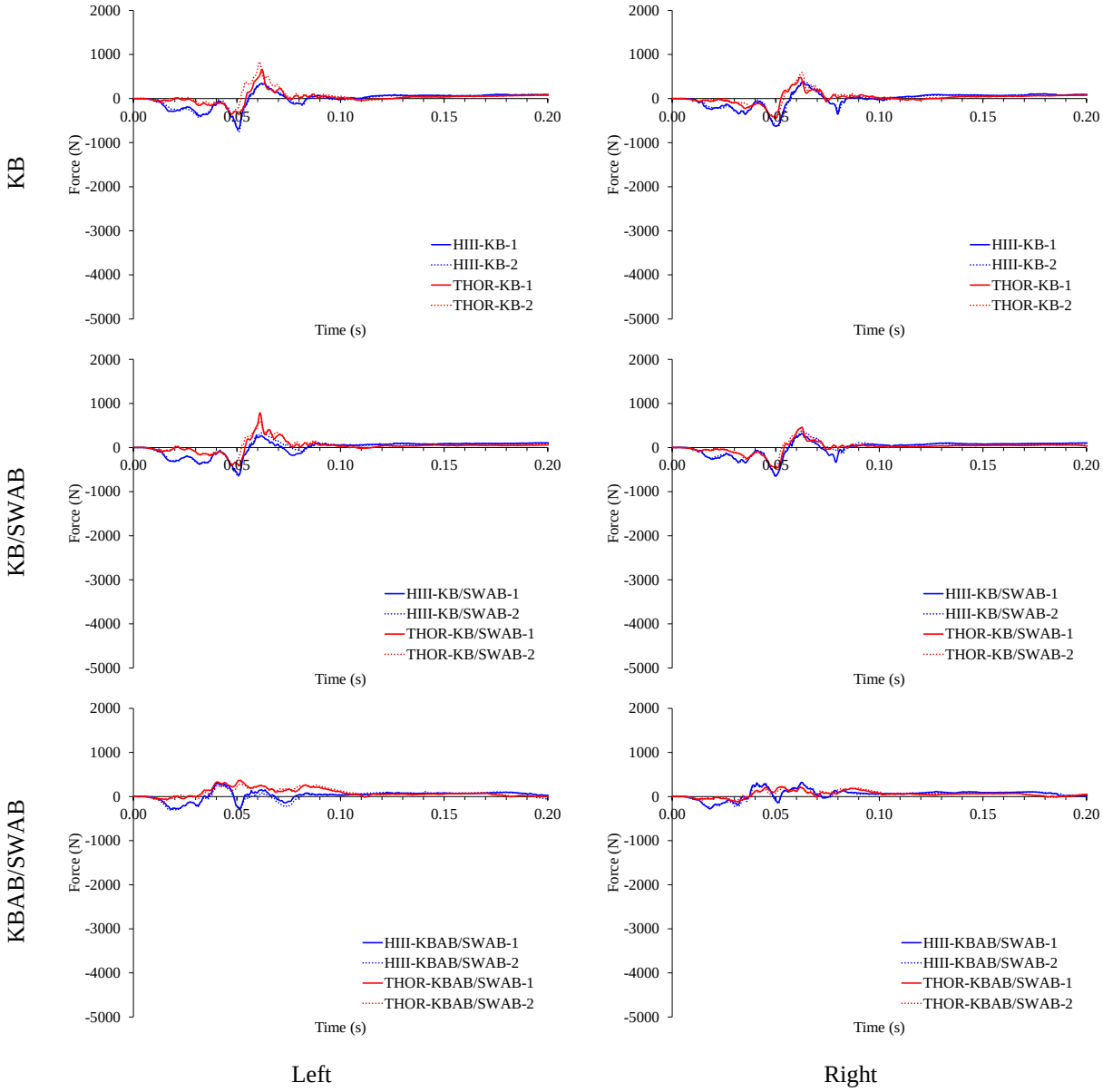

Figure A4.22: Lower tibia AP shear forces (Fx) for the HIII and THOR-M for all conditions. Note: Forward ankle movement and rearward knee movement are positive.

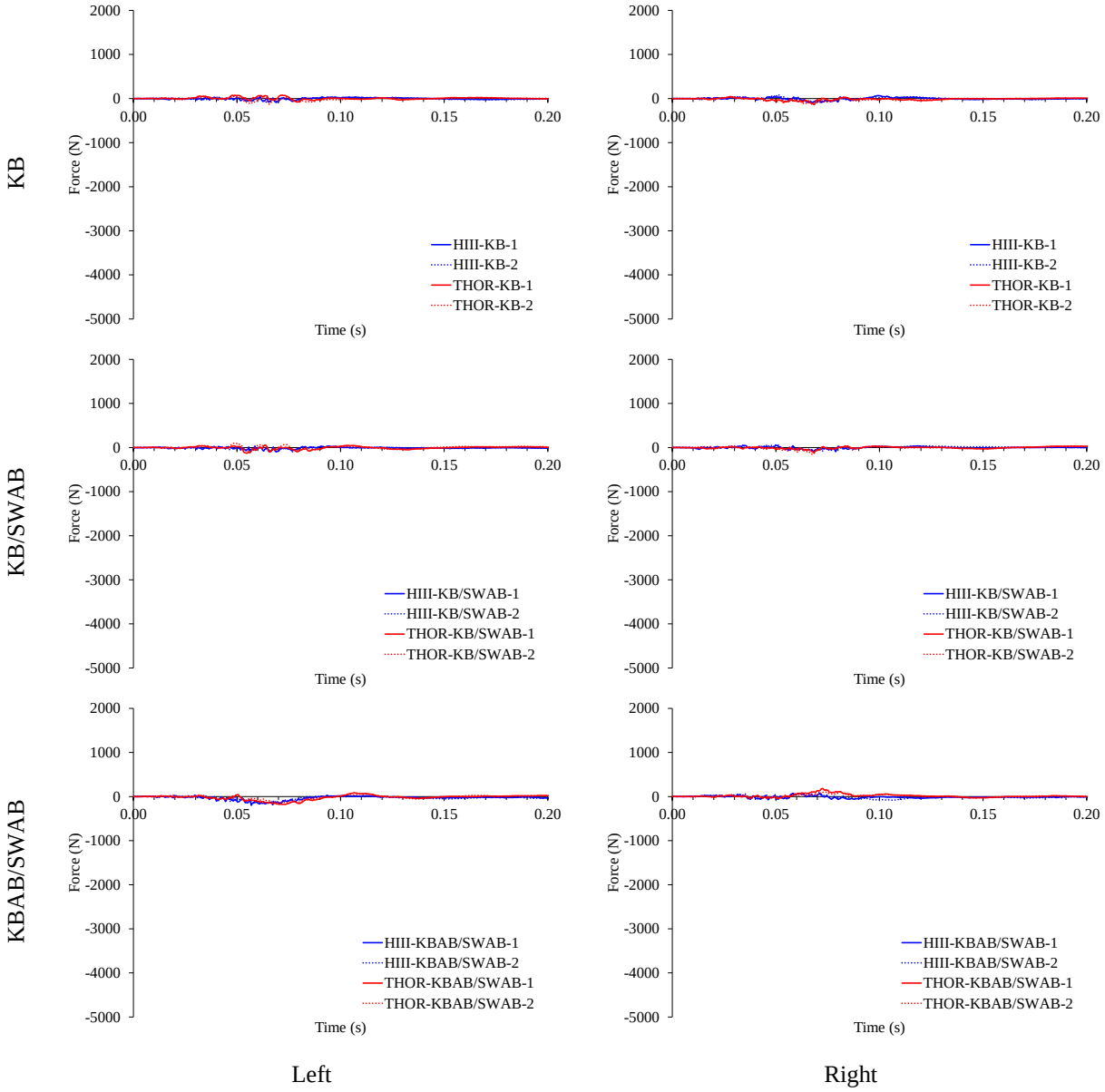

Figure A4.23: Lower tibia ML shear forces (Fy) for the HIII and THOR-M for all conditions. Note: Downward ankle movement and leftward knee movement are positive.

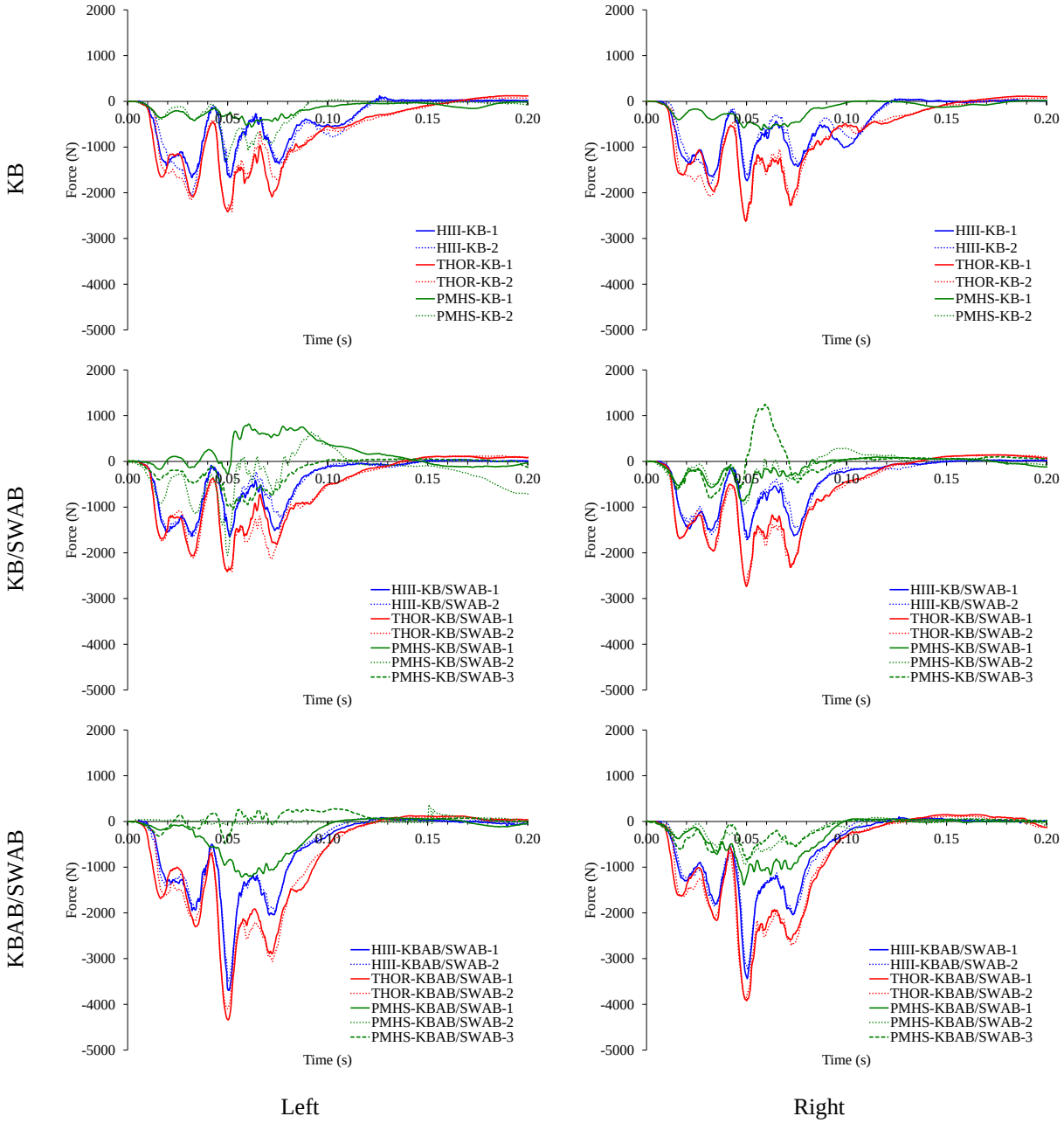

Figure A4.24: Lower tibia axial forces (Fz) for all surrogates and conditions.
Note: Downward ankle movement and upward knee movement are positive.

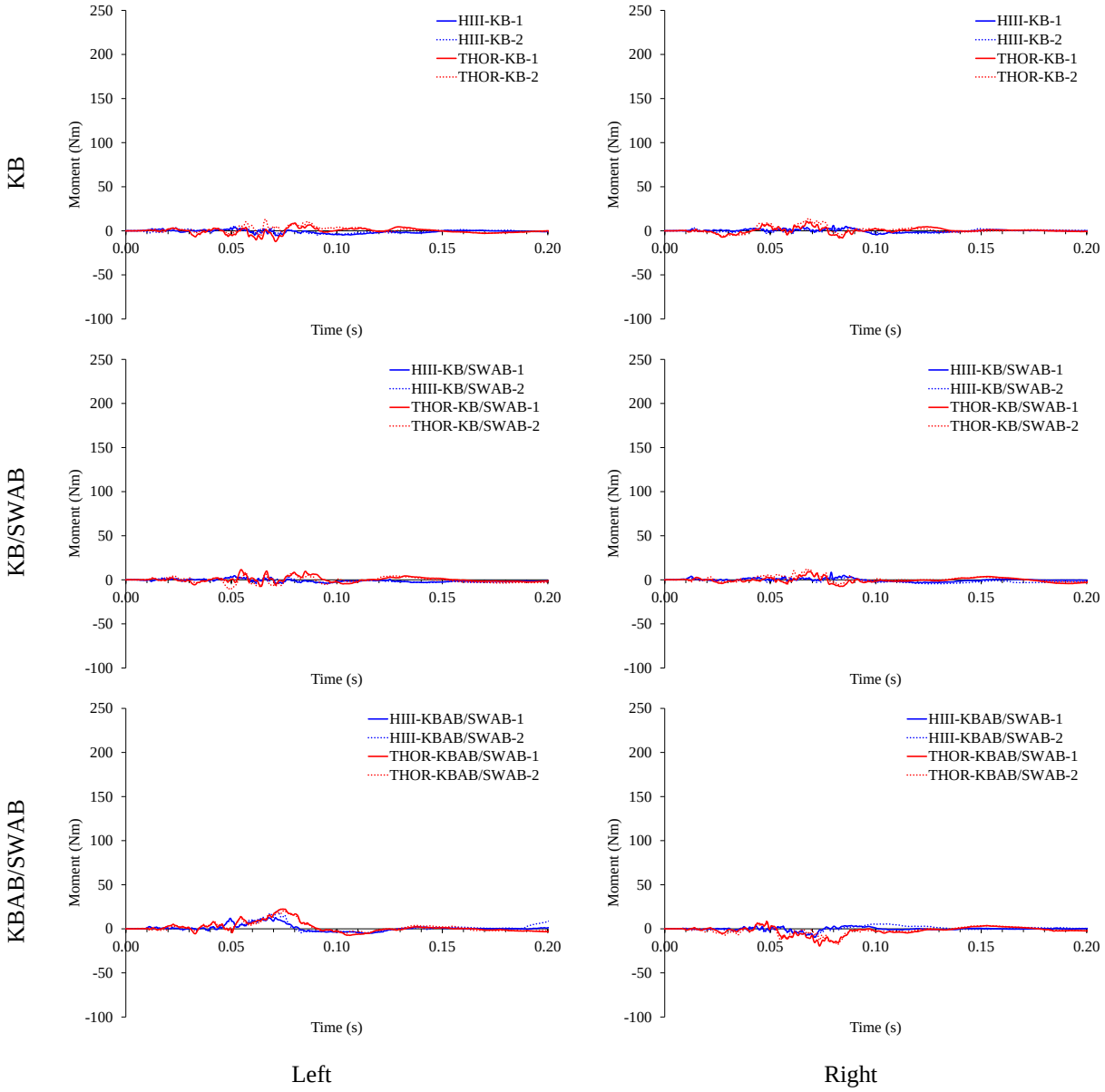

Figure A4.25: Lower tibia moments about the x-axis (Mx) for the HIII and THOR-M for all conditions.
Note: Leftward ankle movement relative to the knee is positive.

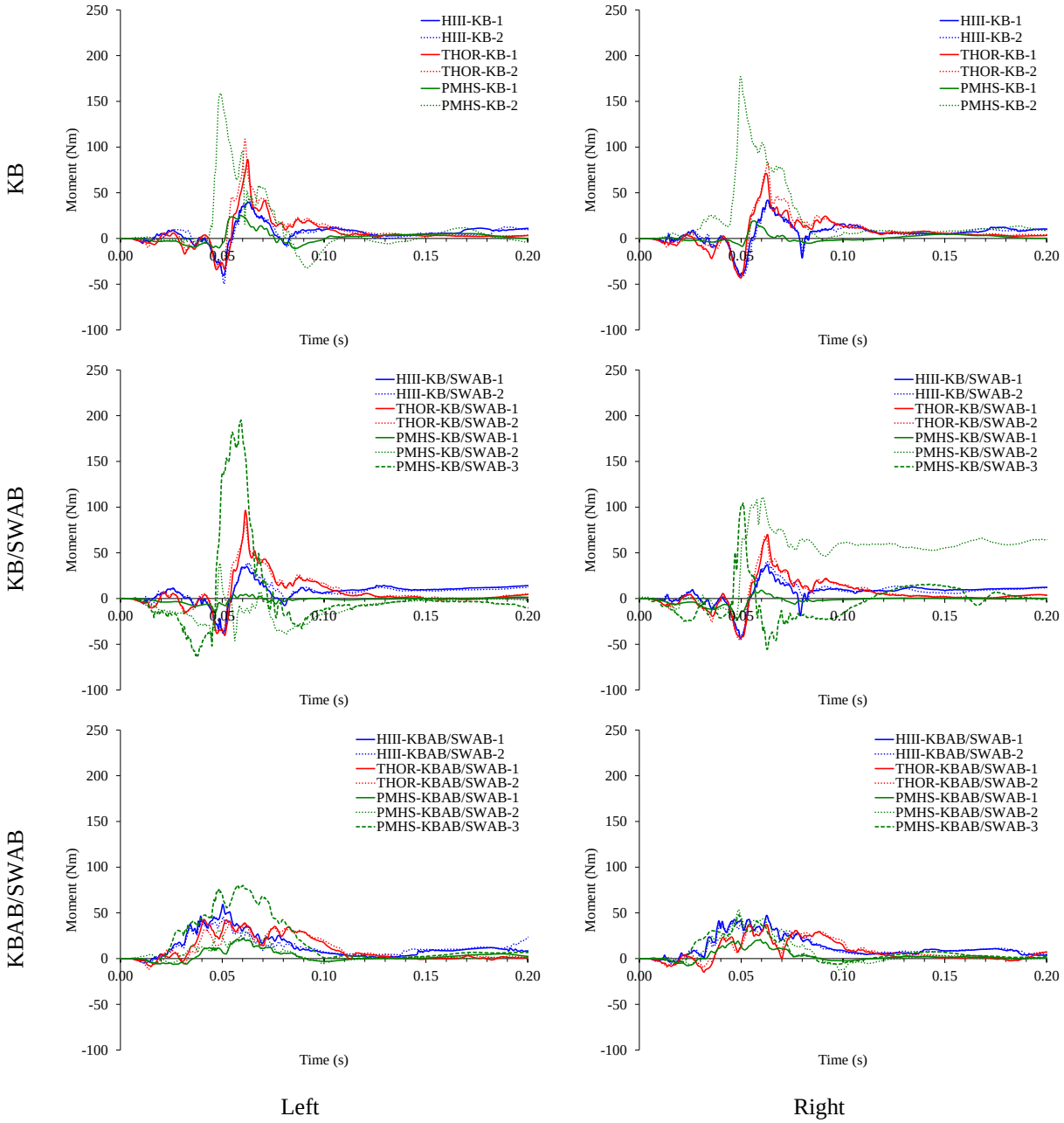

Figure A4.26: Lower tibia AP bending moments (My) for all surrogates and conditions. Note: Forward ankle movement and rearward knee movement are positive.

CHAPTER 5: ABDOMINAL ORGAN RESPONSE OF POST-MORTEM HUMAN SURROGATES AND THE THOR-M DURING FULL-SCALE FRONTAL SLED TESTS

Select contents published in:

Albert DL, Beeman SM, Kemper AR, "A Method for Measuring Pressures in the Liver and Spleen of Post-Mortem Human Surrogates during Full-Scale Frontal Sled Tests," *Biomedical Sciences Instrumentation,* 53, 2017.

Introduction

The liver and spleen are the two most frequently injured abdominal organs in motor vehicle collisions [1,2]. However, there is currently no injury criteria to predict abdominal injury in the current frontal anthropomorphic test devices (ATD). The Hybrid III does not contain any standard abdominal instrumentation, but a more biofidelic abdomen measuring abdominal deflection was developed for the Hybrid III family of ATDs [3,4]. However, the abdomen has yet to be validated under airbag loading. The more recently developed Test device for Human Occupant Restraint (THOR-M) contains standard instrumentation capable of measuring abdominal deflection. Additionally, a recent study successfully instrumented the Test device for Human Occupant Restraint (THOR-M) with an abdominal pressure sensing system [5]. Furthermore, neither ATD was designed with physical representations of abdominal organs, such as the liver and spleen.

While injury mechanisms and predictors for the spleen have been largely unstudied, previous research has been conducted in an effort to determine the best biomechanical predictor for liver injury. Foster *et al.* (2006) first indicated that abdominal aortic pressure may be used to predict liver injury [6]. Sparks *et al.* (2007) conducted drop tests onto the anterior surface of *ex vivo* livers and found that internal liver pressure was well correlated with injury risk [7]. Kremer *et al.* (2011) built upon this work, developing a method for instrumenting the hepatic veins and inferior vena cava of whole-body post-mortem human surrogates (PMHSs), i.e., cadavers, and measured the vascular pressure of the liver during lateral and oblique blunt impact tests [8]. They reprocessed the *ex vivo* data from Sparks *et al.* (2007) and analyzed it in conjunction with their whole-body *in situ* data to find that peak pressure and peak rate of pressure increase were good predictors of injury risk.

Although Kremer *et al.* (2011) were able to measure the internal pressures of the liver, there were some drawbacks to their approach. Namely, their pressure sensors were routed from the right internal jugular vein and right femoral vein to the inferior vena cava and hepatic veins using fluoroscopy [8]. Fluoroscopy requires specialized equipment which may not be available to all research laboratories since C-arm fluoroscopes can cost between $10,000 and $140,000, depending on the capabilities of the system. Additionally, fluoroscopy is limited to two dimensions

which resulted in the misplacement of some sensors [8]. Finally, routing sensors through vasculature peripheral to the target location using fluoroscopy is very time consuming.

Despite previous successes in correlating internal liver pressure to injury risk, splenic pressures have yet to be evaluated for a potential correlation with injury risk. This may be a result of the longer and more convoluted path required to access the spleen through the splenic artery, which makes less invasive approaches more difficult. Therefore, there is a need for a more direct approach to instrumenting solid abdominal organs with pressure sensors that results in increased speed and accuracy of sensor placement, but does not require specialized equipment.

It is hypothesized that the introduction of knee bolster airbags (KBABs) into the vehicle fleet will decrease thoracic and abdominal injuries by reducing the forward motion of the pelvis, decreasing the interaction of the thorax and abdomen with the seatbelt and airbag. However, the influence of different safety restrain conditions on abdominal organ injury has yet to be investigated in a full-scale sled test. With the development of pressure sensing instrumentation for the THOR-M abdomen, it is now possible to evaluate the sensitivity of abdominal organ pressure to different safety restraint conditions, including KBABs, for a 50^{th} percentile male.

The purpose of this study is twofold. First, this study aims to develop and validate a more direct approach for measuring the internal pressures of both the liver and the spleen in PMHSs. Second, this study will quantify and compare abdominal organ pressures for the THOR-M and PMHSs during full-scale frontal sled tests under three safety conditions: knee bolster (KB), knee bolster and steering wheel airbag (KB/SWAB), and knee bolster airbag and steering wheel airbag (KBAB/SWAB).

Methods

A total of 14 full-scale frontal sled tests were performed using the THOR-M and PMHSs to quantify the internal organ response under three safety restraint conditions: KB, KB/SWAB, and KBAB/SWAB. Six tests were performed with the THOR-M, while a total of eight PMHS tests were performed. For the THOR-M tests, two tests were performed for each of the three safety restraint conditions. For the PMHSs, two tests were performed in the KB condition and three tests

each were performed in the KB/SWAB and KBAB/SWAB conditions. Each PMHS was used for only a single test. Detailed methodology for the sled tests was described in Chapter 3. In brief, the sled tests were designed to simulate the 2005 Toyota Camry (KB/SWAB) and 2012 Toyota Camry (KBAB/SWAB) frontal New Car Assessment Program (NCAP) full-scale crash tests [9,10]. All tests were performed on a 1.4 MN ServoSled^{TM} system (Seattle Safety LLC, Kent, WA) with a custom sled buck designed to match the interior of a 2013 Toyota Camry SE. New 2013 Toyota Camry vehicle components, including a three-point, U.S. driver side seatbelt (with a pretensioner, 4kN load limiter, retractor, and buckle), seat, steering wheel, steering column, and steering wheel airbag (when applicable) were used for each test. The KB and KBABs were simulated using 65 and 19 psi rigid polyurethane foams, respectively. The vehicle acceleration pulse of the 2012 Toyota Camry NCAP test (ΔV = 56 kph, peak acceleration = 470 m/s2) was employed for each test.

Positioning of the surrogates and vehicle components (i.e. seat track, seat back, steering column, seat belt, and KB) were guided by the NCAP Test Procedure Document [11] and the NCAP Report for the 2012 Toyota Camry [9]. Detailed positioning information and knee bolster geometry were provided in Chapters 3 and 2, respectively. Overall, the offsets between the surrogate and vehicle components were maintained across tests in order to ensure valid comparisons between conditions and surrogates.

Instrumentation

The THOR-M abdomen was instrumented with the Abdominal Twin Pressure Sensors (APTS) [12] as described in Compigne *et al.* (2015) [5]. The APTS includes left and right bladders embedded in the abdominal insert and equipped with pressure transducers. The anatomical location of the APTS corresponds approximately the hollow organs such as the small intestine (Figure 5.1).

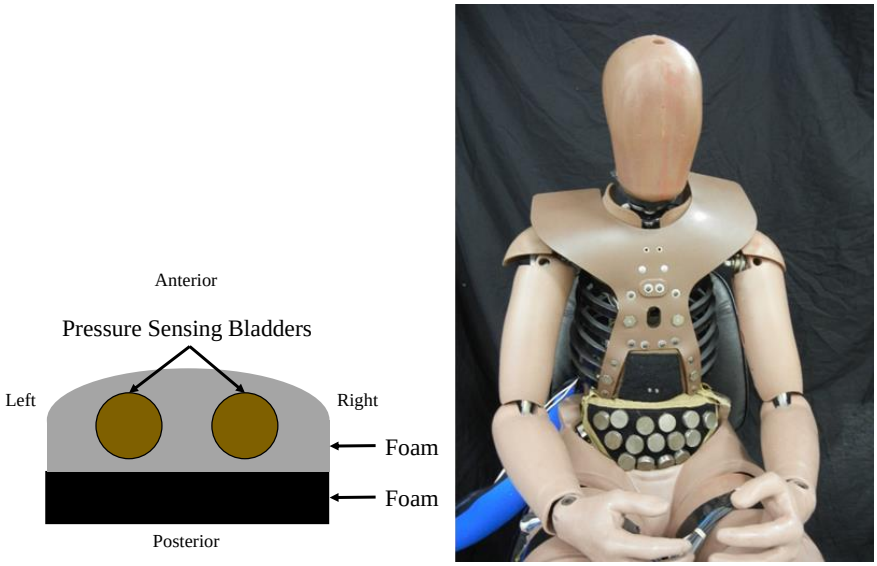

Figure 5.1: Schematic of the APTS abdomen (left) and THOR-M instrumented with the APTS (right).

The livers and spleens of the PMHSs were instrumented with pressure sensors using a direct, invasive method. The abdominal cavities were accessed by making an incision just inferior to the diaphragm. The hepatic and splenic arteries were located after branching from the celiac trunk (Figure 5.2). Both arteries were cut and tied off using suture thread and zip ties on the aortic end to prevent leakage from systemic pressurization. Millar catheter style pressure sensors (Mikro-Tip® Catheter Pressure Transducer, Millar Instruments, Houston, TX) were inserted into the arteries and routed into the liver and spleen. The extravascular portion of the pressure sensor wires were housed in plastic tubing. The vascular end of the tubing was fitted with a barbed plastic junction, which was inserted into the portion of the cut artery that led to the organ. The artery was secured over the barbed junction by tightly tying suture thread and tightening zip ties over the complex. The external plastic tubing was split via a plastic Y-junction with barbed ends, where one branch contained the pressure sensor wire and the other branch led to a pressurization system. Before pressurization, the air was evacuated from the plastic tubing. Then, the pressurization system was briefly activated to check for leaks in the abdominal vasculature. After any apparent leaks were closed, the abdominal incision was sutured closed. The plastic tubing was strain-relieved to the skin using zip ties. Sensors were successfully inserted into the liver and spleen for all tests. For one PMHS (PMHS-KBAB/SWAB-3), the liver pressure sensor was inserted through the hepatic vein because the inner diameter of the hepatic artery was too small.

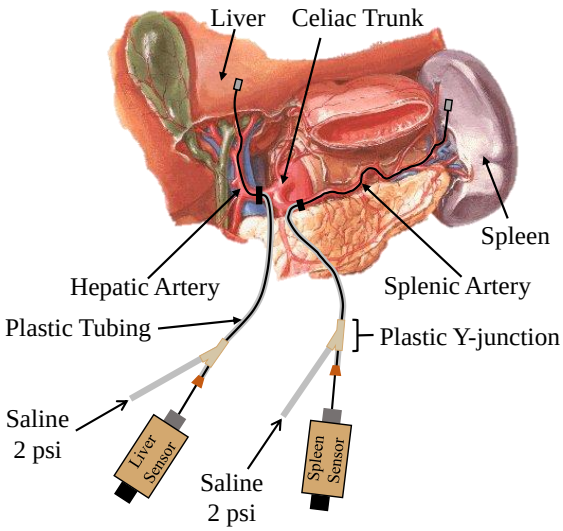

Figure 5.2: Pressurization and sensing schematic of the liver and spleen.

The pressurization system was activated approximately 2 minutes before the start of each test. The hepatic and splenic arteries were pressurized to 2 psi to simulate in vivo conditions [13]. Systemic pressurization was achieved by pressurizing the carotid artery and jugular vein to 2 psi and 0.5 psi, respectively. The pulmonary system was pressurized to 1 psi via a tracheotomy tube. The livers and spleens were examined before and after each test to determine whether any injuries occurred as a result of the sled test.

All pressures were collected at 20 kHz. The hepatic and splenic pressures from the PMHS tests were filtered at SAE channel frequency class (CFC) 600 [14]. The THOR-M left and right abdominal pressures were filtered at CFC 180.

Data Analysis

In order to validate the direct methodology used to collect the PMHS pressures, peak hepatic pressures were compared to the *in situ* peak hepatic vascular pressures (n = 10) reported by Kremer *et al.* (2011) [8] and the *ex vivo* peak hepatic vascular pressures (n = 12) reprocessed by Kremer *et al.* (2011), but originally reported by Sparks *et al.* (2007) [7]. The normality of each dataset was confirmed by performing a Shapiro-Wilk test. The equivalency of variances between the three

datasets was tested using JMP Pro 11 software (SAS Institute Inc, Cary, NC), which performs four statistical tests to test the null hypothesis of equal variances: O'Brien, Brown-Forsythe, Leven, and Bartlett. All tests reported a p-value less than 0.05 (O'Brien: $p = 0.0499$, Brown-Forsythe: $p = 0.0089$, Leven: $p = 0.0088$, and Bartlett: $p = 0.0043$). Therefore, it was concluded that at least one group had an unequal variance, and a Welch's ANOVA was performed to assess whether there was a statistical difference between the group means.

PMHS and THOR-M abdominal pressures were qualitatively compared between surrogates and conditions. The pressures were not quantitatively compared between surrogates using the ISO/TS 18571 specification because the PMHS and THOR instrumentation did not correspond to the same locations and organs within the abdomen.

Results

Peak PMHS abdominal pressures ranged from 40.7 to 76.4 kPa for the liver and 34.3 to 105.1 kPa for the spleen (Table 5.1). Equipment failure for test PMHS-KB/SWAB-1 prevented the splenic pressure data from being collected and presented here. The shapes of the pressure curves and the times at which peaks occurred were not conserved across tests (Figure 5.3). Most tests exhibited one distinct peak; however, test PMHS-KBAB/SWAB-1 had two approximately equal pressure peaks during the test. Only one test related injury was observed out of all of the tests. The spleen in test PMHS-KBAB/SWAB-3 sustained capsule tears, which is an Abbreviated Injury Scale (AIS) 2 injury (Figure 5.4) [15]. The Welch's ANOVA comparing the current hepatic peak pressures to the *in situ* and *ex vivo* vascular pressures (Figure 5.5) in the literature resulted in a p-value of 0.9658, indicating the means of the three groups were not statistically different. The averages of the peak lap belt and shoulder belt loads across all PMHS tests were 3995 N and 4768 N, respectively.

Table 5.1: Peak pressures, peak rate of pressure increase, and their product for the liver and spleen.

Test	Liver			Spleen		
	Peak Pressure (P_{max}) (kPa)	Peak Rate of Pressure Increase ($\dot{P}_{max}$) (kPa/ms)	$P_{max} \cdot \dot{P}_{max}$ (kPa^2/ms)	Peak Pressure (P_{max}) (kPa)	Peak Rate of Pressure Increase ($\dot{P}_{max}$) (kPa/ms)	$P_{max} \cdot \dot{P}_{max}$ (kPa^2/ms)
PMHS-KB-1	72.8	8.7	636	51.9	5.3	275
PMHS-KB-2	58.6	10.2	595	39.3	13.3	523
PMHS-KB/SWAB-1	40.7	4.5	185	N/A	N/A	N/A
PMHS-KB/SWAB-2	76.4	8.9	683	56.0	7.8	439
PMHS-KB/SWAB-3	44.5	5.4	241	105.1	9.5	1002
PMHS-KBAB/SWAB-1	68.0	8.0	544	34.3	6.4	220
PMHS-KBAB/SWAB-2	75.2	6.2	467	53.4	11.8	629
PMHS-KBAB/SWAB-3	66.7	10.5	702	94.2	12.4	1167

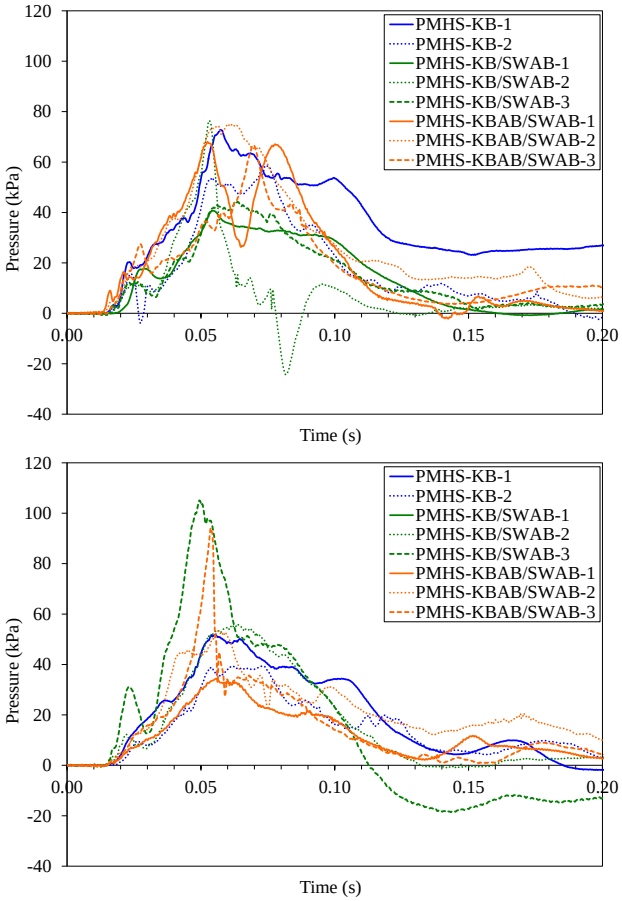

Figure 5.3: Hepatic (left) and splenic (right) pressures for all tests.
Note: The splenic pressure trace for PMHS-KB-1 is not plotted due to equipment failure.

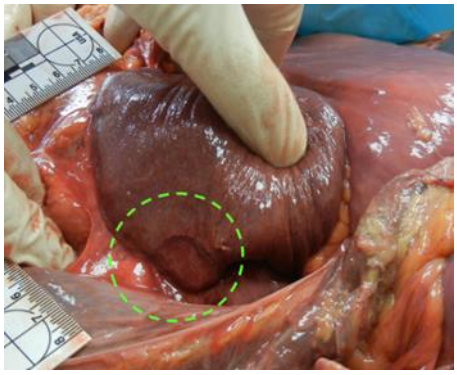

Figure 5.4: Spleen capsule tear (AIS2).

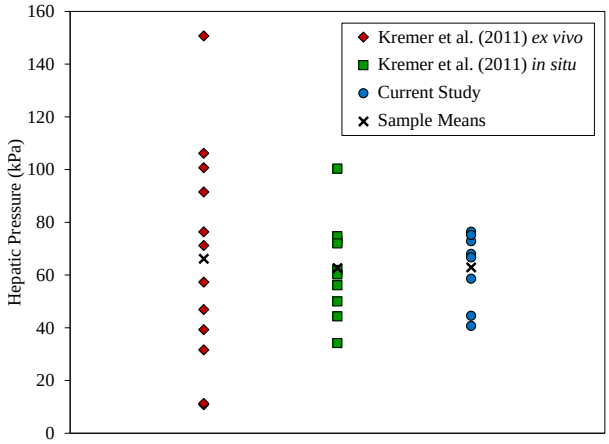

Figure 5.5: Hepatic pressures for the current study and the *ex vivo* and *in situ* testing reported by Kremer *et al.* (2011).

The THOR-M abdominal pressures were more repeatable than those for the PMHS (Figure 5.6). There was little difference in magnitude between the left and right THOR-M abdominal pressures. However, differences were observed between restraint conditions. The KBAB condition resulted in lower abdominal pressures than the other two conditions. The right abdominal pressure for one test, THOR-KB/SWAB-1, had a larger peak than any of the other tests. This may have been the result of the bottom of the rib cage exerting force on the abdomen. PMHS hepatic and splenic pressures were larger than the THOR-M left and right abdominal pressures for all restraint conditions (Figure 5.7). The only exception was the THOR-KB/SWAB-1 right abdominal pressure, which was abnormally large compared to the other THOR-M abdominal pressures as noted above.

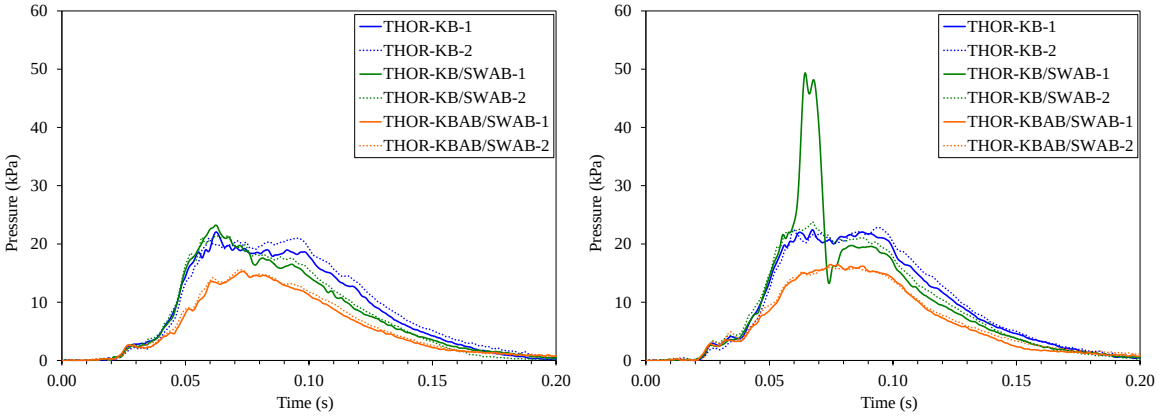

Figure 5.6: Left (left) and right (right) abdominal pressures for the THOR-M.

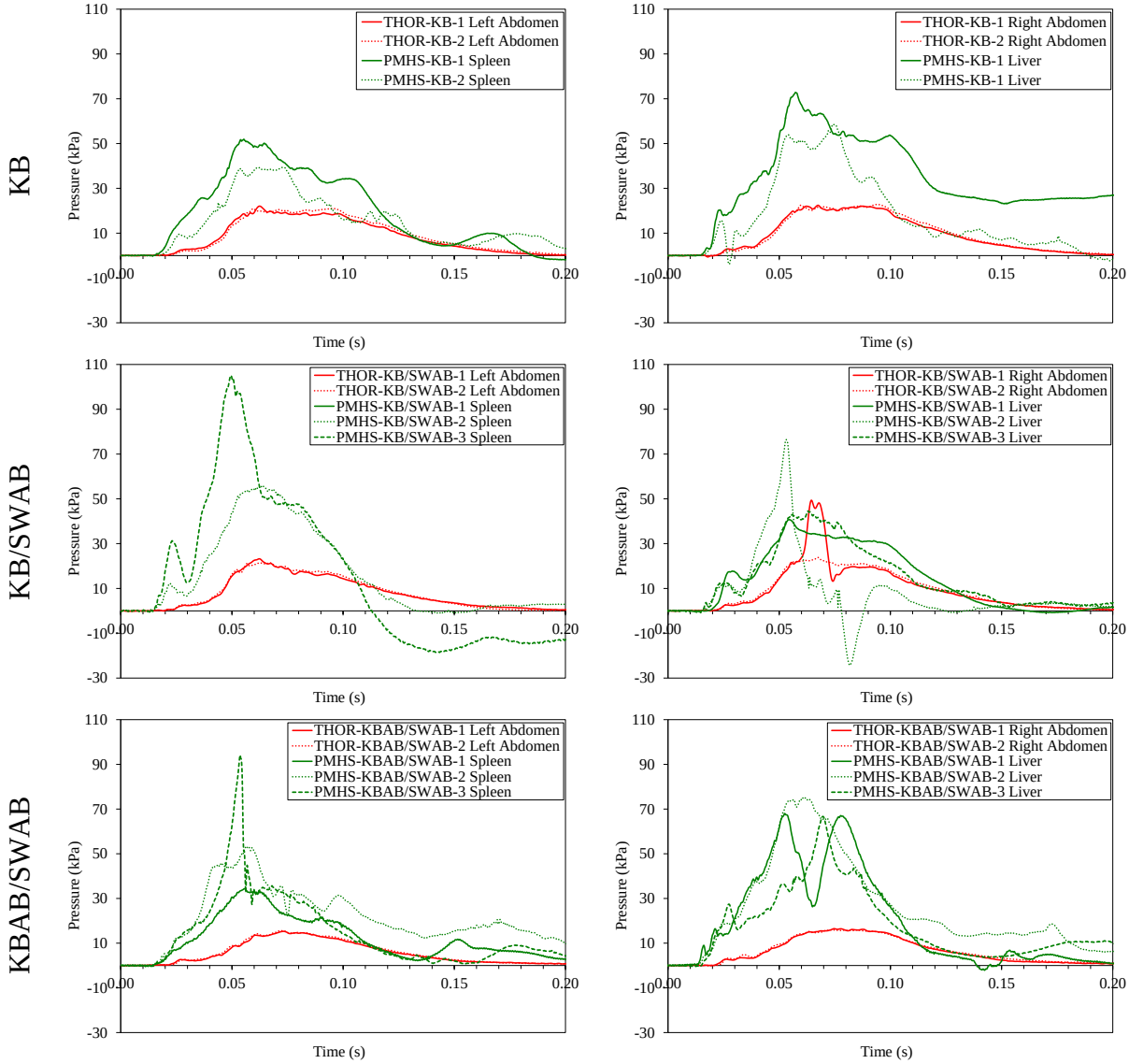

Figure 5.7: Left abdominal THOR-M pressures plotted with PMHS splenic pressures (left) and right abdominal THOR-M pressures plotted with PMHS hepatic pressures (right).

Discussion

Variation was observed in terms of curve shape, peak magnitude, and time at which the peaks occurred for the hepatic and splenic pressure traces. A main source of this variation is likely differences in subject anthropometry, which can encompass organ size and organ location. Organ location can subsequently affect which vehicle components or safety restraints load the organ. The height of a subject's thorax influences where the liver and spleen are located relative to the steering wheel and safety restraints, such as the seatbelt and airbag, leading to possible differences in loading. For instance, the liver could be located directly under the seatbelt for a shorter subject, but above the seatbelt for a taller subject. Therefore, these subjects would experience different magnitudes and durations of loading on the liver.

The hepatic peak pressures were not found to be statistically different from the *in situ* and *ex vivo* peak pressures reported by Kremer et al. (2011) in terms of group means. Furthermore, the average peak forces from the *ex vivo* drop tests (6809 N) and *in situ* whole-body blunt impact tests (4128 N) were similar to the average lap belt and shoulder belt peak loads recorded in the current study (3995 N and 4768 N, respectively), implying that comparable energies were imparted to the liver for all test series. Therefore, the pressures collected by using this study's more invasive methodology are reasonable based upon previous literature that used both invasive and non-invasive methods. Kremer et al. (2011) also developed functions to predict the risk of an AIS3+ injury based on the *in situ* and *ex vivo* data [4]. Several curves were developed using different predictors and combinations of the datasets (*in situ* only, *ex vivo* only, and both). The five risk curves that had statistically significant fits involved all combinations of the datasets and two predictors: peak rate of pressure increase ($\dot{P}_{max}$), and the product of the peak pressure (P_{max}) and $\dot{P}_{max}$, i.e., $P_{max} \cdot \dot{P}_{max}$. The risk curves with the highest significance for each predictor were based on both the *in situ* and *ex vivo* datasets and had cutoff values of 10.2 kPa/ms and 710 kPa^2/ms corresponding to a 50% risk of an AIS3+ injury [4]. One test in the current study (KBAB-3) resulted in a liver predictor variable above these cutoffs (Table 5.1). However, no AIS3+ liver or spleen injuries were observed for any tests.

Unlike the PMHSs, the THOR-M abdominal pressures varied with respect to restraint condition. The lower abdominal pressures for the KBAB/SWAB compared to the other conditions were a result of the lower lap belt forces (see Chapter 3). The PMHS also experienced lower lap belt forces for the KBAB/SWAB condition on average. However, there was more variability in the PMHS organ pressures due to the factors discussed previously, which could have masked any influence of restraint condition.

The THOR-M had lower abdominal pressures than the PMHSs overall. This can be a result of several factors including sensor location and surrogate biofidelity. Regarding sensor location, the PMHS and THOR-M pressure sensors were located in different regions of the abdomen, representing different organs. The PMHS sensors were located in the liver and spleen, which are both situated in the upper abdomen. However, the THOR-M pressure sensors were located in the lower abdomen. Therefore, these sensors would experience different magnitudes of loading, regardless of the degree of biofidelity of the THOR-M as a human surrogate. In order to accurately assess the biofidelity of the THOR-M, abdominal pressure sensors would need to be situated in analogous locations in both surrogates.

This study was limited by its small sample size of one demographic (50^{th} percentile male). This prevented statistically meaningful comparisons from being made between the KB and KBAB conditions. Future work could include conducting additional tests with different restraint conditions to elucidate injury mechanisms and higher severity tests to produce injuries. More injurious and non-injurious tests would be vital in the development of new injury risk curves for the spleen and validation of current injury risk curves for the liver.

Conclusions

This study evaluated the abdominal pressures of the THOR-M and PMHS for three safety restraint conditions. The THOR-M abdomen was instrumented with left and right pressure sensors at the level of the hollow organs. A novel method was developed to instrument the liver and spleen of PMHSs in order to measure internal organ pressure during the sled tests. Pressure sensors were successfully placed in both organs for all tests, and the internal liver pressures were not statistically significantly different from those reported in previous literature based on *ex vivo* data from an

invasive methodology and *in situ* data from a non-invasive methodology. The THOR-M abdominal pressures were lower than the PMHS organ pressures and demonstrated a sensitivity to restraint condition. PMHS organ pressures did not show a sensitivity to restraint condition due to the high amount of inter-subject variation. The organ pressures and instrumentation methodology from this study can be used to validate existing injury risk criteria for the liver and develop injury risk criteria for the spleen.

References

1. Elhagediab AM, Rouhana SW. Patterns of Abdominal Injury in Frontal Automotive Crashes. Paper presented at: The 16th International Technical Conference on the Enhanced Safety of Vehicles1998.
2. Yoganandan N, Pintar FA, Gennarelli TA, Maltese MR. Patterns of Abdominal Injuries in Frontal and Side Impacts. Paper presented at: Annu Proc Assoc Adv Automot Med2000.
3. Gregory T, Howes M, Rouhana S, Hardy W. Deflection Measurement System for the Hybrid Iii Six-Year-Old Biofidelic Abdomen. *Biomedical sciences instrumentation.* 2011;48:149-156.
4. Rouhana SW, Elhagediab AM, Walbridge A, Hardy WN, Schneider LW. Development of a Reusable, Rate-Sensitive Abdomen for the Hybrid Iii Family of Dummies. *Stapp Car Crash Journal.* 2001;45:33-60.
5. Compigne S, Masuda M, Hanen G, Vezin P, Bermond F. Proposal for a Modified Thor Lower Abdomen Including Abdominal Pressure Twin Sensors. Paper presented at: 24th International Technical Conference on the Enhanced Safety of Vehicles2015.
6. Foster CD, Hardy WN, Yang KH, King AI, Hashimoto S. High-Speed Seatbelt Pretensioner Loading of the Abdomen. *Stapp car crash journal.* 2006;50:27.
7. Sparks JL, Bolte JH, Dupaix RB, Jones KH, Steinberg SM, Herriott R, Stammen J, Donnelly B. Using Pressure to Predict Liver Injury Risk from Blunt Impact. *Stapp car crash journal.* 2007;51(10):401-432.
8. Kremer MA, Gustafson HM, Bolte IV JH, Stammen J, Donnelly B, Herriott R. Pressure-Based Abdominal Injury Criteria Using Isolated Liver and Full-Body Post-Mortem Human Subject Impact Tests. *Stapp car crash journal.* 2011;55:317.
9. Janovicz D, Fischer B. *Final Report of New Car Assessment Program Frontal Impact Testing of 2012 Toyota Camry Lee 4-Dr Sedan.* Washington, DC: USDOT; December 16, 2011 2011.
10. Naik S. *Final Report of New Car Assessment Program Testing of a 2005 Toyota Camry Le.* Washington, DC: U.S. Department of Transportation,; March 11, 2005 2005.
11. NHTSA. *Laboratory Test Procedure for New Car Assessment Program (Ncap)- Frontal Impact Testing*. Washington, DC: U.S. Department of Transportation; 2012.

12. Beillas P, Alonzo F, Chevalier M-C, Lesire P, Leopold F, Trosseille X, Johannsen H. Abdominal Twin Pressure Sensors for the Assessment of Abdominal Injuries in Q Dummies: In-Dummy Evaluation and Performance in Accident Reconstructions. *Stapp car crash journal.* 2012;56:387.
13. Khurana I. *Textbook of Medical Physiology*. Elsevier Kundli, India; 2006.
14. SAE. *Instrumentation for Impact Test.* Warrendale, PA: Society of Automotive Engineers;1995.
15. Gennarelli TA, Wodzin E. *Abbreviated Injury Scale 2005 : Update 2008.* Barrington, IL: Association for the Advancement of Automative Medicine; 2008.

Biomechanical Responses of Human Surrogates under Various Frontal Loading Conditions with an Emphasis on Thoracic Response and Injury Tolerance

Devon Albert

Preliminary Examination submitted to the faculty of the Virginia Polytechnic Institute and State University in partial fulfillment of the requirements for the degree of

Doctor of Philosophy
In
Biomedical Engineering

Andrew R. Kemper
Amanda M. Agnew
H. Clay Gabler
Warren N. Hardy
Joel D. Stitzel

4/19/2018
Blacksburg, VA

Keywords: Hybrid III, THOR, PMHS, knee bolster, knee bolster airbag, frontal motor vehicle collision, thoracic injury criterion, rib

TABLE OF CONTENTS

LIST OF FIGURES

LIST OF TABLES

CHAPTER 6: NECK RESPONSES OF THE HYBRID III, THOR-M, AND POST-MORTEM HUMAN SURROGATES UNDER VARIOUS RESTRAINT CONDITIONS IN FULL-SCALE FRONTAL SLED TESTS

Proposed Authors:

Albert DL, Beeman SM, Kemper AR

Introduction

It is estimated that there were an average of 3.9 million emergency department visits per year for motor vehicle traffic related injuries in the United States between 2010 and 2011 [1]. Approximately 23% of these visits resulted in diagnoses of sprains or strains of the neck and back [1]. This percentage is substantially higher than the 3% of visits for neck and back sprains and strains caused by other injury modalities, demonstrating an over-representation of these injuries in motor vehicle collisions [1].

Previous studies have shown that the current standard frontal anthropomorphic test device (ATD), the Hybrid III (HIII), has a stiffer neck response than human volunteers and post-mortem human surrogates (PMHSs) [2-5]. The Test device for Human Occupant Restraint (THOR) is a newer ATD designed to have a more biofidelic neck response than the HIII. Specifically, the THOR neck was designed to have more biofidelic anterior-posterior and medial-lateral responses [6] and be more anatomically biofidelic, including cables external to the central column to simulate neck musculature [7]. A previous study performed component tests comparing the neck response of the HIII and a previous version of the THOR, the THOR-NT [8]. Both ATDs were stiffer than a human neck computational model under axial tension and anterior-posterior bending, but the HIII was stiffer than the THOR-NT. Yoganandan *et al.* (2012) performed matched sled tests with the HIII, THOR-NT, and PMHS at multiple severity levels and found that the THOR-NT produced a more biofidelic neck response. However, these tests were only performed under a belted restraint condition and did not evaluate the comparative neck responses under airbag loading. Pintar *et al.* (2005) reported that the THOR-NT had a more bioficelic neck response than the HIII under high-rate head/neck tensile loading reminiscent of under the chin airbag loading on an out-of-position occupant. Apart from that specific loading scenario, the most recent versions of the THOR have not been evaluated relative to the HIII under airbag loading.

In order to make the THOR more biofidelic, the newest version of the THOR, the THOR-M, was designed with a decreased axial neck stiffness relative to the THOR-NT. This change may affect the neck kinematics, kinetics, and injury prediction of the THOR-M relative to the THOR-NT. Component tests comparing the THOR-M, HIII, and PMHSs reported that the THOR-M had a more biofidelic neck response than the HIII [11]. However, the kinetics of the THOR-M neck have

yet to be evaluated relative to the HIII in full-scale frontal sled tests. Therefore, the objective of this research was to compare the kinetics and predicted injury risks of the Hybrid III (HIII) and THOR-M necks during full-scale frontal sled tests under three safety restraint conditions: knee bolster (KB), knee bolster and steering wheel airbag (KB/SWAB), and knee bolster airbag and steering wheel airbag (KBAB/SWAB).

Methods

Twelve full-scale scale frontal sled tests were performed using the HIII and THOR-M to quantify and compare the neck kinetics and injury risks under three safety restraint conditions: KB, KB/SWAB, and KBAB/SWAB. Two tests were performed per safety restraint condition for a total of six tests per ATD. Matched PMHS tests were performed for each condition using approximately 50^{th} percentile male PMHSs (see Albert *et al.* (2018) or Chapter 3 for demographic information). Three PMHS tests were performed for each condition, except for the KB condition for which only 2 PMHS tests were performed.

The detailed methodology for the sled tests, including details on occupant positioning, was previously published by Albert *et al.* (2018) and was described in Chapter 3. In brief, the sled tests were designed to simulate the 2005 Toyota Camry (KB/SWAB) and 2012 Toyota Camry (KBAB/SWAB) New Car Assessment Program (NCAP) frontal vehicle crash tests [13,14]. A new Camry seat, seatbelt (with a pretensioner, 4kN load limiter, retractor, and buckle), steering wheel, steering column, and steering wheel airbag (when applicable) were used in each test. The KB and KBAB were simulated using 65 psi and 19 psi rigid polyurethane foams, respectively [15]. The tests were performed on a 1.4 MN ServoSled^{TM} system (Seattle Safety LLC, Kent, WA) with a custom designed sled buck and employed the vehicle acceleration pulse of the 2012 Toyota Camry NCAP test (ΔV = 56 kph, peak acceleration = 470 m/s^2).

In order to quantify neck forces and moments, the ATDs were instrumented with neck load cells and head accelerometers, while the PMHSs were instrumented with head accelerometers. The ATDs were instrumented with 6 axis load cells in the upper and lower neck (see Table A6.1 for further information). ATD upper neck bending moments were transformed to the occipital condyles (OC). All surrogates were instrumented with six degree of freedom sensor blocks (Table

A6.1) at the head to record linear accelerations and angular rates for use in inverse dynamics calculations. PMHS sensor blocks were mounted to the posterior aspect of the head so that the sensing axes were approximately aligned with the coordinate axes designated in SAE J211 [16], and the forward pointing (x) axis was approximately in line with the Frankfort plane. All data were collected at 20 kHz (TDAS Pro & G5, DTS, Seal Beach, CA) and filtered using channel frequency classes (CFCs) from SAE J211 [16] (Table A6.2). Neck force and moment polarities conformed to the SAE J211 sign convention (Table A6.3) [16].

Inverse dynamics was used to calculate the upper neck axial force, anterior-posterior (AP) shear force, and bending moment about the y-axis for each PMHS until head contact with the steering wheel/steering hub or SWAB. First, the sensing axes were rotated so the x axis aligned with the Frankfurt plane, as determined by pre-test photos. Second, the accelerations were transformed to the head center of gravity (CG) using rigid body dynamics. The CG was assumed to be at the anterior-superior insertion point of the helix of the ear [17,18]. In order to calculate the bending moment at the OC, the horizontal (r_x) and vertical (r_z) distances between the head CG and OC needed to be determined. The distance between the head CG and auditory meatus/tragus was quantified from pre-test photos, and the OC was assumed to be 18.4 mm posterior and 31 mm inferior to the auditory meatus [19]. Finally, the axial force (F_z), shear force (F_x), and bending moment (M_y) at the OC were calculated using the transformed accelerations and Equations 1-3 (Figure A6.1) [20,21], where θ was the angle of the head with respect to horizontal. The head angle was calculated by integrating the head angular velocity, where the initial head angle was quantified from pre-test photos. The head mass (m) and moment of inertia (I_y) were calculated for each surrogate using Equations 4-5 developed by Clauser *et al.* (1969) and McConville *et al.* (1980).

Equation 1 $$F_x = ma_x + mg \sin\theta$$

Equation 2 $$F_z = ma_z - mg\cos\theta$$

Equation 3 $$M_y = I_y \propto_y - r_z F_x - r_x F_z$$

Equation 4 $$m = 0.104(head\ circumference) + 0.015(total\ body\ mass) - 2.189$$

Equation 5 $$I_y = 17{,}924(head\ circumference) - 794{,}181$$

Upper and lower neck forces and moments were directly compared between the ATDs. However, PMHS upper neck axial forces, shear forces, and bending moments could only be compared to the analogous ATD loads until head contact with vehicle components since the unknown quantity, direction, and point of application of externally applied loads could not be accounted for in the inverse dynamics calculations. PMHS head contact with the SWAB occurred before the onset of appreciable neck loading. As a result, the neck forces and moments from the PMHS SWAB conditions could not be directly compared to the ATD upper neck forces and moments. To determine whether head contact with vehicle components produced pronounced changes in the upper neck load profile, inverse dynamics was used to compute the upper neck axial force, shear force, and bending moment for the ATDs. The calculated forces and moments were then compared to those measured by the load cells. If little difference was observed between a calculated and measured load in the ATDs, then it could be assumed that the same relationship would hold true for the PMHSs. Therefore, a limited, qualitative comparison could be made between the measured ATD loads and calculated PMHS loads even after head contact.

Neck injury risk was quantified for the ATDs and was compared to the observed injuries in the matched PMHS tests. Post-test dissections were performed on the PMHSs to document any cervical spine injuries sustained during testing and the corresponding Abbreviated Injury Scale (AIS) severities [24]. N_{ij} and the corresponding risk of an AIS3+ injury were calculated for each test using Equations 6-7 and the critical values specific to each ATD (Table A6.4) [25]. cN_{ij} and the corresponding risk of an AIS3+ injury was also calculated for the THOR using Equations 8-9 (Table A6.5) [26].

Equation 6 $$N_{ij} = \left(\frac{F_z}{F_{zc}}\right) + \left(\frac{M_y}{M_{yc}}\right)$$

Equation 7 $$p(AIS3+) = \frac{1}{1+e^{3.227-1.969N_{ij}}}$$

Equation 8 $$cN_{ij} = \left(\frac{F_z}{F_{zc}}\right) + \left(\frac{M_y}{M_{yc}}\right)$$

Equation 9 $$p(AIS3+) = 1 - e^{-\left(\frac{cN_{ij}}{0.83}\right)^{2.71}}$$

Results

The time of head contact was very similar for the ATDs, but the PMHSs had earlier head contact times for all conditions (Table 6.1). For the KB condition, PMHS head contact occurred before the forces and moments peaked for the ATDs. However, enough time was available before head contact for the KB condition to make a qualitative comparison between the PMHSs and ATDs. For the other conditions, the PMHSs contacted the SWAB before appreciable loading occurred. Therefore, direct comparisons could not be made between the ATDs and PMHSs for the KB/SWAB and KBAB/SWAB conditions.

Table 6.1: Head contact times (s) for all surrogates.

Test ID	Surrogate		
	HIII	**THOR-M**	**PMHS**
KB-1	0.078	0.078	0.078
KB-2	0.078	0.078	0.074
KB/SWAB-1	0.039	0.041	0.033
KB/SWAB-2	0.040	0.040	0.031
KB/SWAB-3	-	-	0.040
KBAB/SWAB-1	0.040	0.042	0.033
KBAB/SWAB-2	0.040	0.042	0.031
KBAB/SWAB-3	-	-	0.028

Differences were observed between the HIII and THOR-M for all conditions (Figure 6.1 - Figure 6.6). The HIII had substantially higher AP shear forces (Fx) at the upper and lower neck than the THOR-M for the KB condition. Both ATDs had greater peak AP shear forces at the lower neck compared to the upper neck. The THOR-M also had higher medial-lateral (ML) lower neck shear forces (Fy) compared to the upper neck, whereas the opposite was true for the HIII. The axial force (Fz) time histories for the upper and lower neck were very similar for the ATDs. The moments about the x-axis were low in magnitude and differed between the ATDs. While the HIII moments about the x-axis (Mx) were similar between the upper and lower neck for all conditions, the THOR-M had primarily negative moments about the x-axis for the lower neck and oscillated between positive and negative for the upper neck. The ATDs also had very different bending moments about the y-axis (My). The THOR-M experienced negligible upper neck moments about the y-axis, whereas the HIII underwent extension then flexion. For the lower neck, the THOR-M and HIII bending moments were out of phase, but had similar magnitudes for the SWAB conditions. However, the HIII had a greater lower neck bending moment than the THOR-M for the KB

condition. Finally, the THOR-M had negligible upper and lower neck moments about the z-axis (Mz), whereas the HIII experienced a positive z moment for all conditions at the upper neck and for the KB condition at the lower neck.

The HIII and THOR-M responded similarly to changes in restraint condition in all directions except for the y-direction. Both ATDs had higher magnitude AP shear and axial forces for the KB condition compared to the SWAB conditions. Both surrogates also exhibited little difference between conditions for the moments about the x and z axes. However, the HIII and THOR-M responded differently to changes in restraint condition for the forces and moments in the y direction. The THOR-M had higher ML shear forces for the KB condition compared to the SWAB conditions, whereas the HIII showed little difference between conditions. Conversely, the THOR-M showed little difference between conditions for the moments about the y-axis, and the HIII had higher moments about the y-axis for the KB conditions compared to the other conditions.

The relationship between the ATD and PMHS responses for the KB condition varied between the types of signals. For the upper neck AP shear forces, all surrogates experienced negative forces at the time of head contact, but the PMHS forces were more negative than both of the ATDs. All surrogates had similar upper neck axial forces at the time of head contact. Each of the surrogates had different bending moment responses until head contact. The HIII experienced primarily extension moments before head contact. The PMHSs experienced flexion, and the THOR-M experienced negligible bending moments.

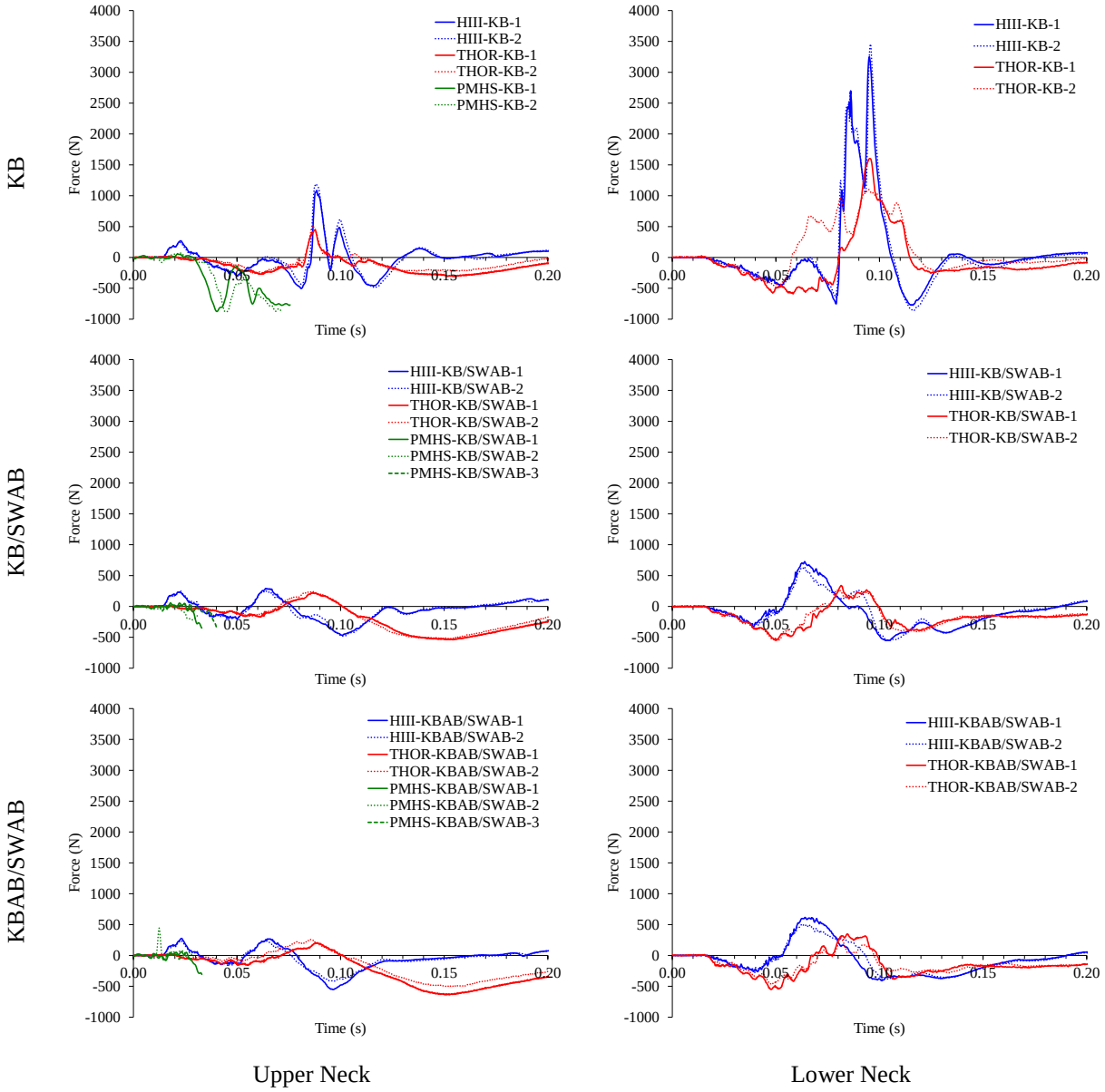

Figure 6.1: Upper neck (left) and lower neck (right) AP shear forces (Fx) for all conditions. Note: Rearward head motion relative to the chest is positive.

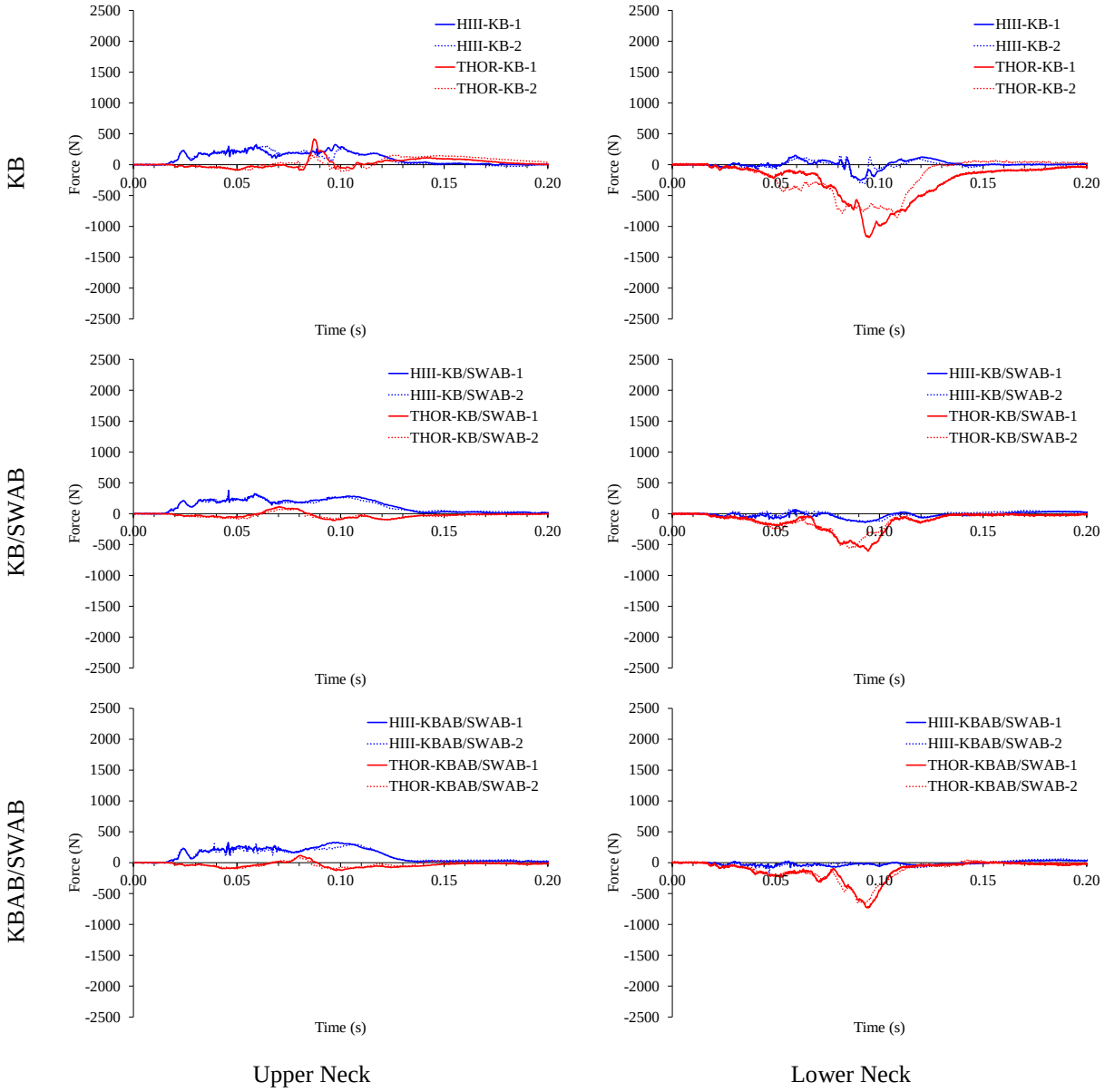

Figure 6.2: Upper neck (left) and lower neck (right) ML shear forces (Fy) for all conditions. Note: Leftward head motion relative to the chest is positive.

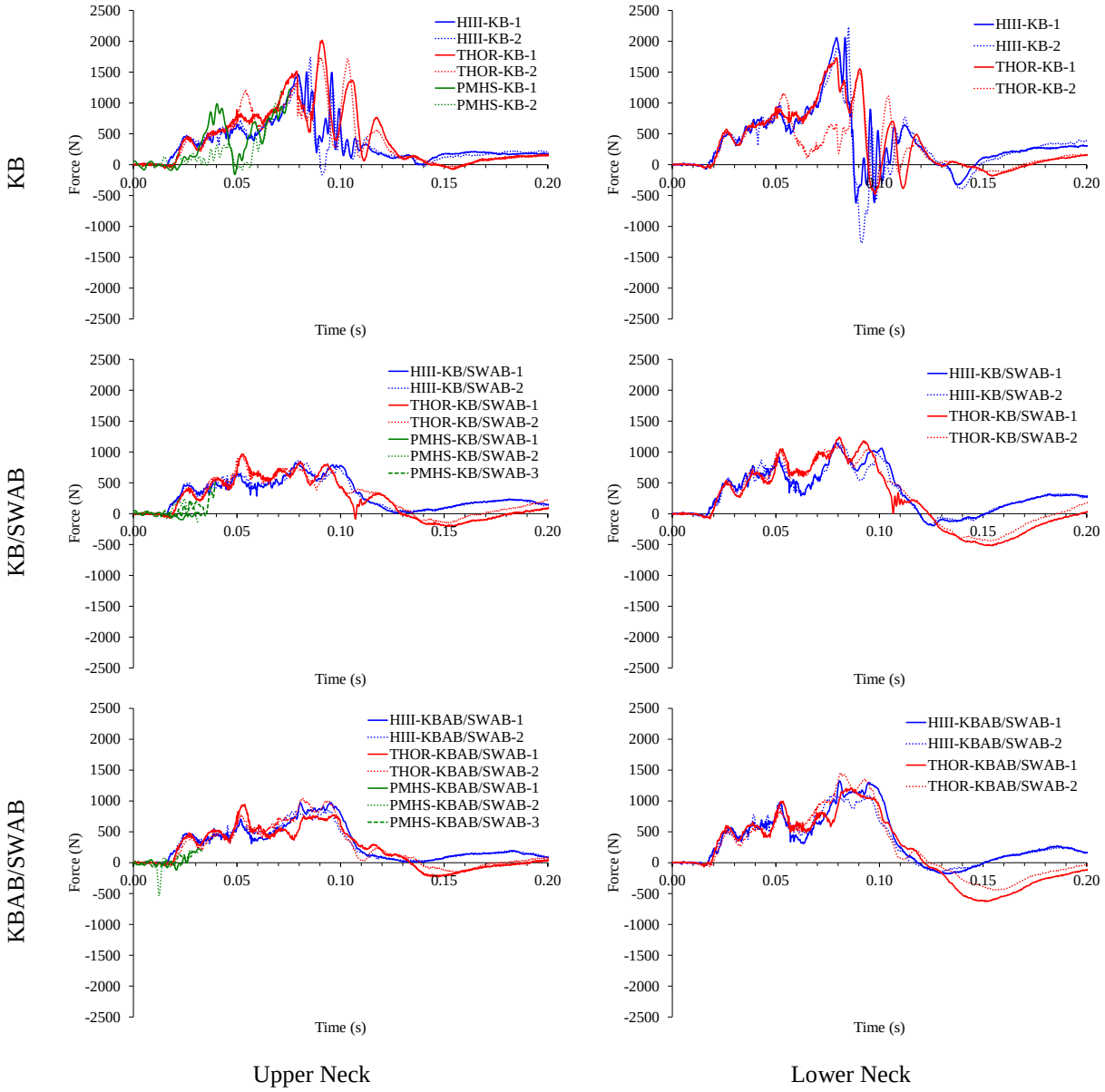

Figure 6.3: Upper neck (left) and lower neck (right) axial forces (Fz) for all conditions. Note: Tension is positive.

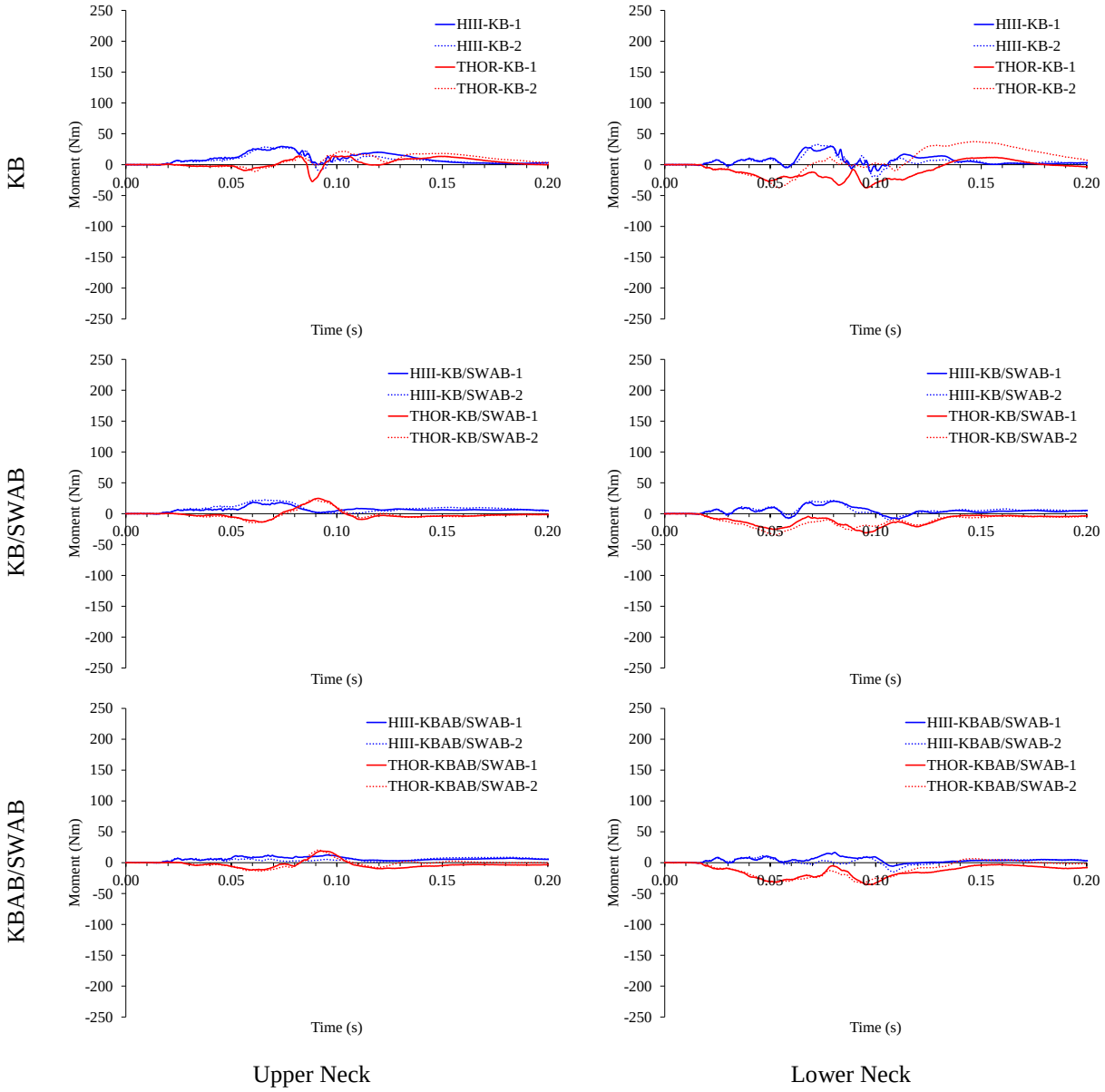

Figure 6.4: Upper neck (left) and lower neck (right) moments about the x-axis (Mx) for all conditions.
Note: Movement of the left ear toward the left shoulder is positive.

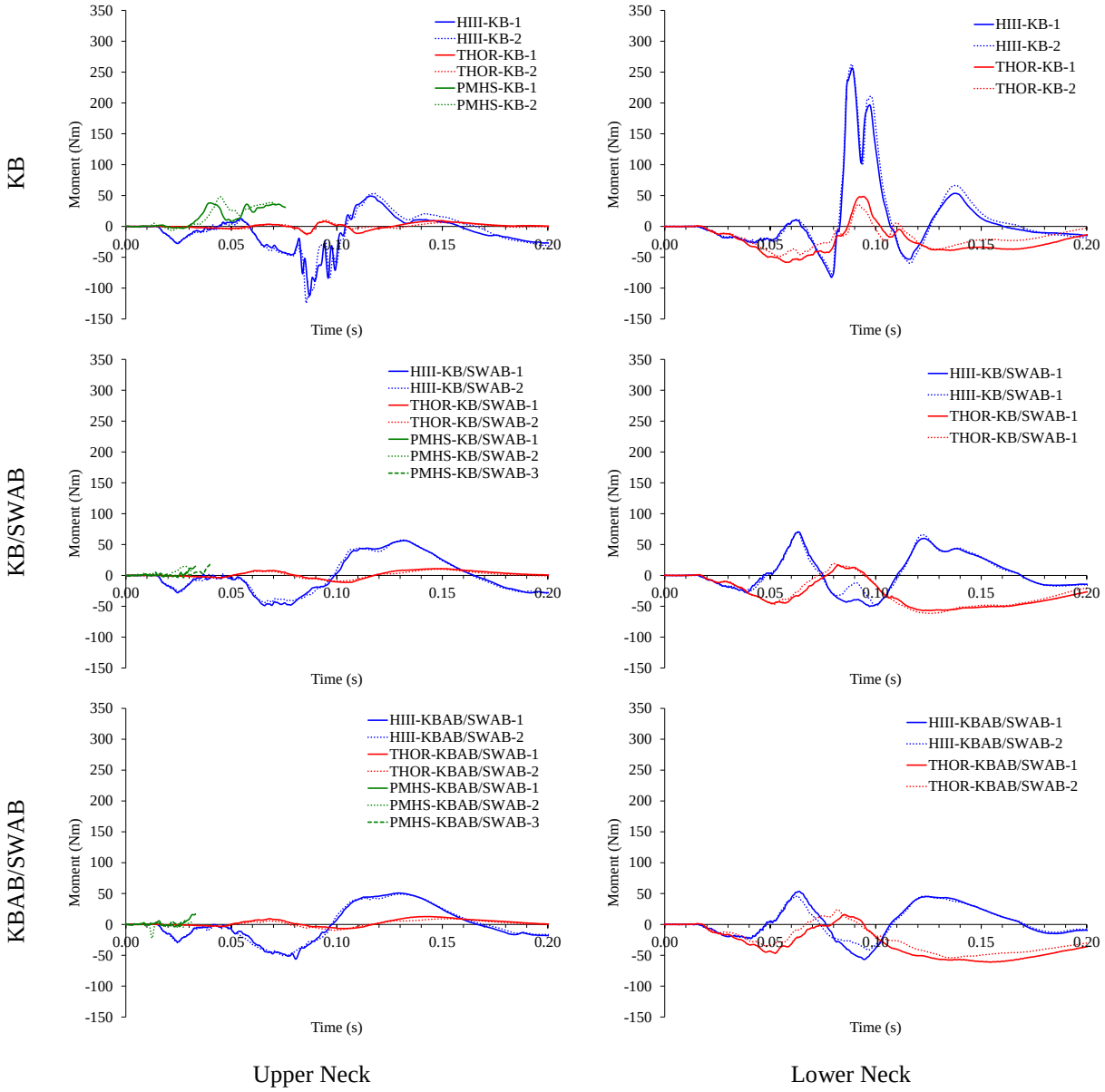

Figure 6.5: Upper neck (left) and lower neck (right) moments about the y-axis (My) for all conditions.
Note: Flexion is positive.

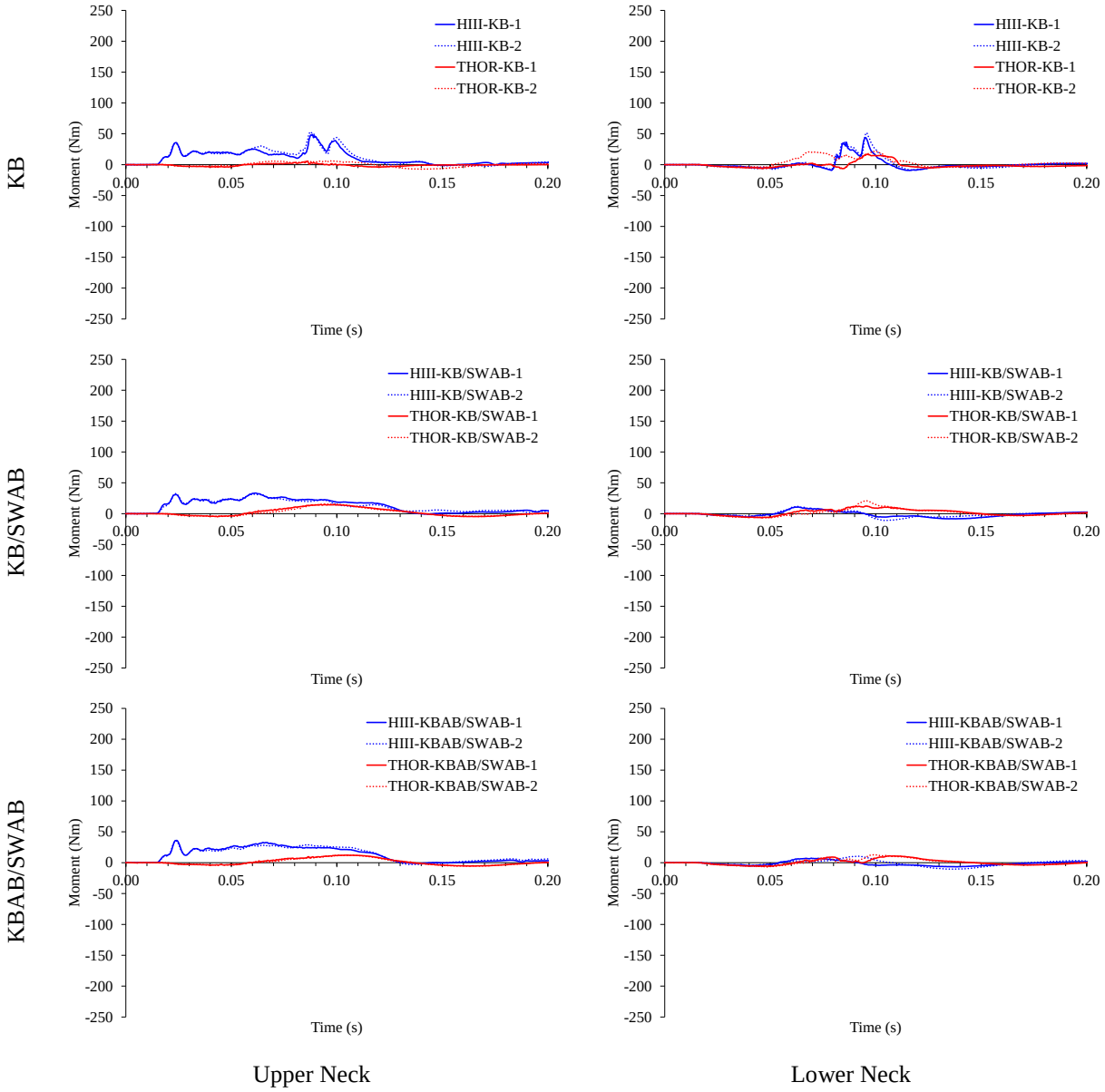

Figure 6.6: Upper neck (left) and lower neck (right) moments about the z-axis (Mz) for all conditions.
Note: Movement of the chin toward the left shoulder is positive.

When the forces and moments measured from the ATD load cells were compared to those calculated from inverse dynamics, the calculated and measured signals matched reasonably well before head contact (Figure A6.2 - Figure A6.4). The only exception was for the HIII AP shear forces and bending moments about the y-axis, which both showed a small peak in the measured forces and moments, corresponding to the initiation and termination of belt motion due to the pretensioner, that was absent in the calculated forces and moments. After head contact, only the measured axial forces for the KB/SWAB and KBAB/SWAB were reasonably approximated by the calculated axial forces for both ATDs. Therefore, it was assumed that the PMHS axial forces after head contact calculated using inverse dynamics would approximate the true PMHS upper neck axial forces. Compared to the ATDs, the approximated PMHS axial forces had similar peak magnitudes (Figure 6.8). There was a small difference in the shape of the time histories between the ATDs and PMHSs. The PMHSs had a delay in the onset of axial force or exhibited two peaks as opposed to the longer, uniform loading experienced by the ATDs.

The injury risk probabilities predicted from the ATD tests agreed with the injuries observed in the PMHS tests. All of the injury risk probabilities calculated for the ATDs indicated less than a 50% risk of an AIS3+ injury (Table 6.2). For both surrogates, the KB condition had a higher risk of AIS3+ injury than the KB/SWAB and KBAB/SWAB conditions. None of the PMHSs experienced an AIS3+ injury to the cervical spine. However, at least one PMHS in each condition experienced an AIS2 cervical spine injury (Table 6.3). In total 5 PMHSs experienced 9 AIS2 injuries. Six injuries consisted of dislocations and disc separations (Figure 6.7). Two injuries were anterior end plate fractures, and one loose joint was observed.

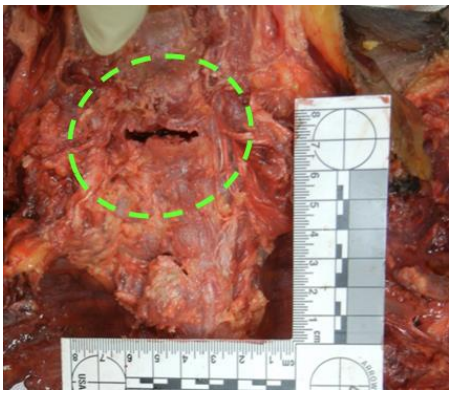

Figure 6.7: Exemplar C6/C7 disc separation.

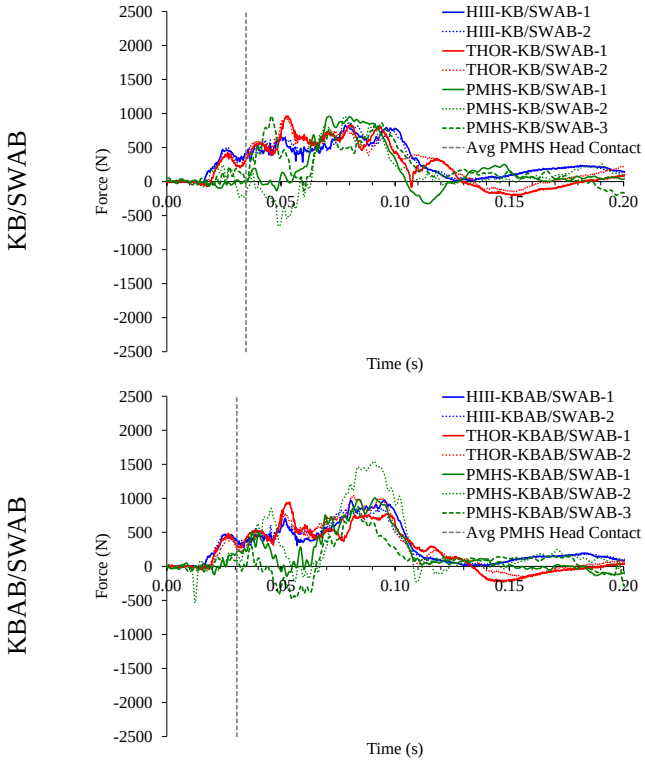

Figure 6.8: Upper neck axial forces for the KB/SWAB and KBAB/SWAB conditions for all surrogates.
Note: PMHS forces after head contact are approximate. Tension is positive.

Table 6.2: ATD injury risks and observed PMHS injuries.

Test ID	**N_{ij}**		**cN_{ij}**		**PMHS Observed Injury**
	N_{ij}	**P(AIS3+)**	**cN_{ij}**	**P(AIS3+)**	
HIII-KB-1	1.0062	0.2234	-	-	PMHS-KB-1: AIS2 PMHS-KB-2: None
HIII-KB-2	1.1822	0.2982	-	-	
HIII-KB/SWAB-1	0.4748	0.0918	-	-	PMHS-KB/SWAB-1: AIS2 PMHS-KB/SWAB-2: AIS2 PMHS-KB/SWAB-3: AIS2
HIII-KB/SWAB-2	0.4200	0.0832	-	-	
HIII-KBAB/SWAB-3	0.5558	0.1060	-	-	PMHS-KBAB/SWAB-1: None PMHS-KBAB/SWAB-2: None PMHS-KBAB/SWAB-3: AIS2
HIII-KBAB/SWAB-3	0.4947	0.0951	-	-	
THOR-KB-1	0.9153	0.1939	0.7094	0.4797	PMHS-KB-1: AIS2 PMHS-KB-2: None
THOR-KB-2	0.7823	0.1562	0.6059	0.3471	
THOR-KB/SWAB-1	0.4549	0.0886	0.3455	0.0888	PMHS-KB/SWAB-1: AIS2 PMHS-KB/SWAB-2: AIS2 PMHS-KB/SWAB-3: AIS2
THOR-KB/SWAB-2	0.4180	0.0829	0.3192	0.0723	
THOR-KBAB/SWAB-1	0.4286	0.0845	0.3322	0.0802	PMHS-KBAB/SWAB-1: None PMHS-KBAB/SWAB-2: None PMHS-KBAB/SWAB-3: AIS2
THOR-KBAB/SWAB-2	0.4972	0.0955	0.3878	0.1195	

Table 6.3: Observed PMHS cervical spine injuries and associated AIS scores.

Test ID	Injury Description	AIS Score
PMHS-KB-1	1) Dislocation/Disc Separation: C6/C7 2) Loose Joint C5/C6	1) AIS2 2) AIS2
PMHS-KB-2	No Injuries Observed	N/A
PMHS-KB/SWAB-1	1) Dislocation/Disc Separation: C3/C4	1) AIS2
PMHS-KB/SWAB-2	1) Dislocation/Disc Separation: C6/C7	1) AIS2
PMHS-KB/SWAB-3	1) Dislocation/Disc Separation: C4/C5 2) Dislocation/Disc Separation: C6/C7 3) Anterior End Plate Fracture: C6 (cortical bone only)	1) AIS2 2) AIS2 3) AIS2
PMHS-KBAB/SWAB-1	No Injuries Observed	N/A
PMHS-KBAB/SWAB-2	1) Osteophyte Fracture: Superior Aspect of C6 (no damage to vertebral body/disc)	N/A
PMHS-KBAB/SWAB-3	1) Dislocation/Disc Separation: C6/C7 2) Anterior End Plate Fracture C6 (cortical bone only)	1) AIS2 2) AIS2

Discussion

The THOR-M neck responses observed in the current study were different from the THOR-NT neck responses reported in the literature. In a previous study, Yoganandan *et al.* (2012) performed belted sled tests using the HIII, THOR-NT, and PMHSs at a similar severity (56.9 kph) as the current test series (56 kph). The peak axial force, AP shear force, and bending moment about the y-axis for the upper and lower neck from the Yoganandan *et al.* (2012) HIII tests were generally between those observed for the KB and SWAB conditions from the current HIII tests. Conversely, the THOR-NT in the Yoganandan *et al.* (2012) tests mostly experienced higher forces and moments than the THOR-M in the current test series. These test series are not directly comparable given the difference in the sled buck, restraint conditions, and sled pulse. However, the performance of the THOR-NT relative to the HIII in the Yoganandan *et al.* (2012) tests can serve as a reference point when comparing the THOR-M and the HIII in the current test series, providing insight regarding how modifications made to the THOR affected its performance relative to the HIII. For example, the upper neck axial forces were much higher for the THOR-NT compared to the HIII in the Yoganandan *et al.* (2012) tests, but the THOR-M and HIII had very similar upper neck axial forces in the current test series regardless of restraint condition. This finding may be a result of the decrease in axial neck stiffness between the THOR-NT and THOR-M [27]. The decrease in axial neck stiffness likely also influenced the upper neck bending moments about the

y-axis. The HIII and THOR-NT had similar upper neck bending moments about the y-axis in the Yoganandan *et al.* (2012) study, whereas the HIII had much greater upper neck bending moments about the y-axis than the THOR-M in the current study.

Not only were the THOR-M upper neck bending moments about the y-axis less than those of the HIII, the THOR-M moments were negligible. This is not consistent with the lower neck moments about the y-axis, which were comparable between the THOR-M and HIII SWAB conditions. The HIII still had greater lower neck bending moments than the THOR-M for the KB condition. However, unlike the upper neck, the THOR-M lower neck moments about the y-axis were appreciable. The low magnitude of the THOR-M upper neck bending moments were analyzed with respect to the kinematics previously reported in Albert *et al.* (2018). Specifically, the head linear and angular accelerations in the sagittal plane were analyzed with respect to the chest for the HIII and THOR-M. The differences between the head and chest kinematics were consistent between the HIII and THOR-M, which did not explain the differences between the upper neck moments. The THOR-M's neck compliance may have contributed to its negligible upper neck moments about the y-axis, but the design of the THOR-M neck may also be a contributing factor. Similar to the current study, Hoofman *et al.* (1998) reported negligible upper neck moments about the y-axis for an early version of the THOR neck. In their tests, the THOR head and neck complex was isolated and exposed to a sled pulse. They attributed the negligible bending moment to the design of the THOR neck, where movement of the head with respect to the neck within a certain range would not produce an upper neck moment, and force could be transmitted between the head and neck via the anterior and posterior cables external to the neck column. Since the loads through these cables would not be recorded by the upper neck load cell, Hoofman *et al.* (1998) suggested accounting for the loads measured at the spring load cells connected to the external cables when quantifying the upper neck moment about the y-axis. However, whether this explanation can be applied to the results of the current study is uncertain for two reasons. First, the design of the THOR neck, including the degree of resistance to head motion at the OC joint, has changed since the Hoofman *et al.* (1998) study [28]. Second, it is unclear whether Yoganandan *et al.* (2012) accounted for the spring loads in the upper neck moment calculation to obtain the appreciable upper neck moments that were observed.

Both ATDs had different responses compared to the PMHSs. The PMHSs experienced head contact earlier than the ATDs for all conditions. A possible explanation for head contact time differences are positioning differences between surrogates. On average, the PMHSs had the same nose to rim distance as the ATDs, but the PMHS chests were 1 cm closer to the steering hub than the ATDs [12]. However, the PMHSs were seated in the same seat detent, if not farther back than their ATD counterparts. Therefore, the PMHS heads were not close enough to the steering rim or SWAB, compared to the ATDs, to warrant an earlier head contact. Surrogate kinematics provide an alternate explanation for head contact differences. The PMHSs had slightly higher initial forward head accelerations [12], possibly due to the highly compliant PMHS neck, which could have produced an earlier head contact time. These higher accelerations could have also influenced the higher shear forces experienced by the PMHSs before head contact during the KB conditions relative to the ATDs. Although all surrogates had similar peak upper neck axial forces, the PMHSs had a different initial loading phase than the ATDs. These differences were reflected in the surrogate kinematics. Specifically, the PMHSs had lower initial vertical accelerations than the ATDs, and the PMHS heads did not move downward as quickly as the ATD heads. All surrogates had very different upper neck bending moments about the y-axis before head contact. The HIII and PMHSs experienced opposite bending moments, which could be due to their known limitations. The HIII neck, which is known to be too stiff, produced an extension moment due to inertial loading. Conversely, the THOR-M experienced a negligible moment before head contact, which was closer to the PMHS response than the HIII. The PMHSs experienced a substantial amount flexion before head contact; however, the degree of flexion may not be representative of a human response due to the lack of active musculature in the PMHS.

Both ATDs experienced a lower neck extension moment about the y-axis during the initial loading phase for all conditions. This was counterintuitive to the expectation that flexion would be experienced as the sled accelerated backward and the head moved forward. High speed video analysis revealed that two factors contributed to the extension moment. First, loading from the belt pretensioner moved the chest relative to head, inciting an inertial extension moment at the lower neck. Second, the motion of the sled backward initiated motion of the lower extremities via the foot plates. Loading through the lower extremities pushed the pelvis downward and backward into

the seat, causing the chest to pitch forward and down. While the chest began moving, the head stayed stationary, resulting in an extension moment.

The AIS3+ injury risk predictions of both ATDs matched the observed PMHS injuries. Only AIS2 injuries were observed for each condition, and none of the ATD injury risk metrics predicted more than a 48% chance of AIS3+ injuries. Both ATDs showed an increased probability of injury for the KB condition, which involved a head strike to the steering rim and/or hub, compared to the SWAB conditions. A threshold of 1.0 is imposed for N_{ij} in FMVSS 208, and the N_{ij} calculated for the HIII for both KB tests exceeded this threshold, whereas the THOR-M did not. For the THOR-M, two injury risks were calculated for each test using the two different injury metrics that were proposed for the future NCAP test [26]. The predicted injury risks were considerably higher for the cN_{ij} metric compared to the N_{ij} metric for the KB condition. This is a result of inherent differences in the risk curves. Specifically, the N_{ij} curve reaches approximately 100% probability at a value of 4, whereas the cN_{ij} curve reaches approximately 100% probability at 1.5. Since the current test series did not produce any AIS3+ injuries, it is unknown which proposed THOR-M metric is more accurate. Both criteria correctly predicted a low risk of AIS3+ injuries; however, the differences in probabilities between the criteria indicate that differences in prediction accuracy may arise under conditions that would produce more severe injuries.

Additional risk curves were proposed for N_{ij} that predict the probability of AIS2+, AIS4+, and AIS5+ injuries [25]. Since cervical spine AIS2 injuries were observed in this study, injury risk prediction was recalculated for the HIII and THOR-M using the AIS2+ curve (Table A6.6). All of the ATD tests under-predicted the observed rate of PMHS injuries for their respective conditions (KB: 50%, KB/SWAB: 100%, KBAB/SWAB: 33%). However, this injury risk curve was developed using different N_{ij} critical values than those used in this study, which were chosen to match those used in the US NCAP and FMVSS 208 [29].

There were several limitations to this study. First, the full PMHS neck force and moment time histories could not be compared to the ATDs due to head contact with vehicle components. However, the inclusion of the PMHS tests did allow an evaluation of ATD injury risk prediction. Additionally, the small sample size of the PMHS tests limited this evaluation. A larger sample

size, higher severity tests, or more frail PMHSs would be needed to validate the proposed THOR-M neck injury metrics since AIS3+ neck injuries were not observed in the current study. Finally, the results of these tests were specific to the experimental conditions. Different occupant compartment designs, restraint conditions, and sled pulses could produce different results.

Conclusions

Overall, the results of this study showed that the HIII and THOR-M had different neck kinetics for these restraint conditions, particularly for AP shear force and bending moment about the y-axis. These differences were likely due to the very different neck designs of the two ATDs. Despite these differences, both ATDs still accurately predicted a low risk of AIS3+ neck injury using N_{ij}. Finally, the decreased axial stiffness of the THOR-M neck relative to the THOR-NT seemed to result in decreased upper neck axial forces and bending moments.

References

1. Albert M, McCaig LF. *Emergency Department Visits for Motor Vehicle Traffic Injuries: United States, 2010-2011*. NCHS; 2015.
2. Lopez-Valdes FJ, Lau A, Lamp J, Riley P, Lessley DJ, Damon A, Kindig M, Kent R, Balasubramanian S, Seacrist T. Analysis of Spinal Motion and Loads During Frontal Impacts. Comparison between Pmhs and Atd. *Knee.* 2010;1404(1398):1402.
3. Seemann MR, Muzzy WH, Lustick LS. *Comparison of Human and Hybrid Iii Head and Neck Dynamic Response.* SAE Technical Paper;1986. 0148-7191.
4. Thunnissen J, Wismans J, Ewing C, Thomas D. *Human Volunteer Head-Neck Response in Frontal Flexion: A New Analysis.* SAE Technical Paper;1995. 0148-7191.
5. Wismans J, Spenny C. *Head-Neck Response in Frontal Flexion.* SAE Technical Paper;1984. 0148-7191.
6. Haffner M, Eppinger R, Rangarajan N, Shams T, Artis M, Beach D. Foundations and Elements of the Nhtsa Thor Alpha Atd Design. Paper presented at: 17th ESV Conference, Paper2001.
7. Hoofman M, van Ratingen MR, Wismans J. Evaluation of the Dynamic and Kinematic Performance of the Thor Dummy: Neck Performance. Proceedings of the International Research Council on the Biomechanics of Injury conference (IRCOBI); September 16-18, 1998.
8. Dibb AT, Nightingale RW, Chancey VC, Fronheiser LE. Comparative Structural Neck Responses of the Thor-Nt, Hybrid Iii, and Human in Combined Tension-Bending and Pure Bending. *Stapp car crash journal.* 2006;50:567.
9. Yoganandan N, Pintar FA, Moore J, Rinaldi J, Schlick M, Maiman DJ. Upper and Lower Neck Loads in Belted Human Surrogates in Frontal Impacts. Paper presented at: Annals of Advances in Automotive Medicine/Annual Scientific Conference; October, 2012; Seattle, WA.
10. Pintar FA, Yoganandan N, Baisden J. Characterizing Occipital Condyle Loads under High-Speed Head Rotation. *Stapp car crash journal.* 2005;49:33.
11. Parent D, Craig M, Moorhouse K. Biofidelity Evaluation of the Thor and Hybrid Iii 50th Percentile Male Frontal Impact Anthropomorphic Test Devices. *Stapp car crash journal.* 2017;61:227-276.

12. Albert DL, Beeman SM, Kemper AR. Occupant Kinematics of the Hybrid Iii, Thor-M, and Postmortem Human Surrogates under Various Restraint Conditions in Full-Scale Frontal Sled Tests. *Traffic injury prevention.* 2018;19(sup1):S50-S58.
13. Janovicz D, Fischer B. *Final Report of New Car Assessment Program Frontal Impact Testing of 2012 Toyota Camry Lee 4-Dr Sedan.* Washington, DC: USDOT; December 16, 2011 2011.
14. Naik S. *Final Report of New Car Assessment Program Testing of a 2005 Toyota Camry Le.* Washington, DC: U.S. Department of Transportation,; March 11, 2005 2005.
15. Albert DL, Beeman SM, McNally C, Kemper AR. Evaluation of Rigid Polyurethane Foam as a Surrogate Material for Knee Bolsters and Knee Bolster Airbags in Full Scale Frontal Sled Tests. Short Communications from Aaam's 60th Annual Scientific Conference. *Traffic Injury Prevention.* 2016/09/12 2016;17(sup1):205-208.
16. SAE. *Instrumentation for Impact Test.* Warrendale, PA: Society of Automotive Engineers;1995.
17. Vital J, Senegas J. Anatomical Bases of the Study of the Constraints to Which the Cervical Spine Is Subject in the Sagittal Plane a Study of the Center of Gravity of the Head. *Surgical and Radiologic Anatomy.* 1986;8(3):169-173.
18. Walker LB, Harris EH, Pontius UR. *Mass, Volume, Center of Mass, and Mass Moment of Inertia of Head and Head and Neck of Human Body.* SAE Technical Paper;1973. 0148-7191.
19. Chancey VC, Ottaviano D, Myers BS, Nightingale RW. A Kinematic and Anthropometric Study of the Upper Cervical Spine and the Occipital Condyles. *Journal of biomechanics.* 2007;40(9):1953-1959.
20. Beeman SM, Kemper AR, Duma SM. Neck Forces and Moments of Human Volunteers and Post Mortem Human Surrogates in Low-Speed Frontal Sled Tests. *Traffic injury prevention.* 2016;17(sup1):141-149.
21. Mertz HJ, Patrick L. *Investigation of the Kinematics and Kinetics of Whiplash.* SAE Technical Paper;1967. 0148-7191.
22. Clauser CE, McConville JT, Young JW. *Weight, Volume, and Center of Mass of Segments of the Human Body.* DTIC Document;1969.

23. McConville JT, Clauser CE, Churchill TD, Cuzzi J, Kaleps I. *Anthropometric Relationships of Body and Body Segment Moments of Inertia.* DTIC Document;1980.
24. Gennarelli TA, Wodzin E. *Abbreviated Injury Scale 2005 : Update 2008.* Barrington, IL: Association for the Advancement of Automative Medicine; 2008.
25. Eppinger R, Sun E, Bandak F, Haffner M, Khaewpong N, Maltese M, Kuppa S, Nguyen T, Takhounts E, Tannous R. Development of Improved Injury Criteria for the Assessment of Advanced Automotive Restraint Systems–Ii. *National Highway Traffic Safety Administration.* 1999:1-70.
26. Federal Register. *Part V. National Highway Traffic Safety Administration Consumer Information: New Car Assessment Program*. U.S. Department of Transportation; 2015.
27. Ridella S, Parent D. Modifications to Improve the Durability, Usability, and Biofidelity of the Thor-Nt Dummy. The 22nd International Technical Conference on the Enhanced Safety of Vehicles; June 13-15, 2011; Washington, DC.
28. Shams T, Rangarajan N, McDonald J, Wang Y, Platten G, Spade C, Pope P, Haffner M. Development of Thor Nt: Enhancement of Thor Alpha–the Nhtsa Advanced Frontal Dummy. Paper presented at: 19th ESV Conference, Paper2005.
29. NHTSA. *Final Decision Notice*. Department of Transportation; 2008.

Appendix

Table A6.1: Sensor information for all surrogates.

Signal Type	Surrogate		
	HIII	**THOR-M**	**PMHS**
Upper Neck Load Cell	1716A, Denton Rochester Hills, MI	10380JI4, Humanetics Plymouth, MI	-
Lower Neck Load Cell	1794A, Denton Rochester Hills, MI	10381JS1I4, Humanetics Plymouth, MI	-
Head Accelerometers	7264B-2000, Endevco San Juan Capistrano, CA	7264C-2000, Endevco San Juan Capistrano, CA	6DX PRO, DTS Seal Beach, CA
Head Angular Rate Sensors	ARS PRO-18K, DTS Seal Beach, CA	ARS PRO-8K, DTS Seal Beach, CA	6DX PRO, DTS Seal Beach, CA

Table A6.2: CFCs used to filter each signal type for all surrogates.

Signal Type	Surrogate		
	HIII	**THOR-M**	**PMHS**
Upper Neck Forces	1000	1000	-
Upper Neck Moments	600	600	-
Lower Neck Forces	1000	1000	-
Lower Neck Moments	600	600	-
Head Linear Accelerations	600	600	180
Head Angular Velocities	100	100	60

Table A6.3: Surrogate movements associated with positive upper and lower neck forces and moments.

Data Channel	Surrogate Movement	Polarity
Fx	Head rearward, chest forward	Positive
Fy	Head leftward, chest rightward	Positive
Fz	Head upward, chest downward	Positive
Mx	Left ear toward left shoulder	Positive
My	Chin toward sternum	Positive
Mz	Chin toward left shoulder	Positive

Table A6.4: N_{ij} critical values for the HIII and THOR-M.

Surrogate	$F_{Compression}$ (N)	$F_{Tension}$ (N)	$M_{Flexion}$ (Nm)	$M_{Extension}$ (Nm)
HIII	6160	6806	310	135
THOR-M	3640	2520	48	72

Table A6.5: cN_{ij} critical values for the THOR-M.

Surrogate	$F_{Compression}$ (N)	$F_{Tension}$ (N)	$M_{Flexion}$ (Nm)	$M_{Extension}$ (Nm)
THOR-M	4227	3216	67	94

Table A6.6: Predicted risks of AIS3+ and AIS2+ injuries for each ATD and the corresponding observed PMHS injuries.

Test ID	N_{ij}	P(AIS3+)	P(AIS2+)	PMHS Observed Injury
HIII-KB-1	1.0062	0.2234	0.2991	PMHS-KB-1: AIS2 PMHS-KB-2: None
HIII-KB-2	1.1822	0.2982	0.3450	
HIII-KB/SWAB-1	0.4748	0.0918	0.1844	PMHS-KB/SWAB-1: AIS2 PMHS-KB/SWAB-2: AIS2 PMHS-KB/SWAB-3: AIS2
HIII-KB/SWAB-2	0.4200	0.0832	0.1748	
HIII-KBAB/SWAB-3	0.5558	0.1060	0.1995	PMHS-KBAB/SWAB-1: None PMHS-KBAB/SWAB-2: None PMHS-KBAB/SWAB-3: AIS2
HIII-KBAB/SWAB-3	0.4947	0.0951	0.1880	
THOR-KB-1	0.9153	0.1939	0.2768	PMHS-KB-1: AIS2 PMHS-KB-2: None
THOR-KB-2	0.7823	0.1562	0.2462	
THOR-KB/SWAB-1	0.4549	0.0886	0.1809	PMHS-KB/SWAB-1: AIS2 PMHS-KB/SWAB-2: AIS2 PMHS-KB/SWAB-3: AIS2
THOR-KB/SWAB-2	0.4180	0.0829	0.1744	
THOR-KBAB/SWAB-1	0.4286	0.0845	0.1763	PMHS-KBAB/SWAB-1: None PMHS-KBAB/SWAB-2: None PMHS-KBAB/SWAB-3: AIS2
THOR-KBAB/SWAB-2	0.4972	0.0955	0.1885	

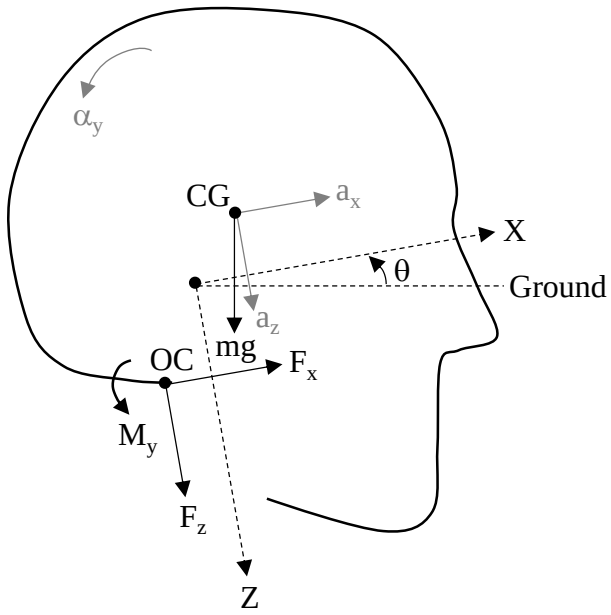

Figure A6.1: Force body diagram for calculation of upper neck forces and moments.

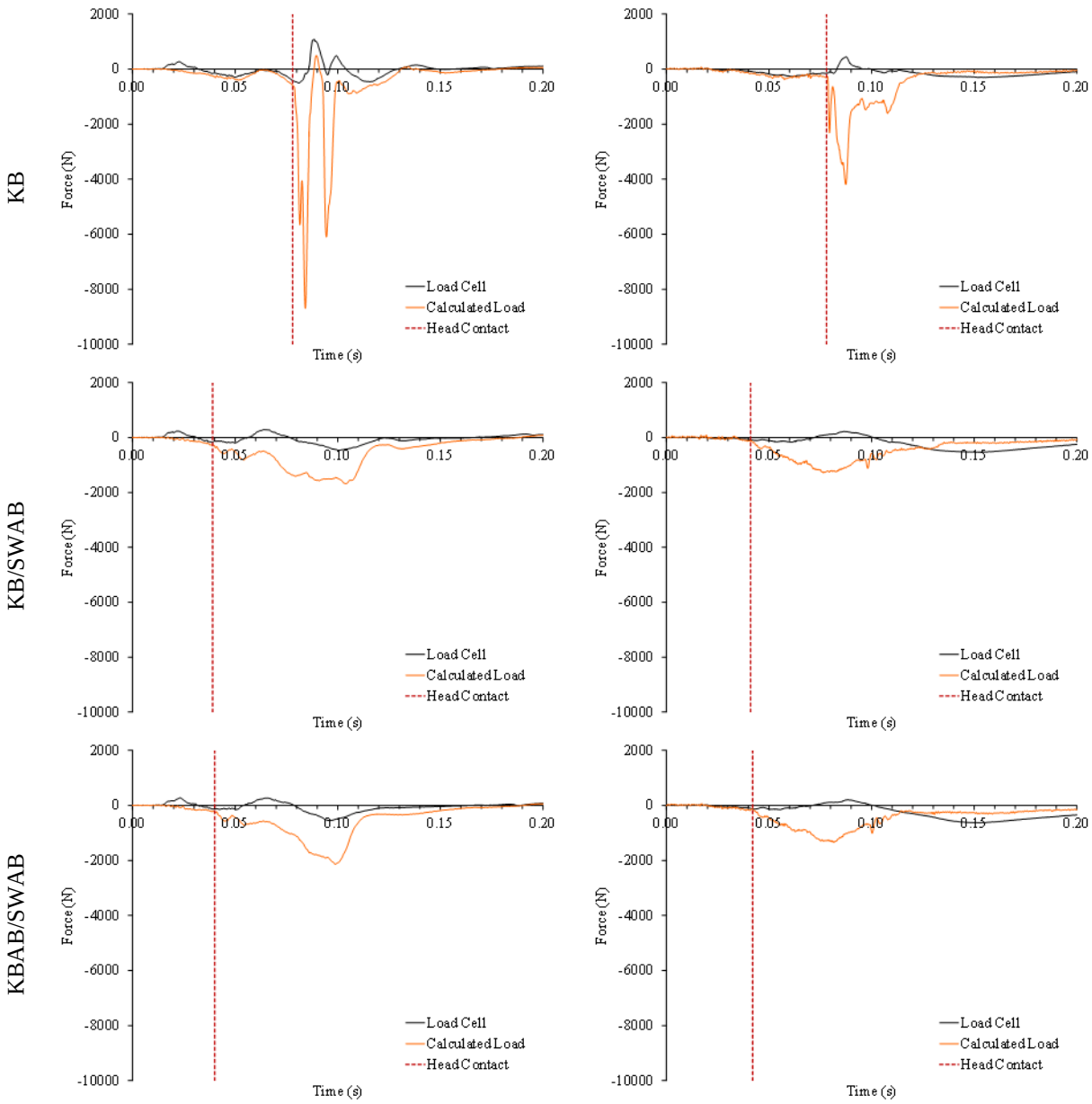

Figure A6.2: Exemplar HIII (left) and THOR-M (right) upper neck measured (load cell) and calculated (inverse dynamics) AP shear forces (Fx) for all conditions.
Note: Rearward head motion relative to the chest is positive.

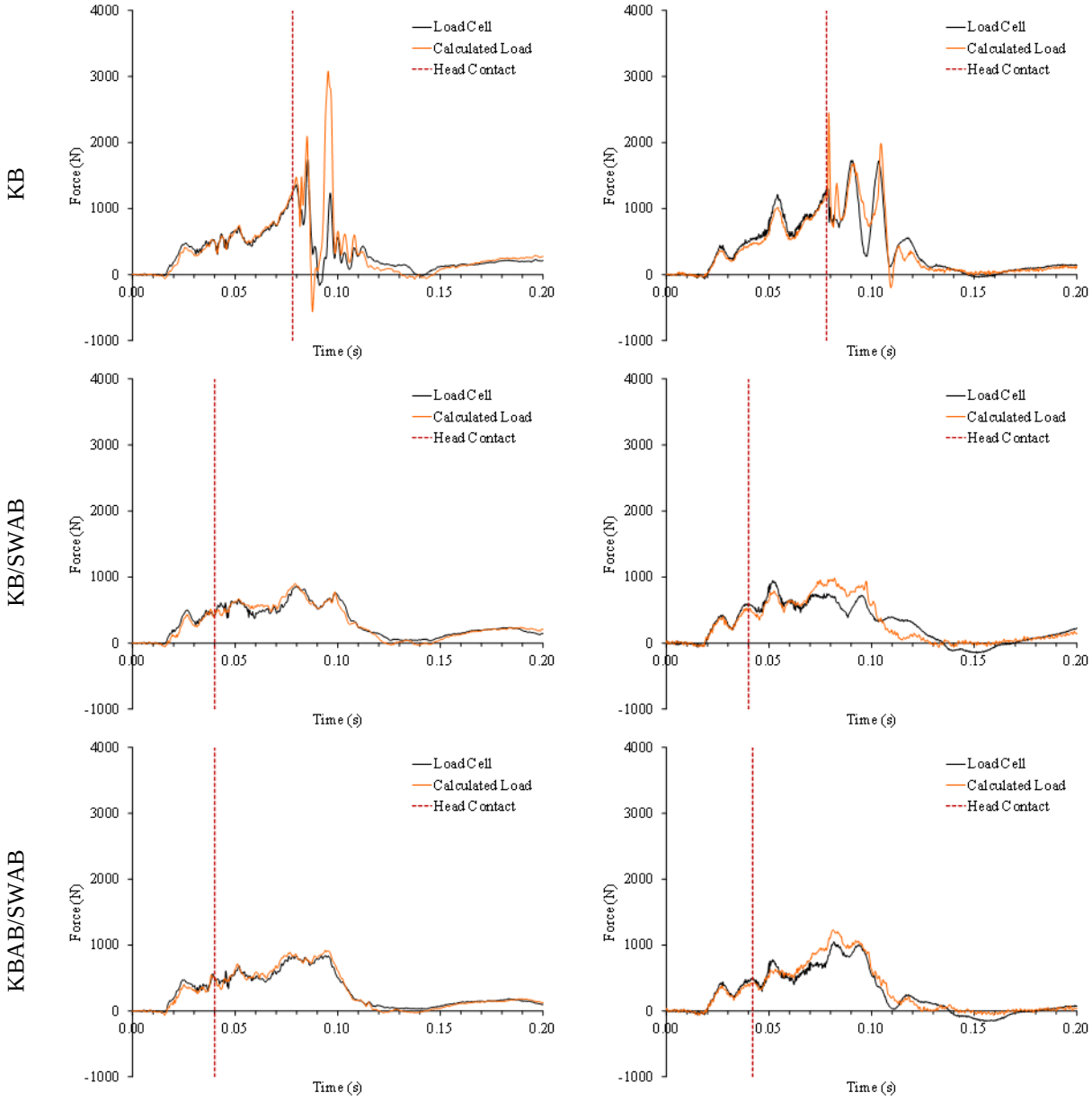

Figure A6.3: Exemplar HIII (left) and THOR-M (right) upper neck measured (load cell) and calculated (inverse dynamics) axial forces (Fz) for all conditions.
Note: Tension is positive.

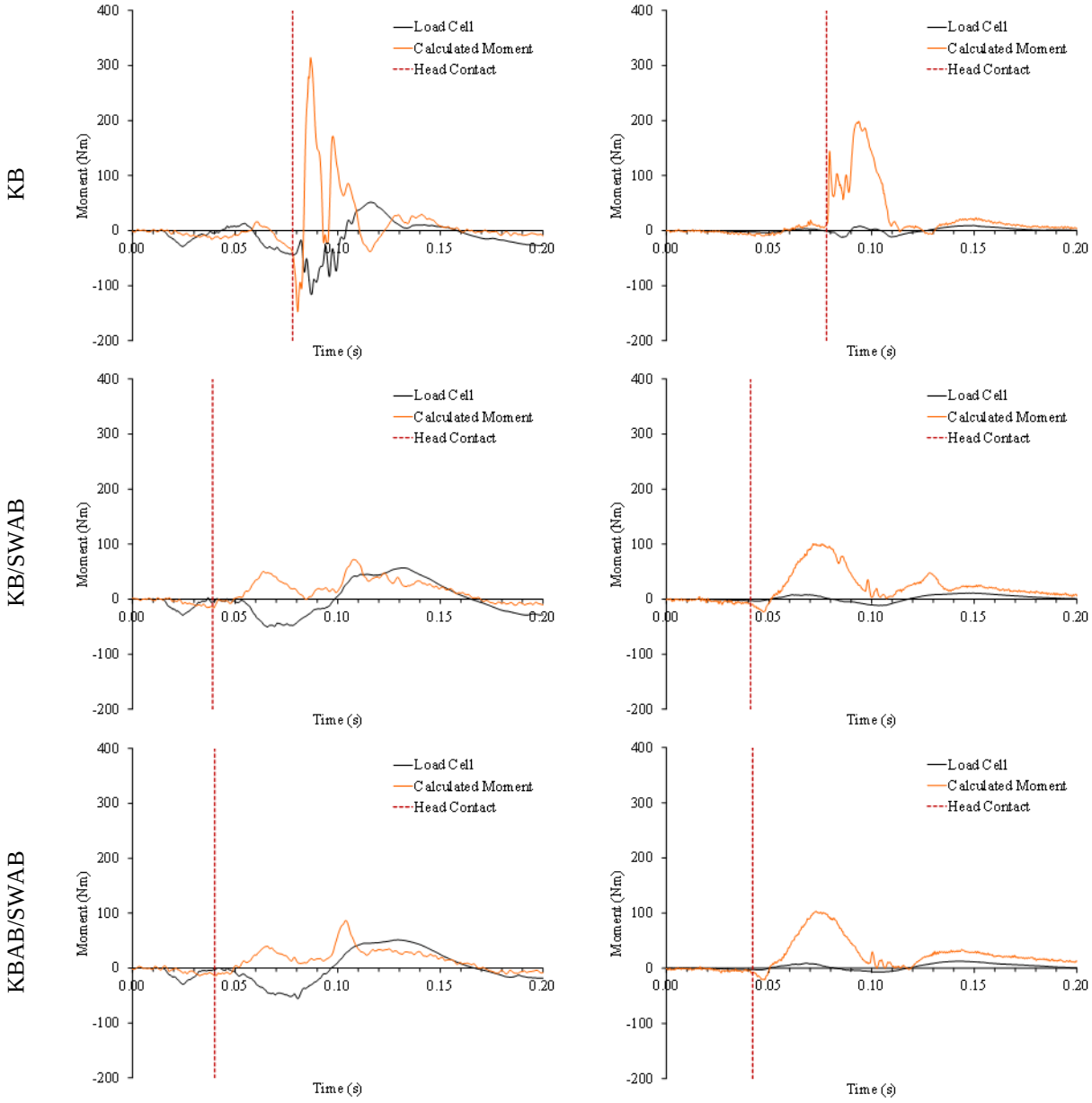

Figure A6.4: Exemplar HIII (left) and THOR-M (right) upper neck measured (load cell) and calculated (inverse dynamics) bending moments about the y-axis (My) for all conditions. Note: Flexion is positive.

Biomechanical Responses of Human Surrogates under Various Frontal Loading Conditions with an Emphasis on Thoracic Response and Injury Tolerance

Devon Albert

Preliminary Examination submitted to the faculty of the Virginia Polytechnic Institute and State University in partial fulfillment of the requirements for the degree of

Doctor of Philosophy
In
Biomedical Engineering

Andrew R. Kemper
Amanda M. Agnew
H. Clay Gabler
Warren N. Hardy
Joel D. Stitzel

4/19/2018
Blacksburg, VA

Keywords: Hybrid III, THOR, PMHS, knee bolster, knee bolster airbag, frontal motor vehicle collision, thoracic injury criterion, rib

TABLE OF CONTENTS

LIST OF FIGURES

LIST OF TABLES

CHAPTER 7: THORACIC RESPONSES OF THE HYBRID III, THOR-M, AND POST-MORTEM HUMAN SURROGATES UNDER VARIOUS RESTRAINT CONDITIONS IN FULL-SCALE FRONTAL SLED TESTS

Proposed Authors:

Albert DL, Beeman SM, Kemper AR

Introduction

In 2015, Motor vehicle collisions (MVCs) resulted in 35,092 fatalities and an estimated 2,443,000 injuries in the United States [1]. Accounting for the location of injuries sustained from MVCs reveals that the chest is the second most frequently injured body region [2]. Rib fractures, in particular, are a commonly observed chest injury for post-mortem human surrogates (PMHSs) as a result of frontal thoracic loading [3-8]. Furthermore, sustaining rib fractures in a MVC significantly increases the risk of in-hospital mortality [9]. In order to improve the thoracic injury prediction capabilities of frontal impact anthropomorphic test devices (ATDs), the Test device for Human Occupant Restraint (THOR) was designed to have a more anatomically biofidelic thorax than its predecessor, the Hybrid III (HIII) [10]. Specifically, the number of ribs were increased for the THOR, and the ribs were designed to have a downward slant. Additionally, the THOR clavicle was designed to be more anatomically correct. Finally, in order to make the response of the thorax more biofidelic, the coupling between adjacent and contralateral ribs was decreased in the THOR relative to the HIII.

Several studies have compared the thoracic responses of previous iterations of the THOR to the HIII and PMHSs during frontal sled tests [11-14]. However, these studies had two major limitations. First, each study only performed matched tests for one restraint condition: 3 point belt with or without an airbag, depending on the study. The biofidelity of the THOR's thoracic response may vary with respect to differences in external loading imposed on the ATD by different restraint conditions. Second, each study was performed on previous iterations of the THOR. The current version of the THOR, the THOR-M, is the product of several modifications made to previous designs [15,16]. With respect to the thorax, the design of the clavicle has been modified between iterations, which can influence shoulder belt interaction and thoracic loading.

Shaw *et al.* (2013) compared the thoracic response of the THOR-M to the HIII and PMHSs, and found that the THOR-M had a more biofidelic response. However, there were three relevant limitations to this study. First, similar to the studies mentioned previously, Shaw *et al.* (2013) only investigated the influence of one safety restraint condition, 3 point belt with no airbag. Second, the surrogates' lower extremities were fully restrained by a rigid knee bolster (KB) for the entire duration of the sled tests, limiting the interaction between the pelvis and lap belt. This constraint

does not replicate real-world crash conditions, where the entire body would translate forward and potentially contact the KB or knee bolster airbag (KBAB) in addition to the rotation of the upper body about the pelvis. Forward translation would alter how the occupant interacts with belt, thereby influencing the thoracic response. Third, this study did not include a belt retractor so the length of the shoulder belt was fixed, which limited torso flexion.

It is necessary to evaluate the comparative biofidelities of the HIII and THOR-M under different safety restraint conditions before the THOR-M is implemented as the standard frontal ATD. Specifically, the ATD thoraxes may exhibit different sensitivities and responses to the concentrated and diffuse loading of the seat belt and airbag, respectively. Furthermore, exposure to KBABs may limit the forward motion of the pelvis compared to a standard KB [18], changing how the ATD thoraxes interact with the belt and airbag. Therefore, the purpose of this study was to compare the thoracic responses of the HIII, THOR-M, and PMHSs during full-scale frontal sled tests under three safety restraint conditions: knee bolster (KB), knee bolster and steering wheel airbag (KB/SWAB), and knee bolster airbag and steering wheel airbag (KBAB/SWAB).

Methods

A total of 20 full-scale frontal sled tests were performed using the HIII, THOR-M, and PMHSs to quantify and compare occupant thoracic responses under three safety restraint conditions: KB, KB/SWAB, and KBAB/SWAB. Six tests each were performed with the HIII and THOR-M ATDs, while a total of eight PMHS tests were performed. For the ATD tests, two tests were performed for each of the three safety restraint conditions per ATD. For the PMHSs, two tests were in the KB condition and three tests each were performed in the KB/SWAB and KBAB/SWAB conditions. Each PMHS was used for only a single test. Detailed methodology for the sled tests was described in Chapter 3. In brief, the sled tests were designed to simulate the 2005 Toyota Camry (KB/SWAB) and 2012 Toyota Camry (KBAB/SWAB) frontal New Car Assessment Program (NCAP) full-scale crash tests [19,20]. All tests were performed on a 1.4 MN ServoSled^{TM} system (Seattle Safety LLC, Kent, WA) with a custom sled buck designed to match the interior of a 2013 Toyota Camry SE. New 2013 Toyota Camry vehicle components, including a three-point, U.S. driver side seatbelt (with a pretensioner, 4kN load limiter, retractor, and buckle), seat, steering wheel, steering column, and steering wheel airbag (when applicable) were used for each test. The KB and KBABs were

simulated using 65 and 19 psi rigid polyurethane foams, respectively. The vehicle acceleration pulse of the 2012 Toyota Camry NCAP test (ΔV = 56 kph, peak acceleration = 470 m/s^2) was employed for each test.

Positioning of the surrogates and vehicle components (i.e. seat track, seat back, steering column, seat belt, and KB) were guided by the NCAP Test Procedure Document [21] and the NCAP Report for the 2012 Toyota Camry [19]. Detailed positioning information and knee bolster geometry were provided in Chapters 3 and 2, respectively. Overall, the offsets between the surrogate and vehicle components were maintained across tests in order to ensure valid comparisons between conditions and surrogates.

Instrumentation

The ATDs were both instrumented with internal sensors to measure deflection of the sternum/rib cage. Sternum deflection was measured in the HIII via a potentiometer and slider assembly. The THOR-M was instrumented with four Infra-Red Telescoping Rod for the Assessment of Chest Compression (IR-TRACC) assemblies (472-3550-R5, Humanetics Innovative Solutions, Farmington Hills, MI) to measure 3 dimensional rib cage deflection at four points: upper right, upper left, lower right, and lower left. The upper points were located approximately 3.8 cm from the sternum at the level of the THOR-M's third rib. The lower points were located approximately 8.3 cm from the sternum at the level of the THOR-M's sixth rib.

All surrogates were also instrumented with chest bands to measure external thoracic deflection because of the limitations of internal deflection instrumentation. For example, the HIII and THOR-M internal deflections were measured at different locations and could not be compared across surrogates. Furthermore, chest bands are commonly used to measure external thoracic deflection of PMHSs due to the limitations associated with invasive, internal deflection measurement techniques. Measurement of internal thoracic deflection using trans-thoracic rods [22,23] requires an unobstructed view of the back of the subject, which was not possible with a production seat. Similarly, the motion capture method developed by Shaw *et al.* (2009), requires an unobstructed view of the anterior chest, which is difficult to maintain with a SWAB deployment [24]. Therefore, each surrogate was instrumented with 59 channel chest bands (8641, Humanetics, Plymouth, MI)

on the upper and lower thorax to obtain external chest deflections. An effort was made to place the chest bands at comparable locations between surrogates based on the distance of each band from the neck or sternal notch of the surrogate (Figure 7.1). As such, the top band was aligned approximately with the lateral aspect of ribs 1, 3, and 4 for the HIII, THOR, and PMHSs, respectively. The lower band was aligned approximately with rib 5 for the ATDs and the xyphoid process for the PMHSs. A heavy duty, double-sided adhesive tape was used to secure the chest bands to the ATDs. The chest bands were secured to the PMHSs by stitching the band to the skin and taping the overlapping sections of the band together. Once the chest bands were secured to the surrogates, co-flex was wrapped around the surrogate chests and chest bands to ensure a tight connection between the bands and the chest and to protect the chest band wires.

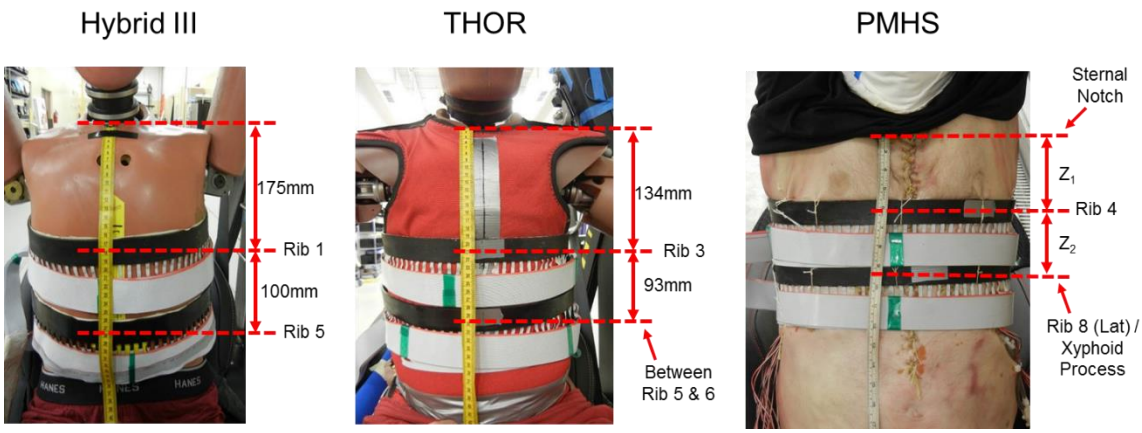

Figure 7.1: Locations of chest bands on each surrogate.
Note: See Table 7.1 for PMHS locations.

Table 7.1: Chest band locations on the PMHS.

Test	Z_1: Distance from Sternal Notch to Upper Band (mm)	Z_2: Distance from Upper Band to Lower Band (mm)
PMHS-KB-1	120	78
PMHS-KB-2	101	88
PMHS-KB/SWAB-1	110	70
PMHS-KB/SWAB-2	85	82
PMHS-KB/SWAB-3	120	84
PMHS-KBAB/SWAB-1	85	108
PMHS-KBAB/SWAB-2	99	82
PMHS-KBAB/SWAB-3	89	101
Average:	101	87

The PMHS thoraces were also instrumented with 23 uniaxial strain gages to measure rib strain during the sled tests (Figure 7.2). One strain gage was applied to the sternum between ribs 3 and 4. Another strain gage was applied to the midpoint of the left clavicle. Fourteen strain gages were applied to the anterior aspect of ribs 2-9 and the lateral aspect of ribs 3-8 on the right side. The remaining seven gages were applied to the anterior aspect of ribs 2-8 on the left side. Anterior gages were positioned approximately 2 cm from the costal-cartilage junction, while the lateral gages were positioned on the lateral-most aspect of the ribs. Before applying the gages, the soft tissue and periosteum were removed from the area of application. The area was cleaned with isopropyl alcohol and dried with acetone. A catalyst (M-Bond 200 Catalyst, Vishay Micro-Measurement, Shelton, CT) was applied to the bone and the back of each strain gage before the gage was adhered to the bone. The adhesive (M-Bond 200 Adhesive, Vishay Micro-Measurement, Shelton, CT) was applied to the gage. Then the gage was positioned on the bone and held in place with pressure for several minutes. A protective coating (M-Coat-D Adhesive, Vishay Micro-Measurement, Shelton, CT) was applied to the top of the gage and the bone immediately surrounding the bone in order to seal the gage against fluids.

All data were collected at 20 kHz (TDAS Pro & G5, DTS, Seal Beach, CA). The HIII and THOR-M internal displacements were filtered at SAE channel frequency class (CFC) 600. The PMHS rib strains were filtered at CFC 600. The chest band data were not filtered.

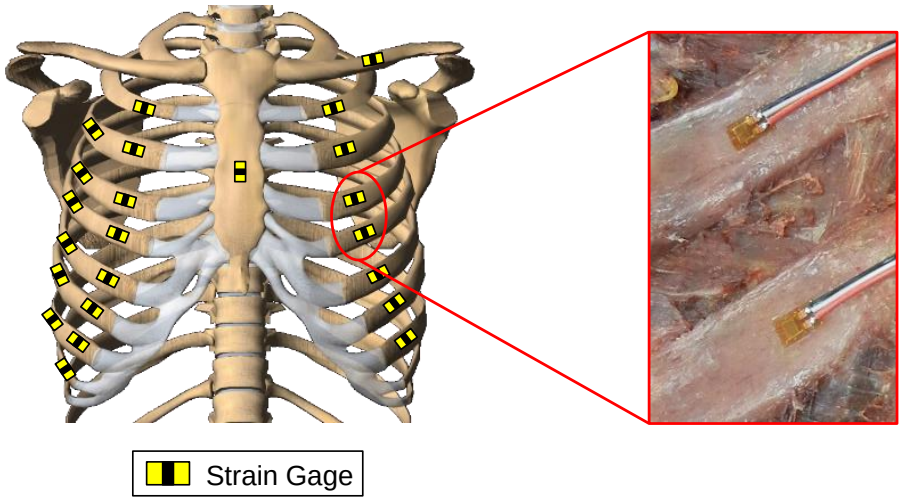

Figure 7.2: PMHS thorax strain gage instrumentation.

Data Analysis

The chest band data were utilized to quantify deflection of the upper and lower anterior chest. First, upper and lower chest contours were generated at 1 ms intervals for each test using the RBandPC software (Conrad Technologies, Paoli, PA). Points on the anterior chest contour were paired with points on the posterior chest contour that were in the same sagittal plane. The chord deflection of each pair (Figure 7.3), including the spine and sternum, were calculated for each chest band at each time point. Each deflection was normalized by the initial anterior/posterior chest depth at that location. The location of maximum deflection was then determined for both the upper and lower chest bands.

Chest band normalized deflections for six locations of interest were qualitatively and quantitatively compared between test conditions and between subject types. The locations of interest included the upper sternum, upper and lower locations of maximum deflection, two points located 3.8 cm to the left and right of the upper sternum on a 50th percentile male, and two points located 8.3 cm to the left and right of the lower sternum on a 50th percentile male. The locations on the left and right sides of the thorax approximately corresponded to the locations of the internal instrumentation of the THOR-M. In order to quantify chest deflection at analogous locations for all surrogates, the left and right locations of interest were scaled for each surrogate. The upper and lower curvilinear distances between the sternum and left/right locations of interest (upper: 3.8 cm,

lower: 8.3 cm) were normalized by the chest circumference of a 50th percentile male [25]. The normalized distances were then scaled to each surrogate using the surrogate's chest circumference. Peak deflections, the timing of peak deflections, and the overall time histories were compared for each location of interest between surrogates and restraint conditions. The locations of maximum deflection were also compared between surrogates and restraint conditions.

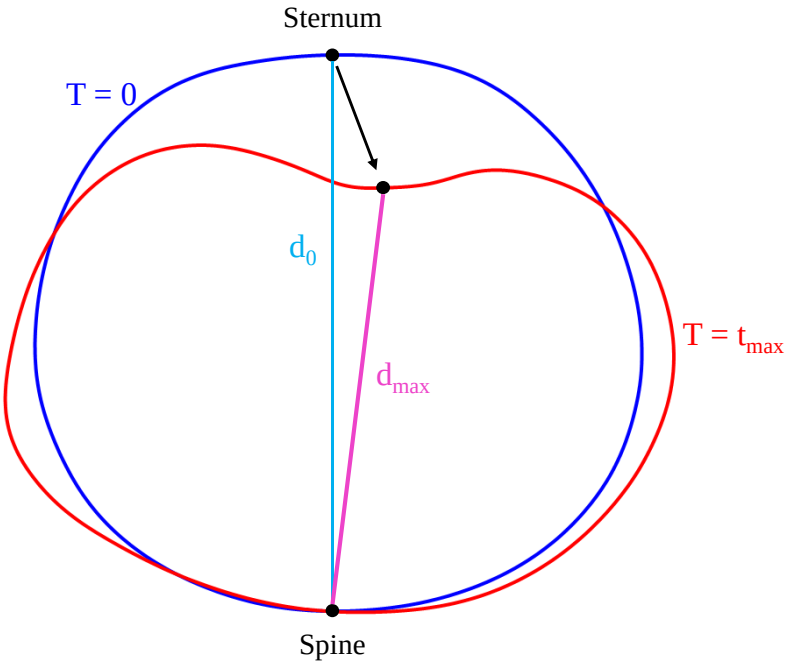

Chord Deflection = $d_{max} - d_0$

Figure 7.3: Calculation of chord chest deflection.

The similarities in deflection time histories between surrogates were evaluated using ISO/TS 18571 (referred to as ISO throughout the chapter) [26] by comparing the PMHS response to the HIII and THOR-M, and the HIII response to the THOR-M within each restraint condition. The ISO rating metric was also used to compare deflection time histories between the KB condition (reference) and the KB/SWAB condition (comparison) and between the KB/SWAB (reference) condition and the KBAB/SWAB condition (comparison) for each surrogate type. The methodology used to apply the ISO rating metric to the kinematic data in Chapter 3 was also used for the thoracic data in this chapter. In brief, a characteristic average was calculated to generate an average deflection time history for each condition within a surrogate. Then, the average deflection

time histories were compared between surrogates and conditions as described in Chapter 3. These comparisons were made for each location of interest, except for the locations of maximum deflection because these could occur at different relative locations on the chest and, consequently, would not be directly comparable. The ISO specification applies qualitative evaluations of excellent (a score over 0.94), good (over 0.8), fair (over 0.58), and poor (0.58 and below) to the calculated scores. These terms may be used throughout the chapter to categorize scores, but analyses will focus on quantitative comparisons between scores.

The internal deflection measurements quantified by the HIII and THOR-M's respective internal thoracic instrumentation were evaluated to determine their sensitivity to restraint condition and how they compared to external chest band measurements. To evaluate the effect of safety restraints, the internal deflections were compared between conditions within each surrogate. The observed trends were then compared to those observed in the chest band deflections. Additionally, ratios were generated between the internal deflections and external deflections at analogous locations to determine whether a consistent relationship existed between the internal and external measures. Finally, the locations of maximum external deflection were compared to the locations of the internal instrumentation. It should be noted, the THOR-M IR-TRACC data was processed according to established methods [27].

Each PMHS was dissected after the sled test to record and categorize any sternum, clavicle, and rib fractures that occurred. The number and locations of fractures were noted and converted to a severity score using the Abbreviated Injury Scale (AIS) [28]. Time of fracture and strain at the time of fracture were quantified for fractured ribs that were instrumented with strain gages. Time of fracture was used to quantify the time of AIS3+ injury and the deflections occurring at the time of injury for the upper sternum, location of maximum deflection, and d_{max} (the maximum deflection at any of the following locations: upper sternum, upper left, upper right, lower left, and lower right) as defined by Kuppa and Eppinger (1998). The deflections at the time of AIS3+ injury were then compared to the peak deflections observed at the specified locations in order to evaluate injury criteria performance.

Thoracic injury risk was evaluated for all surrogates. The risk of sustaining an AIS3+ injury was calculated for the HIII using Equation 1 [30], which incorporates age and the maximum deflection from the HIII chest potentiometer (δ_{max}). The HIII injury risk was calculated for a 35 year old male (equivalent to the Frontal NCAP injury risk function) and the average age of the PMHSs tested for that condition. The risk of sustaining an AIS3+ injury was calculated for the THOR-M using the Multi-point Thoracic Injury Criterion of Peak Resultant Deflection (Rmax) and PCA score [31], which both used the IR-TRACC data (Equations 2 - 5). The THOR-M injury risks were also calculated for a 35 year old male and the average age of the PMHSs tested for that condition. The risk of sustaining an AIS3+ injury was calculated for the PMHSs using two injury risk functions (Equations 6 - 7) from Kuppa and Eppinger (1998) based on maximum deflection (d_{max}) and chest acceleration (A_s) and one injury risk function (Equation 8) from Laituri *et al.* (2005) based on age and sternum deflection ($\overline{UC}$) [29,30]. The PMHS injury risks were first calculated using the censored data (i.e., peak deflections) defined in the injury criteria. Then, the injury risks were calculated using the uncensored deflections that were calculated at the time an AIS3 injury was sustained. The thoracic injuries observed in the PMHS tests were used as a basis to evaluate the accuracy of the calculated injury risks.

Equation 1	$p(AIS3+) = \frac{1}{1+e^{12.597-0.05861(Age)-1.568(\delta_{max})^{0.4612}}}$	HIII risk function (δ_{max})
Equation 2	$R_{max} = max(UL_{max}, UR_{max}, LL_{max}, LR_{max})$ $where\ [U/L\|R/L]_{max} = max\left(\sqrt{[L/R]X^2_{[U/L]S} + [L/R]Y^2_{[U/L]S} + [L/R]Z^2_{[U/L]S}}\right)$	THOR risk function (R_{max})
Equation 3	$p(AIS3+) = 1 - e^{-\left[\frac{R_{max}}{e^{4.4853-0.0113age}}\right]^{5.03896}}$	
Equation 4	$PCA\ Score = 0.485\left(\frac{up_{tot}}{17.509}\right) + 0.499\left(\frac{low_{tot}}{15.526}\right) + 0.493\left(\frac{up_{dif}}{10.479}\right) + 0.522\left(\frac{low_{dif}}{11.996}\right)$ $where\ up_{tot} = \|UL\|_{max} + \|UR\|_{max}, up_{dif} = \|UL - UR\|_{max}, low_{tot} = \|LL\|_{max} + \|LR\|_{max}, low_{dif} = \|LL - LR\|_{max}$	THOR risk function (PCA)
Equation 5	$p(AIS3+) = 1 - e^{-\left[\frac{PCA\ Score}{e^{2.6092-0.0113age}}\right]^{4.4444}}$	
Equation 6	$p(AIS3+) = \frac{1}{1+e^{-(-1.3817+7.6481d_{max})}}$	PMHS risk function (d_{max})
Equation 7	$p(AIS3+) = \frac{1}{1+e^{-(-6.1832+0.0755A_S+13.3052d_{max})}}$	PMHS risk function (d_{max}, A_s)

Equation 8	$p(AIS3+) = \frac{1}{1+e^{-(-12.5972+0.058614Age+26.90118\overline{UC})}}$	PMHS risk function ($\overline{UC}$)

Results

Internally Measured Deflections

The HIII internal deflection instrumentation at the sternum was sensitive to changes in restraint condition (Figure 7.4). The KB condition produced the greatest deflections, while the KBAB/SWAB condition produced the lowest. However, the differences between conditions were relatively small. The difference between the peak deflections for the KB and KB/SWAB conditions was approximately 5 mm. Similarly, the difference between the peak deflections for the KB/SWAB and KBAB/SWAB conditions was approximately 5 mm.

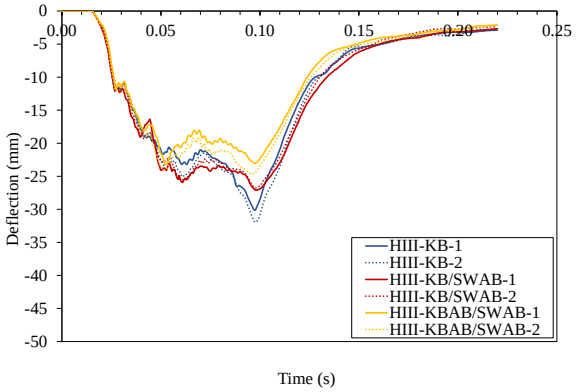

Figure 7.4: Chest deflection from the HIII chest potentiometer.
Note: Compression is negative.

The THOR-M internal deflections varied with respect to location (Figure 7.5, Figure 7.6). For the x direction, the largest deflections were at the upper right location, where the thorax experienced approximately 40 mm of compression. The lower right and upper left thorax also experienced compression with peak deflections in the x direction of approximately 25 mm and 10 mm, respectively. Conversely, the lower left thorax experienced between 10 and 20 mm of expansion. Medial/lateral deflections were low in magnitude compared to the other directions. Both locations on the upper chest predominately deflected medially, presumably toward the seatbelt. For the lower chest, both locations mainly deflected leftward. For the deflections in the z direction, both locations on the left side of the thorax initially experienced a downward deflection, which was

followed by a larger upward deflection. A similar trend was seen at the lower right, where the initial downward deflection was almost negligible. The upper right was the only location that experienced downward deflections that were higher in magnitude than the upward deflections. The downward deflection also had a greater duration at this location.

Similar to the HIII, the THOR-M's internal resultant deflections were sensitive to change in restraint conditions, but the differences were low in magnitude. For both the upper and lower left, the KB condition resulted in the highest resultant deflections, while the KBAB/SWAB condition had the lowest (Figure 7.7). Conversely, the KB condition produced the lowest resultant deflections on the right side. For the upper and lower right, the KB/SWAB condition resulted in slightly higher deflections than the KBAB/SWAB condition. The sizable deflections in the z direction drove some of these differences. For example, calculating the transverse (x,y) resultant deflections, which were more representative of the planar deflections measured by the chest bands, produced a much lower deflection for the upper left than the x,y,z resultant (Figure 7.8). This resulted in different trends between conditions for the transverse resultant. However, it should be noted that the differences in magnitude between conditions were small for all locations, regardless of the type of resultant that was calculated.

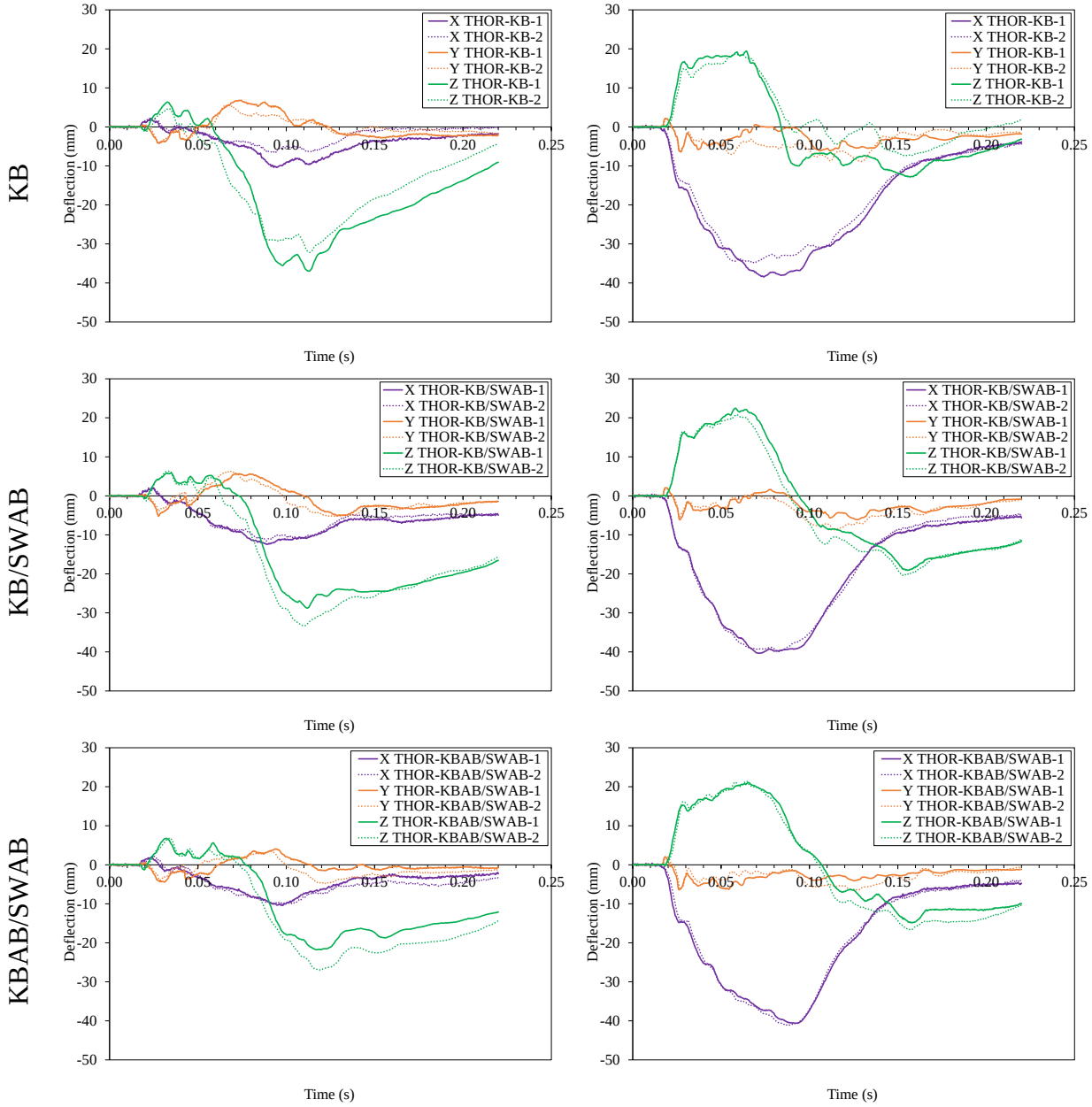

Figure 7.5: THOR IR-TRACC x, y, and z deflections at the upper left (left) and upper right (right) for all conditions.
Note: Chest compression (x) is negative, rightward deflection (y) is positive, and downward deflection (z) is positive.

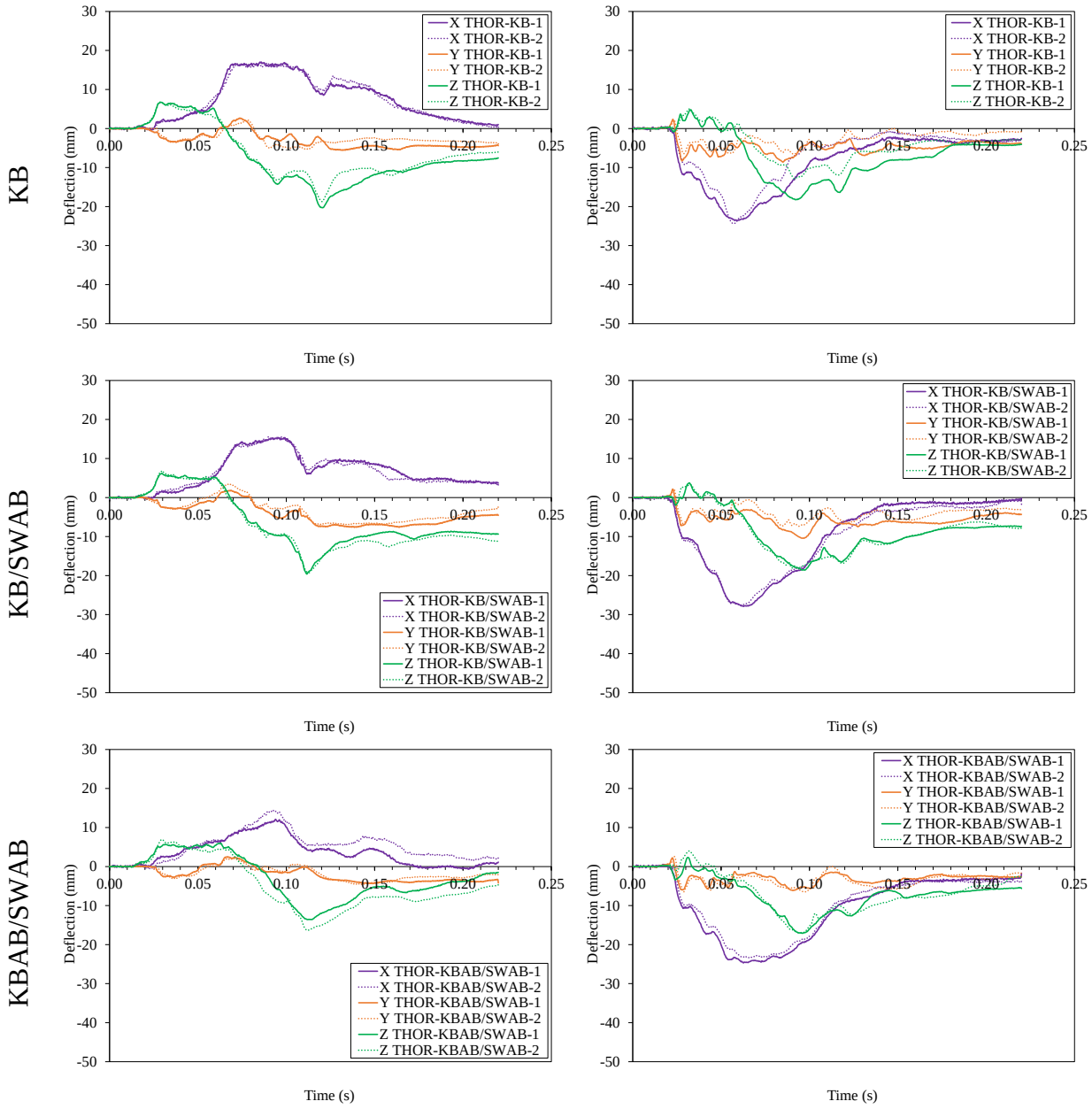

Figure 7.6: THOR IR-TRACC x, y, and z deflections at the lower left (left) and lower right (right) for all conditions.
Note: Chest compression (x) is negative, rightward deflection (y) is positive, and downward deflection (z) is positive.

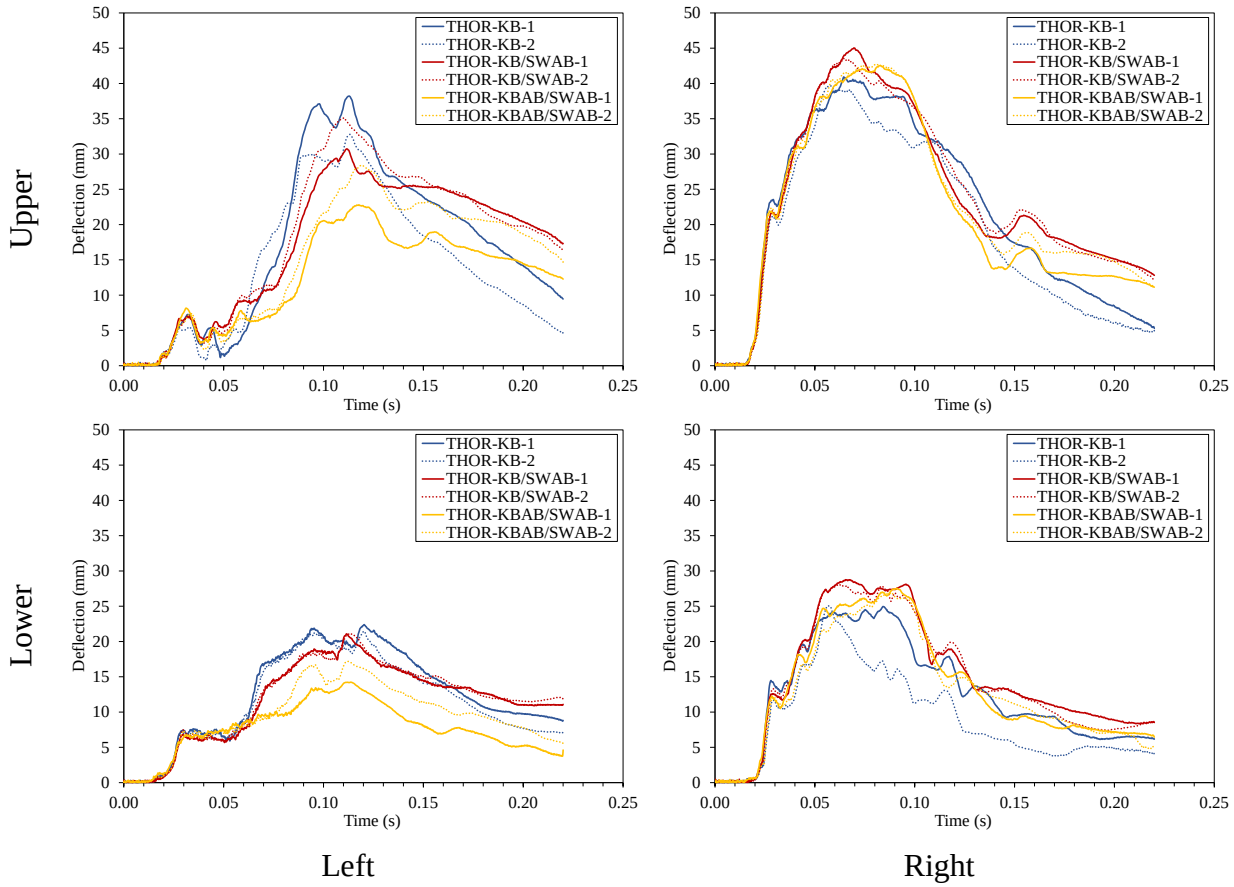

Figure 7.7: Left and right upper (top) and lower (bottom) IR-TRACC resultant (x,y,z) deflection for the THOR-M.

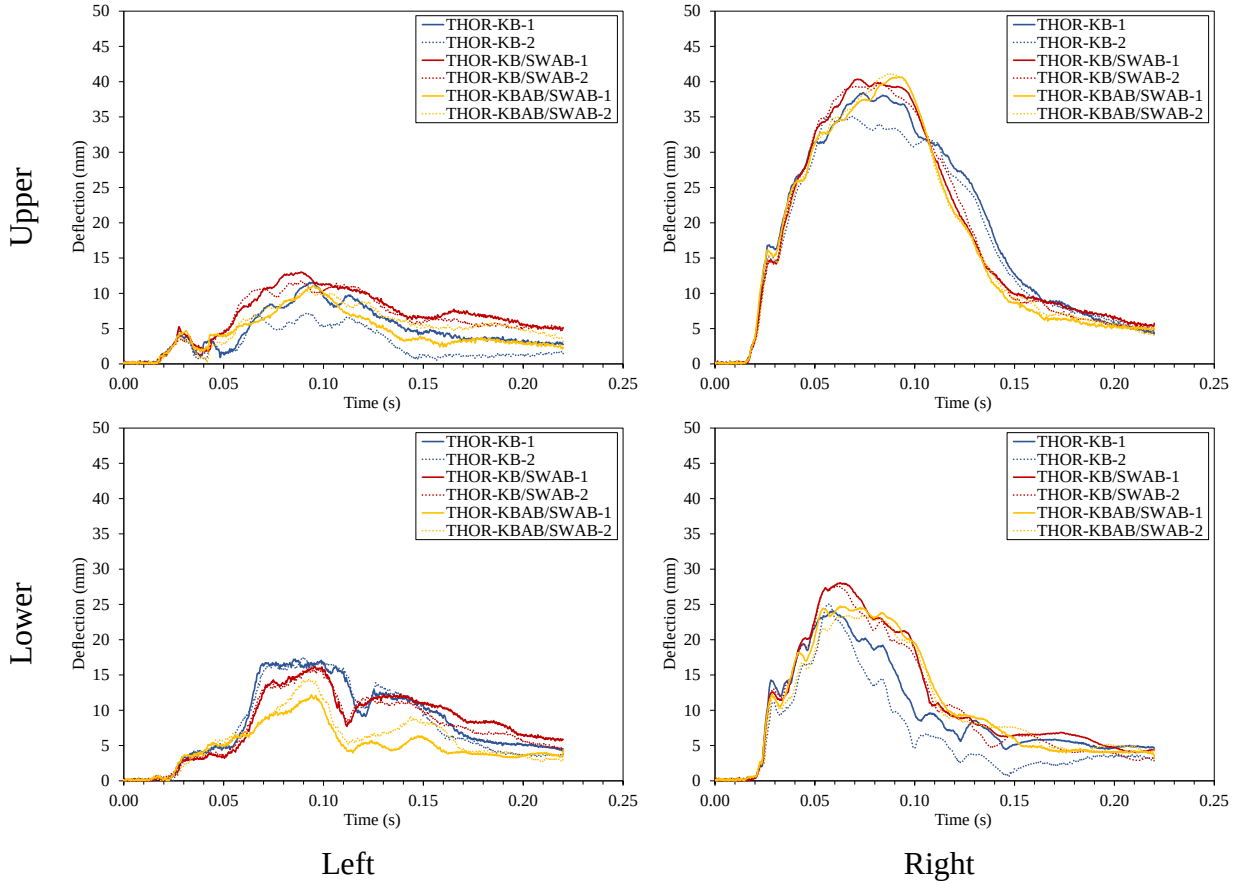

Figure 7.8: Left and right upper (top) and lower (bottom) IR-TRACC transverse resultant (x,y) deflection for the THOR-M.

Chest Band Results

Qualitative inspection of the chest band contours indicated that the THOR-M contours were more similar to the PMHS for the upper chest band, whereas the HIII contours were more similar to the PMHS for the lower band (Figure 7.9, Figure A7.1 - Figure A7.5). The HIII upper chest displayed a more focal loading around the belt with the anterolateral thorax deflecting approximately equally on the left and right sides, regardless of restraint condition. Conversely, both the THOR-M and PMHS displayed more distributed deflections from the belt on the upper chest band with asymmetry between the left and right anterolateral thorax. For the lower chest band, both the HIII and PMHS experienced shallower deflections on the right side relative to the THOR-M. Due to an equipment failure, lower chest band data was not reported for one HIII test: HIII-KB/SWAB-2.

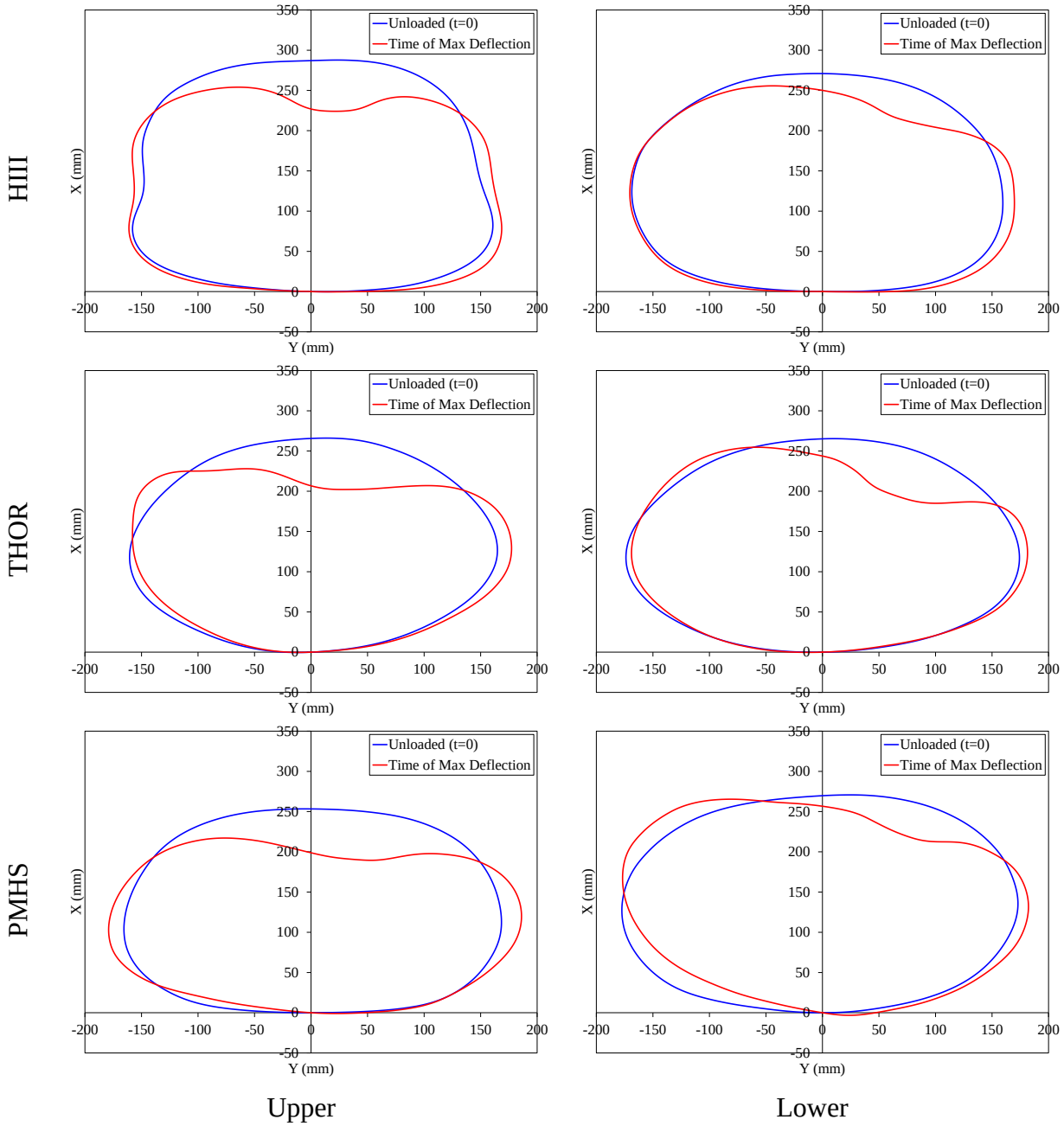

Figure 7.9: Exemplar Upper (left) and lower (right) chest band contours for each surrogate for the KB/SWAB condition at t = 0 and the time of maximum deflection.

The locations of interest experienced mostly compression except for the lower left (Figure 7.14 - Figure 7.16, Figure 7.10 - Figure 7.12, Table A7.7- Table A7.14). The peak deflection was due to expansion at the lower left location of interest for all THOR-M tests and five PMHS tests. Notably, the THOR-M did not experience appreciable compression at the lower left. Furthermore, the peak deflection on the lower band was due to expansion for two PMHS tests. For PMHS-KB-2 and PMHS-KB/SWAB-3, the peak deflections were 31 mm (0.14 mm/mm) and 24 mm (0.10 mm/mm), respectively.

The PMHS deflection time histories at the upper sternum were more similar to the HIII in shape, but more similar to the THOR-M in magnitude (Figure 7.14). Both the HIII and the PMHS exhibited two peaks, whereas the THOR-M exhibited a single rounded peak. However, the average PMHS peak sternum deflections were more similar to the THOR-M than the HIII for all conditions. Furthermore, the THOR-M and PMHS showed similar qualitative sensitivities to restraint conditions. Both the THOR-M and PMHS experienced an increase in average peak upper sternum deflection for the SWAB conditions compared to the KB condition. Conversely, the HIII showed decreased peak deflections for the SWAB conditions compared to the KB condition, particularly for the KBAB/SWAB condition.

The performance of each ATD relative to the PMHS differed between the upper left and upper right (Figure 7.15). The average peak deflections for the PMHS were closer to the analogous HIII values at the upper right for all conditions. However, the peak THOR-M deflections were more similar to the PMHS on the upper left with the exception of the KB condition. As observed at the upper sternum, the shape of the HIII time histories were more similar to the PMHS at the upper left and right. The PMHS showed some sensitivity to restraint condition, but this may have been an artifact of inter-subject variability. The largest difference between restraint conditions for the PMHS was the increased deflections for the KBAB/SWAB condition relative to the other conditions on the upper left. Both ATDs showed little sensitivity to restraint condition on the upper right. At the upper left, the THOR-M experienced a decrease in peak deflection for the KB condition relative to the other two conditions, but the HIII showed little difference.

The deflection time histories were very different for the lower chest band between surrogates (Figure 7.16). On the lower right, the THOR-M experienced much higher deflections than the other two surrogates. The HIII deflections were also greater than the PMHS, but were closer in magnitude. The ATDs showed little sensitivity to restraint condition, whereas the PMHS experienced the highest deflections for the KBAB/SWAB condition and the lowest for the KB condition. On the left side, the THOR-M experienced expansion and negligible compression, whereas the HIII experienced only compression. Interestingly, nearly all PMHSs experienced both compression and expansion. Peak PMHS compression was on average less than the HIII, except for the KBAB/SWAB condition, where one test resulted in a higher peak compression relative to the other tests. Additionally, peak PMHS expansion was on average higher than the THOR-M except for the KBAB/SWAB condition.

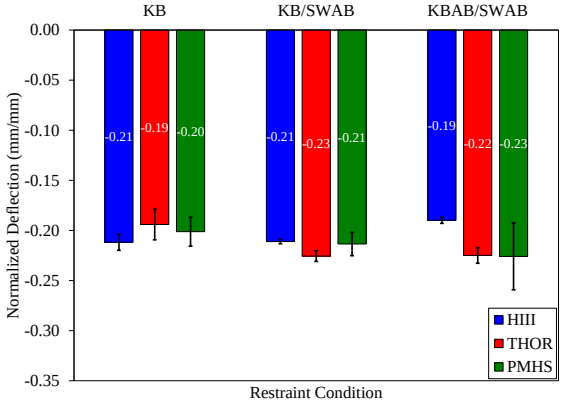

Figure 7.10: Peak normalized chest compression at the upper sternum for all surrogates and conditions.

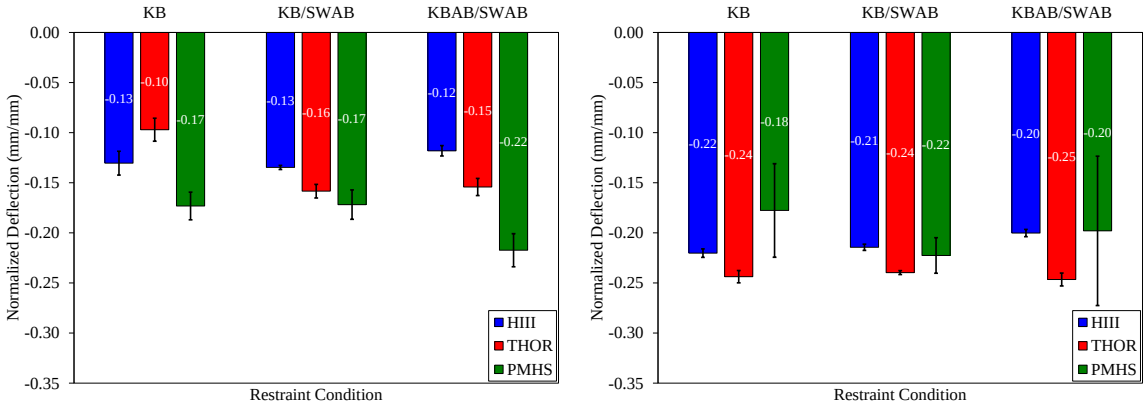

Figure 7.11: Peak normalized chest compression at the upper left (left) and upper right (right) for all surrogates and conditions.

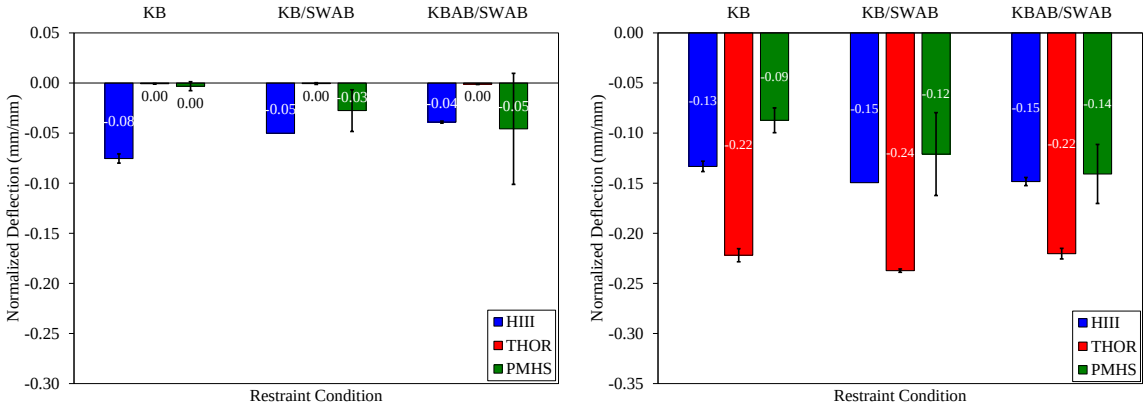

Figure 7.12: Peak normalized chest compression at the lower left (left) and upper right (right) for all surrogates and conditions.

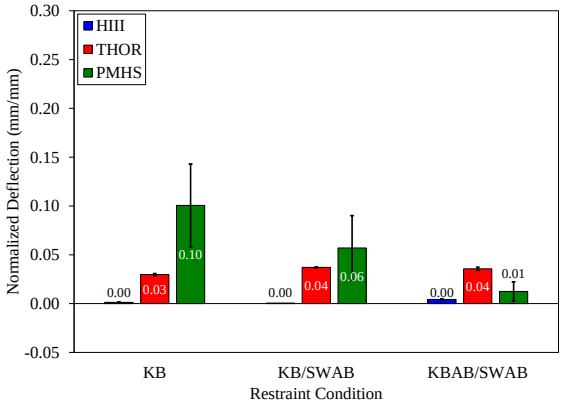

Figure 7.13: Peak normalized chest expansion at the lower left for all surrogates and conditions.

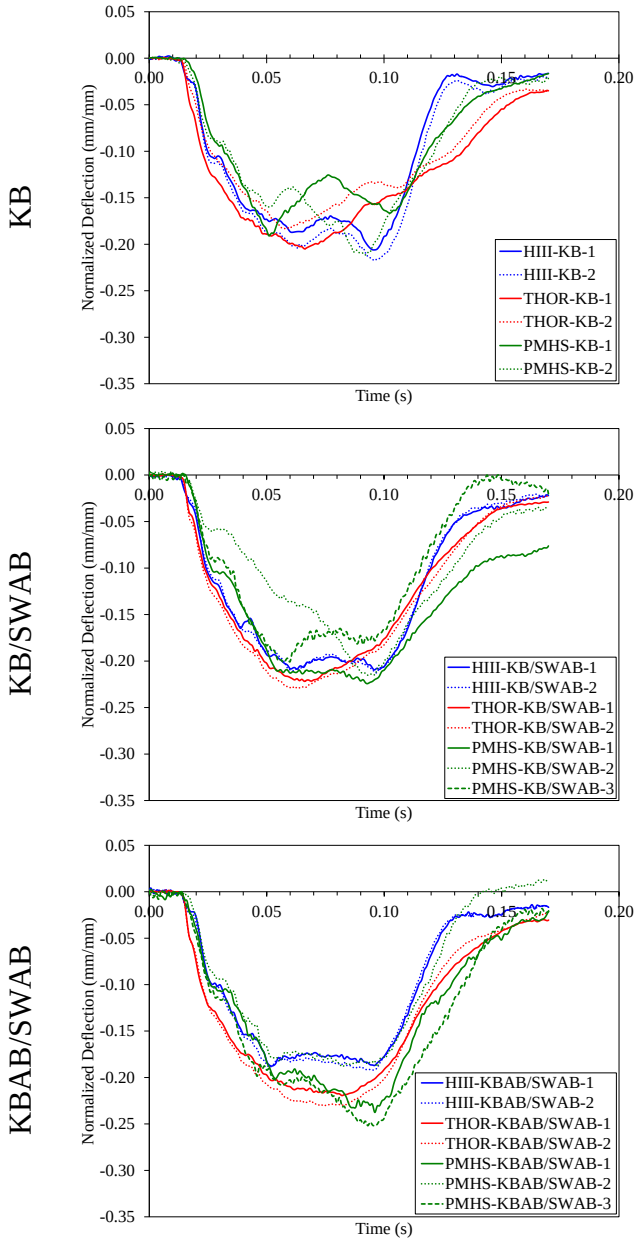

Figure 7.14: Normalized chest band deflections at the upper sternum for all surrogates and all conditions.
Note: Compression is negative.

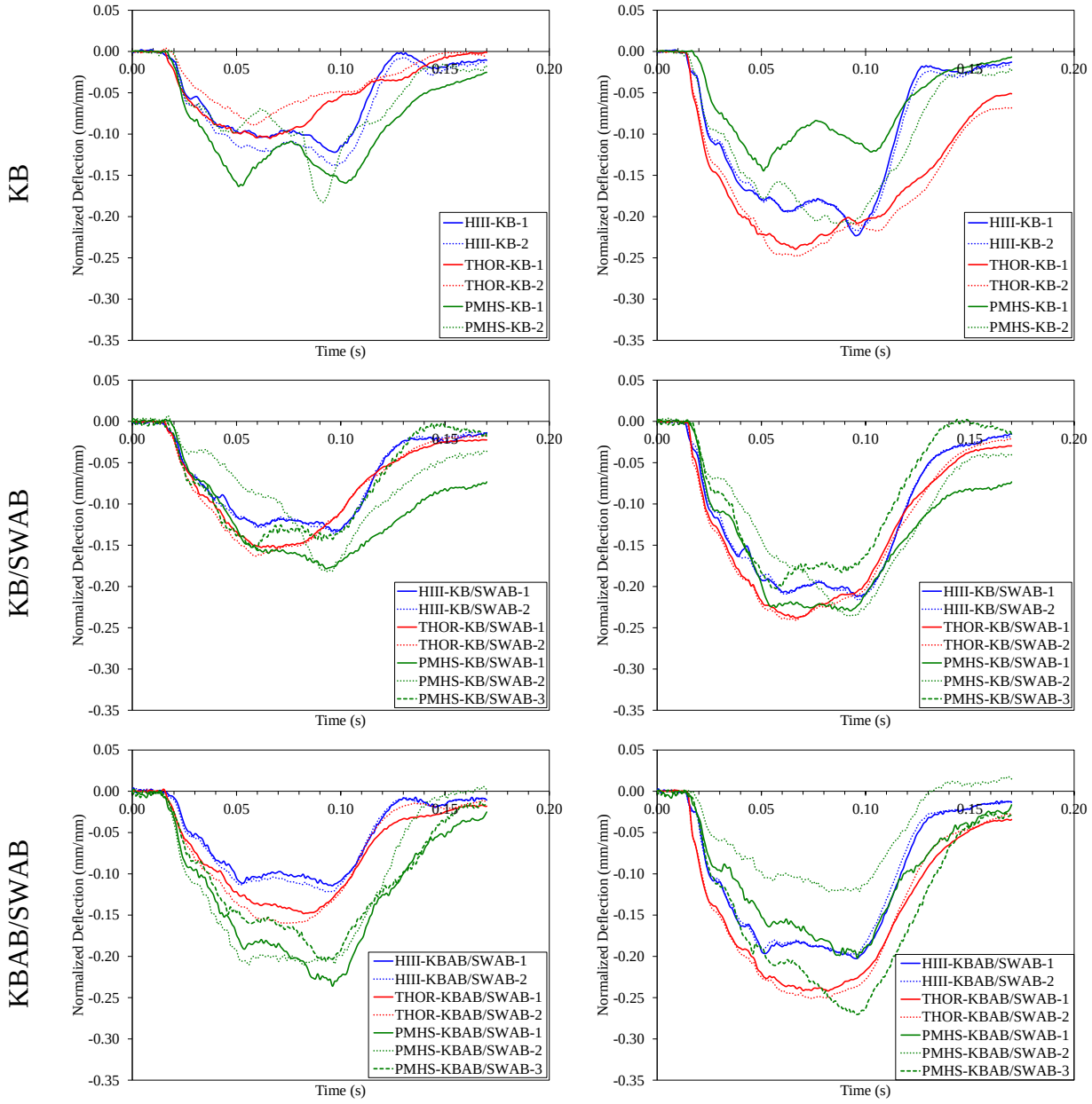

Figure 7.15: Normalized chest band deflections at the left and right upper chest for all surrogates and all conditions.
Note: Compression is negative.

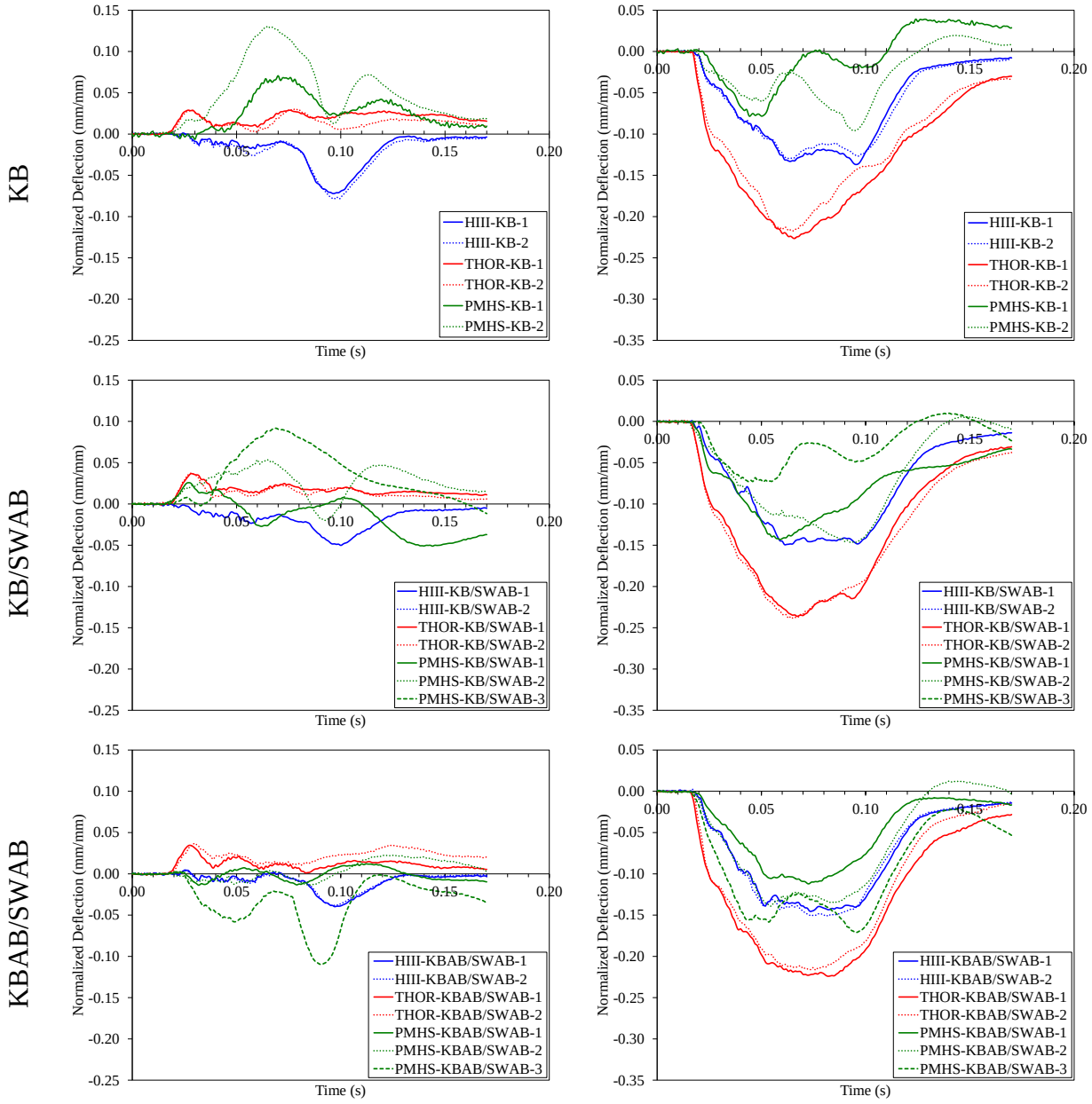

Figure 7.16: Normalized chest band deflections at the left and right lower chest for all surrogates and all conditions.

Note: Compression is negative, and there are differences in the deflection axes between the left and right.

Objective Rating Analysis Results

The results of the ISO objective rating analysis between surrogates showed that the PMHS chest band deflections were more similar to the HIII deflections than the THOR-M deflectins (Table 7.2, Table A7.15). Specifically, the HIII received higher scores when it was compared to the PMHS than when the THOR-M was compared to the PMHS. Both ATDs matched the PMHS response better at upper chest than the lower chest band. However, the HIII received better average scores for both the upper band (HIII: 0.723, THOR-M: 0.660) and the lower band (HIII: 0.411, THOR-M: 0.333). Specifically, the HIII received better average scores for every location of interest except for the upper sternum (HIII: 0.773, THOR-M: 0.776) and lower left (HIII: 0.247, THOR-M: 0.363). When the scores were averaged across all locations, the HIII received a slightly higher score than the THOR-M (HIII: 0.598, THOR-M: 0.529). On average, the PMHS response was more similar to the HIII regardless of condition. Interestingly, both ATDs performed the worst for the KB condition. When comparing between conditions within a surrogate, the HIII was closest to the PMHS response for the KBAB/SWAB condition, while the THOR-M was closest for the KB/SWAB condition.

Table 7.2: ISO scores for between surrogate chest band deflection comparisons.

Location	Condition	PMHS to HIII		PMHS to THOR		HIII to THOR	
		Upper	Lower	Upper	Lower	Upper	Lower
Sternum	KB	0.742	N/A	0.747	N/A	0.755	N/A
	KB/SWAB	0.789	N/A	0.738	N/A	0.875	N/A
	KBAB/SWAB	0.788	N/A	0.843	N/A	0.728	N/A
Left	KB	0.740	0.135	0.560	0.349	0.664	0.309
	KB/SWAB	0.670	0.115	0.638	0.481	0.763	0.165
	KBAB/SWAB	0.491	0.490	0.645	0.259	0.698	0.167
Right	KB	0.658	0.301	0.365	0.217	0.579	0.352
	KB/SWAB	0.828	0.585	0.777	0.290	0.847	0.431
	KBAB/SWAB	0.803	0.839	0.626	0.401	0.659	0.484

Note: Green, yellow, orange, and red shading refer to excellent, good, fair, and poor ISO scores, respectively.

The results of the ISO objective rating analysis between conditions were dependent upon the surrogate and location (Table 7.3, Table A7.16). The PMHS was the most sensitive surrogate to changes in restraint condition (i.e., the PMHS received lower scores for between condition comparisons). However, the PMHS was almost equally sensitive to the addition of either a SWAB or KBAB. A similar trend was observed for the HIII; however, the THOR-M was more sensitive

to the addition of a SWAB than a KBAB. When averaged across all surrogates, the upper sternum was least sensitive to changes in restraint, whereas the lower left was the most sensitive.

Table 7.3: ISO scores for between condition chest band deflection comparisons.

Location	Surrogate	KB to KB/SWAB		KB/SWAB to KBAB/SWAB	
		Upper	Lower	Upper	Lower
Sternum	HIII	0.891	N/A	0.844	N/A
	THOR	0.787	N/A	0.958	N/A
	PMHS	0.802	N/A	0.868	N/A
Left	HIII	0.853	0.815	0.817	0.683
	THOR	0.421	0.672	0.917	0.696
	PMHS	0.798	0.476	0.609	0.156
Right	HIII	0.891	0.783	0.885	0.877
	THOR	0.794	0.906	0.937	0.932
	PMHS	0.651	0.327	0.848	0.735

Note: Green, yellow, orange, and red shading refer to excellent, good, fair, and poor ISO scores, respectively.

Both the location and magnitude of the upper and lower chest band peak chest compression differed between surrogates. The THOR-M had the highest peak compressions on both the upper and lower chest band (Figure 7.17). This difference was more pronounced on the lower chest, where the THOR-M compressed at least 10 mm more than the other surrogates on average. For the lower chest band, the HIII also had higher compressions than the PMHS, but these were closer in magnitude to the PMHS deflections than the THOR-M. For the upper chest band, the HIII or PMHS resulted in the lowest deflections, depending on the condition. The locations of maximum chest compression were not consistent for each surrogate across conditions (Figure 7.18, Figure 7.19). Therefore, the only apparent trend between surrogates was that maximum compression occurred farther away from the sternum for the THOR-M during the KB condition. On average, all surrogates experienced maximum upper chest compression medial to the left and right locations of interest (i.e. the internal THOR-M instrumentation locations). However, the average location of maximum compression was closer to the left and right locations of interest than the sternum. The lower thorax locations of interest were better aligned with the average locations of maximum deflection on the lower chest band.

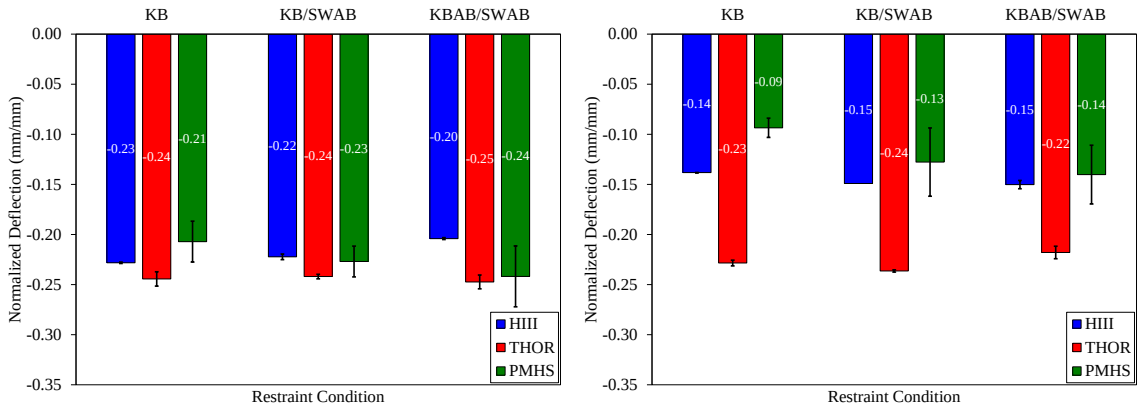

Figure 7.17: Peak normalized chest compression at the location of upper (left) and lower (right) maximum deflection.

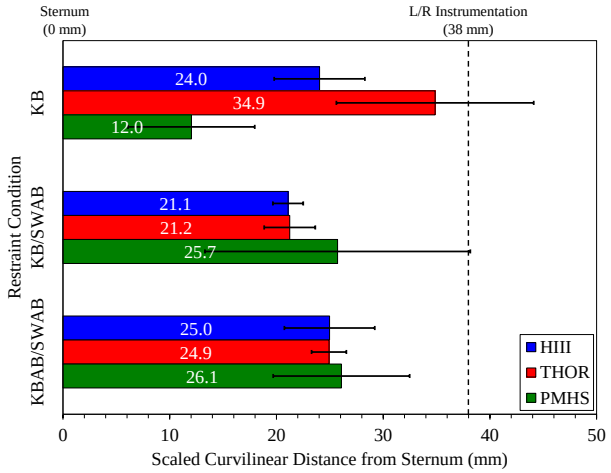

Figure 7.18: Curvilinear distances scaled to a 50th percentile male from the upper sternum to the location of maximum compression on the upper chest band for all surrogates and conditions.

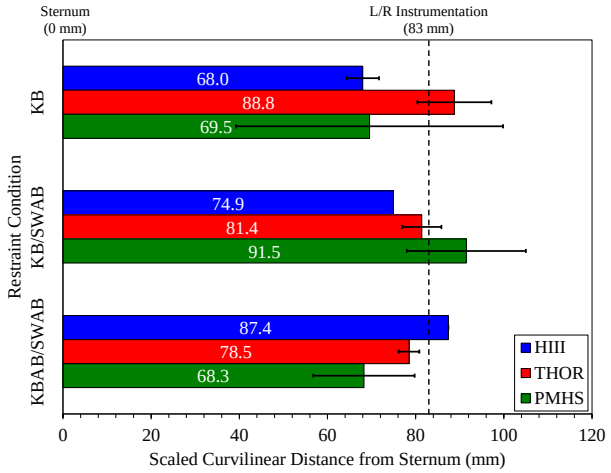

Figure 7.19: Curvilinear distances scaled to a 50th percentile male from the lower sternum to the location of maximum compression on the lower chest band for all surrogates and conditions.

Internal and External Deflection Comparisons

The ratios between the external and internal deflection measurements were reasonably consistent for both ATDs (Table A7.25 - Table A7.29). The HIII produced consistent ratios of 2.0 (external/internal) for the KB condition and 2.3 for the SWAB conditions. The THOR-M chest band deflections were compared to the transverse (x,y) resultant internal deflections since this would be the most direct comparison. Each location predicted a different ratio, but ratios within the same side tended to be more similar between locations. The right side produced the most consistent ratios of approximately -1.7 and -1.1 at the upper and lower right, respectively. The ratios on the left side were generally closer to -4, but contained some outliers. For THOR-KB-2, the initial position of the seat belt across the chest changed at the initiation of the test, resulting in a different belt position relative to the other tests. Therefore, this test had a higher ratio at the upper left and a lower ratio at the lower left.

It should be noted that these ratios were calculated at the time of peak chest band deflection for each test. Consequently, the peak external and internal deflections may not be aligned, and calculating the ratio at another time point may produce a different result. Additionally, adding the z component to the IR-TRACC resultant produced time histories that were more similar to the chest band time histories with regard to peak timing and magnitude for some locations on the thorax.

Observed Injuries and Predicted Injury Risks

All PMHS tests resulted in AIS3 thoracic injuries except for PMHS-KB/SWAB-2 and PMHS-KBAB/SWAB-1, which resulted in AIS4 and AIS2 injuries, respectively (Table A7.17 - Table A7.24). At least one rib fracture occurred in all tests (Figure 7.20). Seven tests resulted in a sternum fracture, and three tests resulted in a left clavicle fracture.

The three PMHS injury risk curves all predicted different injury outcomes (Table 7.4). The criterion from Kuppa and Eppinger (1998) that used d_{max} was the most accurate since it consistently reported over a 50% risk of AIS3+ injury. The other criterion from Kuppa and Eppinger (1998) that used d_{max} and thoracic acceleration (A_s) only reported above a 50% AIS3

injury risk for two tests. Finally, the criterion from Laituri *et al.* (2005) that included age and upper sternum deflection greatly under predicted the observed risk of an AIS3+ injury. A sensitivity to restraint condition was not observed in any of the predicted PMHS injury risk results.

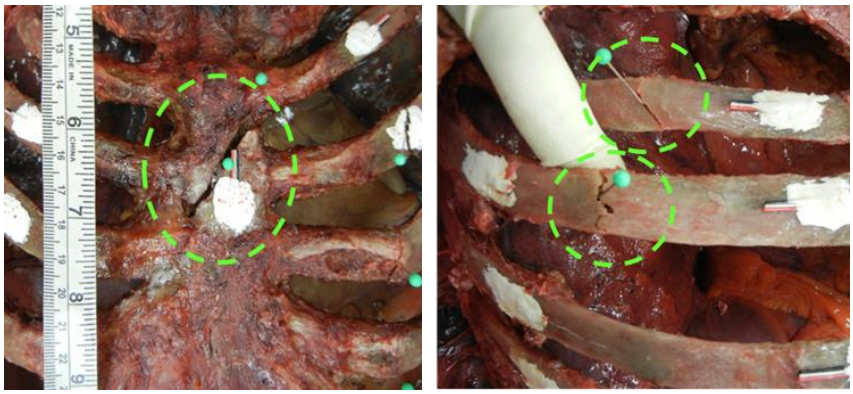

Figure 7.20: Exemplar sternum (left) and rib fractures (right).

The ATDs and their respective injury risk curves predicted different injury outcomes (Table 7.5, Table 7.6). The HIII predicted less than a 50% risk of an AIS3+ injury for all tests regardless of whether the age was matched or age 35 was used. The THOR-M also predicted less than a 50% risk of an AIS3+ injury for all tests when age 35 was used. However, the age matched curves produced over a 50% AIS3+ injury risk for all tests and both injury criteria. Both ATD injury metrics were sensitive to restraint condition. For the HIII, the KB condition produced the highest injury risk, while the KBAB/SWAB condition produced the lowest. For the THOR-M, the KB condition produced the highest injury risk, while the KB/SWAB condition produced the lowest.

The PMHSs sustained AIS3 injuries before the time of peak deflection for almost all tests (Table A7.30 - Table A7.32). For PMHS-KB-1, the AIS3 injury was sustained after peak deflection. For PMHS-KBAB/SWAB-1, no AIS3 injury was sustained. Recalculating the PMHS injury risks using the uncensored deflections from the time of fracture resulted in lower injury risk predictions than with the censored data reported above (Table A7.36 - Table A7.38). All criteria under-predicted injury risk. The criterion based on upper sternum deflection reported less than a 50% risk of an AIS3+ injury for all tests. The criterion using d_{max} predicted over a 50% risk of an AIS3+ injury for only two tests, while the criterion using d_{max} and A_s predicted over a 50% risk for one test.

Table 7.4: Probability of an AIS3+ thoracic injury for each PMHS using three injury risk curves.

Test	$P(d_{max})$	$P(A_s,d_{max})$	P(Age, $\overline{UC}$)	PHMS Age	PMHS Observed Injury
PMHS-KB-1	**0.520**	0.225	0.038	72	**AIS3**
PMHS-KB-2	**0.559**	**0.594**	0.039	63	**AIS3**
PMHS-KB/SWAB-1	**0.592**	**0.621**	0.038	57	**AIS3**
PMHS-KB/SWAB-2	**0.604**	0.376	0.161	88	**AIS4**
PMHS-KB/SWAB-3	**0.542**	0.200	0.037	67	**AIS3**
PMHS-KBAB/SWAB-1	**0.607**	0.400	0.180	80	**AIS2**
PMHS-KBAB/SWAB-2	**0.557**	0.271	0.033	71	**AIS3**
PMHS-KBAB/SWAB-3	**0.665**	0.497	0.223	78	**AIS3**

Note: Bold values indicate a calculated risk greater than 50% (0.500).

Table 7.5: Probability of an AIS3+ thoracic injury for a 35 year old male and age matched male (average age of PMHSs for each condition) using HIII injury risk criteria.

Test	Age = 35 yr	Age Matched	PMHS Observed Injury	Average PMHS Age
HIII-KB-1	0.047	0.303	PMHS-KB-1: AIS3 PMHS-KB-2 AIS3	67.5
HIII-KB-2	0.057	0.347		
HIII-KB/SWAB-1	0.033	0.232	PMHS-KB/SWAB-1: AIS3 PMHS-KB/SWAB-2: AIS4 PMHS-KB/SWAB-3: AIS3	70.7
HIII-KB/SWAB-2	0.032	0.226		
HIII-KBAB/SWAB-1	0.021	0.156	PMHS-KBAB/SWAB-1: AIS2 PMHS-KBAB/SWAB-2: AIS3 PMHS-KBAB/SWAB-3: AIS3	76.3
HIII-KBAB/SWAB-2	0.025	0.183		

Table 7.6: Probability of an AIS3+ thoracic injury for a 35 year old male and age matched male (average age of PMHSs for each condition) using THOR injury risk criteria.

Test	Age = 35 yr		Age Matched		PMHS Observed Injury	Average PMHS Age
	$P(R_{max})$	P(PCA)	$P(R_{max})$	P(PCA)		
THOR-KB-1	0.138	0.203	**0.612**	**0.787**	PMHS-KB-1: AIS3 PMHS-KB-2 AIS3	67.5
THOR-KB-2	0.120	0.178	**0.556**	**0.737**		
THOR-KB/SWAB-1	0.214	0.226	**0.840**	**0.878**	PMHS-KB/SWAB-1: AIS3 PMHS-KB/SWAB-2: AIS4 PMHS-KB/SWAB-3: AIS3	70.7
THOR-KB/SWAB-2	0.184	0.225	**0.789**	**0.877**		
THOR-KBAB/SWAB-1	0.165	0.139	**0.851**	**0.820**	PMHS-KBAB/SWAB-1: AIS2 PMHS-KBAB/SWAB-2: AIS3 PMHS-KBAB/SWAB-3: AIS3	76.3
THOR-KBAB/SWAB-2	0.169	0.154	**0.858**	**0.855**		

Note: Bold values indicate a calculated risk greater than 50% (0.500).

Discussion

This study compared the external thoracic responses of the HIII, THOR-M, and PMHS. In order to assess whether the external deflections were similar to the internal deflections of the ATDs, ratios between the external and internal deflections were generated for each ATD. For the HIII, the ratio between the external and internal deflections was very consistent between tests, and the same trends between restraint conditions were observed in the internal and external deflection time histories. The ratio between the external and internal deflections showed more variation between tests for the THOR-M, but was generally consistent for a given location. It should be noted that the THOR-M chest band deflections were compared to the transverse (x,y) resultant IR-TRACC deflections. The left locations had the most variation in the internal to external deflection ratios, and the left locations had the most pronounced differences in deflection time histories (Figure A7.7 - Figure A7.10). The internal and external deflections on the right side of the THOR-M were mainly different in magnitude. However, the internal and external deflections on the left were different in the overall shape of the time histories. There were several sources of error for the chest band measurements that could contribute to these differences. First, the scaled left and right locations of interest may not have been directly comparable to the true location of the instrumentation. Second, the chest bands may not have been placed exactly over the THOR-M's IR-TRACCs. Furthermore, any vertical deflections of the ribs could exacerbate differences between chest band and IR-TRACC placement. Third, chest bands were placed over the jacket, and the ribs could deflect without producing an analogous movement on the outside of the jacket. Finally, the chest bands deflections were chord deflections, while the IR-TRACC deflections were resultant deflections so the deflections may not be directly comparable. Comparison of the chest band chord and chest band resultant deflections revealed little difference. Therefore, it is probable that any differences between the chest band and IR-TRACC deflections caused by the deflection calculation methodology were minimal.

The THOR-M internal instrumentation measured upward deflection of the ribs at all four locations. The upward deflections followed an initial period of downward deflection at all locations, and the upper left experienced the greatest upward deflections. A previous study that tested the THOR-M as a belted front passenger (ΔV = 40 kph) reported peak upward deflections of 14 mm at the upper right, 7 mm at the upper left, 6 mm at the lower right, and 10 mm at the lower left [17]. Although

these peaks are lower than those observed in the current study, a similar trend was observed between locations, where the most upward deflection was seen on the upper chest opposite belt loading. The test conditions in the previous study were very different from the current study in terms of belt condition, knee bolster restraint, and sled pulse, which may have contributed to the differences in magnitude. High speed video analysis of the tests in the current study showed that the upward deflection of the chest began later in the event when the torso experienced substantial forward flexion. The torso flexion caused the abdomen to load the rib cage, producing an upward deflection of the ribs.

Both the THOR-M and PMHS experienced expansion of the rib cage at the lower left location of interest, while the HIII did not. Several previous studies have reported this phenomenon in both the THOR and PMHS. Shaw *et al.* (2000) and Forman *et al.* (2006) both compared previous versions of the THOR to the HIII and PMHS in belted sled tests and reported that the THOR and PMHS lower chest opposite the belt "bulged out." However, this response was not seen for the HIII. Shaw *et al.* (2010) and Shaw *et al.* (2013) conducted belted tests on the THOR-NT and THOR-M, respectively, and compared the ATD thoracic responses to PMHS [24]. Both the THOR-M and PMHS lower chests experienced expansive deflection on the side opposite the belt, while the THOR-NT did not. Additionally, they reported that the expansion was less prominent for the THOR-M than the PMHS [17]. For the current study, the PMHS also experienced greater peak expansions at the lower left location for the KB and KB/SWAB conditions, but the THOR-M expansion at this location was greater for the KBAB/SWAB condition.

Despite the THOR-M and PMHS experiencing similar responses at the lower left, the THOR-M experienced a much larger peak compression on the lower right compared to the PMHS. This indicated that the THOR-M lower thorax was more compliant than the PMHS thorax, which was also reported in previous studies on earlier versions of the THOR [13,14]. Due to the THOR-M's larger deflections at the lower right thorax, the THOR-M received a much lower ISO score for the lower chest band than the HIII when each ATD response was compared to the PMHS response. Consequently, the HIII had a higher average ISO score across all conditions and locations compared to the THOR-M, indicating better biofidelity for the HIII. Average ISO scores were used to broadly compare between surrogates and conditions. However, as noted above, these averages

can be highly influenced by individual data points. Overall, differences in ISO scores between the HIII and THOR-M were small. Therefore, the ISO score results should not be used as a basis for any definitive conclusions on the biofidelity of each ATD.

The locations of the IR-TRACCs in the THOR-M were reasonably close to the locations of peak deflection observed in this study. Peak deflection on the upper chest band occurred approximately 15 mm medial to the instrumentation locations. However, the average locations of peak deflection were closer to the internal instrumentation than the sternum. Furthermore, the upper sternum was least sensitive to differences between surrogates and conditions out of all locations of interest. Therefore, the upper left and upper right would be better locations for instrumentation intended to evaluate safety restraint performance.

The PMHS had the lowest average ISO score for the between condition comparisons, indicating that the PMHS responses were less comparable between conditions than the ATD responses and more sensitive to changes in restraint condition. The PMHS exhibited differences in peak magnitude between conditions, but these trends were not consistent between the different locations of interest. Additionally, there were no trends in predicted and observed injury risk for the PMHS between conditions. Since clear trends could not be detected across conditions, it is likely that inter-subject variability contributed to the differences between restraint conditions within a given location. Anthropometric measures that vary between individuals, such as torso height and chest circumference, can influence where the chest is loaded by different vehicle components, such as the seat belt and airbag. Different loading locations can produce differences in chest deflection at the location of interest. Therefore, the variability within a location could either mask or create artefactual differences between restraint conditions.

The predicted PMHS injury risks did not show a sensitivity to restraint condition and did not accurately represent the observed thoracic injury risk. The criterion using d_{max} best predicted the observed injuries. However, it only predicted 50-60% injury risk when the actual rate was higher. Furthermore, AIS3 occurred before the time of the peak values used in the PMHS injury criteria for most tests. Using the criteria to recalculate injury risk at the time of AIS3 injury resulted in even poorer injury risk prediction (39-63%). One possible explanation for the under-predicted

injury risk is that all of the injury metrics were developed using AIS 1990, which has a more conservative definition for an AIS3 injury (more than 3 rib fractures unilaterally) compared to AIS 2008 (at least three rib fractures unilaterally or bilaterally). Consequently, the time of AIS3 injury and the chest deflections at that time were recalucated using AIS 1990 (Table A7.33 - Table A7.35). This resulted in chest deflection magnitudes at the time of AIS3 injury that were closer to the peak deflection. Recalculating the PMHS injury risks using the uncensored data coded to AIS 1990 still resulted in poor injury risk prediction (46-58%), but it was improved relative to the predicted injury risk at the time of an AIS3 injury coded with AIS 2008. Regardless of how the injuries were coded, the injury risk curves developed from censored data under-predicted injury risk. Kemper *et al.* (2016) analyzed uncensored data from belted sled tests and table-top belt tests and also found that the current injury risk criteria over-predicted the magnitude of chest deflection necessary to produce an AIS3 injury. The results of both studies indicate a need for a thoracic injury criterion developed using uncensored data in order to more accurately predict thoracic injury risk.

It should be noted that fractures did occur on ribs that were not instrumented with strain gages. As a result, it is uncertain when these fractures occurred during the test. These fractures were not used to quantify the time of AIS3 injury. Consequently, it is possible that an AIS3 injury occurred earlier in time and at lower deflections than those reported in this study. This would be more comparable to the results of Kemper *et al.* (2016), which reported lower deflections at the time of AIS3 injury than those observed in the current study.

The HIII injury risk criterion also under-predicted the risk of AIS3+ injuries. However, the injury risk criterion was developed using a different version of AIS (AIS 1990), and the number of PMHS rib fractures used to determine AIS3 was increased by three since more rib fractures are generally documented in a PMHS than a living human [30]. Both of these factors indicate that the injury risk criterion is more conservative and less likely to predict what is currently defined as an AIS3+ thoracic skeletal injury. Consequently, the observed PMHS injuries in the current study were recoded to match the data that was used to derive the injury risk curve. All recoded injuries received the same scores as originally coded in AIS 2008, except for PMHS-KB-1, which dropped from AIS3 to AIS2. Therefore, even with analogously coded data, the injury risk curve still greatly

under predicted the risk of severe injury. These results are concerning since this injury risk curve is currently used to predict thoracic injury severity in the US frontal NCAP [32].

The proposed THOR-M injury risk curves were able to predict the PMHS injuries observed in this study. However, the metrics used to predict injury, R_{max} and PCA score, are based on the maximum resultant deflections at each location, which are independent of time and loading direction. Consequently, these metrics include the high magnitude of upward deflection observed at the upper left and the expansion observed at the lower left. It is currently unknown if and how these two phenomena contribute to injury risk. As a result, it is unknown whether inclusion of these deflections in the injury criteria is warranted and how these phenomena contribute to injury criteria relative to known injury mechanisms, such as chest compression. Therefore, more research must be completed to evaluate the effect of these deflections on injury risk criteria.

This study had several limitations. First, an effort was made to maintain consistent chest band placement between tests and surrogates. However, differences in placement between tests could have influenced the results. Furthermore, the chest bands were only designed to measure deflection within one plane. As a result, any out of plane motion of the ribs could not be quantified using this external measurement technique. For example, the large internal deflections observed in the z direction for the THOR-M could not be validated using the chest bands. As noted above, variability in the PMHS data may have obscured some trends between surrogates and restraint conditions that would be more apparent with a larger sample size. Finally, the results of this study are specific to the experimental conditions used in this study, including the design of the sled buck, restraint conditions, sled pulse, and occupant position. Variation in these parameters could produce different results.

Conclusions

The current study evaluated the thoracic responses of the HIII and THOR-M relative to PMHSs. The ATDs exhibited several differences in thoracic biofideltiy. The THOR-M experienced expansion at the lower left thorax that was also observed in some PMHS tests. However, the THOR-M lower right thorax was too compliant and deflected much more than the HIII and PMHS, which had comparable responses. The HIII and THOR-M had opposing sensitivities to restraint

condition. The KB condition had the greatest predicted injury risk for the HIII, but the lowest predicted injury risk for the THOR-M. No consistent trends were observed for the PMHSs between restraint conditions so the biofidelity of the ATDs' sensitivity to restraint condition could not be evaluated. The results of the objective rating metric analysis indicated that the HIII had slightly better external thoracic biofidelity than the THOR-M, despite the design changes in the THOR that were intended to improve thoracic biofidelity relative to the HIII. However, the external deflections from the chest band may not completely represent the internal deflections of the ribs due to the skin of the HIII and PMHS and the jacket of the THOR. The results of this study indicate that more work is needed to evaluate the thoracic biofidelity of the THOR-M under more experimental conditions.

References

1. NHTSA. *Traffic Safety Facts 2014: A Compilation of Motor Vehicle Crash Data Form the Fatality Analysis Reporting System and the General Estimates System*. Washington, DC: Transportation USDo; 2014.
2. Cavanaugh JM, Yoganandan N. Thorax Injury Biomechanics. In: Yoganandan N, Nahum AM, Melvin JW, eds. *Accidental Injury Biomechanics and Prevention*. 3 ed. New York: Springer; 2015:331-372.
3. Crandall JR, Bass CR, Pikey W, Miller H, Sikorski J, Wilkins M. Thoracic Response and Injury with Belt, Driver Side Airbag, and Force Limited Belt Restraint Systems. *International Journal of Crashworthiness.* 1996;2(1):119-132.
4. Cromack JR, Ziperman HH. *Three-Point Belt Induced Injuries: A Comparison between Laboratory Surrogates and Real World Accident Victims.* SAE Technical Paper;1975. 0148-7191.
5. Kallieris D, Zerial P, Rizzetti A, Mattern R. Prediction of Thoracic Injuries in Frontal Collisions. Paper presented at: Proc. 18th International Technical Conference on the Enhanced Safety of Vehicles1998.
6. Kemper AR, Beeman SM, Porta DJ, Duma SM. Non-Censored Rib Fracture Data During Frontal Pmhs Sled Tests. *Traffic injury prevention.* 2016;17(sup1):131-140.
7. Patrick L. Frontal Force Impact Tolerance of the Human Thorax. *The Human Thorax-Anatomoy, Injury, and Biomechanics, SAE P-67, Dearborn, MI.* 1976:37-48.
8. Ramet M, Cesari D. Behavior of Restrained Dummies and Cadavers in Frontal Impacts. *Proc. 7th International Research Council on the Biomechanics of Impact.* 1979:210-219.
9. Kent R, Woods W, Bostrom O. Fatality Risk and the Presence of Rib Fractures. Paper presented at: Annals of Advances in Automotive Medicine/Annual Scientific Conference2008.
10. Schneider LW, Haffner MP, Eppinger RH, Salloum MJ, Beebe MS, Rouhana SW, King AI, Hardy WN, Neathery RF. *Development of an Advanced Atd Thorax System for Improved Injury Assessment in Frontal Crash Environments.* SAE Technical Paper;1992. 0148-7191.

11. Forman J, Lessley D, Shaw CG, Evans J. Thoracic Response of Belted Pmhs, the Hybrid Iii, and the Thor-Nt Mid-Sized Male Surrogates in Low Speed, Frontal Crashes. *Stapp car crash journal.* 2006;50:191.
12. Kent R, Shaw G, Lessley D, Crandall J, Kallieris D, Svensson M. Comparison of Belted Hybrid Iii, Thor, and Cadaver Thoracic Responses in Oblique Frontal and Full Frontal Sled Tests. Paper presented at: SAE 2003 World Congress; March 3-6, 2003; Detroit, Michigan.
13. Shaw G, Crandall J, Butcher J. Biofidelity Evaluation of the Thor Advanced Frontal Crash Test Dummy. Paper presented at: IRCOBI Conference on the Biomechanics of Impact2000.
14. Shaw G, Parent D, Purtsezov S, Crandall J, Törnvall F. Torso Deformation in Frontal Sled Tests: Comparision between Thor Nt, Thor Nt with the Chalmers Sd-1 Shoulder, and Pmhs. Paper presented at: International IRCOBI Conference on the Biomechanics of Impact2010.
15. Ridella S, Parent D. Modifications to Improve the Durability, Usability, and Biofidelity of the Thor-Nt Dummy. The 22nd International Technical Conference on the Enhanced Safety of Vehicles; June 13-15, 2011; Washington, DC.
16. Shams T, Rangarajan N, McDonald J, Wang Y, Platten G, Spade C, Pope P, Haffner M. Development of Thor Nt: Enhancement of Thor Alpha–the Nhtsa Advanced Frontal Dummy. Proceedings of the 19th International Technical Conference on the Enhanced Safety of Vehicles, Paper; June 6-9, 2005; Washington, DC.
17. Shaw C, Lessley D, Ash J, Crandall J, Parent D. Response Comparison for the Hybrid Iii, Thor Mod Kit with Sd-3 Shoulder, and Pmhs in a Simulated Frontal Crash. Paper presented at: 23rd ESV Conference, Paper2013.
18. Roychoudhury RS, Conlee JK, Best M, Schenck D. *Blow-Molded Plastic Active Knee Bolsters.* SAE Technical Paper;2004. 0148-7191.
19. Janovicz D, Fischer B. *Final Report of New Car Assessment Program Frontal Impact Testing of 2012 Toyota Camry Lee 4-Dr Sedan.* Washington, DC: USDOT; December 16, 2011 2011.
20. Naik S. *Final Report of New Car Assessment Program Testing of a 2005 Toyota Camry Le.* Washington, DC: U.S. Department of Transportation,; March 11, 2005 2005.
21. NHTSA. *Laboratory Test Procedure for New Car Assessment Program (Ncap)- Frontal Impact Testing*. Washington, DC: U.S. Department of Transportation; 2012.

22. Kroell CK, Allen SD, Warner CY, Perl TR. *Interrelationship of Velocity and Chest Compression in Blunt Thoracic Impact to Swine Ii.* SAE Technical Paper;1986. 0148-7191.
23. Rouhana SW, Bedewi PG, Kankanala SV, Prasad P. Biomechanics of 4-Point Seat Belt Systems in Frontal Impacts. *Stapp Car Crash Journal.* 2003;47:367.
24. Shaw G, Parent D, Purtsezov S, Lessley D, Crandall J, Kent R, Guillemot H, Ridella SA, Takhounts E, Martin P. Impact Response of Restrained Pmhs in Frontal Sled Tests: Skeletal Deformation Patterns under Seat Belt Loading. *Stapp Car Crash Journal.* 2009;53:1.
25. Schneider L. Development of Anthropometrically Based Design Specifications for an Advanced Adult Anthropomorphic Dummy Family, Volume 1. Final Report. 1983.
26. ISO. Road Vehicles - Objective Rating Metric for Non-Ambiguous Signals. ISO/TS 18571. 2014.
27. Wang Z, Watson B. *An Algorithm to Calculate Chest Deflection from 3d Ir-Tracc.* SAE Technical Paper;2016. 0148-7191.
28. Gennarelli TA, Wodzin E. *Abbreviated Injury Scale 2005 : Update 2008.* Barrington, IL: Association for the Advancement of Automative Medicine; 2008.
29. Kuppa SM, Eppinger RH. *Development of an Improved Thoracic Injury Criterion.* SAE Technical Paper;1998. 0148-7191.
30. Laituri TR, Prasad P, Sullivan K, Frankstein M, Thomas RS. *Derivation and Evaluation of a Provisional, Age-Dependent, Ais3+ Thoracic Risk Curve for Belted Adults in Frontal Impacts.* SAE Technical Paper;2005. 0148-7191.
31. Federal Register. *Part V. National Highway Traffic Safety Administration Consumer Information: New Car Assessment Program*. U.S. Department of Transportation; 2015.
32. Federal Register. *Part Ii. National Highway Traffic Safety Administration Consumer Information: New Car Assessment Program*. U.S. Department of Transportation; 2008.

Appendix

Table A7.7: Peak chest band deflection data at the upper sternum.

Test	Time (s)	Peak Deflection (mm)	Normalized Peak Deflection (mm/mm)
HIII-KB-1	0.096	-60	-0.21
HIII-KB-2	0.096	-63	-0.22
HIII-KB/SWAB-1	0.096	-60	-0.21
HIII-KB/SWAB-2	0.097	-61	-0.21
HIII-KBAB/SWAB-1	0.052	-54	-0.19
HIII-KBAB/SWAB-2	0.095	-56	-0.19
THOR-KB-1	0.066	-55	-0.20
THOR-KB-2	0.058	-49	-0.18
THOR-KB/SWAB-1	0.066	-59	-0.22
THOR-KB/SWAB-2	0.062	-61	-0.23
THOR-KBAB/SWAB-1	0.082	-58	-0.22
THOR-KBAB/SWAB-2	0.074	-61	-0.23
PMHS-KB-1	0.051	-45	-0.19
PMHS-KB-2	0.092	-48	-0.21
PMHS-KB/SWAB-1	0.093	-58	-0.22
PMHS-KB/SWAB-2	0.093	-55	-0.22
PMHS-KB/SWAB-3	0.057	-54	-0.20
PMHS-KBAB/SWAB-1	0.096	-59	-0.24
PMHS-KBAB/SWAB-2	0.082	-49	-0.19
PMHS-KBAB/SWAB-3	0.096	-65	-0.25

Note: Compression is negative.

Table A7.8: Peak chest band deflection data at the upper left.

Test	Time (s)	Peak Deflection (mm)	Normalized Peak Deflection (mm/mm)
HIII-KB-1	0.097	-35	-0.12
HIII-KB-2	0.098	-39	-0.14
HIII-KB/SWAB-1	0.098	-38	-0.13
HIII-KB/SWAB-2	0.097	-38	-0.14
HIII-KBAB/SWAB-1	0.096	-33	-0.11
HIII-KBAB/SWAB-2	0.095	-35	-0.12
THOR-KB-1	0.066	-28	-0.11
THOR-KB-2	0.058	-23	-0.09
THOR-KB/SWAB-1	0.069	-40	-0.15
THOR-KB/SWAB-2	0.059	-43	-0.16
THOR-KBAB/SWAB-1	0.082	-39	-0.15
THOR-KBAB/SWAB-2	0.072	-42	-0.16
PMHS-KB-1	0.051	-38	-0.16
PMHS-KB-2	0.092	-41	-0.18
PMHS-KB/SWAB-1	0.093	-45	-0.18
PMHS-KB/SWAB-2	0.093	-46	-0.18
PMHS-KB/SWAB-3	0.060	-40	-0.16
PMHS-KBAB/SWAB-1	0.096	-58	-0.24
PMHS-KBAB/SWAB-2	0.082	-54	-0.21
PMHS-KBAB/SWAB-3	0.093	-52	-0.21

Note: Compression is negative.

Table A7.9: Peak chest band deflection data at the upper right.

Test	Time (s)	Peak Deflection (mm)	Normalized Peak Deflection (mm/mm)
HIII-KB-1	0.095	-65	-0.22
HIII-KB-2	0.096	-63	-0.22
HIII-KB/SWAB-1	0.096	-61	-0.21
HIII-KB/SWAB-2	0.097	-62	-0.22
HIII-KBAB/SWAB-1	0.096	-59	-0.20
HIII-KBAB/SWAB-2	0.095	-57	-0.20
THOR-KB-1	0.066	-63	-0.24
THOR-KB-2	0.068	-65	-0.25
THOR-KB/SWAB-1	0.067	-62	-0.24
THOR-KB/SWAB-2	0.067	-62	-0.24
THOR-KBAB/SWAB-1	0.082	-63	-0.24
THOR-KBAB/SWAB-2	0.074	-65	-0.25
PMHS-KB-1	0.051	-34	-0.14
PMHS-KB-2	0.087	-47	-0.21
PMHS-KB/SWAB-1	0.093	-59	-0.23
PMHS-KB/SWAB-2	0.093	-59	-0.24
PMHS-KB/SWAB-3	0.057	-53	-0.20
PMHS-KBAB/SWAB-1	0.096	-49	-0.20
PMHS-KBAB/SWAB-2	0.082	-30	-0.12
PMHS-KBAB/SWAB-3	0.096	-69	-0.27

Note: Compression is negative.

Table A7.10: Peak chest band deflection data at the location of upper maximum deflection.

Test	Time (s)	Peak Deflection (mm)	Normalized Peak Deflection (mm/mm)
HIII-KB-1	0.095	-66	-0.23
HIII-KB-2	0.096	-66	-0.23
HIII-KB/SWAB-1	0.096	-63	-0.22
HIII-KB/SWAB-2	0.097	-65	-0.22
HIII-KBAB/SWAB-1	0.096	-59	-0.20
HIII-KBAB/SWAB-2	0.095	-59	-0.20
THOR-KB-1	0.066	-63	-0.24
THOR-KB-2	0.068	-65	-0.25
THOR-KB/SWAB-1	0.066	-63	-0.24
THOR-KB/SWAB-2	0.067	-64	-0.24
THOR-KBAB/SWAB-1	0.082	-64	-0.24
THOR-KBAB/SWAB-2	0.074	-66	-0.25
PMHS-KB-1	0.051	-45	-0.19
PMHS-KB-2	0.087	-50	-0.22
PMHS-KB/SWAB-1	0.093	-61	-0.24
PMHS-KB/SWAB-2	0.093	-59	-0.24
PMHS-KB/SWAB-3	0.057	-56	-0.21
PMHS-KBAB/SWAB-1	0.096	-61	-0.24
PMHS-KBAB/SWAB-2	0.082	-54	-0.21
PMHS-KBAB/SWAB-3	0.096	-70	-0.27

Note: Compression is negative.

Table A7.11: Peak chest band compression data at the lower left.

Test	Time (s)	Peak Compression (mm)	Normalized Peak Compression (mm/mm)
HIII-KB-1	0.097	-18	0.07
HIII-KB-2	0.097	-20	0.08
HIII-KB/SWAB-1	0.100	-13	0.05
HIII-KBAB/SWAB-1	0.097	-10	0.04
HIII-KBAB/SWAB-2	0.096	-10	0.04
THOR-KB-1	0.009	0	0.00
THOR-KB-2	0.007	0	0.00
THOR-KB/SWAB-1	0.014	0	0.00
THOR-KB/SWAB-2	0.000	0	0.00
THOR-KBAB/SWAB-1	0.007	0	0.00
THOR-KBAB/SWAB-2	0.011	0	0.00
PMHS-KB-1	0.030	-1	0.01
PMHS-KB-2	0.000	0	0.00
PMHS-KB/SWAB-1	0.144	-12	0.05
PMHS-KB/SWAB-2	0.092	-5	0.02
PMHS-KB/SWAB-3	0.170	-3	0.01
PMHS-KBAB/SWAB-1	0.032	-3	0.01
PMHS-KBAB/SWAB-2	0.085	-3	0.01
PMHS-KBAB/SWAB-3	0.091	-27	0.11

Note: Compression is negative.

Table A7.12: Peak chest band expansion data at the lower left.

Test	Time (s)	Peak Expansion (mm)	Normalized Peak Expansion (mm/mm)
HIII-KB-1	0.024	0	0.00
HIII-KB-2	0.018	0	0.00
HIII-KB/SWAB-1	0.012	0	0.00
HIII-KBAB/SWAB-1	0.025	1	0.01
HIII-KBAB/SWAB-2	0.025	1	0.00
THOR-KB-1	0.027	7	0.03
THOR-KB-2	0.078	7	0.03
THOR-KB/SWAB-1	0.028	9	0.04
THOR-KB/SWAB-2	0.028	9	0.04
THOR-KBAB/SWAB-1	0.028	8	0.03
THOR-KBAB/SWAB-2	0.030	9	0.04
PMHS-KB-1	0.070	16	0.07
PMHS-KB-2	0.065	28	0.13
PMHS-KB/SWAB-1	0.027	6	0.03
PMHS-KB/SWAB-2	0.065	13	0.05
PMHS-KB/SWAB-3	0.069	20	0.09
PMHS-KBAB/SWAB-1	0.110	3	0.01
PMHS-KBAB/SWAB-2	0.125	5	0.02
PMHS-KBAB/SWAB-3	0.023	1	0.00

Note: Compression is negative.

Table A7.13: Peak chest band deflection data at the lower right.

Test	Time (s)	Peak Deflection (mm)	Normalized Peak Deflection (mm/mm)
HIII-KB-1	0.095	-34	-0.14
HIII-KB-2	0.063	-32	-0.13
HIII-KB/SWAB-1	0.061	-37	-0.15
HIII-KBAB/SWAB-1	0.074	-36	-0.15
HIII-KBAB/SWAB-2	0.082	-38	-0.15
THOR-KB-1	0.066	-54	-0.23
THOR-KB-2	0.065	-53	-0.22
THOR-KB/SWAB-1	0.067	-57	-0.24
THOR-KB/SWAB-2	0.065	-56	-0.24
THOR-KBAB/SWAB-1	0.082	-53	-0.22
THOR-KBAB/SWAB-2	0.076	-51	-0.22
PMHS-KB-1	0.044	-17	-0.08
PMHS-KB-2	0.094	-21	-0.10
PMHS-KB/SWAB-1	0.059	-34	-0.14
PMHS-KB/SWAB-2	0.093	-36	-0.15
PMHS-KB/SWAB-3	0.051	-16	-0.07
PMHS-KBAB/SWAB-1	0.073	-25	-0.11
PMHS-KBAB/SWAB-2	0.055	-31	-0.14
PMHS-KBAB/SWAB-3	0.095	-42	-0.17

Note: Compression is negative.

Table A7.14: Peak chest band compression data at the location of lower maximum compression.

Test	Time (s)	Peak Deflection (mm)	Normalized Peak Deflection (mm/mm)
HIII-KB-1	0.096	-35	-0.14
HIII-KB-2	0.063	-36	-0.14
HIII-KB/SWAB-1	0.061	-38	-0.15
HIII-KBAB/SWAB-1	0.074	-36	-0.15
HIII-KBAB/SWAB-2	0.082	-38	-0.15
THOR-KB-1	0.066	-54	-0.23
THOR-KB-2	0.065	-54	-0.23
THOR-KB/SWAB-1	0.067	-57	-0.24
THOR-KB/SWAB-2	0.065	-57	-0.24
THOR-KBAB/SWAB-1	0.082	-53	-0.22
THOR-KBAB/SWAB-2	0.076	-52	-0.21
PMHS-KB-1	0.044	-20	-0.09
PMHS-KB-2	0.094	-21	-0.10
PMHS-KB/SWAB-1	0.059	-34	-0.14
PMHS-KB/SWAB-2	0.093	-37	-0.15
PMHS-KB/SWAB-3	0.055	-18	-0.09
PMHS-KBAB/SWAB-1	0.073	-25	-0.11
PMHS-KBAB/SWAB-2	0.055	-34	-0.14
PMHS-KBAB/SWAB-3	0.096	-42	-0.17

Note: Compression is negative.

Table A7.15: Detailed ISO scores for between surrogate comparisons of chest band deflection.

Location	Condition	Reference	Comparison	Phase	Magnitude	Slope	Corridor	Overall
Upper Sternum	KB	PMHS	HIII	0.891	0.882	0.513	0.712	0.742
		PMHS	THOR	0.973	0.882	0.593	0.643	0.747
		HIII	THOR	0.952	0.863	0.551	0.704	0.755
	KB/SWAB	PMHS	HIII	0.840	0.960	0.556	0.796	0.789
		PMHS	THOR	0.725	0.923	0.587	0.727	0.738
		HIII	THOR	0.963	0.967	0.688	0.879	0.875
	KBAB/SWAB	PMHS	HIII	0.853	0.907	0.604	0.788	0.788
		PMHS	THOR	0.866	0.970	0.682	0.849	0.843
		HIII	THOR	0.993	0.805	0.700	0.571	0.728
Upper Left	KB	PMHS	HIII	0.902	0.853	0.547	0.698	0.740
		PMHS	THOR	0.863	0.453	0.555	0.466	0.560
		HIII	THOR	0.919	0.679	0.524	0.599	0.664
	KB/SWAB	PMHS	HIII	0.721	0.831	0.464	0.668	0.670
		PMHS	THOR	0.508	0.954	0.592	0.569	0.638
		HIII	THOR	0.917	0.857	0.615	0.713	0.763
	KBAB/SWAB	PMHS	HIII	0.868	0.336	0.589	0.330	0.491
		PMHS	THOR	0.800	0.730	0.633	0.531	0.645
		HIII	THOR	0.943	0.698	0.658	0.597	0.698
Upper Right	KB	PMHS	HIII	0.907	0.750	0.504	0.565	0.658
		PMHS	THOR	0.903	0.202	0.553	0.082	0.365
		HIII	THOR	0.825	0.669	0.537	0.433	0.579
	KB/SWAB	PMHS	HIII	0.888	0.962	0.575	0.859	0.828
		PMHS	THOR	0.806	0.925	0.630	0.763	0.777
		HIII	THOR	0.958	0.916	0.694	0.833	0.847
	KBAB/SWAB	PMHS	HIII	0.855	0.971	0.586	0.802	0.803
		PMHS	THOR	0.880	0.699	0.657	0.447	0.626
		HIII	THOR	0.969	0.736	0.704	0.442	0.659
Lower Left	KB	PMHS	HIII	0.000	0.000	0.259	0.208	0.135
		PMHS	THOR	0.288	0.000	0.465	0.495	0.349
		HIII	THOR	0.907	0.000	0.497	0.070	0.309
	KB/SWAB	PMHS	HIII	0.000	0.000	0.129	0.224	0.115
		PMHS	THOR	1.000	0.340	0.341	0.362	0.481
		HIII	THOR	0.174	0.000	0.443	0.104	0.165
	KBAB/SWAB	PMHS	HIII	0.532	0.470	0.547	0.451	0.490
		PMHS	THOR	0.690	0.000	0.396	0.105	0.259
		HIII	THOR	0.280	0.000	0.372	0.092	0.167
Lower Right	KB	PMHS	HIII	0.720	0.000	0.488	0.148	0.301
		PMHS	THOR	0.584	0.000	0.323	0.089	0.217
		HIII	THOR	0.936	0.130	0.504	0.095	0.352
	KB/SWAB	PMHS	HIII	0.784	0.654	0.491	0.497	0.585
		PMHS	THOR	0.899	0.000	0.436	0.057	0.290
		HIII	THOR	0.900	0.356	0.599	0.149	0.431
	KBAB/SWAB	PMHS	HIII	0.954	0.867	0.665	0.854	0.839
		PMHS	THOR	0.996	0.179	0.612	0.109	0.401
		HIII	THOR	0.947	0.454	0.629	0.195	0.484

Note: Green, yellow, orange, and red shading refer to excellent, good, fair, and poor ISO scores, respectively.

Table A7.16: Detailed ISO scores for between condition comparisons of chest band deflection.

Location	Surrogate	Reference	Comparison	Phase	Magnitude	Slope	Corridor	Overall
Upper Sternum	HIII	KB	KB/SWAB	0.955	0.959	0.722	0.910	0.891
		KB/SWAB	KBAB/SWAB	0.946	0.910	0.681	0.842	0.844
	THOR	KB	KB/SWAB	0.955	0.888	0.676	0.708	0.787
		KB/SWAB	KBAB/SWAB	0.993	0.996	0.846	0.976	0.958
	PMHS	KB	KB/SWAB	0.921	0.877	0.660	0.775	0.802
		KB/SWAB	KBAB/SWAB	0.944	0.954	0.676	0.882	0.868
Upper Left	HIII	KB	KB/SWAB	0.961	0.921	0.650	0.866	0.853
		KB/SWAB	KBAB/SWAB	0.957	0.875	0.652	0.799	0.817
	THOR	KB	KB/SWAB	0.873	0.222	0.567	0.221	0.421
		KB/SWAB	KBAB/SWAB	0.979	0.989	0.747	0.936	0.917
	PMHS	KB	KB/SWAB	0.947	0.899	0.620	0.762	0.798
		KB/SWAB	KBAB/SWAB	0.859	0.768	0.517	0.450	0.609
Upper Right	HIII	KB	KB/SWAB	0.950	0.965	0.700	0.920	0.891
		KB/SWAB	KBAB/SWAB	0.948	0.955	0.696	0.914	0.885
	THOR	KB	KB/SWAB	0.863	0.939	0.674	0.747	0.794
		KB/SWAB	KBAB/SWAB	0.984	0.982	0.845	0.937	0.937
	PMHS	KB	KB/SWAB	0.919	0.663	0.629	0.521	0.651
		KB/SWAB	KBAB/SWAB	0.987	0.888	0.697	0.835	0.848
Lower Left	HIII	KB	KB/SWAB	0.969	0.815	0.623	0.833	0.815
		KB/SWAB	KBAB/SWAB	0.990	0.566	0.693	0.583	0.683
	THOR	KB	KB/SWAB	0.997	0.699	0.598	0.532	0.672
		KB/SWAB	KBAB/SWAB	0.993	0.652	0.523	0.656	0.696
	PMHS	KB	KB/SWAB	0.687	0.250	0.577	0.433	0.476
		KB/SWAB	KBAB/SWAB	0.000	0.000	0.139	0.319	0.156
Lower Right	HIII	KB	KB/SWAB	0.939	0.864	0.669	0.721	0.783
		KB/SWAB	KBAB/SWAB	0.900	0.988	0.664	0.916	0.877
	THOR	KB	KB/SWAB	0.968	0.975	0.795	0.896	0.906
		KB/SWAB	KBAB/SWAB	0.958	0.975	0.820	0.954	0.932
	PMHS	KB	KB/SWAB	0.776	0.000	0.585	0.136	0.327
		KB/SWAB	KBAB/SWAB	0.972	0.797	0.631	0.638	0.735

Note: Green, yellow, orange, and red shading refer to excellent, good, fair, and poor ISO scores, respectively.

Table A7.17: PMHS-KB-1 thoracic fracture data.

Location	Time of Fracture (s)	Strain (µstrain)	Distance to Closest Gage (cm)
Sternum	0.03445	-9979	0.3
Right Rib 3	0.06910	12492	0.9
Left Clavicle	0.07830	-11866	0.2
Left Rib 2	0.09115	7549	1.5
Left Rib 3	0.09610	12355	3.5
Left Rib 1	N/A	N/A	N/A

Table A7.18: PMHS-KB-2 thoracic fracture data.

Location	Time of Fracture (s)	Strain (μstrain)	Distance to Closest Gage (cm)
Sternum	0.03790	-2129	1.1
Right Rib 6	0.03870	-5132	2.5
Left Rib 4	0.04680	6238	3.0
Left Rib 5	0.04915	7809	3.2
Left Rib 2	0.05625	6937	2.8
Left Rib 3	0.06965	17649	0.6
Left Rib 1	N/A	N/A	N/A

Table A7.19: PMHS-KB/SWAB-1 throacic fracture data.

Location	Time of Fracture (s)	Strain (μstrain)	Distance to Closest Gage (cm)
Sternum	0.04580	-8592	0.5
Right Rib 4	0.05080	4930	5.0
Right Rib 3	0.05415	8478	3.5
Right Rib 5	0.05425	7426	5.5
Left Rib 2	0.06925	10130	1.0
Right Rib 6	0.08825	-2835	1.7
Right Rib 5	0.09140	-4813	2.5

Table A7.20: PMHS-KB/SWAB-2 thoracic fracture data.

Location	Time of Fracture (s)	Strain (μstrain)	Distance to Closest Gage (cm)
Right Rib 5	0.03435	-3679	0.7
Left Rib 2	0.04335	4322	0.7
Right Rib 2	0.04570	1332	3.5
Right Rib 6	0.04980	-4742	0.8
Right Rib 3	0.05395	5282	3.3
Right Rib 9	0.05450	10095	1.8
Right Rib 4	0.06045	7723	2.2
Right Rib 6	0.06280	6893	3.2
Right Rib 2	0.07100	1475	11.4
Right Rib 5	0.07490	3815	3.7
Right Rib 7	0.07610	11373	3.0
Left Rib 5	0.08230	8135	1.0
Left Rib 4	0.08400	4088	10.4
Left Rib 3	0.08835	5186	4.9
Left Clavicle	0.08995	-6109	2.6
Right Rib 7	0.13700	409	8.7
Left Rib 3	N/A	N/A	18.7
Left Rib 1	N/A	N/A	N/A
Left Rib 11	N/A	N/A	N/A
Right Rib 1	N/A	N/A	N/A
Right Rib 1	N/A	N/A	N/A

Table A7.21: PMHS-KB/SWAB-3 thoracic fracture data.

Location	Time of Fracture (s)	Strain (μstrain)	Distance to Closest Gage (cm)
Sternum	0.03540	-2926	5.9
Right Rib 6	0.04000	-2186	9.2
Left Rib 3	0.04185	4612	4.8
Right Rib 3	0.04490	3641	5.1
Right Rib 4	0.04785	4325	6.9
Left Rib 2	0.05145	3183	2.3
Left Rib 4	0.05360	6672	5.8
Right Rib 2	0.05535	1735	4.7
Right Rib 5	0.05545	4707	5.7
Right Rib 7	N/A	N/A	2.0

Table A7.22: PMHS-KBAB/SWAB-1 thoracic fracture data.

Location	Time of Fracture (s)	Strain (μstrain)	Distance to Closest Gage (cm)
Sternum	0.03660	-6889	2.2
Left Rib 2	0.05145	6040	1.2

Table A7.23: PMHS-KBAB/SWAB-2 thoracic fracture data.

Location	Time of Fracture (s)	Strain (μstrain)	Distance to Closest Gage (cm)
Sternum	0.03390	-7057	2.3
Left Clavicle	0.03715	-11227	1.8
Left Rib 3	0.03795	6402	2.0
Right Rib 3	0.04150	5253	0.0
Right Rib 2	0.04630	6582	0.3
Left Rib 2	0.05005	21062	1.4
Right Rib 4	0.07380	2433	5.0
Right Rib 6	0.07845	6955	1.3
Left Rib 4	N/A	N/A	0.0
Right Rib 5	N/A	N/A	1.3
Right Rib 7	N/A	N/A	1.7

Table A7.24: PMHS-KBAB/SWAB-3 thoracic fracture data.

Location	Time of Fracture (s)	Strain (μstrain)	Distance to Closest Gage (cm)
Sternum	0.03585	-4540	7.6
Right Rib 2	0.07100	3441	3.6
Right Rib 4	0.07330	3825	4.8
Right Rib 3	0.08275	7205	4.0
Left Rib 2	0.08585	9111	7.2
Left Rib 1	N/A	N/A	N/A
Right Rib 1	N/A	N/A	N/A

Table A7.25: Comparison of deflections for the HIII internal instrumentation and chest band at the time of peak chest band deflection.

Test	Deflection (mm)		Ratio of Chest Band to Internal Deflections
	Chest Band	Internal	
HIII-KB-1	-59.6	-30.1	2.0
HIII-KB-2	-62.8	-31.9	2.0
HIII-KB/SWAB-1	-60.1	-27.1	2.3
HIII-KB/SWAB-2	-61.2	-26.8	2.3
HIII-KBAB/SWAB-1	-54.2	-23.2	2.3
HIII-KBAB/SWAB-2	-55.5	-24.7	2.3

Note: Chest band compression is negative.

Table A7.26: Comparison of deflections for the upper left THOR chest band IR-TRACC at the time of peak chest band deflection.

Test	Deflection (mm)		Ratio of Chest Band to IR-TRACC Deflections
	Chest Band	IR-TRACC	
THOR-KB-1	-27.6	6.5	-4.2
THOR-KB-2	-23.3	2.6	-8.9
THOR-KB/SWAB-1	-40.0	10.2	-3.9
THOR-KB/SWAB-2	-42.7	9.0	-4.7
THOR-KBAB/SWAB-1	-38.7	9.0	-4.3
THOR-KBAB/SWAB-2	-42.1	7.9	-5.3

Note: IR-TRACC data is the transverse (x,y) resultant. Chest band compression is negative.

Table A7.27: Comparison of deflections for the upper right THOR chest band IR-TRACC at the time of peak chest band deflection.

Test	Deflection (mm)		Ratio of Chest Band to IR-TRACC Deflections
	Chest Band	IR-TRACC	
THOR-KB-1	-62.8	36.8	-1.7
THOR-KB-2	-65.2	34.9	-1.9
THOR-KB/SWAB-1	-62.2	39.1	-1.6
THOR-KB/SWAB-2	-62.2	39.1	-1.6
THOR-KBAB/SWAB-1	-62.8	39.3	-1.6
THOR-KBAB/SWAB-2	-65.1	38.2	-1.7

Note: IR-TRACC data is the transverse (x,y) resultant. Chest band compression is negative.

Table A7.28: Comparison of deflections for the lower left THOR chest band IR-TRACC at the time of peak chest band deflection.

Test	Deflection (mm)		Ratio of Chest Band to IR-TRACC Deflections
	Chest Band	IR-TRACC	
THOR-KB-1	7.1	1.8	3.9
THOR-KB-2	7.4	16.1	0.5
THOR-KB/SWAB-1	8.7	2.5	3.6
THOR-KB/SWAB-2	9.1	2.3	3.9
THOR-KBAB/SWAB-1	8.4	2.5	3.4
THOR-KBAB/SWAB-2	9.0	2.1	4.4

Note: IR-TRACC data is the transverse (x,y) resultant. Chest band compression is negative.

Table A7.29: Comparison of deflections for the lower right THOR chest band IR-TRACC at the time of peak chest band deflection.

Test	Deflection (mm)		Ratio of Chest Band to IR-TRACC Deflections
	Chest Band	IR-TRACC	
THOR-KB-1	-54.3	36.6	-1.5
THOR-KB-2	-52.9	34.6	-1.5
THOR-KB/SWAB-1	-56.6	39.2	-1.5
THOR-KB/SWAB-2	-56.4	38.9	-1.5
THOR-KBAB/SWAB-1	-53.0	39.2	-1.4
THOR-KBAB/SWAB-2	-51.5	38.5	-1.3

Note: IR-TRACC data is the transverse (x,y) resultant. Chest band compression is negative.

Table A7.30: Comparison of chest band deflection at the location of maximum deflection at the time of an AIS3 injury and at peak compression using AIS 2008 coding.

Test	Fractures with Unknown Timing	Time (s)		Deflection (mm/mm)		AIS3/Peak Deflection
		AIS3	Peak	AIS3	Peak	
PMHS-KB-1	1	0.0961	0.0511	-0.16	-0.19	0.83
PMHS-KB-2	1	0.0492	0.0870	-0.17	-0.22	0.78
PMHS-KB/SWAB-1	0	0.0543	0.0928	-0.23	-0.24	0.97
PMHS-KB/SWAB-2	5	0.0457	0.0930	-0.12	-0.24	0.52
PMHS-KB/SWAB-3	1	0.0449	0.0571	-0.17	-0.21	0.82
PMHS-KBAB/SWAB-1	0	N/A	0.0961	N/A	-0.24	N/A
PMHS-KBAB/SWAB-2	3	0.0463	0.0821	-0.17	-0.21	0.82
PMHS-KBAB/SWAB-3	2	0.0828	0.0957	-0.25	-0.27	0.93

Table A7.31: Comparison of chest band sternum deflection at the time of an AIS3 injury and at peak sternum compression using AIS 2008 coding.

Test	Fractures with Unknown Timing	Time (s)		Deflection (mm/mm)		AIS3/Peak Deflection
		AIS3	Peak	AIS3	Peak	
PMHS-KB-1	1	0.0961	0.0511	-0.16	-0.19	0.82
PMHS-KB-2	1	0.0492	0.0919	-0.16	-0.21	0.75
PMHS-KB/SWAB-1	0	0.0543	0.0928	-0.21	-0.22	0.94
PMHS-KB/SWAB-2	5	0.0457	0.0932	-0.10	-0.22	0.47
PMHS-KB/SWAB-3	1	0.0449	0.0573	-0.17	-0.20	0.83
PMHS-KBAB/SWAB-1	0	N/A	0.0960	N/A	-0.24	N/A
PMHS-KBAB/SWAB-2	3	0.0463	0.0822	-0.15	-0.19	0.79
PMHS-KBAB/SWAB-3	2	0.0828	0.0956	-0.23	-0.25	0.92

Table A7.32: Comparison of maximum chest band deflection as defined by Kuppa and Eppinger (1998) (d_{max}) at the time of an AIS3 injury and at peak using AIS 2008 coding.

Test	Fractures with Unknown Timing	Time (s)		Deflection (mm/mm)		AIS3/Peak Deflection
		AIS3	Peak	AIS3	Peak	
PMHS-KB-1	1	0.0961	0.0511	-0.16	-0.19	0.82
PMHS-KB-2	1	0.0492	0.0919	-0.17	-0.21	0.82
PMHS-KB/SWAB-1	0	0.0543	0.0927	-0.22	-0.23	0.98
PMHS-KB/SWAB-2	5	0.0457	0.0930	-0.12	-0.24	0.52
PMHS-KB/SWAB-3	1	0.0449	0.0570	-0.17	-0.20	0.83
PMHS-KBAB/SWAB-1	0	N/A	0.0960	N/A	-0.24	N/A
PMHS-KBAB/SWAB-2	3	0.0463	0.0821	-0.17	-0.21	0.83
PMHS-KBAB/SWAB-3	2	0.0828	0.0956	-0.25	-0.27	0.93

Table A7.33: Comparison of chest band deflection at the time of an AIS3 injury and at peak compression using AIS 1990 coding.

Test	Fractures with Unknown Timing	Time (s)		Deflection (mm/mm)		AIS3/Peak Deflection
		AIS3	Peak	AIS3	Peak	
PMHS-KB-1	1	N/A	0.0511	N/A	-0.19	N/A
PMHS-KB-2	1	0.0697	0.0870	-0.19	-0.22	0.84
PMHS-KB/SWAB-1	0	0.0883	0.0928	-0.23	-0.24	0.98
PMHS-KB/SWAB-2	5	0.0540	0.0930	-0.16	-0.24	0.68
PMHS-KB/SWAB-3	1	0.0554	0.0571	-0.21	-0.21	1.00
PMHS-KBAB/SWAB-1	0	N/A	0.0961	N/A	-0.24	N/A
PMHS-KBAB/SWAB-2	3	0.0785	0.0821	-0.20	-0.21	0.97
PMHS-KBAB/SWAB-3	2	N/A	0.0957	N/A	-0.27	N/A

Table A7.34: Comparison of chest band sternum deflection at the time of an AIS3 injury and at peak sternum compression using AIS 1990 coding.

Test	Fractures with Unknown Timing	Time (s)		Deflection (mm/mm)		AIS3/Peak Deflection
		AIS3	Peak	AIS3	Peak	
PMHS-KB-1	1	N/A	0.0511	N/A	-0.19	N/A
PMHS-KB-2	1	0.0697	0.0919	-0.16	-0.21	0.77
PMHS-KB/SWAB-1	0	0.0883	0.0928	-0.22	-0.22	0.97
PMHS-KB/SWAB-2	5	0.0540	0.0932	-0.13	-0.22	0.60
PMHS-KB/SWAB-3	1	0.0554	0.0573	-0.20	-0.20	0.99
PMHS-KBAB/SWAB-1	0	N/A	0.0960	N/A	-0.24	N/A
PMHS-KBAB/SWAB-2	3	0.0785	0.0822	-0.18	-0.19	0.97
PMHS-KBAB/SWAB-3	2	N/A	0.0956	N/A	-0.25	N/A

Table A7.35: Comparison of maximum chest band deflection as defined by Kuppa and Eppinger (1998) (d_{max}) at the time of an AIS3 injury and at peak using AIS 1990 coding.

Test	Fractures with Unknown Timing	Time (s)		Deflection (mm/mm)		AIS3/Peak Deflection
		AIS3	Peak	AIS3	Peak	
PMHS-KB-1	1	N/A	0.0511	N/A	-0.19	N/A
PMHS-KB-2	1	0.0697	0.0919	-0.19	-0.21	0.90
PMHS-KB/SWAB-1	0	0.0883	0.0927	-0.23	-0.23	0.98
PMHS-KB/SWAB-2	5	0.0540	0.0930	-0.16	-0.24	0.68
PMHS-KB/SWAB-3	1	0.0554	0.0570	-0.20	-0.20	1.00
PMHS-KBAB/SWAB-1	0	N/A	0.0960	N/A	-0.24	N/A
PMHS-KBAB/SWAB-2	3	0.0785	0.0821	-0.21	-0.21	0.97
PMHS-KBAB/SWAB-3	2	N/A	0.0956	N/A	-0.27	N/A

Table A7.36: Probability of an AIS3+ thoracic injury for each PMHS predicted from censored and uncensored data using P(Age, $\overline{UC}$).

Test	Censored	Uncensored AIS 2008	Uncensored AIS 1990
PMHS-KB-1	0.038	0.015	N/A
PMHS-KB-2	0.039	0.009	0.011
PMHS-KB/SWAB-1	0.038	0.027	0.032
PMHS-KB/SWAB-2	0.161	0.009	0.018
PMHS-KB/SWAB-3	0.037	0.015	0.035
PMHS-KBAB/SWAB-1	0.180	N/A	N/A
PMHS-KBAB/SWAB-2	0.033	0.012	0.028
PMHS-KBAB/SWAB-3	0.223	0.140	N/A

Table A7.37: Probability of an AIS3+ thoracic injury for each PMHS predicted from censored and uncensored data using $P(d_{max})$.

Test	Censored	Uncensored AIS 2008	Uncensored AIS 1990
PMHS-KB-1	**0.520**	0.454	N/A
PMHS-KB-2	**0.559**	0.488	**0.517**
PMHS-KB/SWAB-1	**0.592**	**0.582**	**0.584**
PMHS-KB/SWAB-2	**0.604**	0.390	0.462
PMHS-KB/SWAB-3	**0.542**	0.475	**0.541**
PMHS-KBAB/SWAB-1	**0.607**	N/A	N/A
PMHS-KBAB/SWAB-2	**0.557**	0.488	**0.546**
PMHS-KBAB/SWAB-3	**0.665**	**0.630**	N/A

Note: Bold values indicate a calculated risk greater than 50% (0.500).

Table A7.38: Probability of an AIS3+ thoracic injury for each PMHS predicted from censored and uncensored data using $P(A_s,d_{max})$.

Test	Censored	Uncensored AIS 2008	Uncensored AIS 1990
PMHS-KB-1	0.225	0.155	N/A
PMHS-KB-2	**0.594**	0.471	**0.522**
PMHS-KB/SWAB-1	**0.621**	**0.604**	**0.607**
PMHS-KB/SWAB-2	0.376	0.117	0.181
PMHS-KB/SWAB-3	0.200	0.136	0.199
PMHS-KBAB/SWAB-1	0.400	N/A	N/A
PMHS-KBAB/SWAB-2	0.271	0.187	0.256
PMHS-KBAB/SWAB-3	0.497	0.431	N/A

Note: Bold values indicate a calculated risk greater than 50% (0.500).

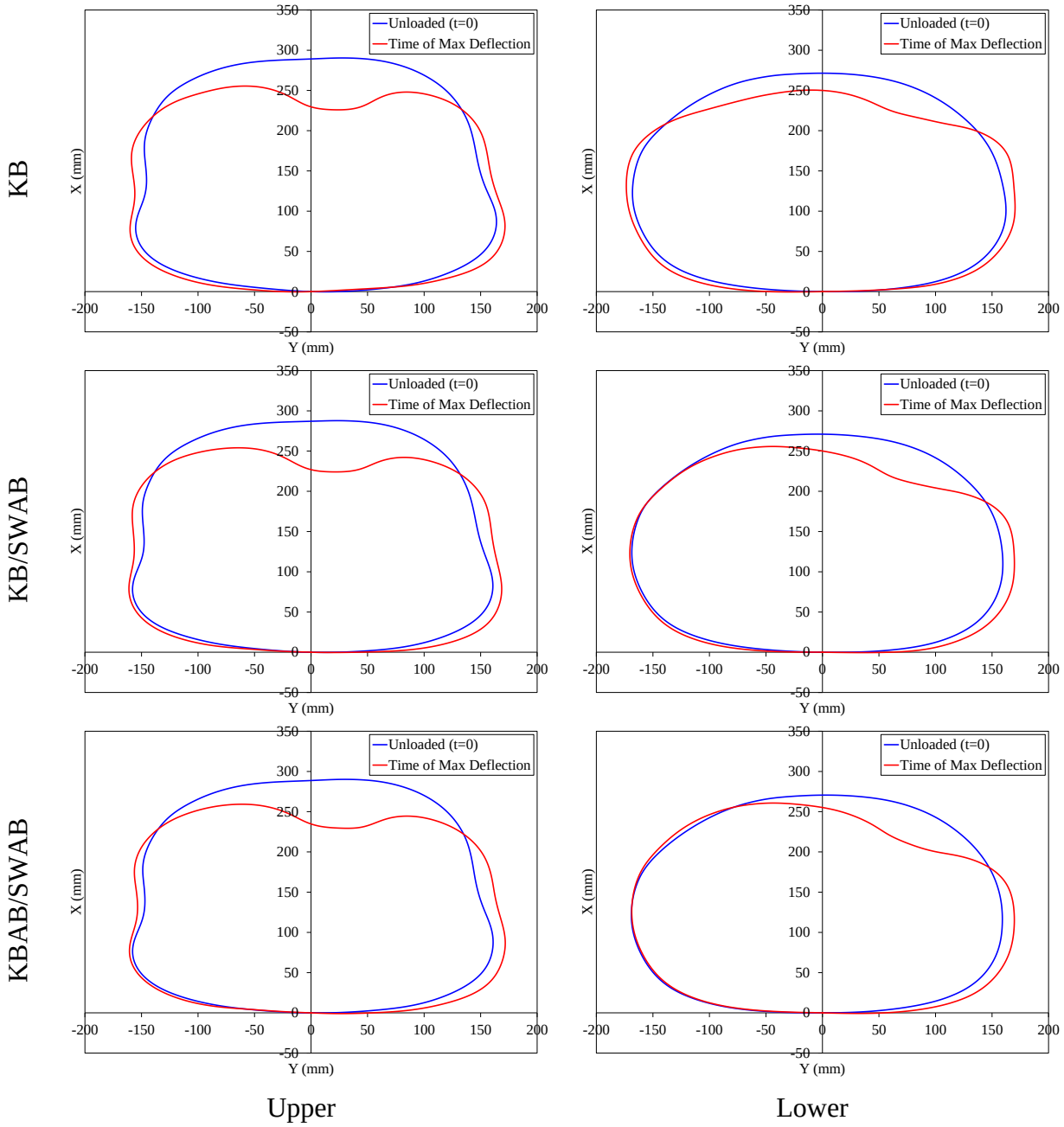

Figure A7.1: Exemplar Upper (left) and lower (right) chest band contours for the HIII at t = 0 and the time of maximum deflection.

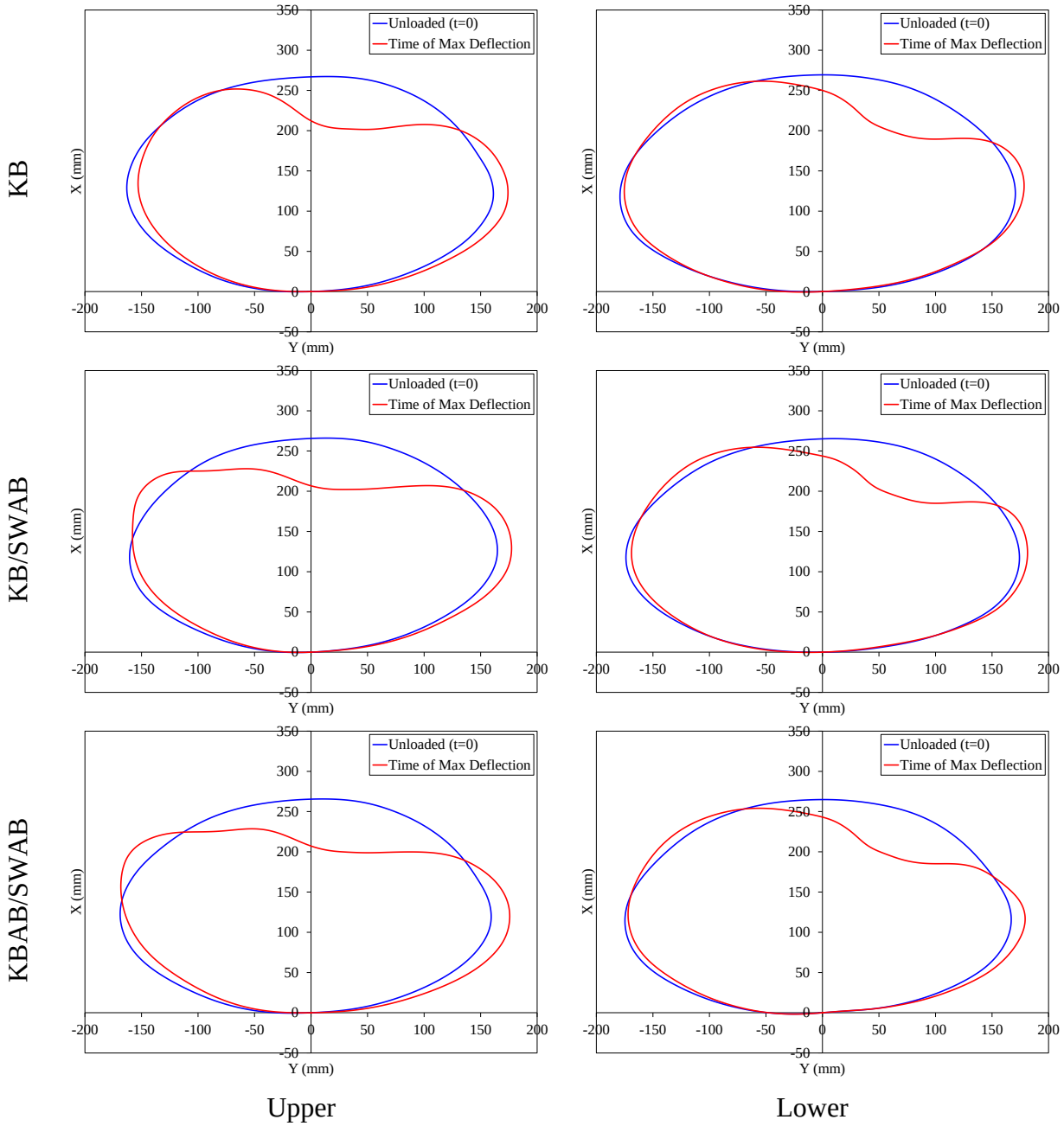

Figure A7.2: Exemplar Upper (left) and lower (right) chest band contours for the THOR-M at t = 0 and the time of maximum deflection.

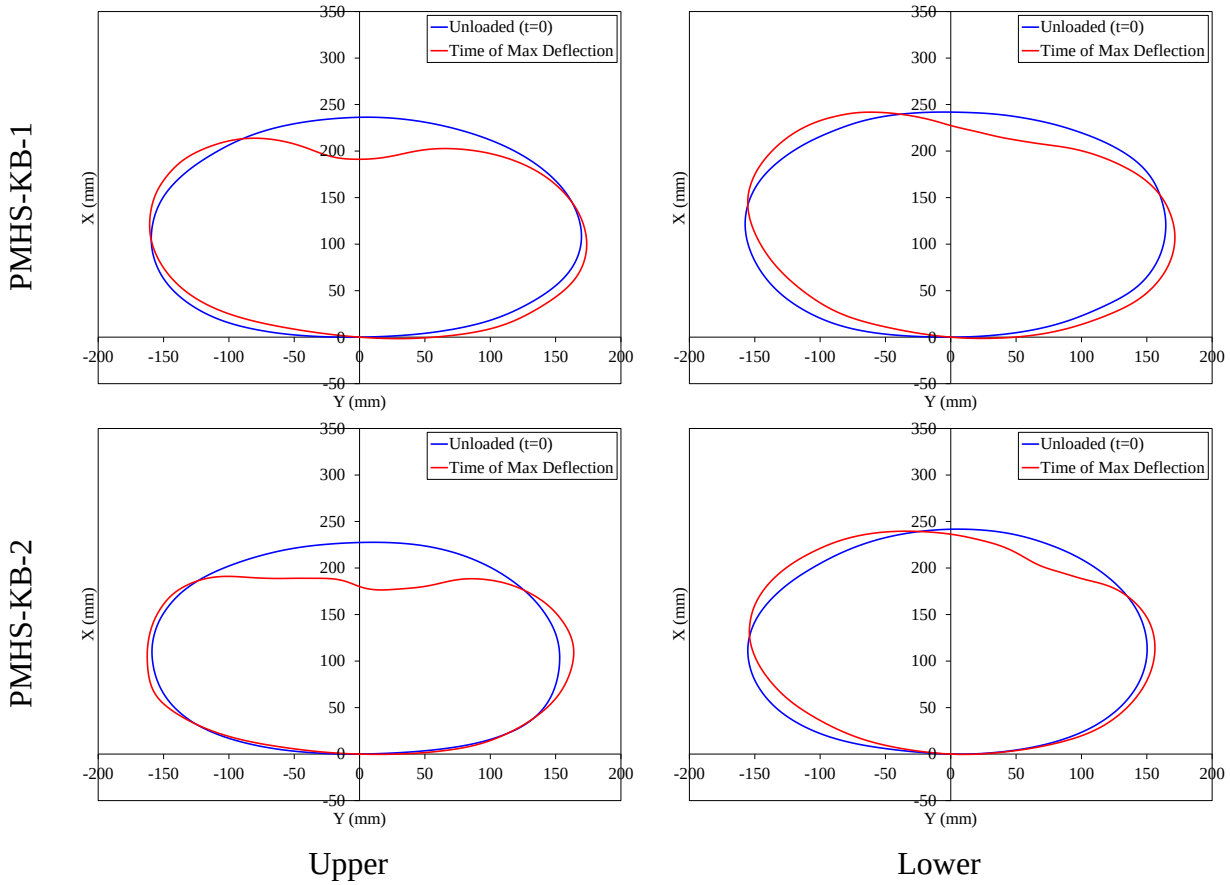

Figure A7.3: Upper (left) and lower (right) chest band contours for the PMHS KB condition at t = 0 and the time of maximum compression.

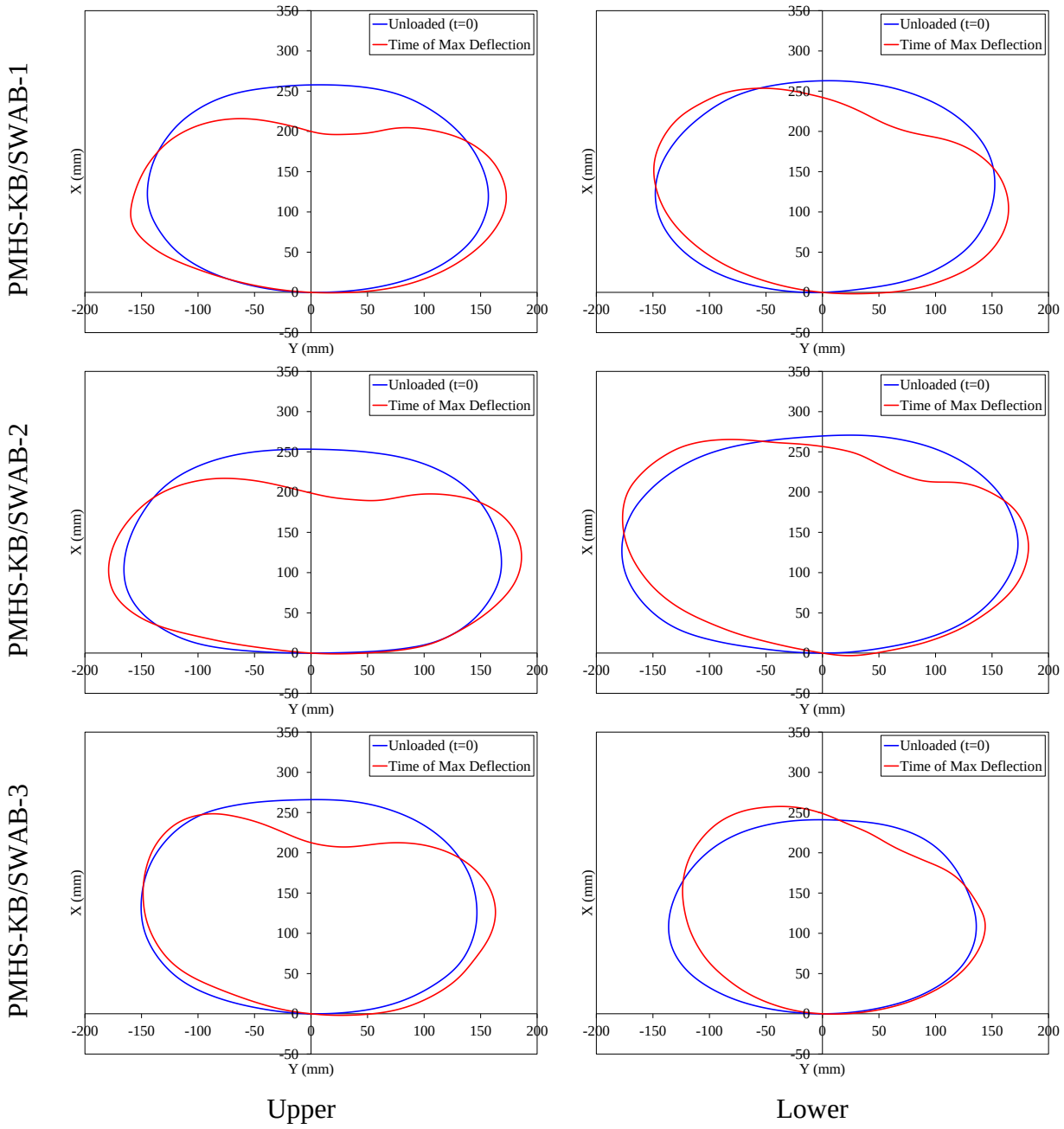

Figure A7.4: Upper (left) and lower (right) chest band contours for the PMHS KB/SWAB condition at t = 0 and the time of maximum compression.

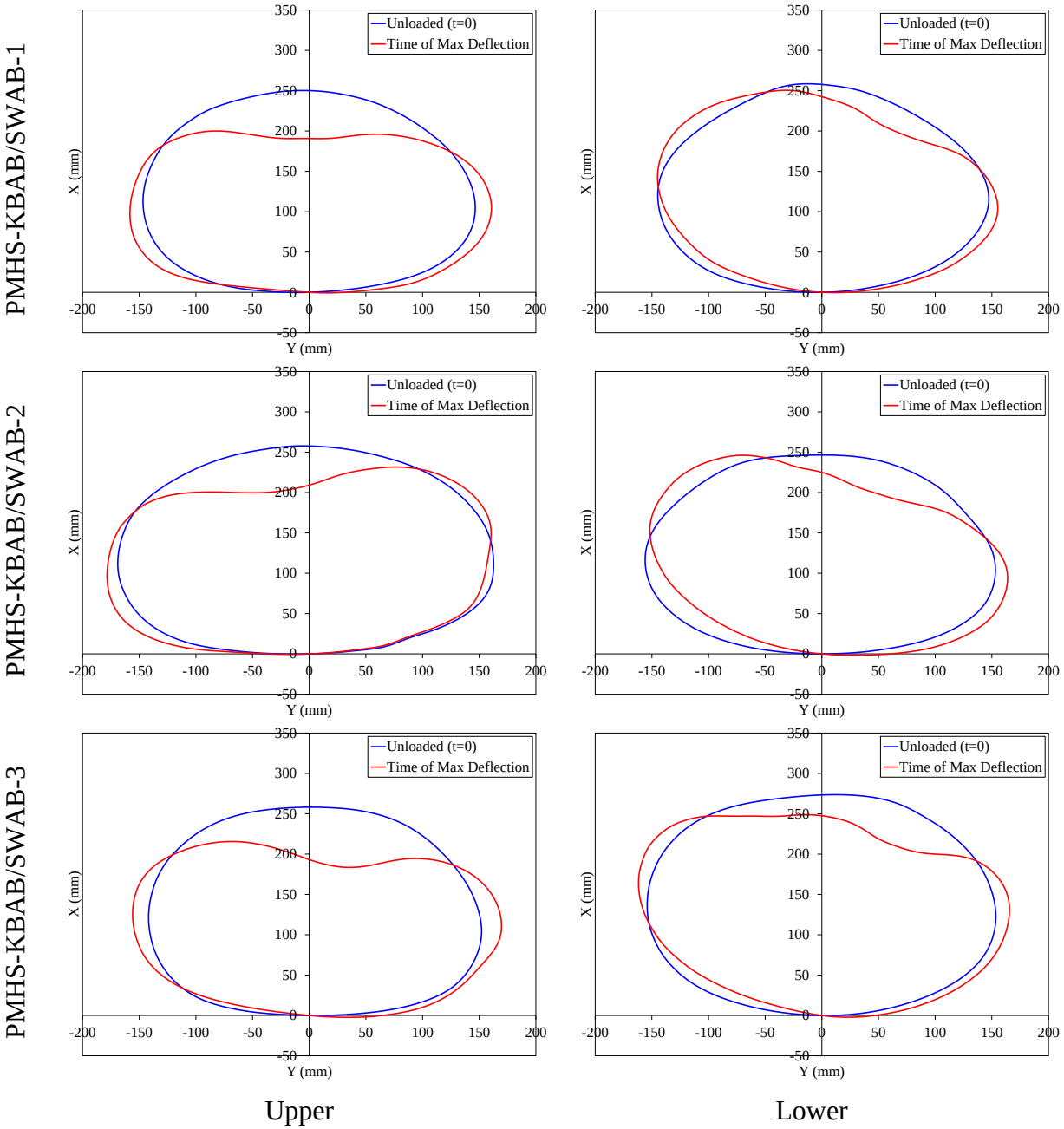

Figure A7.5: Upper (left) and lower (right) chest band contours for the PMHS KBAB/SWAB condition at t = 0 and the time of maximum compression.

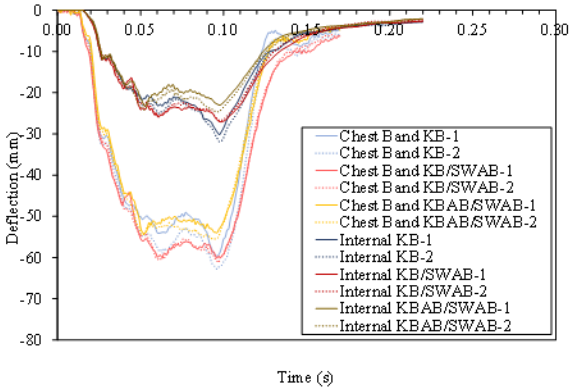

Figure A7.6: HIII chest band and internal chest deflection at the upper sternum for all conditions.

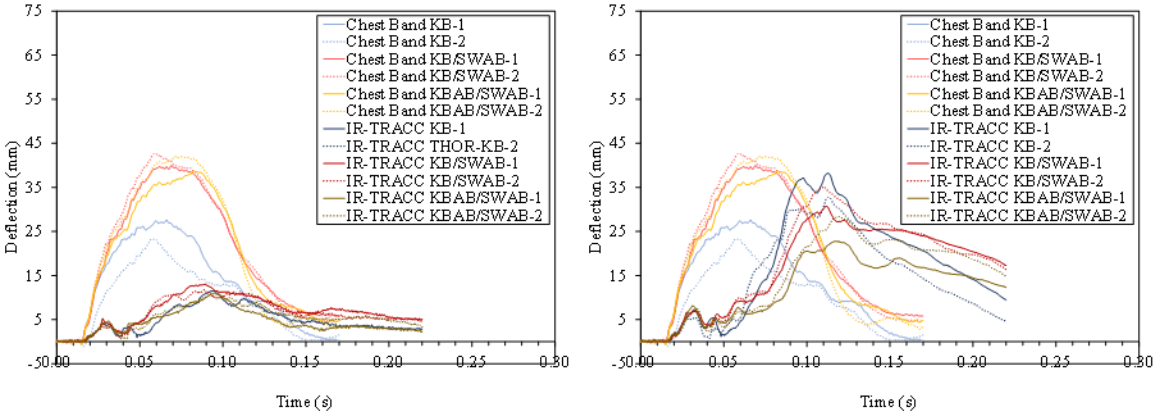

Figure A7.7: THOR chest band and IR-TRACC (left: transverse (x,y) resultant; right: x,y,z resultant) at the upper left for all conditions.
Note: Chest band compression is positive.

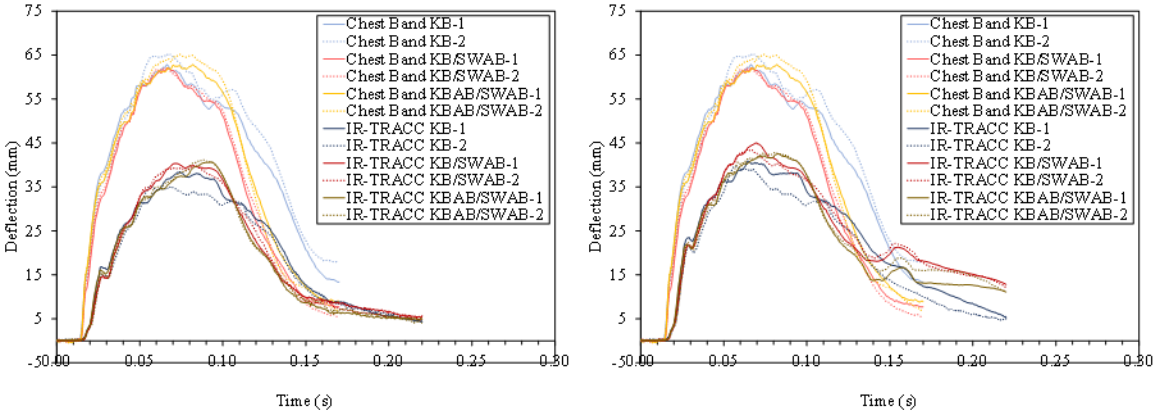

Figure A7.8: THOR chest band and IR-TRACC (left: transverse (x,y) resultant; right: x,y,z resultant) at the upper right for all conditions.
Note: Chest band compression is positive.

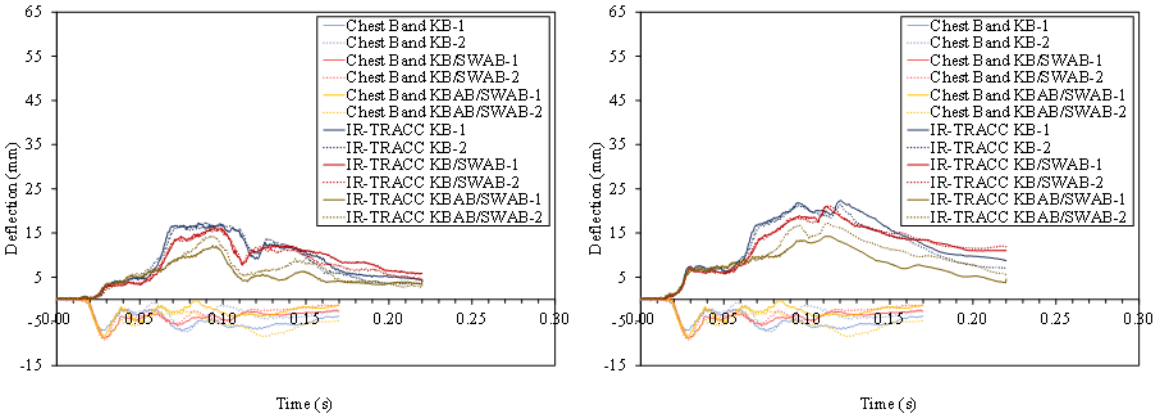

Figure A7.9: THOR chest band and IR-TRACC (left: transverse (x,y) resultant; right: x,y,z resultant) at the lower left for all conditions.
Note: Chest band compression is positive.

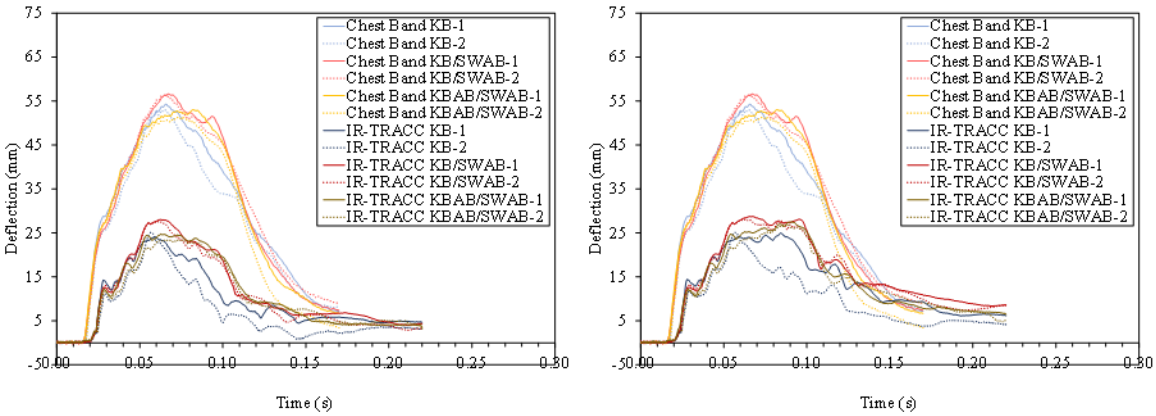

Figure A7.10: THOR chest band and IR-TRACC (left: transverse (x,y) resultant; right: x,y,z resultant) at the lower right for all conditions.
Note: Chest band compression is positive.

CHAPTER 8: INVESTIGATION OF RIB MATERIAL PROPERTIES WITH RESPECT TO SEX, AGE, AND STRUCTURAL PROPERTIES

Select contents published in:

Albert DL, Kang YS, Agnew AM, Kemper AR, "A Comparison of Rib Structural and Material Properties from Matched Whole Rib Bending and Tension Coupon Tests," *IRCOBI Conference Proceedings,* Sept 13-15, Antwerp, Belgium, 2017.

Introduction

The chest is the second most injured body region in motor vehicle collisions (MVC), contributing to approximately 65% of all blunt chest trauma [1,2]. After an MVC, in-hospital mortality risk significantly increases if the patient sustained severe (AIS3+) rib fractures [3]. Older occupants, in particular, are 2.5 times more likely to succumb to injuries resulting from an MVC if they suffered severe rib fractures [3]. Not only do older occupants have a higher mortality risk from severe chest injuries [3-5], older occupants are more likely than their younger counterparts to sustain severe chest injuries during MVCs [6-10]. Older females appear to be even more at risk as they are 6.5 times more likely sustain a thorax injury than younger females, compared to males whose thoracic injury risk is 2.8 times higher for older individuals [8]. For every decade aged, females are 1.77 times more likely to sustain a severe thoracic injury, while this figure for males is 1.37 [9]. In support of these epidemiological findings, experimental testing has shown that thoracic injury tolerance decreases with age [11-14]. This decrease has been attributed to several factors including changes in bone quality and rib geometry, which would influence rib material and structural properties.

Previous studies reported a degradation in cortical bone material properties with age in the femur, tibia, and humerus [15-17]. Burstein *et al.* (1976) noted differences in how age influenced the material properties of femur and tibia cortical bone, suggesting the relationship between age and bone material properties may vary throughout the body. In two separate studies, Kemper *et al.* assessed how rib cortical bone tensile properties varied with age [18,19]. In the earlier study, the ultimate strain, strain energy density (SED), and modulus were significantly correlated with age [18]. However, the later study found no correlation with age for any of the tensile material properties [19]. One notable difference between the two studies that may have contributed to the conflicting results was subject demographics. The study that found significant changes in material properties with age contained both male and female subjects and one 18 year old subject [18], whereas the study that found no significant correlation contained only older male subjects [19].

The influence of sex on bone material properties has also produced conflicting results. Kemper *et al.* (2005) found that female rib cortical bone was more brittle than male rib cortical bone [18]. However, Stitzel *et al.* (2003) found no correlation between sex and rib cortical bone material

properties [20]. Outside of the rib, Burstein *et al.* (1976) and Lindahl and Lindgren (1967) found no correlation between cortical bone material properties and sex [15,16], whereas McCalden *et al.* (1993) reported that female cortical bone was stronger than male cortical bone even after accounting for differences in porosity [17]. The conflicting results on the influence of sex and age on rib cortical bone material properties may be the product of the limitations of previous studies. Despite testing a large number of samples, Kemper *et al.* (2005), Kemper *et al.* (2007), and Stitzel *et al.* (2003) conducted their studies on a small number of subjects: six, six, and four, respectively. Kemper *et al.* (2005) and Stitzel *et al.* (2003) both tested equal numbers of male and female subjects, while Kemper *et al.* (2007) tested only male subjects. Furthermore, the interaction between sex and age could not be tested in the Kemper 2005 study due to the small sample size, but this interaction could have influenced the results. Therefore, the material properties of a larger number of male and female subjects must be quantified in order to assess how sex and age influence rib cortical bone material properties.

Rib material properties, gross geometry, and cross-sectional geometry are all thought to contribute to rib structural properties. A recent study showed that both cross-sectional and whole rib geometry explained a large amount of variance (35 – 75%) in rib structural response [21]. The remaining unexplained variance may be at least partially explained by the rib material properties. Few studies have attempted to investigate the relationship between rib structural and material properties. Kemper *et al.* (2007) conducted matched 3-point bending tests and coupon tension tests at different regions along the rib and at different rib levels in order to determine whether variation in material properties contributed to the within subject variation observed in the structural response of the rib [19]. No significant difference in material properties was observed across rib region or level, while variation in the structural properties with respect to rib region and rib level were attributed to variation in rib cross-sectional geometry. However, the structural testing was performed on relatively straight whole rib sections, as opposed to the entire rib. Therefore, the structural responses obtained cannot be extrapolated to the structural response of the whole rib, which encompasses more complex geometries. Additionally, the study did not assess the degree of correlation between the measured material and structural properties. Consequently, further research is necessary to link the structural response of the whole rib to the material properties of

the rib cortical bone in order to assess the relative contributions of material properties and geometry on thoracic injury tolerance.

The purpose of this study was twofold. The first objective was to quantify the rib cortical bone material properties throughout adulthood for both sexes in order to investigate the relationships of the material properties with sex and age. The second objective was to evaluate potential correlations between the whole-rib structural properties and rib cortical bone material properties.

Methods

Paired sixth ribs from 27 individuals (15 male, 12 female), ranging from 34 to 99 years of age (mean: 70.5 ± 18.1 years), were included in this study. Subject specific demographics are given in Table 8.1. The ribs were ethically obtained through the Body Donor Program at The Ohio State University and Lifeline of Ohio. The full length of the left and right ribs was excised from each donor soon after the time of death, wrapped in saline soaked gauze, stored in plastic bags, and frozen to a temperature of -20°C until testing so that the material properties of the bone would not be altered [22-26]. The left or right rib was randomly selected to undergo a whole rib bending test to quantify the structural properties, while the contralateral rib was selected to undergo coupon tension testing to determine the material properties. It was assumed that the material properties would be consistent between matched left and right ribs because Kemper *et al.* [18,19] observed no significant differences in rib material properties with respect to rib region (anterior, lateral, and posterior) or rib level within the same subject. Before both types of testing, the ribs were thawed, and the soft tissue was removed. Specimens were kept hydrated with saline during both the preparation and experimental phases of both the bending and tension tests.

Table 8.1: Subject demographics.

Subject Number	Sex	Age (years)	Height (cm)	Mass (kg)
219	F	51	157	77
220	M	60	188	94
221	F	74	155	44
222	F	34	173	73
223	F	82	160	59
224	F	76	157	83
225	M	78	183	102
226	M	94	175	100
227	F	66	167	63
229	F	50	168	77
231	F	92	142	32
233	M	59	168	60
234	M	89	183	83
235	M	83	173	84
236	F	84	165	46
239	F	70	-	-
240	F	35	155	71
241	F	99	160	51
242	M	59	191	75
244	M	57	175	89
245	M	97	150	58
246	M	66	168	63
247	M	58	185	93
248	M	95	178	58
249	M	54	183	79
250	M	73	183	63
251	M	69	187	86

Whole Rib Bending Tests

The whole rib anterior/posterior bending tests were conducted at The Ohio State University using a custom pendulum fixture, as described in Agnew *et al.* (2015) and Schafman *et al.* (2016), which was designed to simulate a frontal thoracic impact (Figure 8.1) [27,28]. The pendulum impacted the ribs at approximately 2 m/s, causing the sternal end of the rib to translate toward the fixed vertebral end. This produced a strain rate of approximately 0.5 strain/s. The ribs were instrumented with four uniaxial strain gages applied to the pleural and cutaneous surfaces at approximately 30% and 60% of the rib curve length from the vertebral end. The test fixture was instrumented with a 6-axis reaction load cell (CRABI neck load cell, IF-954, Humanetics, Plymouth, MI) to measure

forces and moments. The linear displacement of the sternal end of the rib was measured using a string potentiometer (Rayelco P-20A, AMETEK, Inc., Berwyn, PA). The forces and linear displacements were filtered using SAE channel filter class (CFC) 180 [29]. The peak force was defined as the maximum force in the direction of impact as measured from the reaction load cell. It should be noted that this value cannot be assumed to be constant along the length of the rib. The maximum percent linear displacement (referred to as failure displacement) was calculated as a percentage of the total span length. The yield force and yield percent linear displacement (referred to as yield displacement) were calculated as the point on the force displacement curve that intersected with a line parallel to the slope of the elastic portion of the force-displacement curve, but was offset 0.1% displacement from the origin. Linear structural stiffness was calculated as the slope of 20–80% of the elastic portion of the force-displacement curve. The total energy was defined as the area under the force-displacement curve until the time of fracture. Elastic energy and plastic energy were defined as the areas under the force-displacement curve before and after the yield point, respectively. High speed video (Phantom, Vision Research, Inc., Fort Wayne, IN) of the bending tests was collected at 1000 frames/s.

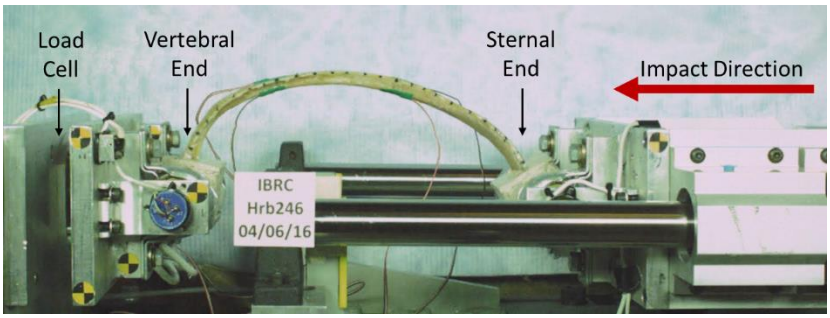

Figure 8.1: Whole rib bending test setup.

Coupon Tension Tests

Cortical bone tension coupons were fabricated from sixth ribs that were contralateral to the ribs used in the whole rib bending tests. The coupons were tested to failure in tension according to the methodology presented in Kemper *et al.* (2005) and Kemper *et al.* (2007) [18,19]. In brief, rectangular sections (30 mm long and 9 mm wide) of the cutaneous cortical bone were cut using a custom-made low-speed circular saw with a diamond encrusted blade. The rectangular sections were aligned with the main axis of the rib and were cut from the anterior or lateral aspect of the

rib. In two separate studies, Kemper *et al.* found no significant difference in material properties between the anterior, lateral, and posterior aspects of the rib [18,19]. Therefore, coupons were obtained from the location along the rib with sufficient width and the least amount of natural curvature, regardless of the anatomical region. Because the posterior aspect has a higher curvature than the rest of the rib, samples were only taken from the anterior and lateral aspects. In the event that the rib was too narrow to obtain a sample with the correct width, the sample was cut to the maximum width possible. Decreasing grits of sand paper (240, 320, 400, and 600) were used to sand both sides of the specimen until the sample thickness was uniform within 0.127 mm. Then, the sample was milled into a dog-bone shape using a Computer Numerical Control (CNC) mill (MAXNC 10, Ximotion LLP, Gilbert, AZ) (Figure 8.2). After the milling process was completed, each samples was sanded to a final thickness, which was uniform within ±0.0127 mm across the entire sample. The thickness and width of the gage length of each sample was measured with calipers in order to calculate stress during the tensile tests.

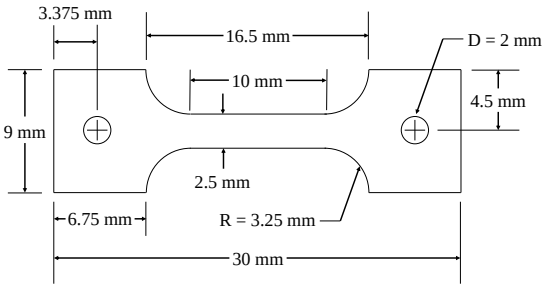

Figure 8.2: Coupon schematic.

Uniaxial tensile tests were performed on a high-rate servo-hydraulic Material Testing System (810 MTS, MTS Systems Corporation, Eden Prairie, MN) using custom designed coupon grips and a slack adapter (Figure 8.3). The custom slack adapter was used to ensure that the coupons experienced a constant strain rate throughout the entire test. Care was taken to confirm the alignment of the top and bottom grips so that the coupons were experiencing a purely tensile load [18]. Coupons were pulled in tension past the point of failure at a target strain rate of 0.5 strain/s. Data from the uniaxial load cell (1500ASK-100, Interface, Scottsdale, AZ) and extensometer (632.13F-20, MTS, Eden Prairie, MN) were collected at 40100.2 Hz and filtered at SAE CFC 180 [29]. Strain was calculated from the extensometer output by dividing the change in length between

the extensometer arms by the initial length between the arms. Stress was calculated by dividing the force by the initial cross-sectional area of the coupon gage length. The yield point was calculated as the point of intersection between the stress-strain curve and a straight line at a 0.1% strain offset that was parallel to the elastic portion of the curve [30]. The elastic modulus was calculated as the slope between two points on the stress-strain curve that were approximately 10% and 50% of the yield point. The failure stress and failure strain were defined as the stress and strain at the time of failure. SED was calculated as the integral of the stress-strain curve. Lastly, elastic SED and plastic SED were defined as the areas under the stress-strain curve before and after the yield point, respectively.

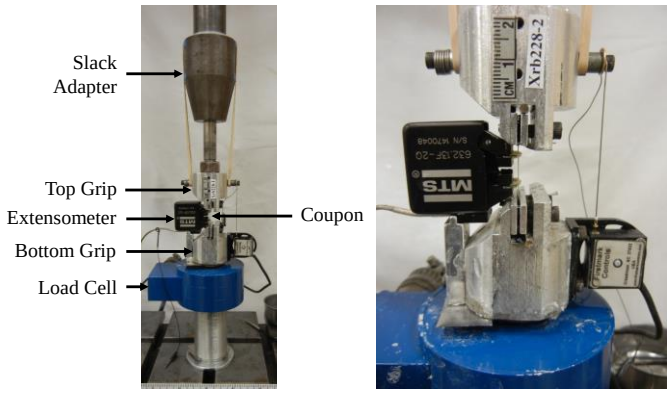

Figure 8.3: Coupon tensile test setup.

Data Analysis

The degree of linear correlation between analogous pairs of material and structural properties from the coupon and bending tests, respectively, was statistically assessed. The pairs included the coupon elastic modulus and whole rib stiffness, coupon yield strain and whole rib yield displacement, coupon yield stress and whole rib yield force, coupon failure strain and whole rib failure displacement, coupon failure strain and whole rib peak tensile strain, coupon failure stress and whole rib failure force, coupon SED and whole rib total energy, coupon elastic SED and whole rib elastic energy, and coupon plastic SED and whole rib plastic energy. All properties were tested for normality using a Shapiro-Wilk test. At least one property was not normally distributed. Therefore, the non-parametric Spearman's rank correlation coefficient (ρ) was determined for each pair in addition to the Pearson correlation coefficient (r), which assumes normality. The statistical significance of each test statistic was calculated using a Students t-test. Significance was

ascertained using an alpha level of 0.05 for all analyses. The coefficient of determination (R^2) was also calculated for each comparison based on a linear regression in order to assess the percent variance of the structural property explained by the material property. Finally, the root mean square error (RMSE) was quantified to assess the error in the data about the regression line.

In order to assess whether the material properties derived from the coupon tests were influenced by the age or sex of the subjects from which ribs were acquired, a two-way ANOVA was performed for each material property. The tested effects were age, sex, and the interaction between age and sex. The degree of linear correlation between age and each of the material properties was assessed using the Pearson correlation coefficient (r). The statistical significance of r was calculated using a Students t-test. RMSE and R^2 were also quantified for the regressions between the material properties and age. All variables were tested for normality using a Shapiro-Wilk test (W) before parametric statistical analyses were performed. Significance was ascertained using an alpha level of 0.05 for all analyses.

Results

During the bending tests, translation of the sternal end of the rib toward the vertebral end resulted in increased rib curvature (Figure 8.4). The cutaneous cortex of the rib experienced tensile loading, while the pleural cortex experienced compressive loading. The ribs were loaded to failure, resulting in one or two fractures. Ribs with two fractures experienced both fractures almost simultaneously as their times of fracture could not be distinguished using the high speed video. Fracture location varied between specimens, but fractures mostly occurred in the anterior and lateral regions of the rib. It was not always possible to confirm that fracture initiated on the cutaneous (tensile) surface of the rib during the bending tests using the high speed video due to the rapidity of the event. However, a previous study using the same experimental setup was able to confirm that fracture initiated on the tensile surface for all tested ribs and provided a more complete description of fracture mechanisms [31].

In order to determine whether the cutaneous cortex of the rib in the bending tests and the coupons in the tensile tests experienced comparable loading, the strain rates and direction of principal strain were compared. The average strain rates from the bending and coupon tests were 0.522 and 0.509

strain/s, respectively. Additionally, an analysis of principal strains for one rib instrumented with rosette strain gages during a bending test showed that the maximum principal strain was within 10 degrees of the main axis of the rib. This coincides with the coupon tests since the coupons were fabricated to align with the main axis of the rib. Therefore, the cortical bone experienced similar loading in both the bending and coupon tests.

Figure 8.4: Video stills from a bending test with the rib in the initial position (left), displaced before fracture (middle), and during fracture (right).

The means of the structural and material properties are presented in Table 8.2. Analogous structural properties and material properties from the bending tests and coupon tests, respectively, were plotted (Figure 8.5 - Figure 8.13). The structural properties of yield displacement ($W = 0.8851$, $p = 0.0062$), failure displacement ($W = 0.8580$, $p = 0.0017$), total energy ($W = 0.8815$, $p = 0.0052$), elastic energy ($W = 0.8731$, $p = 0.0034$), and plastic energy ($W = 0.8882$, $p = 0.0073$) were not found to be normally distributed. This prompted a non-parametric analysis of correlation (Spearman correlation) in addition to the Pearson correlation for the material-structural property pairs that were normally distributed. The results of both analyses for all pairs are reported in Table 8.3. The correlations were positive between all pairs, except for whole rib yield displacement and coupon yield strain. The pairs with significant correlations ($p < 0.05$) included coupon failure strain and whole rib peak tensile strain, coupon failure stress and whole rib failure force, coupon SED and whole rib total energy, and coupon plastic SED and whole rib plastic energy. All linear regressions between the material and structural properties resulted in R^2 values below 0.5 (Table 8.3), indicating that the material properties explained less than 50% of the variance in structural properties. The lowest R^2 value was observed for the yield strain and yield displacement ($R^2 = 0.0013$), while the highest value was observed for SED and total energy ($R^2 = 0.4840$). This demonstrated that the yield strain explained approximately 0.1% of the variance in yield displacement, while SED explained almost half of the variance in the total energy.

The material properties were significantly influenced by age, but not by sex. The two-way ANOVA revealed a significant effect of age on the modulus, yield stress, failure strain, failure stress, SED, and plastic SED (Table 8.4). Yield strain and elastic SED were the only material properties that were not significantly influenced by age. Sex and the interaction between sex and age were not significant for any of the material properties. All material properties were negatively correlated with age (Table 8.5, Figure 8.14 - Figure 8.21). The correlations with age were significant for all material properties except for yield strain and elastic SED. The stress-strain curves for all coupon tension tests were plotted in groups according to age and sex (Figure 8.22 - Figure 8.28). Until 60 years of age, the initial slopes of the stress-strain curves (moduli) were very similar for subjects within the same decade of age regardless of sex. However, more variation was observed above 60 years of age. Variation in failure stress and failure strain was observed regardless of decade.

Table 8.2: Mean material and structural properties.

Test Type	Property	Units	Mean	Standard Deviation
Structural Whole Rib Test	Stiffness	N/mm	2.80	1.38
	Yield Displacement	%	10.05	4.65
	Yield Force	N	53.85	25.34
	Peak Tensile Strain	μstrain	11562	3990
	Failure Displacement	%	20.17	8.13
	Failure Force	N	81.25	33.86
	Total Energy	N-mm	2351.26	1640.81
	Elastic Energy	N-mm	701.51	483.26
	Plastic Energy	N-mm	1649.75	1379.06
Material Tension Coupon Test	Modulus	GPa	12.74	3.04
	Yield Strain	μstrain	6481	1025
	Yield Stress	MPa	70.83	22.48
	Failure Strain	μstrain	23728	8442
	Failure Stress	MPa	106.54	33.53
	SED	MPa- μstrain	2014646	1176649
	Elastic SED	MPa- μstrain	268611	112946
	Plastic SED	MPa- μstrain	1746035	1112708

Table 8.3: Regression parameters for each material property/structural property comparison.

Material Property	Structural Property	Pearson		Spearman		R^2	RMSE	RMSE Unit
		r	p-value	ρ	p-value			
Modulus	Stiffness	0.2806	0.1562	0.2631	0.1848	0.0787	1.30	N/mm
Yield Strain	Yield Displacement*	-0.0359	0.8589	-0.0305	0.8799	0.0013	4.56	%
Yield Stress	Yield Force	0.2195	0.2712	0.2344	0.2392	0.0482	24.26	N
Failure Strain	Peak Tensile Strain	**0.4943**	**0.0088**	**0.4060**	**0.0356**	0.2443	3403	μstrain
Failure Strain	Failure Displacement*	0.3904	0.0441	0.3748	0.0540	0.1524	7.35	%
Failure Stress	Failure Force	**0.4115**	**0.0330**	0.3773	0.0524	0.1693	30.28	N
SED	Total Energy*	0.6957	< .0001	**0.6087**	**0.0008**	0.4840	1157	N-mm
Elastic SED	Elastic Energy*	0.1197	0.5522	0.0598	0.7669	0.0143	471	N-mm
Plastic SED	Plastic Energy*	0.6594	0.0002	**0.5446**	**0.0033**	0.4348	1017	N-mm

Note: An asterisk (*) indicates a parameter that was not normally distributed. Bolded text indicates a significant p-value.

Table 8.4: ANOVA generated p-values for the model effects of sex, age, and the interaction of sex and age (sex*age) on each material property.

Material Property	Sex	Age	Sex*Age
Modulus	0.4039	**0.0035**	0.5018
Yield Strain	0.9414	0.7200	0.5645
Yield Stress	0.6436	**0.0375**	0.9481
Failure Strain	0.9777	**0.0069**	0.2770
Failure Stress	0.8237	**0.0027**	0.6631
SED	0.8079	**0.0030**	0.4901
Elastic SED	0.6938	0.1355	0.7620
Plastic SED	0.8324	**0.0029**	0.4439

Note: Bolded text indicates a significant p-value.

Table 8.5: Regression parameters for each material property with age.

Material Property	r	p-value	R^2	RMSE	RMSE Unit
Modulus	-0.5329	**0.0042**	0.2840	2.52	GPa
Yield Strain	-0.1028	0.6099	0.0106	1001	μstrain
Yield Stress	-0.4142	**0.0317**	0.1716	20.08	MPa
Failure Strain	-0.4996	**0.0080**	0.2496	7176	μstrain
Failure Stress	-0.5691	**0.0019**	0.3239	27.06	MPa
SED	-0.5547	**0.0027**	0.3077	960729	MPa- μstrain
Elastic SED	-0.3143	0.1104	0.0988	105218	MPa- μstrain
Plastic SED	-0.5546	**0.0027**	0.3076	908595	MPa- μstrain

Note: Bolded text indicates a significant p-value.

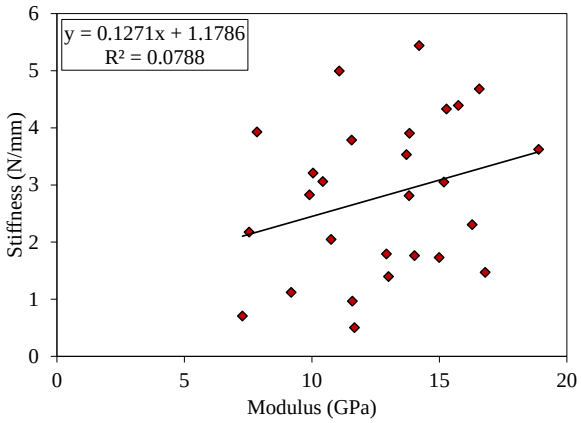

Figure 8.5: Linear trend line for whole rib stiffness and coupon modulus.

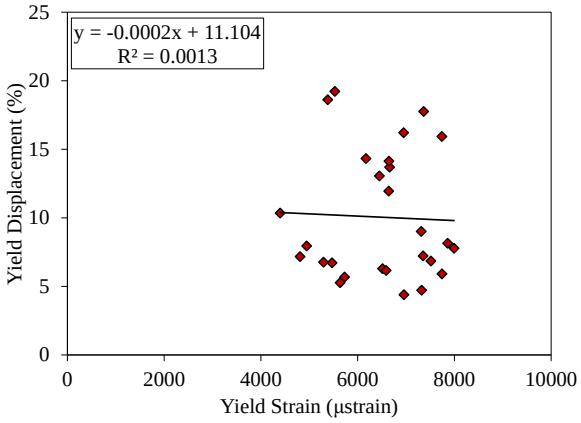

Figure 8.6: Linear trend line for whole rib yield displacement and coupon yield strain.

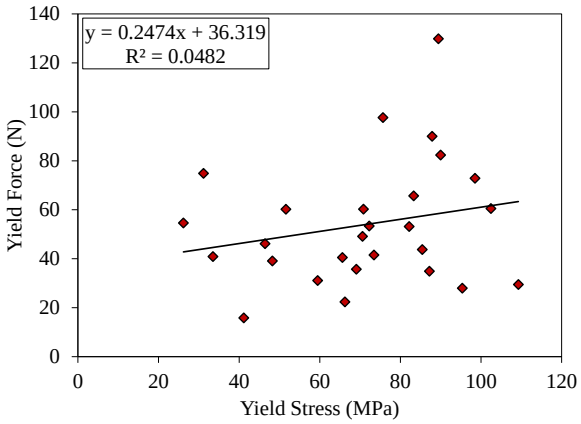

Figure 8.7: Linear trend line for whole rib yield force and coupon yield stress.

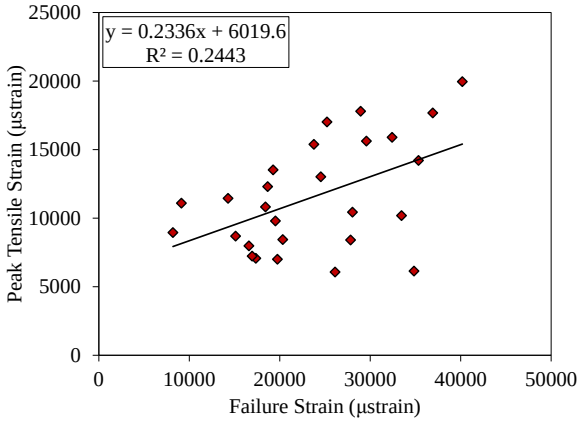

Figure 8.8: Linear trend line for whole rib peak tensile strain and coupon failure strain.

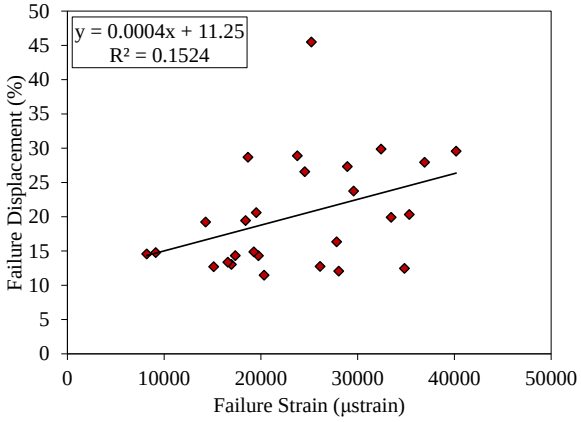

Figure 8.9: Linear trend line for whole rib failure displacement and coupon failure strain.

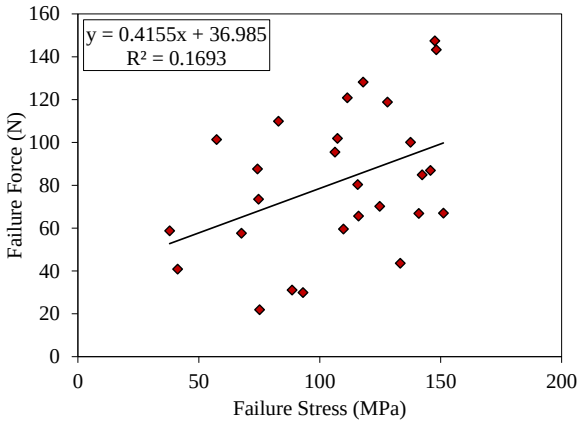

Figure 8.10: Linear trend line for whole rib failure force and coupon failure stress.

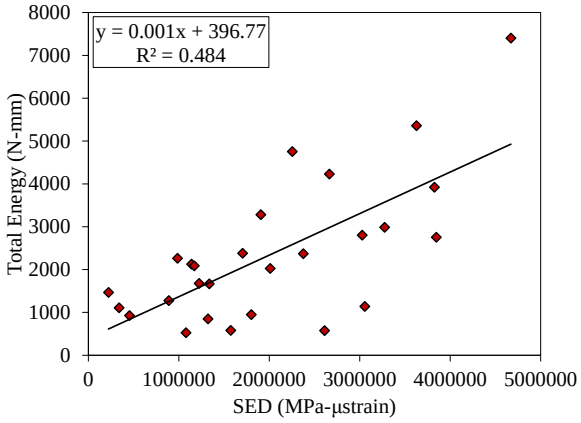

Figure 8.11: Linear trend line for whole rib total energy and coupon SED.

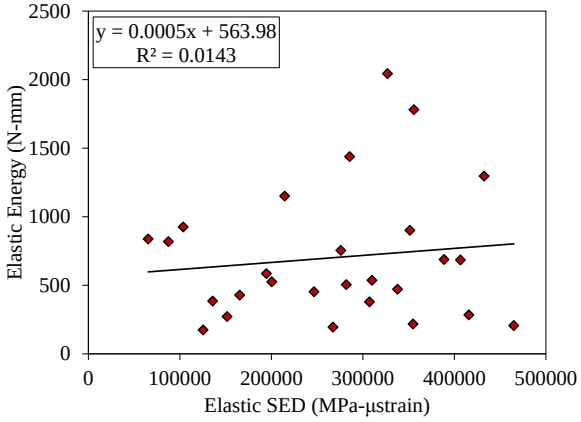

Figure 8.12: Linear trend line for whole rib elastic energy and coupon elastic SED.

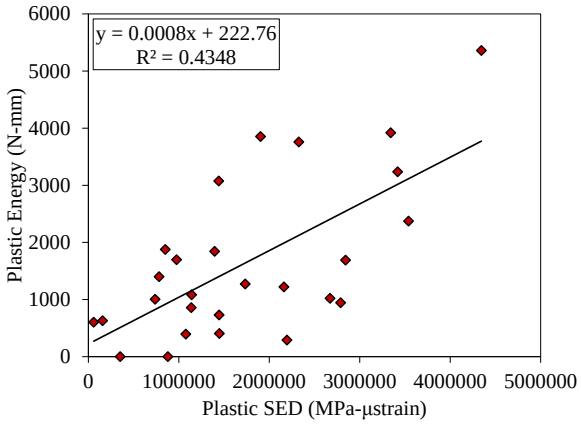

Figure 8.13: Linear trend line for whole rib plastic energy and coupon plastic SED.

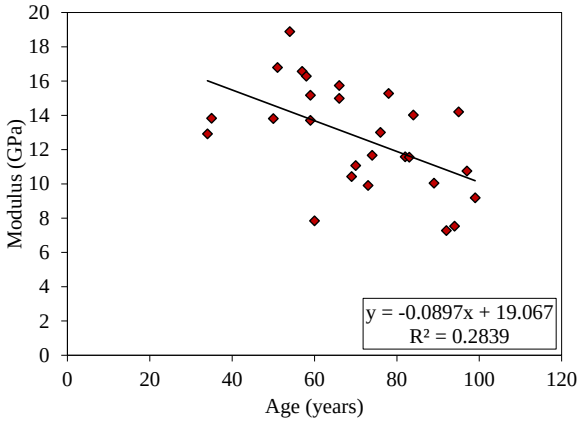

Figure 8.14: Linear trend line for coupon modulus and age.

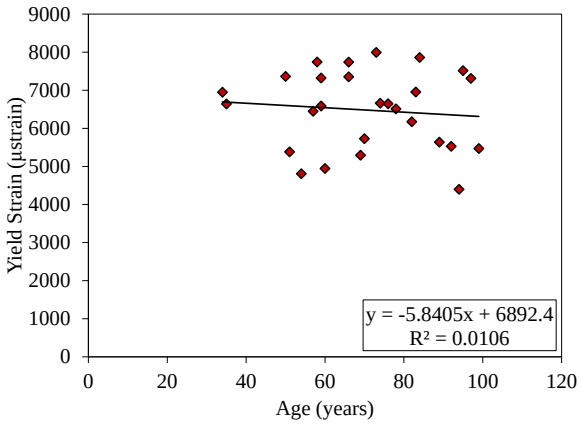

Figure 8.15: Linear trend line for coupon yield strain and age.

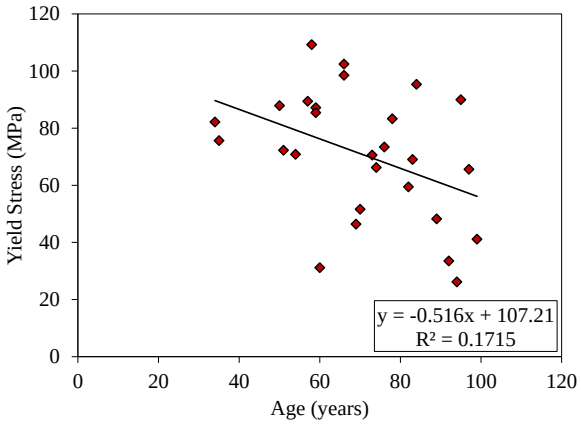

Figure 8.16: Linear trend line for coupon yield stress and age.

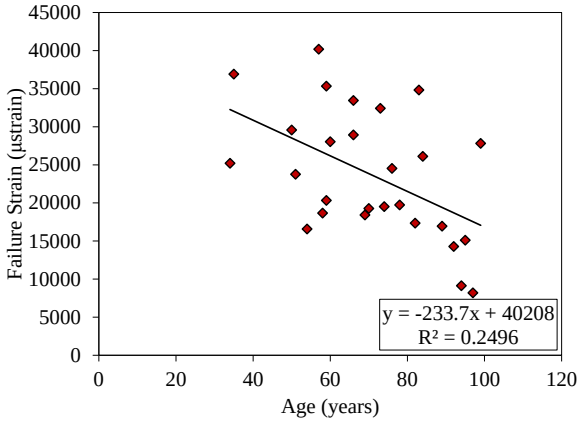

Figure 8.17: Linear trend line for coupon failure strain and age.

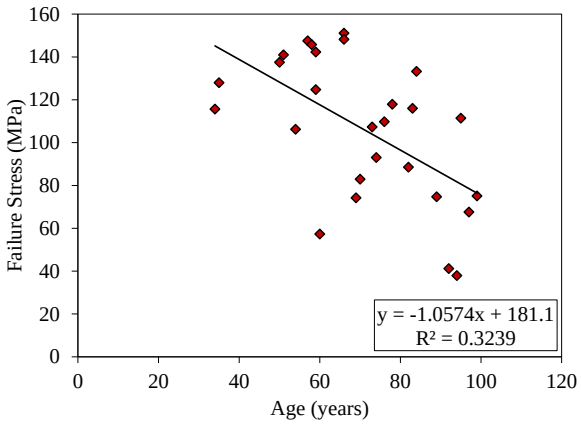

Figure 8.18: Linear trend line for coupon failure stress and age.

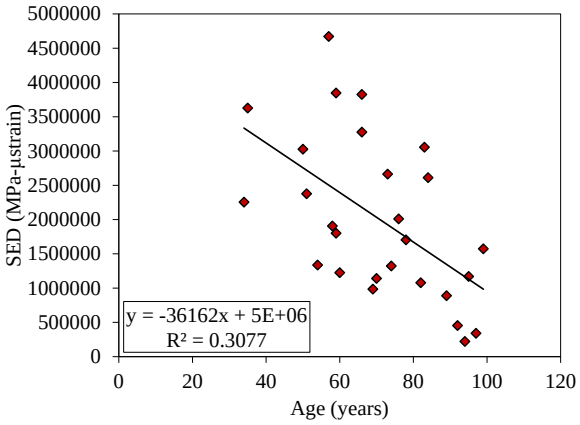

Figure 8.19: Linear trend line for coupon SED and age.

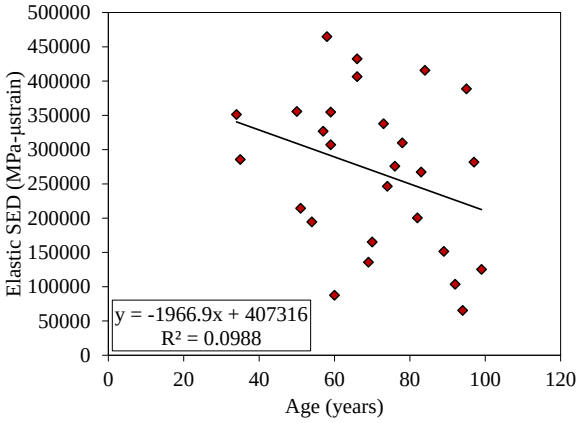

Figure 8.20: Linear trend line for coupon elastic SED and age.

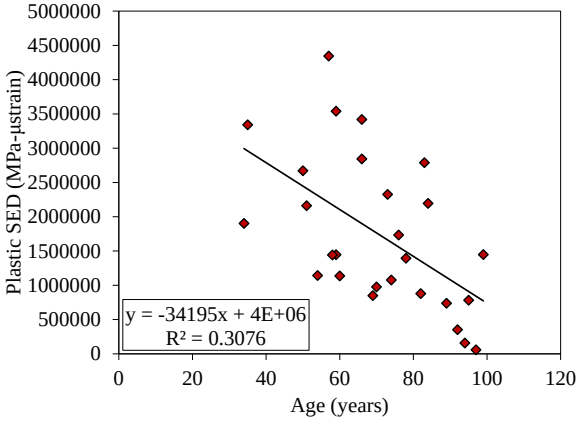

Figure 8.21: Linear trend line for coupon elastic SED and age.

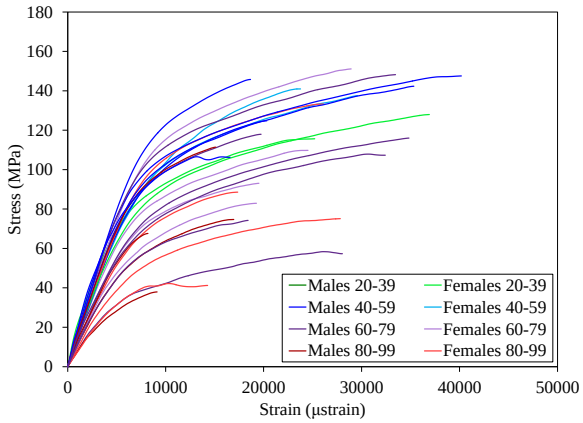

Figure 8.22: Stress-strain curves delineated by sex and age.

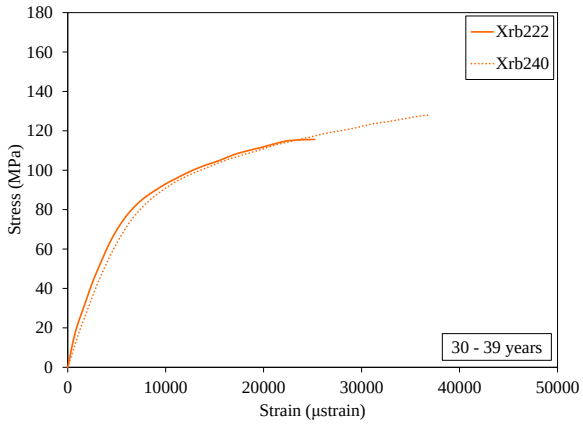

Figure 8.23: Stress-strain curves for males (blue) and females (orange) 30 to 39 years of age. Note: No data were available for subjects under 30 years of age.

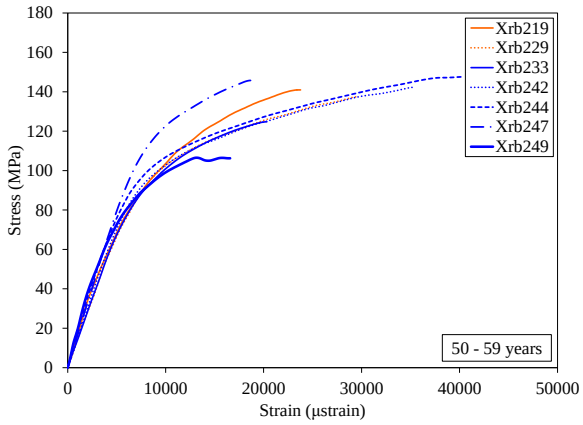

Figure 8.24: Stress-strain curves for males (blue) and females (orange) 50 to 59 years of age. Note: No data were available for subjects between 40 and 49 years of age.

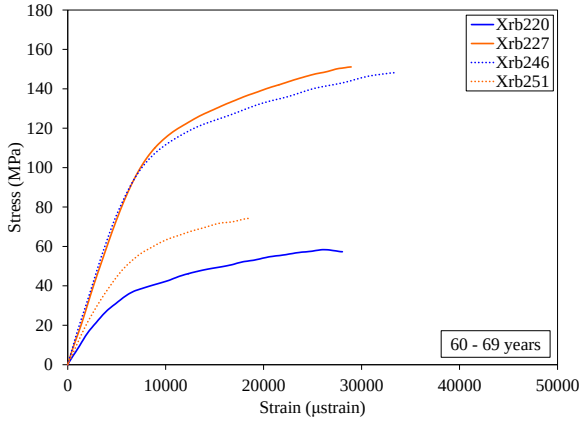

Figure 8.25: Stress-strain curves for males (blue) and females (orange) 60 to 69 years of age.

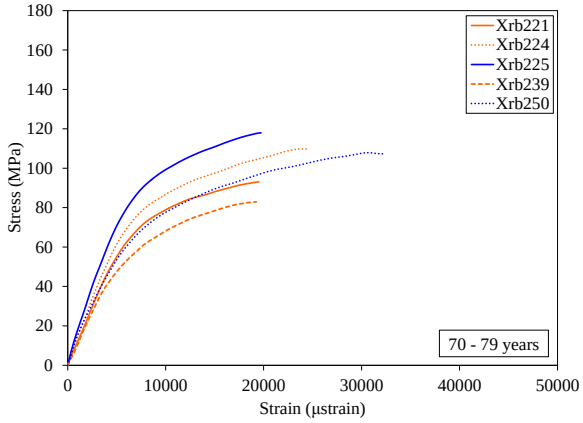

Figure 8.26: Stress-strain curves for males (blue) and females (orange) 70 to 79 years of age.

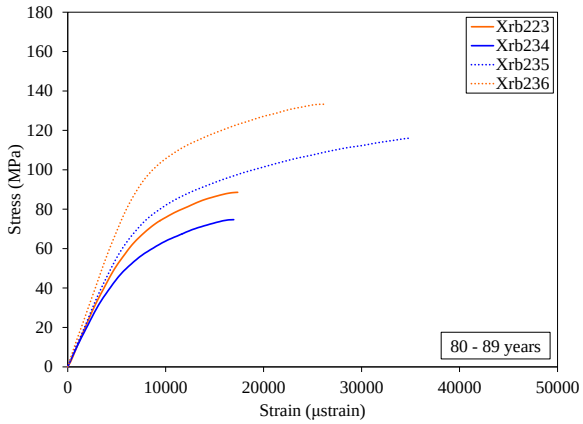

Figure 8.27: Stress-strain curves for males (blue) and females (orange) 80 to 89 years of age.

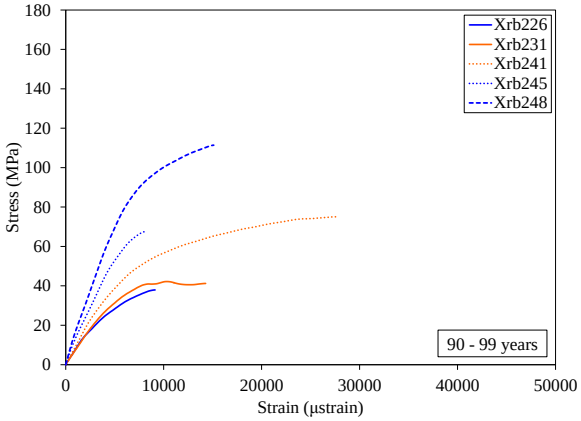

Figure 8.28: Stress-strain curves for males (blue) and females (orange) 90 to 99 years of age.

Discussion

Three previous studies have quantified the tensile material properties of rib cortical bone at a similar strain rate as this study [18,19,32]. The same coupon fabrication and experimental setup were used in this study as in Kemper *et al.* (2005) and Kemper *et al.* (2007). The average moduli, failure strains, and failure stresses (Table 8.6) reported in these studies were comparable to the average values found in this study, with the averages from this study being slightly lower than the previous studies. These small differences can be attributed to between subject variation. Overall, the material properties found in this study were consistent with those previously reported for rib cortical bone.

Table 8.6: Comparison to mean material properties from previous studies.

Study	Number of Subjects	Age (years)	Strain Rate (strain/s)	Modulus (GPa)	Failure Strain (µstrain)	Failure Stress (MPa)
Current Study	27	71 ± 18	0.5	12.7	23728	106.5
Kemper *et al.* (2005)	6	50 ± 18	0.5	13.9	26829	123.2
Kemper *et al.* (2007)	6	60 ± 15	0.5	14.4	25110	130.9

The structural properties observed in this study were also consistent with those reported by previous studies that performed similar whole rib anterior/posterior bending tests (Table 8.7) [27,28,31,33]. The average structural properties of the current study were most similar to those reported by Charpail *et al.* (2005) and were least comparable to those reported by Schafman *et al.* (2016). However, it is important to note that linear stiffness was calculated differently by Charpail *et al.* (2005) and Kindig *et al.* (2011) and may not be directly comparable to the results of this

study. Additionally, the tests conducted by Kindig *et al.* (2011) were performed under quasi-static conditions, whereas the tests performed by Charpail *et al.* (2005), Schafman *et al.* (2016), and the current study comprised dynamic impacts at 1 to 2 m/s. The differences between Schafman *et al.* (2016) and the current study may be attributed to between subject variation related to differences in sample demographics. Although both studies encompassed a wide range of ages, Schafman *et al.* (2016) included pediatric subjects whereas the current study did not. Furthermore, the number of males and females included in the current study is more balanced than in Schafman *et al.* (2016), which included more male subjects.

Table 8.7: Comparison to mean structural properties from previous studies.

Study	Number of Subjects	Age (years)	Loading Velocity (m/s)	Stiffness (N/mm)	Failure Displacement (%)	Failure Force (N)
Current Study	27	71 ± 18	2.0 ± 0.0	2.80	20.17	81.25
Charpail *et al.* (2005)	5	65 ± 4	1.7 ± 0.1	2.34	20.67	86.63
Kindig *et al.* (2011)	3	56 ± 10	0.002	2.31	33.04	60.67
Schafman *et al.* (2016)	93	50 ± 25	1-2	3.6	25.60	116.0

The positive correlations observed for most analogous pairs of structural and material properties indicates those material properties had some influence on the corresponding structural property. The pair with a negative correlation (whole rib yield displacement and coupon yield strain) had a correlation coefficient close to zero, indicating almost no relationship. This negative correlation was non-significant, as were four other pairs: whole rib stiffness and coupon modulus, whole rib yield force and coupon yield stress, whole rib failure displacement and coupon failure strain, and whole rib elastic energy and coupon elastic SED. This indicates that rib geometry may be contributing more to the stiffness, yield force, failure displacement, and elastic energy than the material properties. SED and total energy had the highest degree of correlation of all pairs. This is logical because energy absorption is primarily a function of the material.

Several studies have attempted to use modeling and theoretical approaches to gain insight into the mechanics of this simplified bending scenario with limited success. Charpail *et al.* (2005) used a finite element model of three ribs that incorporated simplified rib-specific geometry, but constant material properties across all ribs, in an attempt to predict the fracture locations in the corresponding experimental tests based on the strains observed in the model. The model was able

to approximately match the fracture locations, but was unable to match fracture timing. Charpail *et al.* (2005) concluded that discrepancies between the model and experiments were a result of the simplified rib geometry used for the model. Daegling *et al.* (2008) performed similar bending tests on ribs instrumented with strain gages in order to study rib fracture mechanics. They used beam theory to predict the stresses occurring at the rib locations instrumented with strain gages and a non-specific elastic modulus to calculate "observed" stresses. Substantial differences between the observed and theoretical stresses were reported, and the authors attributed these differences to the assumption of elasticity and an oversimplification of rib geometry. Perz *et al.* (2013) developed a finite element beam model using rib-specific geometry derived from CT data and non-specific material properties. The model was able to reasonably match the elastic portion of the force-deflection curves from bending tests based on geometric properties alone. However, their model limitations prevented additional analyses of plastic and failure behavior.

Charpail *et al.* (2005), Daegling *et al.* (2008), and Perz *et al.* (2013) demonstrated the importance of rib geometry on structural properties and mechanical behavior through modeling. Furthermore, a recent study by Murach *et al.* (2017) showed that both cross-sectional and whole rib geometry explained a large amount of variance (35 – 75%) in rib structural response in the same bending scenario used in the current study. However, none of these studies attempted to account for rib-specific material properties in their models. The current study showed that rib material properties were only a partial contributor to the structural properties and that some material properties were more influential than others. The results of this study in conjunction with the literature empirically confirm the long-standing hypothesis that both material properties and rib geometry contribute to rib structural properties. This study is a first step toward a larger goal of quantifying the relative contributions of material properties and geometry on rib structural responses. Future analyses incorporating rib-specific cross-sectional and whole rib geometry will be performed as the necessary data are collected, and multivariate models will be constructed to understand the influence of all variables and their potential interactions. The data included in this study and future studies will provide a basis for improved modeling of rib mechanics and injury prediction.

The observed significant correlations between material properties and age were all supported by at least one previous study on rib, femur, tibia, or humeral cortical bone. However, the influence

of advancing age on cortical bone material property may vary across the body [15]. Previous studies that explored the relationship between rib cortical bone material properties and age were limited to six subjects each, which may have influenced results [18,19]. Of the two previous studies, Kemper *et al.* (2005) included both sexes and a larger range of ages. Therefore, the results of this study were primarily compared to the results of Kemper *et al.* (2005). While the current study reported a significant decrease in modulus with age, Kemper *et al.* (2005) observed a significant increase in modulus with age. However, this was due to the inclusion of an 18 year old male in the previous study. Bone may not be fully mature at 18 years of age, and removal of this data point led to no significant relationship between modulus and age. Kemper *et al.* (2005) reported that the yield strain did not vary with age, while the current study observed both a significant negative correlation between yield stress and age and no significant correlation between yield strain and age. Furthermore, previous studies on femur and tibia cortical bone reported decreases in yield stress and strain with advancing age [15,17]. It is possible that the variation between studies is due to differences in how the yield point was determined. The current study, Kemper *et al.* (2005), and Burstein *et al.* (1976) all used different methods to determine the yield point, while McCalden *et al.* (1993) did not specify the method used. Other reasons for the differences in the influence of age on the yield point that were observed between studies include sample size, type of bone, and subject demographics. It should also be noted that the correlation between age and yield stress in the current study resulted in the lowest R^2 value out of all of the material properties that had significant correlations with age. For failure strain (ultimate strain), both Kemper *et al.* (2005) and the current study observed a significant negative correlation with age. Conversely, failure stress (ultimate stress) had a significant correlation with age in the current study, but no significant correlation in Kemper *et al.* (2005). Previous studies on femur, tibia, and humerus cortical bone agreed with the current study, reporting a significant decrease in ultimate stress with advancing age [15-17]. Finally, both the current study and the previous study observed a significant negative correlation between SED and age [18]. Kemper *et al.* (2005) did not separate SED into elastic and plastic components; however, they reported in accordance with other studies [15,17] that a decrease in cortical bone plasticity accompanied aging. The partially conflicting results between the current study and Kemper *et al.* (2005) emphasize the sensitivity of this analysis to the subject sample size and demographics. Adding more subjects to the data from the current study could change the results, but would strengthen the analysis.

No significant differences in material properties were observed between the sexes in the current study. Previous studies on rib, femur, and humerus cortical bone tensile material properties also observed no significant sex differences [16,20]. However, Kemper *et al.* (2005) reported a significantly higher elastic modulus for females and a significantly higher ultimate strain for males. As noted above, the results of the correlation analyses seem to be highly dependent on the subject sample. The females in the Kemper *et al.* (2005) study were older on average than their male counterparts, which could have influenced the results. Furthermore, the Kemper *et al.* (2005) study had too few subjects to conduct a statistically powerful analysis of the interaction between sex and age. The current study included more subjects and was able to perform this analysis. However, no significant interactions were observed. This result was surprising since the increase in cortical bone porosity with aging is known to be higher in women, and an increase in porosity has been correlated to a decrease in ultimate stress [17]. Although the current study had a large, more diverse subject sample than previous studies on rib material properties, there was still a lack of data for earlier decades of life, biasing the sample toward older subjects. Including more subjects, particularly between the ages of 20 and 50 could lead to different results.

A limitation of this study was the assumption that there was no difference in the structural and material properties between the left and right ribs or along the length of a single rib. The results of previous research indicate that the assumption of left/right symmetry in rib material and structural properties is reasonable. Yoganandan and Pintar (1998) tested this assumption with regard to structural properties using three-point bending tests, and found no difference in the modulus, force, and deflection between matched left and right ribs. Furthermore, Kemper *et al*. [18,19] reported no significant within subject differences in material properties with respect to rib region or level on the same side of the rib cage. A logical extension of this finding is that no difference would be observed between the left and right sides of the rib cage.

Another limitation of this study was that the data analysis for the bending tests assumed that all motion was relegated to one plane and the ribs only experienced bending. However, some out of plane motion is possible and could result in torsion and shear loading. Structural properties derived

from shear loading would not be directly comparable to the tensile material properties derived from the coupon tests.

Finally, this study assumed that rib cortical bone is a homogenous material despite its true nature as a composite material. The microstructure of bone is known to influence the macroscale material properties. Increases in intracortical porosity and number of secondary osteons have been shown to decrease material properties [17,37-41]. Some studies have reported that the degree of mineralization influences bone material properties [38,39]. However, this link was not observed in all studies [17,18,42,43]. Variation in cortical bone microstructure along the length of the rib may have influenced the structural and material properties reported in this study. However, as noted above, Kemper *et al.* [18,19] found in two previous studies that tensile material properties did not significantly vary along the length of the rib so any impact of microstructural variation on material property variation within a rib is likely small. Variation in rib microstructural organization and composition between individuals has been established in prior studies specific to the rib [44,45], and likely contributed to the inter-subject variation in material and structural properties observed in this study. Therefore, future work will investigate the influence of cortical bone microstructure on rib material and structural properties. Additionally, the effect of age and sex on the relationship between the material and structural properties should be assessed on a larger and more inclusive sample as microstructural changes are thought to influence age and sex differences.

Conclusions

Positive correlations were observed for most pairs of structural and material properties. Coupon strain energy density and whole rib total energy had the highest correlation, while coupon modulus and whole rib stiffness had the lowest correlation. The structural properties with significant correlations (peak tensile strain, failure force, total energy, and plastic energy) were more influenced by material properties compared to the structural properties without significant correlations (stiffness, yield displacement, yield force, failure displacement, and elastic energy). All structural/material property comparisons resulted in R^2 values below 0.5, indicating the material properties did not explain the majority of the variance of the structural properties. Given that the structural response is dependent on both the material and geometric properties, this finding lends further support to the hypothesis that local and global rib geometries likely have a strong

influence on the structural properties. Negative correlations with age were observed for all material properties. The correlations with age were significant for the modulus, yield stress, failure strain, failure stress, SED, and plastic SED. Conversely, yield strain and elastic SED did not significantly correlate with age. Both sex and the interaction between sex and age did not significantly influence the material properties. However, a larger, more diverse sample may be needed to further explore the relationships between the material properties, sex, and age. This study is the first step in determining the relative contributions of material properties and geometry on the structural response of whole ribs, which will provide a basis for improved modeling of rib mechanics. Elucidating the influences of these variables on the structural response of the rib will provide insight into the sources of thoracic injury tolerance variability between different populations.

References

1. Cavanaugh JM, Yoganandan N. Thorax Injury Biomechanics. In: Yoganandan N, Nahum AM, Melvin JW, eds. *Accidental Injury Biomechanics and Prevention*. 3 ed. New York: Springer; 2015:331-372.
2. Galan G, Pe alver J, Par s F, Caffarena Jr J, Blasco E, Borro J, Garc a-Zarza A, Padilla J, Pastor J, Tarrazona V. Blunt Chest Injuries in 1696 Patients. *European journal of cardio-thoracic surgery.* 1992;6(6):284-287.
3. Kent R, Woods W, Bostrom O. Fatality Risk and the Presence of Rib Fractures. Paper presented at: Annals of Advances in Automotive Medicine/Annual Scientific Conference2008.
4. Bulger EM, Arneson MA, Mock CN, Jurkovich GJ. Rib Fractures in the Elderly. *Journal of Trauma and Acute Care Surgery.* 2000;48(6):1040-1047.
5. Kent R, Henary B, Matsuoka F. On the Fatal Crash Experience of Older Drivers. Paper presented at: Annu Proc Assoc Adv Automot Med2005.
6. Augenstein J, Digges K, Bahouth G, Dalmotas D. Investigation of the Performance of Safety Systems for Protection of the Elderly. *Annual Proceedings: Association for the Advancement of Automotive Medicine.* 2005;49:361.
7. Morris A, Welsh R, Hassan A. Requirements for the Crash Protection of Older Vehicle Passengers. Paper presented at: Annu Proc Assoc Adv Automot Med2003.
8. Rhule H, Mallory A, Hagedorn A. Real World Older Occupant Crash Data and Sensitivity of Thor-Nt and Worldsid Dummy Thoraces. Paper presented at: Proceedings of the 22nd Conference on the Enhanced Safety of Vehicles, Paper2011.
9. Ridella SA, Rupp JD, Poland K. Age-Related Differences in Ais 3+ Crash Injury Risk, Types, Causation and Mechanisms. Paper presented at: Ircobi Conference2012.
10. Welsh R, Morris A, Hassan A, Charlton J. Crash Characteristics and Injury Outcomes for Older Passenger Car Occupants. *Transportation research part F: traffic psychology and behaviour.* 2006;9(5):322-334.
11. Foret-Bruno J-Y, Hartemann F, Thomas C, Fayon A, Terrière C, Got C, Patel A. *Correlation between Thoracic Lesions and Force Values Measured at the Shoulder of 92 Belted Occupants Involved in Real Accidents.* SAE Technical Paper;1978. 0148-7191.

12. Kent R, Patrie J. Chest Deflection Tolerance to Blunt Anterior Loading Is Sensitive to Age but Not Load Distribution. *Forensic science international.* 2005;149(2):121-128.
13. Marcus JH, Morgan RM, Eppinger RH, Kallieris D, Mattern R, Schmidt G. *Human Response to and Injury from Lateral Impact.* SAE Technical Paper;1983. 0148-7191.
14. Neathery RF, Kroell CK, Mertz HJ. *Prediction of Thoracic Injury from Dummy Responses.* SAE Technical Paper;1975. 0148-7191.
15. Burstein AH, Reilly DT, Martens M. Aging of Bone Tissue: Mechanical Properties. *J Bone Joint Surg Am.* 1976;58(1):82-86.
16. Lindahl O, Lindgren AG. Cortical Bone in Man. Ii. Variation in Tensile Strength with Age and Sex. *Acta orthopaedica Scandinavica.* 1967;38(2):141.
17. McCalden RW, McGeough JA, Barker MB. Age-Related Changes in the Tensile Properties of Cortical Bone. The Relative Importance of Changes in Porosity, Mineralization, and Microstructure. *J Bone Joint Surg Am.* 1993;75(8):1193-1205.
18. Kemper AR, McNally C, Kennedy EA, Manoogian SJ, Rath AL, Ng TP, Stitzel JD, Smith EP, Duma SM, Matsuoka F. Material Properties of Human Rib Cortical Bone from Dynamic Tension Coupon Testing. *Stapp Car Crash J.* 2005;49(11):199-230.
19. Kemper AR, McNally C, Pullins CA, Freeman LJ, Duma SM, Rouhana SM. The Biomechanics of Human Ribs: Material and Structural Properties from Dynamic Tension and Bending Tests. *Stapp Car Crash Journal.* 2007;51:235-273.
20. Stitzel JD, Cormier JM, Barretta JT, Kennedy EA. Defining Regional Variation in the Material Properties of Human Rib Cortical Bone and Its Effect on Fracture Prediction. *Stapp car crash journal.* 2003;47:243-265.
21. Murach MM, Kang Y-S, Goldman SD, Schafman MA, Schlecht SH, Moorhouse K, Bolte JH, Agnew AM. Rib Geometry Explains Variation in Dynamic Structural Response: Potential Implications for Frontal Impact Fracture Risk. *Annals of Biomedical Engineering.* 2017:1-15.
22. Borchers RE, Gibson LJ, Burchardt H, Hayes WC. Effects of Selected Thermal Variables on the Mechanical Properties of Trabecular Bone. *Biomaterials.* 1995;16(7):545-551.
23. Hamer A, Strachan J, Black M, Ibbotson C, Stockley I, Elson R. Biomechanical Properties of Cortical Allograft Bone Using a New Method of Bone Strength Measurement. *Bone & Joint Journal.* 1996;78(3):363-368.

24. Linde F, Sørensen HCF. The Effect of Different Storage Methods on the Mechanical Properties of Trabecular Bone. *Journal of biomechanics.* 1993;26(10):1249-1252.
25. Panjabi MM, Krag M, Summers D, Videman T. Biomechanical Time-Tolerance of Fresh Cadaveric Human Spine Specimens. *Journal of Orthopaedic Research.* 1985;3(3):292-300.
26. Pelker RR, Friedlaender GE, Markham TC, Panjabi MM, Moen CJ. Effects of Freezing and Freeze-Drying on the Biomechanical Properties of Rat Bone. *Journal of Orthopaedic Research.* 1983;1(4):405-411.
27. Agnew AM, Schafman M, Moorhouse K, White SE, Kang Y-S. The Effect of Age on the Structural Properties of Human Ribs. *Journal of the mechanical behavior of biomedical materials.* 2015;41:302-314.
28. Schafman MA, Kang Y-S, Moorhouse K, White SE, Bolte JH, Agnew AM. Age and Sex Alone Are Insufficient to Predict Human Rib Structural Response to Dynamic Ap Loading. *Journal of Biomechanics.* 2016;49(14):3516-3522.
29. SAE. *Instrumentation for Impact Test.* Warrendale, PA: Society of Automotive Engineers;1995.
30. Unger S, Blauth M, Schmoelz W. Effects of Three Different Preservation Methods on the Mechanical Properties of Human and Bovine Cortical Bone. *Bone.* 2010;47(6):1048-1053.
31. Charpail E, Trosseille X, Petit P, Laporte S. Characterization of Pmhs Ribs: A New Test Methodology. *Stapp car crash journal.* 2005;49:183-198.
32. Subit D, de Dios EdP, Valazquez-Ameijide J, Arregui-Dalmases C, Crandall J. Tensile Material Properties of Human Rib Cortical Bone under Quasi-Static and Dynamic Failure Loading and Influence of the Bone Microstucture on Failure Characteristics2011.
33. Kindig M, Lau AG, Kent RW. Biomechanical Response of Ribs under Quasistatic Frontal Loading. *Traffic injury prevention.* 2011;12(4):377-387.
34. Daegling DJ, Warren MW, Hotzman JL, Self CJ. Structural Analysis of Human Rib Fracture and Implications for Forensic Interpretation. *Journal of forensic sciences.* 2008;53(6):1301-1307.
35. Perz R, Toczyski J, Kindig M, Ito D, Ejima S, Kamiji K, Yasuki T, Crandall J, Subit D. Evaluation of the Geometrical Properties Distribution Along the Human Ribs Using

Different X-Ray Imaging Methods. Paper presented at: International Research Council on the Biomechanics of Injury Conference2013; Gothenburg, Sweden.

36. Yoganandan N, Pintar F. Biomechanics of Human Thoracic Ribs. *Transactions-American Society of Mechanical Engineers Journal of Biomechanical Engineering.* 1998;120:100-105.
37. Currey J. Differences in the Tensile Strength of Bone of Different Histological Types. *Journal of anatomy.* 1959;93(Pt 1):87-95.
38. Currey JD. The Effect of Porosity and Mineral Content on the Young's Modulus of Elasticity of Compact Bone. *Journal of biomechanics.* 1988;21(2):131-139.
39. Schaffler MB, Burr DB. Stiffness of Compact Bone: Effects of Porosity and Density. *Journal of biomechanics.* 1988;21(1):13-16.
40. Vincentelli R, Grigoroy M. The Effect of Haversian Remodeling on the Tensile Properties of Human Cortical Bone. *Journal of biomechanics.* 1985;18(3):201-207.
41. Zioupos P. Ageing Human Bone: Factors Affecting Its Biomechanical Properties and the Role of Collagen. *Journal of Biomaterials Applications.* 2001;15(3):187-229.
42. Mueller KH, Trias A, Ray RD. Bone Density and Composition: Age-Related and Pathological Changes in Water and Mineral Content. *Journal of Bone & Joint Surgery - American Volume.* 1966;48(1):140-148.
43. Yeni Y, Brown C, Norman TL. Influence of Bone Composition and Apparent Density on Fracture Toughness of the Human Femur and Tibia. *Bone.* 1998;22(1):79-84.
44. Agnew AM, Dominguez VM, Sciulli PW, Stout SD. Variability of in Vivo Linear Microcrack Accumulation in the Cortex of Elderly Human Ribs. *Bone reports.* 2017;6:60-63.
45. Agnew AM, Stout SD. Brief Communication: Reevaluating Osteoporosis in Human Ribs: The Role of Intracortical Porosity. *American journal of physical anthropology.* 2012;148(3):462-466.

CHAPTER 9: THE EFFECT OF INJURIOUS WHOLE RIB LOADING ON RIB CORTICAL BONE MATERIAL PROPERTIES

Proposed Authors:

Albert DL, Kang YS, Agnew AM, Kemper AR

Introduction

The chest is one of the most frequently injured body regions in motor vehicle collisions (MVCs). In a study of the National Automotive Sampling System's Crashworthiness Data System (NASS-CDS) from 1993 to 2004, 80% of AIS4+ injuries sustained by United States drivers were to the head and chest [1]. Sustaining AIS3+ rib fractures in a MVC significantly increases a patient's in-hospital mortality risk [2]. Additionally, older adults who suffer severe rib fractures during a MVC are 2.5 times more likely to succumb to their injuries [2].

Finite element models are useful tools to evaluate the effectiveness of thoracic injury mitigation strategies. However, finite element models require validation data, such as subject-specific structural and material properties. While structural tests, such as rib bending tests or thoracic impact tests, require most if not all of a rib, material testing only requires a small section of bone. Therefore, it is possible to obtain cortical bone material properties from a rib that has already undergone structural testing, given that the necessary amount of intact cortical bone remains. This would increase the amount of validation data available for finite element models and decrease the amount of bone material needed to derive both structural and material properties. However, it is currently not known whether the loading experienced during structural tests affects rib cortical bone material properties.

Previous studies have shown that the moduli of cortical bone coupons decrease after being loaded beyond the yield point [3-6]. Consequently, any intact bone remaining after a structural test may have altered material properties, if the bone was loaded beyond the yield point. Unfortunately, previous studies did not evaluate how loading beyond the yield point affected other material properties apart from the modulus. Additionally, some of these studies were performed at lower strain rates (0.001 strain/s) than what would be experienced during an MVC or other traumatic event. Therefore, their results may not be valid at higher strain rates [4,5]. Therefore, the purpose of this study was to quantify the tensile material properties of previously fractured ribs at a strain rate representative of thoracic belt loading during a MVC and compare them to the material properties of unloaded ribs from the same individuals.

Methods

Paired sixth ribs from 18 individuals (10 male, 8 female), ranging from 35 to 99 years of age (mean: 73.2 ± 17.7 years), were included in this study. The ribs were ethically obtained through the Body Donor Program at The Ohio State University and Lifeline of Ohio. The left or right rib was randomly selected to undergo a whole rib anterior-posterior bending test intended to simulate a frontal thoracic impact with a strain rate of approximately 0.5 strain/s [7-9]. During the bending test, the sternal end of the rib was impacted at approximately 2 m/s, causing it to translate toward the vertebral end. Thus, the cutaneous cortex of the rib was loaded in tension. All bending tests resulted in at least one fracture along the length of the rib. Cortical bone from the ribs that sustained fractures during the bending tests as well as the contralateral, untested (control) ribs underwent tension coupon tests to quantify the material properties. The details of the tension coupon preparation, testing, and data analysis are presented in the following sections. Material properties for some of the contralateral ribs were previously reported in Chapter 8 [10].

Specimen Preparation

Dog-bone coupons were fabricated and tested according to the methodology presented in [10-12]. Rectangular sections of the cutaneous cortical bone, measuring 30 mm long and 9 mm wide, were cut from the ribs using a custom-made low-speed circular saw with a diamond encrusted blade. The samples were obtained from the anterior, lateral, and posterior regions of the rib since previous studies have found no significant difference in cortical bone material properties between anatomical regions of the rib within an individual [11,12]. The specific location along the rib that the samples were cut from depended on several factors. Cortical bone was not obtained posterior to the angle of the rib or within an inch of the transition to costal cartilage. Additionally, locations with minimal natural curvature and sufficient width to accommodate a coupon were targeted. For the fractured ribs, an effort was made to obtain cortical bone as far from the fracture as possible. Finally, all samples were aligned with the main axis of the rib. If a rib was not wide enough to accommodate a sample 9 mm in width, the sample was cut to the maximum possible width. After cutting, the sample was wet sanded to a uniform thickness using decreasing grits of sand paper (240, 320, 400, and 600). The sample was then milled into a dog-bone shape using a Computer Numerical Control (CNC) mill (MAXNC 10, Ximotion LLP, Gilbert, AZ) (Figure 9.1). Lastly, the coupons were sanded to a final thickness, which was uniform within ± 0.0127 mm across the entire coupon.

Tension Tests

Each coupon underwent a uniaxial tensile test on a high rate servo-hydraulic Material Testing System (810 MTS, MTS Systems Corporation, Eden Prairie, MN) (Figure 9.2). The coupons were pulled in tension past the point of failure. A custom slack adapter was used to maintain a constant strain rate of approximately 0.5 strain/s. During testing, the coupons were held in place using custom designed grips, which were aligned before testing to ensure the coupons experienced a purely tensile load [11,12]. An extensometer (632.13F-20, MTS, Eden Prairie, MN) measured the change in length of the gage length, while a uniaxial load cell (1500ASK-100, Interface, Scottsdale, AZ) measured the tensile force. All data were collected at 40100.2 Hz and filtered at SAE channel filter class (CFC) 180 [13]. Strain was calculated from the extensometer output by dividing the change in length between the extensometer arms by the initial length between the arms. Stress was calculated by dividing the force by the initial cross-sectional area of the coupon gage length, measured before the test using calipers. The yield point was calculated as the point of intersection between the stress-strain curve and a straight line at a 0.1% strain offset that was parallel to the elastic portion of the curve [14]. The elastic modulus was calculated as the slope between two points on the stress-strain curve that were approximately 10% and 50% of the yield point. The failure stress and failure strain were defined as the stress and strain at the time of failure. Lastly, the strain energy density was calculated as the integral of the stress-strain curve.

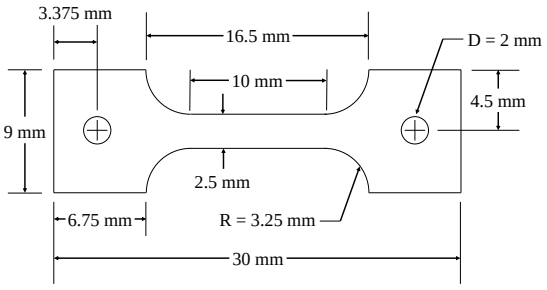

Figure 9.1: Coupon schematic.

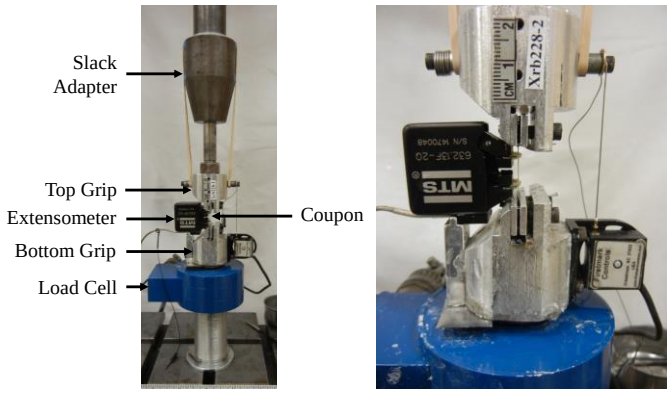

Figure 9.2: Coupon tensile test setup.

Data Analysis

Paired t-tests were used to determine whether there was a significant difference between the material properties of the fractured and control ribs. Additionally, statistical analyses were performed on the data from the previously fractured ribs to determine whether the distance between the coupon location and fracture location (distance to fracture) influenced the material properties. First, the distance to fracture and material properties were tested for normality using a Shapiro-Wilk test. Distance to fracture was not normally distributed ($W = 0.8686$, $p = 0.0169$) so the correlation between distance to fracture and each material property was determined using the non-parametric Spearman's rank correlation (ρ). However, this correlation could be affected by inter-subject variability since it only evaluates the post-fracture material properties and does not account for the difference in material properties between the fractured and control ribs within a subject. In an effort to minimize the influence of inter-subject material property variability on the correlation results, the difference between the fractured and control material properties for each rib was computed. The correlation between the difference in material properties and distance to fracture was then assessed using Spearman's rank correlation. All statistical tests were performed using JMP Pro 13 (SAS Institute Inc., Cary, NC) with an alpha level of 0.05.

Results

Differences were observed between the material properties of the fractured and control ribs. The average modulus, failure stress, and strain energy density were slightly higher for the fractured ribs, while the average yield strain, yield stress, and failure strain were higher for the control ribs

(Table 9.1). Only the yield strain and yield stress were significantly different between the fractured and control ribs (Table 9.1). The stress-strain curves for the fractured ribs showed a less distinct transition from the elastic to plastic regions, with yielding occurring lower on the curve compared to the control ribs (Figure 9.3).

The average distance between the center of the coupon to the location of fracture on the previously tested ribs was 55.3 ± 27.8 mm (range: 17 to 131 mm). The modulus was the only material property that had a significant correlation with distance to fracture (Table 9.2). However, accounting for inter-subject variation by taking the difference between the material properties of the fractured and control ribs resulted in no significant correlation with distance to fracture (Table 9.2).

Table 9.1: Measured material properties and t-test results.

Material Property	Units	Control Average	Fractured Average	t	p-value
Modulus	GPa	12.46	13.42	1.2507	0.2280
Yield Strain	μstrain	6491	5185	5.2579	**< 0.0001**
Yield Stress	MPa	69.64	59.33	3.6621	**0.0019**
Failure Strain	μstrain	24444	24252	0.1945	0.8481
Failure Stress	MPa	105.67	108.65	0.9725	0.3444
Strain Energy Density	MPa- μstrain	2084269	2238447	0.7842	0.4437

Note: Bolded values indicate significance at $p < 0.05$.

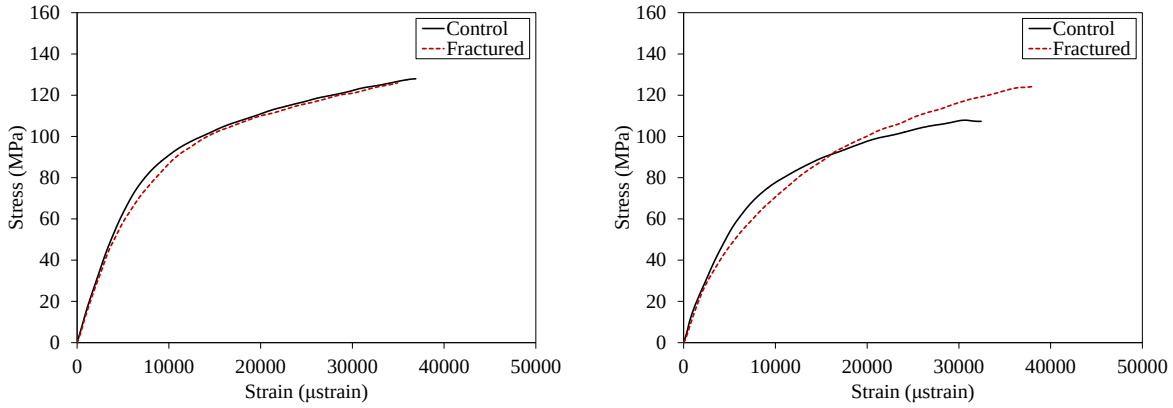

Figure 9.3: Exemplar stress-strain curves from two subjects.

Table 9.2: Statistical correlations with distance to fracture.

Material Property	Fractured Material Properties		Difference Between Fractured and Control Material Properties	
	Spearman's ρ	p-value	Spearman's ρ	p-value
Modulus	0.4707	**0.0487**	0.0321	0.8993
Yield Strain	0.0902	0.7219	-0.2250	0.3694
Yield Stress	0.3971	0.1027	-0.2478	0.3215
Failure Strain	0.1182	0.6404	0.0881	0.7280
Failure Stress	0.3577	0.1450	-0.2322	0.3537
Strain Energy Density	0.2291	0.3604	0.0073	0.9772

Note: Bolded values indicate significance at $p < 0.05$.

Discussion

The current study evaluated the difference in cortical bone material properties between intact ribs and ribs previously loaded to failure. Previous studies on human and bovine cortical bone coupons reported decreases in modulus [3,4,6], a "softening" of the yield point on the stress-strain curve [3,15], and increasing non-linearity of the stress-strain curve [4] as a result of repetitive loading. The results of the current study also showed a less distinct yield point and a smaller linear region in the stress-strain curve for the cortical bone from previously fractured ribs. However, no decrease in modulus was observed for the previously fractured ribs, which did not align with the decrease in modulus reported in the literature. It should be noted that the results of the current study are not a direct comparison to those reported in the literature since the single bending test that loaded the cortical bone in this study is inherently different from the repetitive, fatigue loading conducted on the cortical bone coupons in the literature. Additionally, the results of previous studies may be dependent on the method used to calculate the modulus. For example, Courtney *et al.* (1996) exposed human femur cortical bone coupons to two consecutive tensile loading cycles beyond the yield point to 0.01 strain [5]. They reported a 33% decrease in modulus for the second loading cycle. However, the modulus was calculated using different methods for the first and second loading cycles, which may have influenced this result.

For the current study, care was taken to calculate the modulus consistently between the fractured and control ribs. For all tests, the modulus was calculated over a region of the stress-strain curve defined as 10-50% of the yield point. Since the yield point was significantly lower for the fractured

ribs, the modulus was calculated over a lower range of stress and strain compared to the control ribs. In order to determine whether this difference influenced the outcome of the study, the moduli of the control ribs were recalculated over the same range of stresses as their fractured counterparts. A paired t-test was used to compare the adjusted modulus of the control ribs to the modulus of the fractured ribs and no significant difference was observed ($p = 0.4491$).

The range of the stress-strain curve used to calculate the modulus was carefully chosen to encompass the linear portions of the stress-strain curves for both the fractured and control ribs. As noted above, this linear region was smaller for the fractured ribs. If the modulus was evaluated over a higher percentage of the yield point, this would still encompass the linear region of the stress-strain curves for the control ribs, but would include part of the nonlinear region of the stress-strain curve (i.e. the area around the yield point) for the fractured ribs. Including some of the nonlinear region of the stress-strain curve in the modulus calculation for the fractured ribs would likely result in a lower modulus value. However, this would not be an accurate representation of the modulus for the fractured ribs since the modulus would be defined over a nonlinear region.

Composite materials, such as bone, typically exhibit a decreased modulus and ultimate stress after being loaded beyond the yield point [4]. Therefore, the finding that only yield stress and yield strain were significantly different between the fractured and control ribs was unexpected. A possible explanation for the lack of significance for the modulus and failure stress is that intra-subject variation confounded the results. In order to evaluate this possibility, the average absolute differences between the fractured and control ribs for each material property were compared to the intra-subject standard deviations observed in previously published tests conducted using the same test setup (Table 9.3) [11,12]. The average absolute differences were less than the intra-subject standard deviations for all material properties except for yield stress and failure stress. This indicates that the average absolute difference between the fractured and control ribs for yield stress and failure stress exceeds the expected amount of intra-subject standard deviation. Therefore, an increased sample size may increase the statistical power enough to detect a significant difference in failure stress.

Another factor to consider when interpreting the results of this study was whether the distance between the sample and the fracture location influenced the material properties of the fractured ribs. More cortical bone damage (i.e. amount of microcracks) would be expected immediately adjacent to the fracture location as opposed to several centimeters away from the fracture location. Therefore, a gradient of damage may exist along the length of the rib relative to the fracture location, such that the amount of cortical bone damage decreases with increasing distance from the fracture location. This gradient of damage would likely correspond to a gradient of material property changes, with the greatest material properties changes occurring adjacent to the fracture. When the influence of distance to fracture on the material properties was statistically assessed, a significant positive correlation was found between the modulus and distance to fracture. However, this result and the lack of statistical significance for the other material properties could have been confounded by inter-subject variability, which is of particular importance since the subjects in this study spanned a wide age range. Consequently, the correlation between distance to fracture and the difference between the fractured and control material properties for each rib pair was assessed. None of the material property differences were significantly correlated with distance to fracture, which may be a result of two factors. First, it is possible that samples were taken over a range of distances that was too narrow to detect significant differences in material properties caused by a gradient of damage. Second, the coupons may have been obtained from a region of the rib that was sufficiently far from the fracture such that the cortical bone was not loaded beyond the yield point. This explanation assumes that damage would be localized to the area around the fracture. Therefore, the material properties of a coupon taken a certain distance away from the fracture would not be significantly influenced by a damage gradient. Given that yield stress and yield strain were significantly different between the fractured and control ribs, some damage had to be present in the coupons from the fractured ribs to cause a change in material properties. This lends support to the first explanation. However, the disparity between the current study and the literature on whether the modulus is significantly affected by post-yield loading may indicate that the coupons from the current study were taken too far from the fracture to affect the modulus. Therefore, it is likely that the results were influenced by the coupons being taken both from a narrow range of locations as well as too far from the fracture for some material properties to be affected.

The main limitations of this study were due to subject size and sample demographics. A larger sample size would provide more statistical power to overcome inter-subject variability. Additionally, the design of this study was based upon on the findings of previous studies that rib material properties do not vary significantly within a subject [11,12]. However, intra-subject variability can still influence the results if only one sample is taken from each subject for each test condition, as was done in this study. Testing multiple samples would reduce the influence of intra-subject variability on material properties and results, but is not always feasible when a limited amount of bone is available. Finally, the subjects included in this study spanned a wide range of ages, but only one subject was less than 50 years old. Courtney *et al.* (1996) reported differences in damage accumulation between cortical bone samples from young (26 ± 5 years) and elderly (72 ± 6 years) subjects that were loaded in tension to failure [5]. Therefore, it is possible that the material properties of younger and older subjects could be affected differently by post-yield loading.

Table 9.3: Comparison of average absolute differences to intra-subject standard deviations from the literature.

Material Property	**Units**	**Average Absolute Difference Between Fractured and Control Material Properties**	**Intra-subject Standard Deviation from [11,12]**
Modulus	GPa	2.54	3.28
Yield Strain	μstrain	1515	1609
Yield Stress	MPa	17.78	15.76
Failure Strain	μstrain	8295	9943
Failure Stress	MPa	29.54	27.59
Strain Energy Density	MPa-μstrain	1186956	1413554

Conclusions

The current study found that the material response of cortical bone obtained from previously fractured ribs was qualitatively and quantitatively different from the cortical bone obtained from the control ribs. Yielding occurred earlier and more gradually in the stress-strain curve for the fractured ribs. Consequently, the fractured ribs had significantly lower yield stresses and yield strains compared to the control ribs. However, the modulus, failure stress, failure strain, and strain energy density were not significantly different between the fractured and control ribs. Therefore, it may be possible to estimate the pre-failure modulus, failure strain, failure stress, and strain

energy density of the cortical bone from a rib that was tested in similar conditions as the whole rib bending tests, provided the tested coupon is sufficiently far from the location of fracture. This finding can facilitate the derivation of subject-specific material and structural properties for use in finite element models. However, due to the limited sample size and variance within an individual, additional testing is needed to more thoroughly evaluate how injurious loading affects material properties along the length of a rib.

References

1. Liu C, Utter D, Chen C-L. *Characteristics of Crash Injuries among Young, Middle-Aged, and Older Drivers.* 2007.
2. Kent R, Woods W, Bostrom O. Fatality Risk and the Presence of Rib Fractures. Paper presented at: Annals of Advances in Automotive Medicine/Annual Scientific Conference2008.
3. Burstein A, Reilly D, Frankel V. Failure Characteristics of Bone and Bone Tissue. *Perspectives in Biomedical Engineering*: Springer; 1973:131-134.
4. Carter D, Hayes WC. Compact Bone Fatigue Damage—I. Residual Strength and Stiffness. *Journal of Biomechanics.* 1977;10(5-6):325-337.
5. Courtney AC, Hayes WC, Gibson LJ. Age-Related Differences in Post-Yield Damage in Human Cortical Bone. Experiment and Model. *Journal of biomechanics.* 1996;29(11):1463-1471.
6. Nyman JS, Roy A, Reyes MJ, Wang X. Mechanical Behavior of Human Cortical Bone in Cycles of Advancing Tensile Strain for Two Age Groups. *Journal of Biomedical Materials Research Part A.* 2009;89(2):521-529.
7. Agnew AM, Schafman M, Moorhouse K, White SE, Kang Y-S. The Effect of Age on the Structural Properties of Human Ribs. *Journal of the mechanical behavior of biomedical materials.* 2015;41:302-314.
8. Murach MM, Kang Y-S, Goldman SD, Schafman MA, Schlecht SH, Moorhouse K, Bolte JH, Agnew AM. Rib Geometry Explains Variation in Dynamic Structural Response: Potential Implications for Frontal Impact Fracture Risk. *Annals of Biomedical Engineering.* 2017:1-15.
9. Schafman MA, Kang Y-S, Moorhouse K, White SE, Bolte JH, Agnew AM. Age and Sex Alone Are Insufficient to Predict Human Rib Structural Response to Dynamic Ap Loading. *Journal of Biomechanics.* 2016;49(14):3516-3522.
10. Albert DL, Kang Y-S, Agnew AM, Kemper AR. A Comparison of Rib Structural and Material Properties from Matched Whole Rib Bending and Tension Coupon Tests. Paper presented at: IRCOBI Conference Proceedings2017.

11. Kemper AR, McNally C, Kennedy EA, Manoogian SJ, Rath AL, Ng TP, Stitzel JD, Smith EP, Duma SM, Matsuoka F. Material Properties of Human Rib Cortical Bone from Dynamic Tension Coupon Testing. *Stapp Car Crash J.* 2005;49(11):199-230.
12. Kemper AR, McNally C, Pullins CA, Freeman LJ, Duma SM, Rouhana SM. The Biomechanics of Human Ribs: Material and Structural Properties from Dynamic Tension and Bending Tests. *Stapp Car Crash Journal.* 2007;51:235-273.
13. SAE. *Instrumentation for Impact Test.* Warrendale, PA: Society of Automotive Engineers;1995.
14. Unger S, Blauth M, Schmoelz W. Effects of Three Different Preservation Methods on the Mechanical Properties of Human and Bovine Cortical Bone. *Bone.* 2010;47(6):1048-1053.
15. Fondrk M, Bahniuk E, Davy D, Michaels C. Some Viscoplastic Characteristics of Bovine and Human Cortical Bone. *Journal of biomechanics.* 1988;21(8):623-630.

CHAPTER 10: SUMMARY

The objective of this dissertation was to evaluate the biomechanical responses of human surrogates under various frontal loading conditions. In order to meet this objective, full-scale frontal sled tests were performed on three different human surrogates: the 50th percentile male Hybrid III (HIII) anthropomorphic test device (ATD), the 50th percentile male Test Device for Human Occupant Restraint (THOR-M) ATD, and approximately 50th percentile male post-mortem human surrogates (PMHS). All surrogates were tested under three safety restraint conditions: knee bolster (KB), KB and steering wheel airbag (KB/SWAB), and knee bolster airbag and SWAB (KBAB/SWAB). The kinematic, lower extremity, abdominal, thoracic, and neck responses were then compared between surrogates and restraint conditions. Additionally, material property testing was performed on human rib cortical bone at a strain rate similar to those observed in frontal impacts. The influence of age, sex, and injurious loading on the material properties was investigated, and the relationships between analogous structural and material properties were quantified.

Incorporating KBs and KBABs from production vehicles into laboratory sled tests can be challenging. Therefore, rigid polyurethane foams were proposed as surrogate KB and KBABs. In order to assess the human surrogate responses to KB and KBAB loading during the frontal sled tests, the foam KBs and KBABs had to be validated. Indentation tests on a range of foams with different compressive strength ratings showed that the stiffness of the 65 psi foam was representative of production sedan KBs. The 19 psi foam had the lowest stiffness and was selected to represent the KBAB. Then, the selected foam KBs and KBABs were used in frontal sled tests with the HIII that were designed to match New Car Assessment Program (NCAP) full vehicle tests for the 2005 (KB) and 2012 (KBAB) Toyota Camry. The HIII femur forces, tibia forces, pelvis accelerations, and chest accelerations from the sled tests matched those observed in the NCAP tests for the respective restraint conditions. Therefore, the 65 psi and 19 psi foams were found to be acceptable surrogates for KBs and KBABs, respectively, and these foams were used in the subsequent sled tests that compared surrogate responses under the three safety restraint conditions.

First, the kinematic responses of the HIII, THOR-M, and PMHS were evaluated for the three safety restraint conditions. All surrogates were instrumented with accelerometers and angular rate sensors

at the head, chest, and pelvis. Additionally, motion capture was used to quantify the head, should, hip, knee, and ankle excursions of each surrogate. All surrogates showed sensitivity to changes in restraint condition. For example, the use of a KBAB decreased the pelvis accelerations and the forward excursions of the knees and hips for all surrogates. However, these trends were not observed for the thorax, shoulders, and head, which showed more sensitivity to the presence of the SWAB. An objective rating metric was used to compare the ATD responses to the PMHS, in order to assess the biofidelity of each ATD. The results of the objective rating analysis indicated that the HIII and THOR-M had comparable overall biofidelity scores, but the HIII's score was slightly higher. The THOR-M slightly out-performed the HIII for the acceleration and angular velocity data. However, the HIII scored slightly better than the THOR-M for the excursion data. The most notable difference in biofidelity was for the knee excursions, where the HIII had a much higher average ISO score.

Second, the lower extremity responses of the HIII, THOR-M, and PMHS were evaluated for the three safety restraint conditions. ATD lower extremity forces and moments were quantified using load cells. However, PMHS lower extremity forces and moments were measured using arrays of strain gages (bone cells). In order to validate the PMHS femur forces and moments, the ratio of the measured lower extremity forces to forces measured by external reaction load cells at the bolster supports and foot supports was compared between all surrogates. The PMHS femur forces produced ratios that were comparable to the other surrogates. However, limitations in the instrumentation at the foot support precluded validation of the tibia forces. Due to the complexity of the loading environment, the PMHS lower extremity moments could not be validated in a similar fashion. When comparing the time histories between surrogates, the ATDs generally experienced similar lower extremity forces and moments. The PMHS femur axial forces were similar to the ATDs, but slightly lower in magnitude for the KB conditions. The PMHS tibia axial force time histories were similar in shape to the ATDs, but were much lower in magnitude for all conditions. The PMHS AP bending moments showed more variability in peak timing and magnitude; therefore, trends were difficult to observe. Established injury risk curves were used to predict ATD lower extremity injury risk. The predicted injury risks partially supported the findings of real-world crash analyses, i.e., KBABs decreased the risk of femur injury. However, the effect of KBABs on tibia injury prediction varied with respect to surrogate type, injury metric, and location

on the tibia. Future work will perform more controlled calibrations on the PMHS bone cells so that the ATD lower extremity responses can be assessed using validated PMHS force and moment data.

Third, the abdominal pressures of the THOR-M and PMHS were evaluated for the three safety restraint conditions. The THOR-M abdomen was instrumented with left and right pressure sensors at the level of the hollow organs. A novel method was developed to instrument the liver and spleen of PMHSs in order to measure internal organ pressure during the sled tests. Pressure sensors were successfully placed in both organs for all PMHS tests, and the internal liver pressures were not statistically significantly different from those reported in previous literature based on *ex vivo* data from an invasive methodology and *in situ* data from a non-invasive methodology. The THOR-M abdominal pressures were lower than the PMHS organ pressures and demonstrated a sensitivity to restraint condition. PMHS organ pressures did not show a sensitivity to restraint condition due to the high amount of inter-subject variation.

Fourth, the neck kinetics of the HIII, THOR-M, and PMHS were evaluated for the three safety restraint conditions. ATD neck forces and moments were quantified at the upper and lower neck using load cells. Inverse dynamics was used to quantify the PMHS neck kinetics. However, head contact with vehicle components occurred before appreciable loading occurred so any comparisons made between the PMHS and ATDs were limited. Overall, the HIII and THOR-M had different neck kinetics, particularly for anterior/posterior shear force and bending moment about the y-axis. Specifically, the HIII experienced higher upper neck bending moments about the y-axis compared to the THOR-M. This is likely due to the very different neck designs of the two ATDs. Despite these differences, both ATDs still accurately predicted a low risk of AIS3+ neck injury.

Fifth, the thoracic responses of the HIII, THOR-M, and PMHS were evaluated for the three safety restraint conditions. Internal thoracic deflection was measured for the ATDs at the sternum for the HIII and the upper left, upper right, lower right, and lower left for the THOR-M. External deflections were quantified for each surrogate at locations analogous to the internal deflection measurement locations of each ATD. Since external deflection could not be measured at analogous locations for all surrogates, the external deflections were used to evaluate ATD thoracic biofideltiy. Overall, the ATDs exhibited several differences in thoracic biofideltiy. The THOR-M experienced

expansion at the lower left thorax that was also observed in some PMHS tests. However, the THOR-M lower right thorax was too compliant and deflected much more than the HIII and PMHS, which had comparable responses. The HIII and THOR-M had opposing sensitivities to restraint condition. The KB condition had the greatest predicted injury risk for the HIII, but the lowest predicted injury risk for the THOR-M. No consistent trends were observed for the PMHSs between restraint conditions so the biofidelity of the ATDs' sensitivity to restraint condition could not be evaluated. An objective rating metric was used to compare the ATD responses to the PMHS, in order to assess the biofidelity of each ATD. The results of this analysis indicated that the HIII had slightly better biofidelity than the THOR-M, despite the design changes in the THOR that were intended to improve thoracic biofidelity relative to the HIII. However, the external deflections from the chest band may not completely represent the internal deflections of the ribs due to the skin of the HIII and PMHS and the jacket of the THOR. Current injury risk metrics under-predicted the observed injury rate for the HIII and PMHS, while the proposed THOR-M injury metrics more accurately predicted the observed injuries. The time of AIS3 injury was quantified for each PMHS and was compared to the time of peak deflection. For most tests, AIS3 injuries occurred before peak deflection and at relatively low predicted injury risks. This indicates that the current injury risk criteria that rely on peak deflection are over-predicting the magnitude of chest deflection necessary to cause injuries, thereby under-predicting injury risk.

Finally, statistical analyses were used to: investigate the influence of age, sex, and injurious loading on the rib cortical bone material properties and explore the relationships between whole rib structural properties and cortical bone material properties. Whole rib bending tests, intended to simulate rib loading during a frontal impact, were performed to quantify the whole rib structural properties. Tensile coupon tests were performed on uninjured rib cortical bone from the same subjects to quantify the matched material property response. Positive correlations were observed for most pairs of structural and material properties. Coupon strain energy density and whole rib total energy had the highest correlation, while coupon modulus and whole rib stiffness had the lowest correlation. Peak tensile strain, failure force, total energy, and plastic energy were more influenced by material properties compared to the stiffness, yield displacement, yield force, failure displacement, and elastic energy. All structural/material property comparisons resulted in R^2 values below 0.5, indicating the material properties did not explain the majority of the variance of

the structural properties. Given that the structural response is dependent on both the material and geometric properties, this finding lends further support to the hypothesis that local and global rib geometries likely have a strong influence on the structural properties. Negative correlations with age were observed for all material properties. The correlations with age were significant for the modulus, yield stress, failure strain, failure stress, SED, and plastic SED. Conversely, yield strain and elastic SED did not significantly correlate with age. Neither sex nor the interaction between sex and age significantly influenced the material properties. However, a larger, more diverse sample may be needed further explore the relationships between the material properties, sex, and age.

Tensile material testing was also performed on cortical bone coupons from the fractured ribs that underwent the whole rib bending test. The material response of cortical bone obtained from previously fractured ribs was qualitatively and quantitatively different from the cortical bone obtained from the uninjured (control) ribs. Yielding occurred earlier and more gradually in the stress-strain curve for the fractured ribs. Consequently, the fractured ribs had significantly lower yield stresses and yield strains compared to the control ribs. However, the modulus, failure stress, failure strain, and strain energy density were not significantly different between the fractured and control ribs. Therefore, it may be possible to estimate the pre-failure modulus, failure strain, failure stress, and strain energy density of the cortical bone from a rib that was tested in similar conditions as the whole rib bending tests, provided the tested coupon is sufficiently far from the location of fracture.

Expected Publications

The expected publications for this research are shown in Table 10.1.

Table 10.1: Expected Publications.

Citation	Chapter
Devon L. Albert, Stephanie M. Beeman, Craig McNally, Andrew R. Kemper, "Evaluation of rigid polyurethane foam as a surrogate material for knee bolsters and knee bolster airbags in full scale frontal sled tests. Short communications from AAAM's 60th annual scientific conference," *Traffic Injury Prevention*, 17(sup1), pp205-208, 2016.	2
Devon L. Albert, Stephanie M. Beeman, Craig McNally, Andrew R. Kemper, "Foam surrogates for use as knee bolsters and knee bolster airbags in frontal sled tests: evaluation of compressive properties and responses due to occupant loading," *Biomedical Sciences Instrumentation*, 53, 2017.	2
Devon L. Albert, Stephanie M. Beeman, Andrew R. Kemper, "Occupant kinematics of the Hybrid III, THOR-M, and postmortem human surrogates under various restraint conditions in full-scale frontal sled tests," *Traffic Injury Prevention*, 19(sup1), ppS50-S58, 2018.	3
Devon L. Albert, Stephanie M. Beeman, Warren N. Hardy, "Lower Extremity Responses of the Hybrid III, THOR-M, and Post-Mortem Human Surrogates under Various Restraint Conditions in Full-Scale Frontal Sled Tests," **(proposed)**	4
Devon L. Albert, Stephanie M. Beeman, Andrew R. Kemper, "A method for measuring pressures in the liver and spleen of post-mortem human surrogates during full-scale frontal sled tests," *Biomedical Sciences Instrumentation*, 53, 2017.	5
Devon L. Albert, Stephanie M. Beeman, Andrew R. Kemper, "Evaluation of Hybrid III and THOR-M Neck Kinetics and Injury Risk under Various Restraint Conditions during Full-Scale Frontal Sled Tests," *Traffic Injury Prevention*, **(proposed)**	6
Devon L. Albert, Stephanie M. Beeman, Andrew R. Kemper, "Thoracic Responses of the Hybrid III, THOR-M, and Post-Mortem Human Surrogates under Various Restraint Conditions in Full-Scale Frontal Sled Tests," *Stapp Car Crash Journal*, **(proposed)**	7
Devon L. Albert, Yun-Seok Kang, Amanda M. Agnew, Andrew R. Kemper, "A Comparison of Rib Structural and Material Properties from Matched Whole Rib Bending and Tension Coupon Tests," *IRCOBI Conference Proceedings*, Sept 13-15, Antwerp Belgium, 2017.	8
Devon L. Albert, Yun-Seok Kang, Amanda M. Agnew, Andrew R. Kemper, "The Influence of Sex and Age on Rib Cortical Bone Material Properties," **(proposed)**	8
Devon L. Albert, Yun-Seok Kang, Amanda M. Agnew, Andrew R. Kemper, "The Effect of Injurious Whole Rib Loading on Rib Cortical Bone Material Properties," *IRCOBI Conference Proceedings*, **(proposed)**	9